ΕΛΛΗΝΙΚΗ ΔΗΜΟΚΡΑΤΙΑ
Εθνικόν και Καποδιστριακόν
Πανεπιστήμιον Αθηνών
ΙΔΡΥΘΕΝ ΤΟ 1837

NATIONAL AND KAPODISTRIAN UNIVERSITY OF ATHENS
Department of Chemistry

AGRICULTURAL UNIVERSITY OF ATHENS
DEPARTMENT OF FOOD SCIENCE AND HUMAN NUTRITION

POSTGRADUATE PROGRAMME
"ORGANIC SYNTHESIS AND ITS APPLICATIONS IN THE CHEMICAL INDUSTRY"

RESEARCH THESIS

«Computational study of SARS - CoV - 2 protein / ligand interactions with the aim of testing already known molecules and designing new drugs» & «Synthesis of Co^{II} Complexes Coordinated with Pincer Ligands bearing NHC Donors and Their Use in Ketone Hydrogenation Reactions»

LIGIELLI IRENE
CHEMIST

ATHENS
OCTOBER 2021

RESEARCH THESIS

«Computational study of SARS - CoV - 2 protein / ligand interactions with the aim of testing already known molecules and designing new drugs» & «Synthesis of Co^{II} Complexes Coordinated with Pincer Ligands bearing NHC Donors and Their Use in Ketone Hydrogenation Reactions»

LIGIELLI IRENE
A.M.: 191516

SUPERVISOR: Georgios C. Vougioukalakis, Associate Professor

THREE-MEMBER EXAMINATION COMMITTEE:

Georgios C. Vougioukalakis, Associate Professor
Thomas Mavromoustakos, Professor
Andreas Danopoulos, Professor

October 2021

ABSTRACT

Computational rational drug design is a useful tool, both in testing the efficiency of already known molecules, and in designing new drugs. Typically, drugs act on specific target compounds, such as proteins, DNA, or lipid bilayers. Based on the functionality of the AutoDock program, the proteins of SARS - CoV - 2, also known as the coronavirus, the virus that causes the respiratory disease COVID-19, which is responsible for the pandemic that we are experiencing to this day, were examined. During the molecular binding experiments, specific algorithms and evaluation functions are used in order to study the strength of the binding score with the receptor, as well as the type of interactions. AutoDock is a program that uses a set of algorithms to solve specific problems. Such algorithms are the Monte Carlo Simulated Annealing (SA), Genetic Algorithm (GA), and the hybrid local search GA algorithm, also known as the Lamarckian Genetic Algorithm (LGA). Molecular binding experiments in the protein receptors using sartans and their analogues and derivatives of curcumin were performed using AutoDock, in order to better understand their mechanism of action. This was followed by testing the activity of known drugs, which have been used or are being studied against the coronavirus. A total of 5 receptors were examined: a) the active site of the main protease, b) the receptor binding site of the Spike protein, c) ACE2 after ligation with the Spike protein, d) the B chain of the Spike protein, and e) the metallocenter of the Spike protein. The aim was to understand whether the creation by nature of hybrid composite forms lead in more favorable binding and the comparison between them.

NHCs (N-heterocyclic carbenes) have become well-established ligands in transition metal catalysis. Being 2 electron donor-ligands, like phosphines, along with their tendency for strong σ donation make NHCs a unique family of ligands. Although the entry of NHCs into the modern organometallic and coordination chemistry scene coincides with the introduction of the stable imidazol-2-ylidenes by Arduengo, some of the first attempts to access complexes by trapping transient or *in situ* generated NHCs started much earlier and many involved 3d base metals including cobalt. Furthermore, NHCs are known to form strong bonds with transition metals, thereby enhancing the stability of the complex and improving the catalytic efficiency. The remarkable advances of N-heterocyclic carbene (NHC)

transition metal complexes that followed their availability, have a major impact in fundamental and applied chemistry, as documented in the rapidly increasing number of books and review articles dedicated to these topics.

Pincer ligands are continually attracting attention owing to the unusual properties they impart on metal centers and, therefore, on the complexes they are involved in. These ligands and their metal complexes have assisted in the understanding of a number of processes mediated by organometallic and non-organometallic systems. In homogenous catalytic transformations, pincer ligands provide improved chemical and thermal stability. These ligands also offer the ability to fine tune the electronic and the steric properties of the metal center, thereby increasing the scope of their applications. Non-innocent ligands sometimes play a role in stabilizing such complexes, rendering the 'observed oxidation-state' of the metal center ambiguous. Non-noble metal catalysts based on pincer type ligands are of special interest for organometallic chemistry and organic synthesis. Next to iron and manganese, currently cobalt–pincer type complexes are successfully applied in a range of catalytic reactions.

Based on the above, in the present Research Thesis, two complexes of Co^{II} with Pincer ligands containing NHCs, were synthesized in order to study their catalytic activity in the reduction reactions of ketones. In order to examine this reaction, two different paths were followed depending on the Hydrogen source. In one case the hydrogenation of ketones was carried out with the assistance of an autoclave, which provided H_2 pressured gas. In the other case, *i*-PrOH, was used both as a solvent and as a Hydrogen source in a transfer hydrogenation reaction. During the development of the catalytic protocol, emphasis was placed on the efficient use of low catalytic loading.

SUBJECT AREA: Molecular Docking, Drug Design, Organometallic Chemistry, NHC Ligands
KEYWORDS: Molecular modeling, Drug design, SARS - CoV - 2, COVID - 19, AutoDock, Proteins, Organometallic chemistry, Catalysis, N-heterocyclic carbenes, Pincer ligands, Cobalt, Organometallic Synthesis, Hydrogenation, Transfer Hydrogenation

ΠΕΡΙΛΗΨΗ

Ο υπολογιστικός ορθολογικός σχεδιασμός αποτελεί ένα χρήσιμο εργαλείο για τόσο στον έλεγχο αποδοτικότητας ήδη γνωστών μορίων, όσο στο σχεδιασμό νέων φαρμακευτικών σκευασμάτων. Συνήθως, οι φαρμακευτικές ουσίες δρουν σε συγκεκριμένες ενώσεις-στόχους, όπως για παράδειγμα πρωτεΐνες, DNA ή λιπιδικές διπλοστιβάδες. Με βάση τη λειτουργικότητα του προγράμματος AutoDock, εξετάστηκαν οι πρωτεΐνες του SARS - CoV - 2, γνωστός και ως κορονοϊός, είναι ο ιός που προκαλεί την αναπνευστική ασθένεια COVID-19, που ευθύνεται για την πανδημία, που βιώνουμε μέχρι και σήμερα. Στη διάρκεια των πειραμάτων της μοριακής πρόσδεσης γίνεται χρήση συγκεκριμένων αλγορίθμων και συναρτήσεων αξιολόγησης προκειμένου να μελετηθεί η ισχύς της αλληλεπίδρασης του προσδέτη με τον υποδοχέα, αλλά και το είδος των αλληλεπιδράσεων. Το AutoDock είναι ένα πρόγραμμα το οποίο χρησιμοποιεί ένα σύνολο αλγορίθμων για την επίλυση συγκεκριμένων προβλημάτων. Τέτοιοι αλγόριθμοι είναι οι Monte Carlo Simulated Annealing (SA), Genetic Algorithm (GA) και ο υβριδικός αλγόριθμος local search GA, γνωστός και ως Lamarckian Genetic Algorithm (LGA). Διεξήχθησαν πειράματα μοριακής πρόσδεσης μέσω του AutoDock σε πρωτεϊνικούς υποδοχείς με τη χρήση σαρτανών και παραγώγων τους, παραγώγων της κουρκουμίνης, με σκοπό την πληρέστερη κατανόηση του μηχανισμού δράσης τους. Ύστερα ακολούθησε έλεγχος της δραστικότητας, γνωστών σκευασμάτων, τα οποία έχουν χρησιμοποιηθεί ή μελετώνται για την αντιμετώπιση του κορονοϊού. Συνολικά εξετάστηκαν 5 υποδοχείς: α) το ενεργό κέντρο της κύριας πρωτεάσης, β) την περιοχή δέσμευσης υποδοχέα (RBD) της πρωτεΐνης Spike, γ) το ACE2 μετά τη σύμπλεξη με την πρωτεΐνη Spike, δ) την αλυσίδα Β της πρωτεΐνης Spike και ε) το μεταλλικό κέντρο της πρωτεΐνης Spike. Στόχος ήταν να κατανοηθεί εάν η δημιουργία από τη φύση υβριδικών συνθέτων μορφών οδηγεί σε μόρια με ευνοϊκή πρόσδεση και η σύγκριση μεταξύ τους.

Τα NHC (N-ετεροκυκλικά καρβένια) έχουν γίνει καλά εδραιωμένοι υποκαταστάτες στην κατάλυση με χρήση μετάλλων μετάπτωσης. Το γεγονός ότι είναι δότες 2 ηλεκτρονίων, όπως οι φωσφίνες, σε συνδυασμό με την τάση τους για ισχυρή σ δοτικότητα, καθιστούν τα NHCs μια μοναδική οικογένεια υποκαταστατών. Παρόλο που η είσοδος των NHC στη σύγχρονη οργανομεταλλική χημεία και χημεία συντονισμού συμπίπτει με την εισαγωγή των σταθερών ιμιδαζολ-2-υλιδενίων από

τον Arduengo, μερικές από τις πρώτες προσπάθειες σύνθεσης συμπλόκων με την παγίδευση παροδικών ή επί τόπου παραγόμενων NHCs ξεκίνησαν πολύ νωρίτερα και πολλές συμπεριλάμβαναν 3d μέταλλα, συμπεριλαμβανομένου και του κοβαλτίου. Επιπλέον, είναι γνωστό ότι οι NHC υποκαταστάτες σχηματίζουν ισχυρούς δεσμούς με τα μέταλλα μεταπτώσεως, ενισχύοντας έτσι τη σταθερότητα των συμπλόκων και βελτιώνοντας την καταλυτική τους απόδοση. Η αξιοσημείωτη πρόοδος των συμπλόκων με μετάλλα μετάπτωσης και Ν-ετεροκυκλικά καρβένια (NHC) που ακολούθησαν, σε συνδυασμό με τη διαθεσιμότητά τους, έχουν σημαντικό αντίκτυπο στη θεμελιώδη και εφαρμοσμένη χημεία, όπως τεκμηριώνεται στον ταχέως αυξανόμενο αριθμό βιβλίων και άρθρων αφιερωμένων σε αυτά τα θέματα.

Οι υποκαταστάτες τύπου Pincer προσελκύουν συνεχώς την προσοχή λόγω των ασυνήθιστων ιδιοτήτων που προσδίδουν στο μεταλλικό κέντρο και, ως εκ τούτου, στα σύμπλοκα στα οποία εμπλέκονται. Αυτοί οι υποκαταστάτες και τα αντίστοιχα μεταλλικά τους σύμπλοκα έχουν βοηθήσει στην κατανόηση μιας σειράς διαδικασιών που προκαλούνται από οργανομεταλλικά και μη οργανομεταλλικά συστήματα. Σε ομοιογενείς καταλυτικούς μετασχηματισμούς, οι υποκαταστάτες τύπου Pincer παρέχουν βελτιωμένη χημική και θερμική σταθερότητα. Αυτοί οι υποκαταστάτες προσφέρουν επίσης τη δυνατότητα ρύθμισης των ηλεκτρονικών και τις στερικών αλληλεπιδράσεων του μεταλλικού κέντρου, αυξάνοντας έτσι το εύρος των εφαρμογών τους. Οι μη αθώοι υποκαταστάτες μερικές φορές παίζουν ρόλο στη σταθεροποίηση τέτοιων συμπλόκων, καθιστώντας την παρατηρούμενη οξειδωτική κατάσταση του μεταλλικού κέντρου ασαφή. Οι καταλύτες με μη ευγενή μέταλλα και υποκαταστάτες τύπου Pincer παρουσιάζουν ιδιαίτερο ενδιαφέρον για την οργανομεταλλική χημεία και την οργανική σύνθεση. Εκτός από το σίδηρο και το μαγγάνιο, τα σύμπλοκα κοβαλτίου - Pincer εφαρμόζονται με επιτυχία σε μια σειρά καταλυτικών αντιδράσεων.

Με βάση τα παραπάνω, στην παρούσα ερευνητική εργασία, δύο σύμπλοκα Co^{II} με υποκαταστάτες Pincer που περιέχουν NHC, συντέθηκαν προκειμένου να μελετηθεί η καταλυτική τους δράση σε αντιδράσεις αναγωγής κετονών. Για να εξεταστεί αυτή η αντίδραση, ακολουθήθηκαν δύο διαφορετικές πορείες ανάλογα με την πηγή Υδρογόνου. Στην πρώτη περίπτωση η υδρογόνωση των κετονών πραγματοποιήθηκε με τη βοήθεια ενός αυτόκλειστου, το οποίο παρείχε υπό πίεση αέριο H_2. Στην άλλη περίπτωση, η *i*-PrOH, χρησιμοποιήθηκε τόσο ως διαλύτης όσο

και ως πηγή υδρογόνου σε μια αντίδραση μεταφοράς υδρογόνου. Κατά την ανάπτυξη του καταλυτικού πρωτοκόλλου, δόθηκε έμφαση στην αποτελεσματική χρήση χαμηλού καταλυτικού φορτίου.

ΘΕΜΑΤΙΚΗ ΠΕΡΙΟΧΗ:**: Μοριακή πρόσδεση, Σχεδιασμός φαρμάκων, Οργανομεταλλική χημεία, NHC υποκαταστάτες**
ΛΕΞΕΙΣ -ΚΛΕΙΔΙΑ: Μοριακή μοντελοποίηση, Σχεδιασμός φαρμάκων, SARS - CoV - 2, COVID -19, AutoDock, Πρωτεΐνες, Οργανομεταλλική χημεία, Κατάλυση, N -ετεροκυκλικοί καρβένες, υποκαταστάτες Pincer, Κοβάλτιο, Οργανομεταλλική σύνθεση, Υδρογόνωση, μεταφορά υδρογόνου

Στην οικογένειά μου

ΕΥΧΑΡΙΣΤΙΕΣ

Πρωτίστως, θα ήθελα να ευχαριστήσω τους καθηγητές Γεώργιο Βουγιουκαλάκη, Θωμά Μαυρομούστακο και Αντρέα Δανόπουλο για την εμπιστοσύνη που μου έδειξαν και για την ευκαιρία να εργαστώ στις ερευνητικές τους ομάδες. Θα ήθελα να τους ευχαριστήσω, επιπλέον, για τη βοήθεια τους και την πολύτιμη επιστημονική καθοδήγηση κατά τη διάρκεια εκπόνησης της παρούσας διπλωματικής εργασίας.

Βασικό ρόλο στην εκπόνηση της παρούσας διπλωματικής εργασίας έπαιξαν οι υποψήφιοι διδάκτορες Ζαχαρόπουλος Νίκος, Ζορμπά Λέανδρος, Χαλκίδης Σάββας και Συριοπούλου Αγγελική. Θα ήθελα να τους ευχαριστήσω για τη συνεχή επιστημονική βοήθεια τους, για την άψογη συνεργασία μας στο εργαστήριο, και πάνω από όλα για τη στήριξη τους.

Θα ήθελα να ευχαριστήσω και τα υπόλοιπα μέλη του εργαστηρίου για το όμορφο κλίμα και για την άριστη συνεργασία: Μαριάννα Δανοπούλου, Δημήτρη Γιαννόπουλο, Στάθη Τώνη, Άντζυ Καπλανάι, Ιωάννα Ζγουλέτα, Ελεάνα Μαρινάκη, Φαίη Φρούσιου, Μαρία Δρυμώνα, Μαρία Μάη, Γιώργο Ρώτα και Καλλιόπη Μόσχοβου.

Τέλος, θα ήθελα να ευχαριστήσω τους πολύ δικούς μου ανθρώπους, την οικογένεια μου και τους φίλους μου, για τη συνεχή υποστήριξή τους όλο αυτό το διάστημα.

Table of Contents

Table of Figures

Table of Tables

Chapter 1: Computational study of SARS - CoV - 2 protein / ligand interactions with the aim of testing already known molecules and designing new drugs

1.1 Introduction

1.1.1 Historical background - Genesis of Computational Chemistry

In 1928, theoretical scientists made an effort to solve the Schrödinger equation using hand-cranked calculating machines. In the 1940s computer technology started to develop rapidly and efficiently. With that advancement, the solutions of elaborate wave equations for complex atomic systems began to seem more achievable. As a result, theoretical chemists became extensive users of the early digital computers. In the early 1950s, the first semi-empirical atomic orbital calculations were performed. That can be considered the roots of Computational chemistry. Later, in 1956 the first *ab initio* Hartree–Fock method calculations on diatomic molecules were performed at MIT, using a basis set of Slater orbitals followed by the first polyatomic calculations and the first configuration interaction calculations in Cambridge computer in the late 1950s both using Gaussian orbitals. While there were several papers detailing the use of computers in chemistry during the 1960s and 1970s, the first companies organized to address the new areas of chemical databases and molecular modeling were Molecular Design, Ltd. (1978) and Tripos Associates, Inc. (1979) respectively. In the early 1970s, efficient *ab initio* computer programs such as ATMOL, Gaussian, IBMOL, and POLYAYTOM, began to be used to speed *ab initio* calculations of molecular orbitals as well as methods of molecular mechanics (*eg*. MM2 force field). On October 5, 1981, Fortune magazine published a cover article entitled the “Next Industrial Revolution: Designing Drugs by Computer at Merck” (Van Drie, 2007). Some have credited this as being the start of intense interest in the potential for computer-aided drug design (CADD).[1–5]

The contribution of computational chemistry in several advancements (*eg*. Development of drugs) has been huge throughout the decades. This resulted not only in high impact publications but in several Nobel Prize awards as well.

Most notably in 1998 Walter Kohn received the Nobel Prize, "for his development of the density-functional theory", and in 2013 John Pople, "for his development of computational methods in quantum chemistry". In 2013 Martin Karplus, Michael Levitt and Arieh Warshel received the Nobel Prize in Chemistry for "the development of multiscale models for complex chemical systems".[1,6,7]

1.1.2. Fields in Computational Chemistry

Computational chemistry describes the use of computer modelling and simulation, including *ab initio* approaches based on quantum chemistry, and empirical approaches to assist scientists in solving chemical problems like understanding the structures and properties of molecules. Examples of such properties are structure (*i.e*. the expected positions of the constituent atoms), absolute and relative (interaction) energies, electronic charge density distributions, dipoles and higher multipole moments, vibrational frequencies, reactivity, or other spectroscopic quantities, and cross sections for collision with other particles. The calculations of computational chemistry can be used both to predict the results of future experiments and to aid in the interpretation of existing results. A useful tool in structural molecular biology and computer-assisted drug design is molecular docking. Molecular docking has been applied for more than three decades and thanks to its ability and its constant development, a plethora of new drugs have been discovered and developed. Drug discovery is all about finding small molecules that interact in a desired way with larger molecules, namely proteins and other macromolecules in the human body. It is the first frontier of rational design where molecular targets have a known three-dimensional structure and is a very useful tool in drug design. Indeed, is considered as a reference point in the rational design of drugs as it is used to determine whether a compound can be used as an inhibitor of a protein or not. It is one of the most applied virtual screening methods, especially, when the 3D structure of target protein is available. This virtual screening can even be applied to compounds that have yet to be synthesized, as opposed to "real" screening that requires cost- and labor-

intensive laboratory testing with previously synthesized drug compounds. *In silico* screening is becoming routine part of most modern lead-compounds discovery programs. Molecular docking can predict both the binding affinity between the ligand and the protein, but also the orientation of the protein–ligand complex, which is useful information for drug optimization.[8–11]

1.1.3. Drug design

The first step in drug design is to understand the molecular basis of the disease and identify the responsible macromolecule from which it is caused. Initially, the evaluation of the biological target of the candidate drug is performed. Targeting the drug to inhibit the action of an enzyme-protein is a crucial step. Of great importance, is also locating and understanding the active center of the receptor in order to make drug design more efficient. That way it is easier not only to test the binding of already existing and well-known drugs or natural products, but also to facilitate the synthesis of new effective substances. Knowing the tertiary structure of the active center informs about the characteristics that a molecule (potentially drug) must have to enter and bind to the active center (*eg.* lipophilia, ionization capacity, aromatics, hydrophilicity). Achieving optimal binding energy is the initial stage of *in silico* application of Molecular Binding in rational drug design to design lead-molecules. From this process of simulations, some molecules will be discarded as possible drugs, as they will not meet the structural criteria to interact with the biological target. Next, the synthesis of potential lead-compounds, as well as some of their analogues, begins, so that their biochemical activity can be tested. In order to achieve that, various software tools are used that simulate cellular conditions. It is therefore very useful to utilize any computer tool that can give valid results in terms of functionality and toxicity of a possible drug. Then, possible lead-compounds that have passed the biochemical tests, are tested for their activity in *in vitro* cell cultures and if proven successful, will then be used in *in vivo* experiments, on animals and finally on humans.[12–16]

1.1.4. Molecular docking

Rational design begins with the knowledge of the molecular basis of the disease and its mechanism, as well as the receptor responsible for its manifestation. This receptor (target) is a biomolecule that is associated with or contained in a metabolic or biomarker pathway related to a specific disease. There are several models that describe the relationship of a receptor to a ligand besides the lock-key model. According to this model, which was proposed by Fischer, the receptor is the lock, and the key is the ligand which fits into the active center of the receptor like the key in the lock. In terms of molecular docking, the initial methods were based on the lock-key model and the ligands were treated as rigid structures. Later, the induced fit hypothesis proposed by Koshland changed the data because it exorcised the lock key model. In this model it is assumed that the binding of a ligand to the active site of an enzyme or protein leads to a change in the modulation of the site of action or ligand or both. This theory led to the conclusion that during molecular binding the ligand and receptor should be treated as flexible structures and molecular docking is based on that. Molecular modeling is an important tool in the development and design of new drug molecules. The development of algorithms and software that predict the molecular binding of small molecules to receptors is a strong advantage of computer techniques. Molecular docking is a computational method of prediction of the preferred orientation of a molecule when it binds to another molecule, as well as the calculation of its binding affinity. Knowing the preferred orientation of a molecule can be useful to predict the strength of the binding between two molecules. The term molecular docking refers to the algorithm used to predict whether a compound can bind to the active or allosteric center of a protein as well as to determine the interactions of the compound with the amino acids of the active or allosteric center. These interactions are provided quantitatively by the software as a difference in the free energy during the binding (scoring function). Through these *in silico* experiments it is possible to visualize the interactions between molecules at the atomic level, allowing the evaluation of the chemical behavior of the ligands at the active site of a receptor as well as the elucidation of important biochemical processes. On the other hand, when the location of the active site is not known, either other programs can be used to determine it (*eg.* Grid, Pocket.), or a molecular binding experiment takes place throughout the structure of the

protein (blind docking). The search algorithm in molecular docking, as its name implies, looks for various configurations and orientations of the ligand in the active center resulting in different poses. Over time, different search algorithms have been developed that meet the necessary criteria in order to predict the configurations that a potential drug will have and are available to program users.[10,12,17–20]

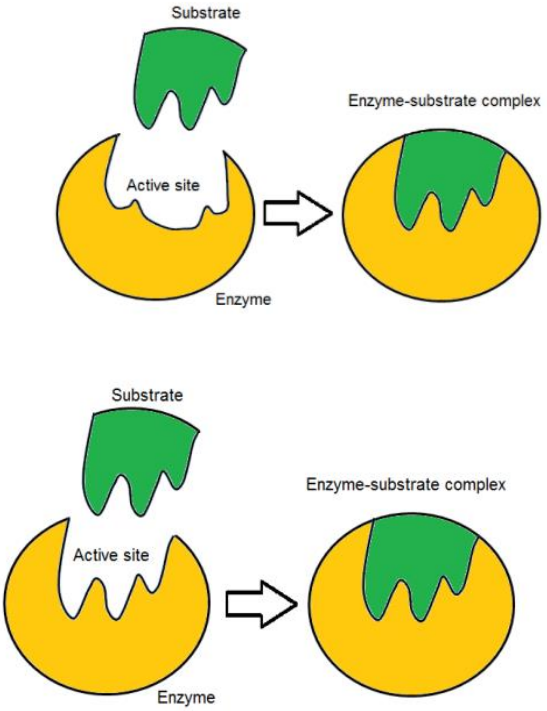

Figure 1: The induced Fit Hypothesis (top) compared to the Lock & Key Hypothesis (bottom) [21]

Of course, it should be outlined that there are many experimental techniques that give information on the binding of a substrate to the receptor. An example is the Nuclear Magnetic Resonance Technique, “Saturation Transfer Diffusion” (STD). These experimental techniques complement theoretical calculations and sometimes guide them.

1.1.5. Autodock

AutoDock is a "package" of molecular binding tools and was designed to determine how three-dimensional small molecule structures bind to the active site of a receptor. This software contains a variety of search algorithms, as well as a scoring function based on an extended range of forces. Both AutoDock and Vina are currently maintained by Scripps Research, specifically the Center for Computational Structural Biology (CCSB) led by Dr. Arthur J. Olson and were initially released in 1989. The objective of AutoDock is to perform fast and accurate molecular docking. This software is especially effective for protein-ligand docking: the prediction of the position and orientation of a small molecule when it binds to a protein or enzyme. This method is particularly useful in screening virtual libraries of molecules in order to obtain clues about which of them are promising for further drug development. It also allows researchers to determine a compound's orientation when it binds to a target protein, and to calculate its affinity and level of activity with this target protein. As a result Autodock tools is an asset to drug discovery. [22–25]

AutoDock is a free access software and its ease to use. It is designed to determine how three-dimensional small-molecular structures bind to the active center of a receptor and is especially effective for protein-ligand docking. This software contains a variety of search algorithms, as well as a scoring function based on an extended force field. Below is the extended force field scoring function used by AutoDock software. For two atoms i and j, the energy in pairs is calculated from the sum of the energy of the Van der Waals forces, the hydrogen bonds, the Coulomb energy and the dissolution. The terms "W" of the equation are weighted factors for calibrating the empirical free energy. [23,26]

$$V = W_{vdw} \sum_{i,j} \left(\frac{A_{ij}}{r_{ij}^{12}} - \frac{B_{ij}}{r_{ij}^{6}}\right) + W_{hbond} \sum_{i,j} E(t) \left(\frac{C_{ij}}{r_{ij}^{12}} - \frac{D_{ij}}{r_{ij}^{10}}\right) + W_{elec} \sum_{ij} E(t) \frac{q_i q_j}{\varepsilon(r_{ij}) r_{ij}} + W_{sol} \sum_{ij} (S_i V_j + S_j V_i) e^{-r_{ij}^2 / 2\sigma^2}$$

Figure 2: Extended force scoring function used by AutoDock software [23, 26]

AutoDock uses the Lamarckian Genetic Algorithm as the primary search algorithm. Initially, a population of experimental configurations is created and then those with the lowest binding energy are selected. It also allows the

incorporation of intramolecular energies into the intended free binding energy. The Lamarckian is an additional feature in this search algorithm, which allows individual configurations to search for their own configuration space, find the local minimums and then transmit the information to the next generation. AutoDockTools is the graphical interface of AutoDock. It facilitates the formatting of registered files, using a set of methods that lead to protonation, load calculations and the determination of the rotating bonds of the ligand and receptor. The two main tools of AutoDockTools are Autogrid and Autodock. The first computes the grids (the grid refers to the energy interaction space for different types of atoms), using parameters based on the force field, which describes the receptor or the active center of the receptor. In essence, the program generates a file containing a set of maps, atomic type maps for each receptor atom, a resolution map, an electrostatic map and a map for each type of ligand atom. Autodock then performs the molecular binding of the ligand to the grids that have been created and then a file that contains parts of the intramolecular energy force field is generated.[9,27,28]

1.1.6. COVID-19 and SARS-CoV-2

In December 2019, the World Health Organization (WHO) was informed about an outbreak of pneumonia in Wuhan, Hubei Province, China, and the etiology was not identified and now has spread worldwide and turned into a global pandemic known as COVID-19. On January 30, 2020, WHO declared that COVID-19 was discovered to be caused by the severe acute respiratory syndrome coronavirus 2 (SARS-CoV-2) and on the same month, the Center for Disease Control and Prevention (CDC) received a clinical specimen collected from the first reported U.S. patient infected with SARS-CoV-2. CDC immediately placed the specimen into cell culture to grow a sufficient amount of virus for study. Then the SARS-CoV-2 genetic sequence data was shared through the global database on sharing avian influenza data (GISAID), and by 19 March, the global pharmaceutical industry announced a major commitment to address COVID-19. As of April 2021, 17 vaccines are authorized by at least one national regulatory authority for public use: two RNA vaccines (Pfizer –

BioNTech and Moderna), eight conventional inactivated vaccines (BBIBP-CorV, CoronaVac, Covaxin, CoviVac, COVIran Barakat, Minhai-Kangtai and QazVac, WIBP-CorV), five viral vector vaccines (Sputnik Light, Sputnik V, O AstraZeneca, Convidecia, and Johnson & Johnson), and two protein subunit vaccines (EpiVacCorona and RBD-Dimer). In total, as of March 2021, 308 vaccine candidates are in various stages of development, with 73 in clinical research, including 24 in Phase I trials, 33 in Phase I – II trials, and 16 in Phase III development. Although the development of these vaccines is a huge scientific achievement that happened in a short time, the discovery of useful drugs that can prevent the virus from entering and growing in the human body and spreading is an urgent need.[29–32]

1.1.7. The coronavirus family

Bioinformatic analyses showed that SARS-CoV-2 had characteristics typical of coronavirus family and specifically it belongs to the betacoronavirus 2B lineage. Coronaviruses (CoVs) are a group of related viruses that can cause respiratory tract infection in humans ranging from mild symptoms to lethal outcomes. Features that are in common among these groups of coronaviruses are their large RNA genomes (26-35 kb). In addition, they have a highly conserved genomic organization with a large replicase, that precedes the structural and accessory genes, expression of non-structural genes. This is achieved by ribosomal frameshifting, unique enzymatic activities encoded within the replicase polyprotein, and expression of downstream genes by synthesis of 3' nested mRNAs. Until now, there are seven genera of CoVs that are known to infect humans. Coronaviruses are large, enveloped, positive-stranded RNA viruses, responsible for infecting a wide variety of mammalian and avian species. The genome of CoVs (27–32 kb) is a single-stranded positive-sense RNA (+ssRNA) which is larger than any other RNA viruses. The nucleocapsid protein (N) formed the capsid outside the genome and the genome is further packed by an envelope which is associated with three structural proteins: membrane protein (M), spike protein (S), and envelope protein (E). The S protein consists of subunits S1 and S2, responsible for the attachment and membrane fusion, respectively. These viruses contain spike-like projections of

glycoproteins on their surface, which appear like a crown under the electron microscope; hence, they are referred to as coronaviruses. [33,34]

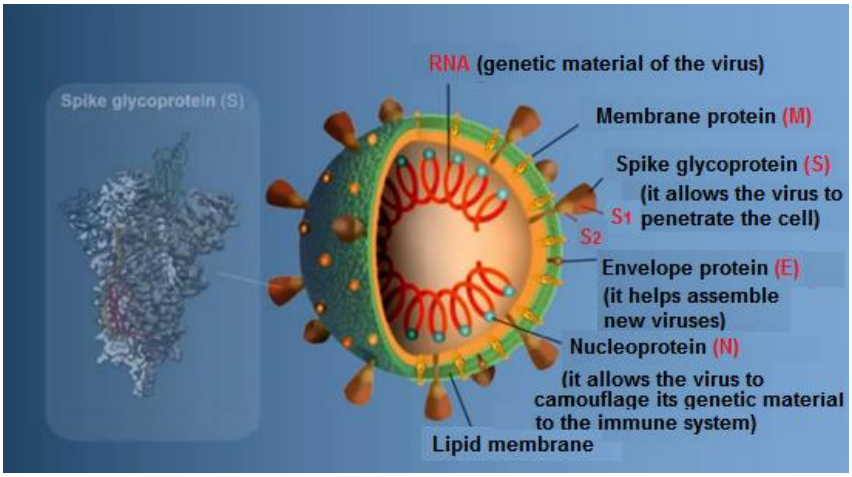

Figure 3: Structural anatomy of SARS-CoV-2 [35]

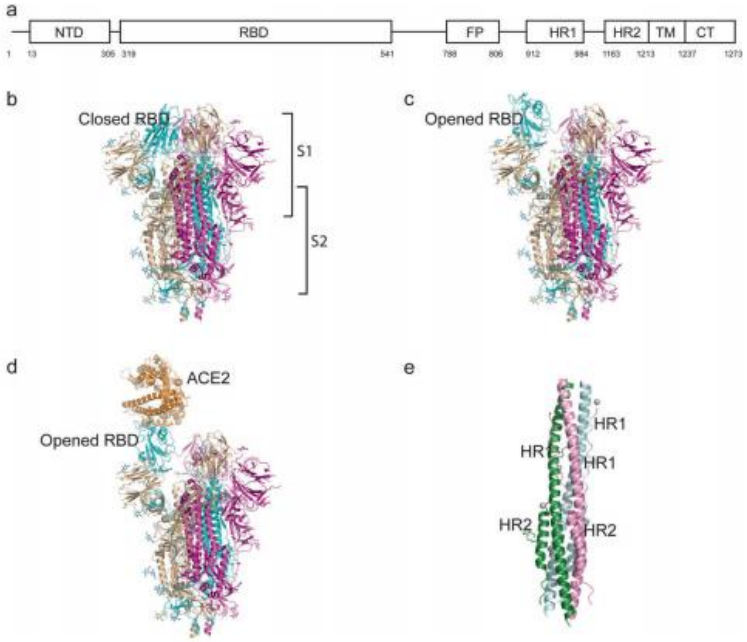

Figure 4: Structure of the SARS-CoV-2 S protein. a) Schematic representation of the SARS-CoV-2 spike. b–c) Closed and opened status of the S protein RBD. d) The S

protein binds to ACE2 with opened RBD in the S1 subunit. e) The six-helix structure formed by HR1 and and HR2 of the S2 subunit. [33,34]

1.1.8. ACE2 mechanism

Angiotensin-converting enzyme 2 (ACE2) is not only an enzyme but also a functional receptor on cell surfaces through which SARS-CoV-2 enters the host cells. Angiotensin 2 is a component of a hormonal complex called the renin-angiotensin-aldosterone complex (RAAS). Specifically, renin is an enzyme that is secreted by the parasympathetic cells of the corresponding kidney function. Once renin is released into the bloodstream, it breaks down a small polypeptide, Angiotensin I, from a large plasma protein complex called angiotensinogen, which is produced by the liver. Angiotensin I then undergoes further degradation and the active agent of the system, Angiotensin II, is formed. Angiotensin II exerts many effects but the most important are the secretion of aldosterone and the contraction of arteries. In addition to the direct vasoactive effects that indirectly increase mean arterial Angiotensin II increases cardiac contractility, reduces renal plasma flow and thus increases sodium reabsorption and the vasopressin agent in the kidneys and in the Central Nervous System and stimulates the sensation of thirst. The main role of ACE2 is the degradation of Ang II resulting in the formation of Angiotensin 1–7 (Ang 1–7) which opposes the actions of Ang II. Not surprisingly, current therapeutic strategies for ACE2 involve augmenting its expression using ACE2 adenoviruses, recombinant ACE2 or compounds in these diseases thereby affording some organ protection. The ACE2 receptor has been targeted by other viruses in the past. Results indicate the closest relationship of SARS-CoV-2 with the bat SARS-like coronavirus strain BatCov RaTG13, with an identity of 96%. These studies suggest that SARS-CoV-2 could be of bat origin, and SARS-CoV-2 might be naturally evolved from bat coronavirus RaTG13. SARS-CoV-2 shares genetic and physical characteristics with other recent viruses including SARS-CoV and MERS-CoV making it the third zoonotic human coronavirus of the century. [31,36–38]

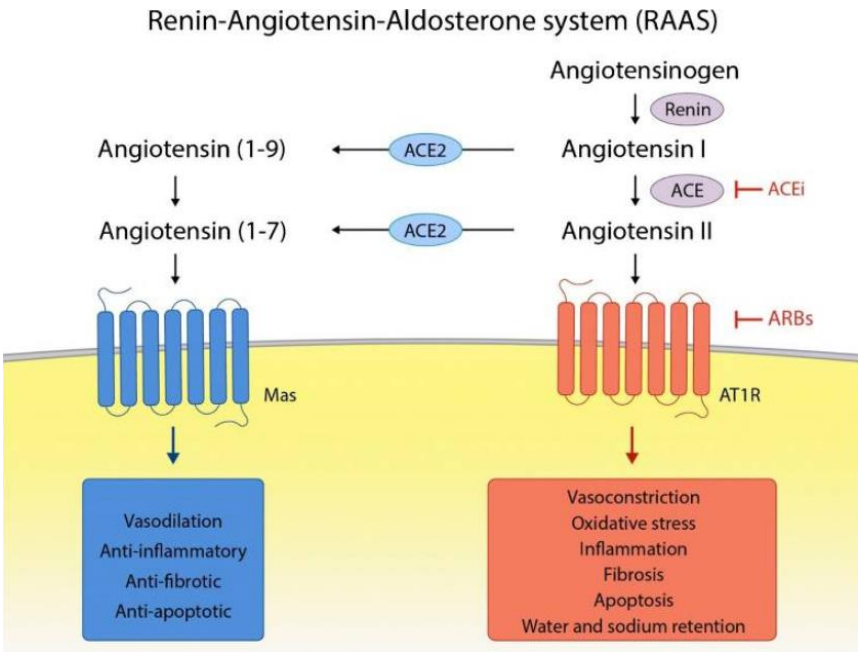

Figure 5: Renin – angiotensin – aldosterone system (RAAS): ACE / ACE2 balance, pathophysiological mechanisms, and the impact of the RAAS blockers (ACEi and ARBs). ACEi, angiotensin-converting enzyme inhibitors; ARBs, angiotensin receptor blockers [36]

1.1.9. Insertion of SARS-CoV-2 in cells

SARS-CoV-2 is the novel virus that causes the COVID-19 disease. It is important to understand the receptor recognition mechanism of the SARS-CoV-2, which determines the infectivity, host range, and pathogenesis of the virus. The virus surface is covered with spike proteins, which mediate SARS-CoV-2 entry into cells. In the native state, the CoV Spike (S) protein exists as an inactive precursor. During viral infection, target cell proteases activate the S protein by cleaving it into S1 and S2 subunits, which is necessary for activating the membrane fusion domain after viral entry into target cells. To fulfill its function, SARS-CoV-2 S protein binds to its receptor human ACE2 (hACE2) through its receptor-binding domain (RBD) and is proteolytically activated by human proteases. The ACE2 receptor exists in abundance on the surface of

lung cells and is a target for SARS-CoV-2 virus. ACE2 proteins are important to enzymatic functions, influencing blood flow to the organs such as lungs, heart and kidneys. The combination of immune evasion and high infectivity may contribute to the wide spread of SARS-CoV-2. SARS-CoV-2 causes ACE / ACE2 balance disruption and RAAS activation, which leads ultimately to COVID-19 progression, especially in patients with comorbidities, such as hypertension, diabetes mellitus, and cardiovascular disease. The life cycle of coronaviruses begins when the virion binds to the host cell receptor *via* its Spike protein S1 subunit. The S protein, protruding from the virus, attacks ACE2 receptors to gain access to the interior of the human cell where they can replicate. When the virus connects with the ACE2, it is speculated to reduce the enzymatic functions of the ACE2. After receptor binding, the virus gains access to the cytosol by acid-dependent proteolytic cleavage of the S protein into S1 and S2 subunits by a protease, followed by S2-assisted fusion of the viral and cellular membranes. After release of the viral genome, the replicase is translated from the genomic RNA and then viral RNA synthesis follows with the assembly of viral replication-transcription complexes. The viral structural proteins (S, E, and M) are translated from the RNA, insert into the endoplasmic reticulum and move to the endoplasmic reticulum-Golgi intermediate compartment (ERGIC). Multiple copies of the nucleocapsid protein (N) pack genomic RNA into helical structures (riboncleoprotein complexes) in the cytoplasm and interact with hydrophobic envelope protein (M protein) in the ERGIC that serve to direct assembly of the virion. Virions budded from the membranes of the ERGIC are then transported *via* the constitutive exocytic pathway out of the cell. [31,36,38–40]

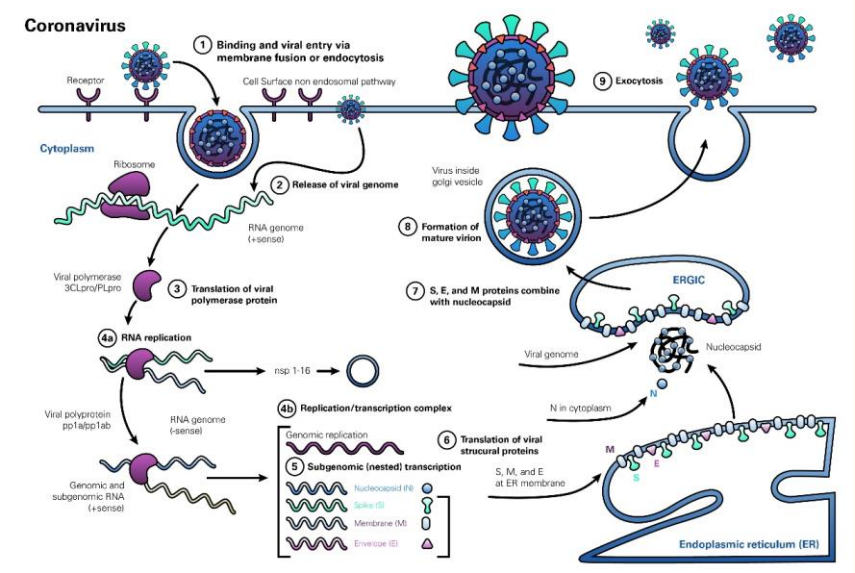

Figure 6: SARS-CoV-2 life cycle: from binding to ACE2 receptor to shedding [41]

1.1.10. Remdesivir, Chloroquine / Hydroxychloroquine, Cholecalciferol (Vitamin D) against COVID-19

Remdesivir is an antiviral agent, which was first used for the Ebola pandemic in 2014 that broke out in Africa and is now used as a medicine against the SARS-CoV-2 infection due to the new coronavirus. Its most popular adverse effects are nausea, vomiting and transaminitis (sudden increase in liver enzymes). This compound should only be used in hospitalized patients in need of oxygen therapy and is inserted *via* intravenous (IV) injection or infusion. The total duration of treatment should be at least 5 days and not more than ten days. Based on *in vitro* experiments against SARS-CoV-2, as well as SARS-CoV and MERS-CoV it seems that it is quite effective against coronaviruses, that's why it is currently in use. It is worth noting that Remdesivir is co-administered with Dexamethasone and has better results than monotherapy but there is reduced antiviral activity when co-administered with chloroquine or hydroxychloroquine.[42–45]

As remdesivir invades the human cell it is converted to its active form GS-441522. Its active form is a nucleotide analogue of adenosine without a phosphate group (C-adenosine). This results in RNA-dependent RNA polymerase (RDRP) incorporating the active form of remdesivir into the viral RNA and inhibiting the viral replication process as the protein contacts the corresponding strand of the viral RNA chain. In addition the viral RNA normally produces 3'-5' exoribonuclease (ExoN), which is a protein that detects and fixes problems in the viral RNA strands, but remdesivir overcomes the ExoN activity. [45,46]

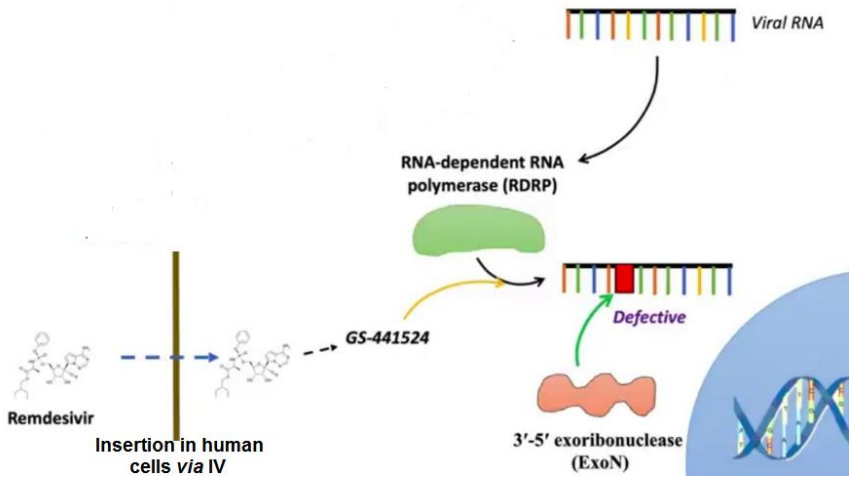

Figure 7: The mechanistic pathway of remdesivir against SARS-CoV-2 [47]

Another frequently used combination of drugs is chloroquine / hydroxychloroquine. They are 4-aminoquinolone derivatives and antimalarial drugs, but also have immunomodulatory effects. In contradiction to remdesivir, these drugs are administered orally, but in small amounts due to their increased toxicity. Hydrochloroquine is an alternative to chloroquine for the prevention of very large volume of distribution and is concentrated in erythrocytes, liver, kidneys, lungs, melanin-containing tissues in leukocytes. They also enter the CNS and penetrate the placenta, where they are dealkylated by certain metabolic pathways of the liver. In terms of their side effects, the main ones are gastrointestinal disorders, rashes, headaches, and vision problems. It should

be noted and used with caution in patients with hepatic impairment, severe gastrointestinal problems or neurological disorders and should not be used in patients with psoriasis or porphyria. In Greece, this combination is no longer administered to patients. However, regarding their mechanism in the treatment of SARS-CoV-2 infection, these molecules inhibit the multiplication of the virus in three potential ways:

1) Increasing the pH in the lysosome, because of their alkaline nature and inhibition of the proton pump function (vATPase) thus inhibiting the process of endocytosis

2) Chloroquine has the ability to transfer zinc to the human cell which binds to RNA-dependent RNA polymerase and inhibits the above enzyme which is necessary for the transcription of viral genetic material.

3) They can bind to sialic acid and release it next to the ACE2 receptor. This causes the viral protein to bind to the sialic acid and not to the ACE2 receptor, a process that marks the onset of viral endocytosis. [42,43,48,49]

Also, vitamin D3 has been shown to decrease risk of respiratory infections and / or the severity of respiratory infections. In addition, Vitamin D3 insufficiency is associated with increased susceptibility to some infections. For example, that phenomenon is prominent in the acute respiratory tract infections, that is why, it is important to test vitamin D as a preventative measure. Vitamin D is a fat-soluble vitamin, involved in calcium homeostasis and in immune system modulation. Specifically, Vitamin D3, also known as cholecalciferol is the form made naturally by the body in response to sunlight.[50]

Vitamin D receptors are present in many immunological cells (*i.e.* in B-cells, T-cells, macrophages and dendritic cells). By activating those receptors, Vitamin D modulates innate and adaptive immune system function, by regulating the immune system proteins. These proteins have antibacterial, antiviral and antifungal properties.[51]

That way, Vitamin D reduces the cytokine storm (cytokine release syndrome) that can cause increasing morbidity and mortality in respiratory infections.

Also, Vitamin D reduces T helper cell inflammatory cytokine production. [52]

In addition, its supplementation modulates levels of interleukins. [53]

An additional drug used to treat respiratory infections and complications caused by the modern coronavirus is tocilizumab. Tocilizumab is the first marketed interleukin-6 (IL-6) blocking antibody through targeting IL-6 receptors and has proved its safety and efficiency in therapy for rheumatoid arthritis. The First Affiliated Hospital of University of Science and Technology of China and Anhui Fuyang Second People's Hospital were recruited and given tocilizumab therapy. From the 21 patients, who were treated tocilizumab, 20 patients have been recovered and discharged within 2 weeks and the other patient was discharged a little later. In addition, no adverse effects were reported during the treatment with tocilizumab. It is known that when virus cells infect the respiratory system, the body's immune response is activated by the defense cells. This results in the secretion of an abundance of cytokines and the development of hyperinflammatory syndrome. The products of inflammation settle on the cells of the pulmonary parenchyma, resulting in the obstruction of gas exchange in the alveoli and the formation of ARDS (acute respiratory distress syndrome). More specifically, when the defense cells are activated, the T lymphocytes produce the granulocyte macrophage colony stimulating factor (GM CSF) and the interleukin-6 proteins necessary for the arrival of the rest of the cells. Tocilizumab is a monoclonal antibody that binds to interleukin 6 receptors thus blocking the hyperinflammatory syndrome caused by cytokine hypersecretion and is responsible for ARDS and multiorgan failure.[54,55]

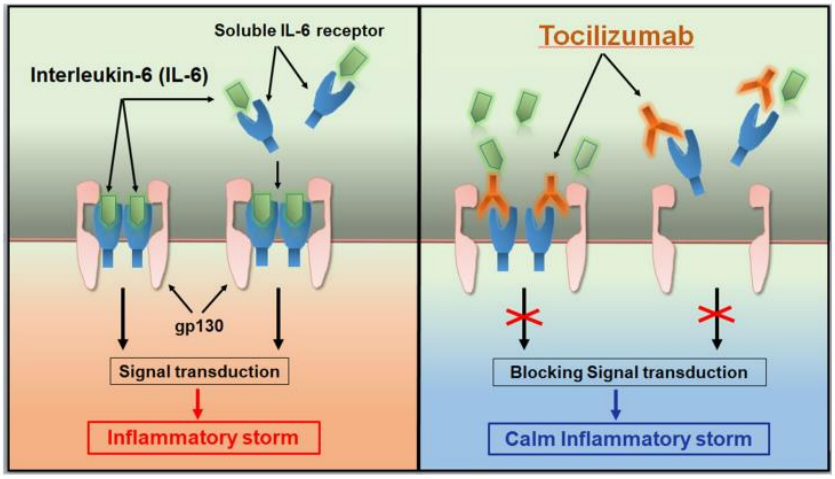

Figure 8: Tocilizumab calms the inflammatory storm through blocking IL-6 receptors [54]

Lastly, in some patients of COVID-19, doctors use Dexamethasone. Cortisone (Dexamethasone) is a pregnane (21-carbon) steroid hormone. It is a naturally-occurring corticosteroid metabolite that is also used as a pharmaceutical prodrug. Normally, it is used to reduce swelling and / or inflammation caused by many different conditions such as allergic disorders. It was tested in hospitalized patients with COVID-19 in the United Kingdom's national clinical trial RECOVERY and was found to have benefits for critically ill patients. According to that survey, at 2104 patients were administered 6 mg of Dexamethasone. To the patients, who were in need of ventilator or mechanical assistance, the mortality rate was decreased from 41% to 28% (Figure 9). Also, Dexamethasone was shown to reduce mortality in hospitalized patients with COVID-19 who required supplemental oxygen from 25% to 20%. A percentage of the patients with COVID-19 can develop a systemic inflammatory response that can lead to lung injury and multisystem organ dysfunction known as ARDS. As a result, the levels of inflammatory markers like CRP and ferritin d-dimer increase, due to the inflammation caused by interleukin-6, which is a driver of inflammation in the body. Based on the anti-inflammatory effects of corticosteroids, they might prevent or

mitigate these deleterious effects. The timing is the most important aspect to be considered. If Dexamethasone or other corticosteroids are administered when the virus is highly replicating in the body, then the virus replication can be increased and expedited. On the other hand, if the virus is at its peak, then the patients could end up with severe ARDs. So, the administration should be between those periods. Also, steroids should be avoided if the patient has another infection simultaneously or high blood sugar. This drug's cost is relatively low, so it could be a potential cure for the symptoms in developing countries as well. [56]

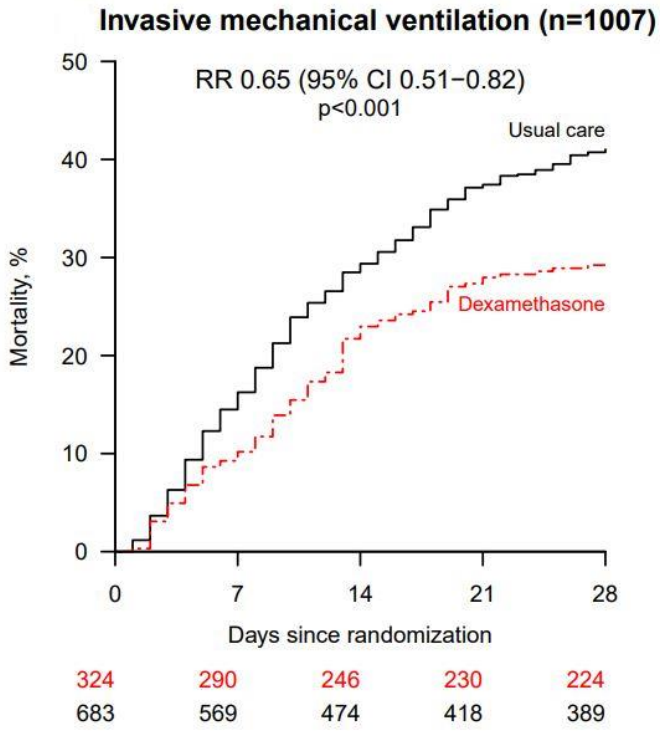

Figure 9: Mortality over 28 days for 1007 COVID-19 patients on mechanical ventilation at time of randomization: 324 patients who received dexamethasone (red) compared to 683 who received standard hospital care (black) [57]

1.2. Experimental section

1.2.1. Molecular Docking

In the present research work, the AutoDock software was used for the molecular docking calculations and more specifically the Lamarkian-Genetic algorithm. The process will be described in detail later in the chapter. The X-ray crystal structures of Main protease (PDB ID: 6LU7) and spike protein (PDB ID:6LZG) were downloaded to the AutoDock program for study from the RCSB PDB (Protein Data Bank) database. The crystal 3D structure of the following compounds was retrieved from PubChem database. ‘‘Auto-Dock Tools’’ were used to prepare, run, and analyze the ligands under study using docking simulations. Plip and PyMOL software were then used to visualize the results. [58,59]

1.2.2. Preparation of ligands

Docking is a reference point for computational drug design as it is used mainly to define if a compound could be an inhibitor to a certain protein or not. In fact, docking is a successful approach for identifying potential effective molecules with Drug likeliness. It is important to mention that docking can be restrictive due to the fact that flexibility of both protein residues and docked ligand are partially ignored, hence the ranking and ordering of the compounds only by their corresponding docking scores may not potentially lead to the identification of potential drugs. On the other hand, molecular docking studies give an initial insight into protein-ligand interactions and as a result it is always helpful to test the compounds beforehand using dynamical studies such as molecular dynamics (MD) simulations before performing *in vitro* or *in vivo* experiments Taking into consideration the cost and effort for drug design and production it became necessary to also use computational chemistry techniques that will reduce the probability of failure. [9,26,60]

The potential COVID-19 inhibitors studied were designed in the ChemBioOffice program suite. Initially, their two-dimensional structures were designed in

ChemDraw, and then, using the Chem3D program, their three-dimensional structures were identified. In addition, using the same program, their energy was minimized. A MM2 forcefield was used to minimize energy. In some cases the total energy of the potential ligands was minimized efficiently using Maestro MacroModel 10.8, where all hydrogens were added and molecules were subjected to complete structure minimization. For the minimization, water was chosen as a solvent, OPLS3 force field and the algorithm Polak-Ribiere (PRCG, convergence value 0.01 kcal mol^{-1} $Å^{-1}$) were used. Since the ligands that we tested are not peptides, Gasteiger charge was assigned and then the non-polar hydrogens were merged. AutoDock requires pre-calculated grid maps, one for each atom type, present in the ligand being docked as it stores the potential energy arising. This grid must surround the active site of the macromolecule for the binding energy score to be as close to the reality as possible.[26,27,61,62]

1.2.3. Preparation of proteins

As mentioned earlier, two protein molecules, were studied using the AutoDock program. In both cases, the molecules were used as provided by the "ProteinDataBank-PDB" database. The spike-ACE2 complex was examined in the metallocentre of the ACE2, in the active site of the ACE2, in the RBD (Receptor-Binding Domain) and the general core of the spike protein. Their crystallized structures were processed in AutoDock and the process is described later in the chapter. The main protease (Mpro) molecule has PDB ID: 6LU7, while for the complex of the spike protein and the ACE2 has PDB ID: 6LZG. At first Kollman (or Gastgeiger which was used only for the metallocentre of the spike protein) united atom charges, solvation parameters and polar hydrogens were added to the receptors / proteins in order to prepare them for the docking. Then all hydrogens were added before computing Kollman (or Gastgeiger) charge and subsequently the non-polar hydrogens were merged.[26]

1.2.4. Validation of target protein-ligand complex structures

Autodock 4.0 methodology was validated with the respective co-crystallized ligands of target proteins not only to ensure the virtual screening process but also to compare the effectiveness of the compounds.

Main protease aka 3CLpro was tested with its co-crystalized inhibitor N3 (n-[(5-methylisoxazol-3-yl)carbonyl]alanyl-l-valyl-n~1~-((1R,2Z)-4-(benzyloxy)-4-oxo-1-{[(3R)-2oxopyrrolidin-3-yl]methyl}but-2-enyl)-l leucinamide) which is a Peptide-like / Inhibitor. In the case of the spike protein is co-crystalized with non-standard biopolymers (4 molecules) that served as stabilizing agents. Those molecules in detail are 2-acetamido-2-deoxy-beta-D-glucopyranoses in both chain A and B. [39,63]

Every molecule except the protein is removed before each run. Each of these compounds was docked to the 6LU7 and to the 6LZG structures, using Autodock 4.0 with full ligand flexibility. For both structures, the docking was applied initially in the whole protein using blind docking to determine where the ligand is forming bonds with the protein and later repeated by focusing on the part of the protein where the ligand is bound, using the flexible residues method.[26,27]

1.2.5. Visualization of Results

After the end of the calculations, the Autodock, Plip and PyMOL programs were used, in order to visualize the results, so that the connection between the molecules (ligand / receptor) could be understood. The developed pictures do not show the Autodock bonds. On PyMOL, the strong hydrogen bonds are shown as yellow straight lines, and the various types of interactions shown using Plip, follow the indication bellow (Figure 10). It is also important to note that in these pictures the carbon atoms are green or cyan, the oxygen atoms are red, the nitrogen atoms are blue, the phosphorus atoms orange and the zinc and pseudo zinc atoms are dark grey.[64,65]

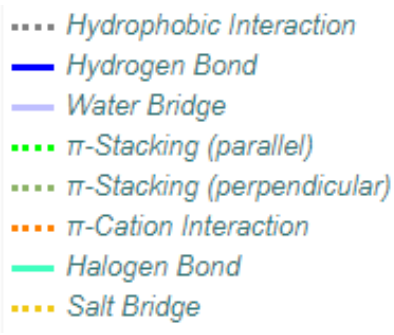

Figure 10: Depiction of the various protein-ligand interactions, according to Plip.

1.2.6. AutoDock - User Guide / Experimental Procedure

AutoDock was used *via* the AutoDock Tools (GUI: Graphica lUser Interface). Both AutoDock and the other programs used in the study are installed on Windows 10. AutoDock has many applications, but in this work, it was used to study molecular docking in protein / ligand systems. All the molecular docking experiments were performed three times for each ligand in each receptor and the average values for the binding affinity and inhibition constant were recorded. The deviation of each compound was around ±0.5 both on the binding energy as well as in the inhibition constant and the procedure followed is described below step by step. In detail, we are going to describe the steps for an accurate molecular docking for the 3CLpro (which are the same for the spike protein). In this case the receptor is a protein with a known active site. [22,27]

Molecular docking

Open ADT (AutoDockTools) by clicking the appropriate icon on the desktop.

- Define "work folder" (startupdirectory)

At this point a specific folder is selected, where all the files generated by the program (output files) are saved. The files to be imported into the program should also be saved in this folder. In this folder also, the files that will be inserted into the program (inputfiles) should be saved, beforehand.

The introduction of the three-dimensional receptor structure (Mpro) in the program can be done in two ways but we only chose to import a saved 3D structure to the computer.

Preparation of the receptor

- Deletion of waters: before calculating the molecular docking, the waters that have co-crystallized with the molecule are deleted.

- Deletion of molecules not useful for computation (heteroatoms): deletion of the molecule that has co-crystallized with the protein in the event that the protein molecule is downloaded to the program from the Protein Data Bank, having another molecule bound to its active center.

- Addition of hydrogens in order to properly operate the program force field.

- Addition of charges to the receptor molecule is an important step, as the scoring function contains electrostatic contributions.

- Selecting polar hydrogens and deleting the rest, polar hydrogens are the ones that form hydrogen bonds between molecules and are therefore useful.

- Save the processed receptor structure to be used for molecular docking next.

Insertion and preparation of the ligand in the program.

- Insert the ligand by selecting the appropriate file, either as a .mol2 or a .pdb file
- Save the ligand to another file format (.pdbqt), this file will be used by the program to determine the ligand configurations

Preparation of the Grid Box

- In this step, the area (grid) where the co-crystallized molecule was or a potential ligand will be located, is prepared. In this case the region was defined based on the coordinates of the amino acid CYS 145, which according to the literature is included in the active center of the protein.
- Select an atom belonging to the amino acid CYS 145 (for example O), following the steps mentioned earlier.
- Open the CovalentGridParametersTab tab and select the "UseselectionforAttachmentAtom" box. In this way, the x, y and z coordinates show the values of the coordinates of the selected atom.

The GridBox tab sets the values for the GridBox dot number as follows:

X = 60

Y = 60

Z = 60

- Set the dot distance to 0.375 Å (default)
- Define the center of the grid using the coordinates obtained from the previous step:

X = -10.450

Y = 11.928

Z = 69.963

For the spike protein the size of the grid box was the same and the coordinates for each case are the following:

Coordinates	Protein / Receptor			
	Chain A	Chain B	RBD	Metallocenter
X	-25.56	-35.30	-39.34	-25
Y	0.39	21.725	29.11	12
Z	-39.03	26.612	9.25	-18

Table 1: The coordinates for each receptor/protein for the grid box

- Save the grid parameters before closing the tab.

Preparing the "AutoGrid Parameter file (.gpf)".

AutoDock does not use the receptor directly in the molecular docking calculation process, but a set of maps generated by the program and stored in the .gpf file. This set of maps includes a map for each type of atom and two more, a resolution map and a map of electrostatic interactions. Therefore, the

resulting map types depend on the ligand, and so AutoDock prepares an energy grid for each atom in the ligand.

Macromolecule selection: in this step the molecule to be selected as a receptor is saved as a .pdbqt file.

Ligand selection: the selected structures of the desired ligand.

Import "Parameter Filename Library" parameter library: the program will use individual parameters contained in this file in order to optimize the accuracy of the calculation.

"AD4.1_bound.dat" file: This file contains various force field parameters, such as van der Waals parameters.

Save the AutoGrid (.gpf) file: this file contains information about the intermolecular aspects of the force field.

Run AutoGrid4

- Select the "Run AutoGrid" key to run AutoGrid. Pressing Launch The program runs.

- Define the program pathname: select the file that the program needs to run.

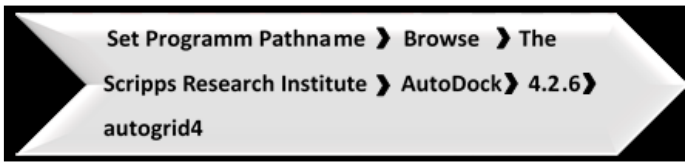

- Define the file that the program will use to run AutoGrid (.gpf).

Pressing Launch the program runs.

- Prepare the configuration file for AutoDock4
- Macromolecule selection: the receptacle file saved earlier during the preparation of the AutoGrid file is selected.

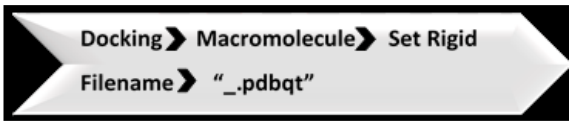

Ligand selection: sorting of the structures to be used in the calculation of the molecular docking. At this point a window opens in which the parameters of the ligand can be adjusted. At this point a window opens in which the parameters of the ligand can be adjusted, in this experimental procedure they were set "by default", (*i.e*. automatically).

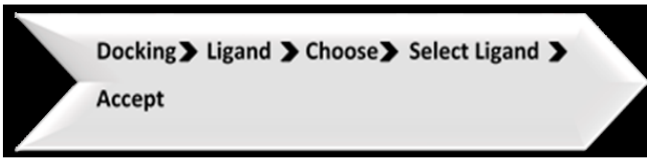

Search Algorithm: selection of the appropriate algorithm for the respective calculation. As before, a window opens from which the algorithm parameters can be configured. The genetic algorithm was chosen here. To obtain the most accurate result, we increased the population size to 175 as well the maximum number of evals to 5000000. By using a population of 175, as specified by the

'ga_pop_size' parameter, means that in every generation, there will be 175 energy evaluations to compute the fitness of all the members of the population. AutoDock stops a docking if either the maximum number of evaluations or the maximum number of generations is reached, whichever comes first. In this case, the docking is terminated based on reaching the maximum number of energy evaluations, namely 25 million evals, since there are fewer than 27000 generations in these runs. In order to avoid that and based on our increased number of torsions to 5000000, it is helpful to increase the population to 175 as well.

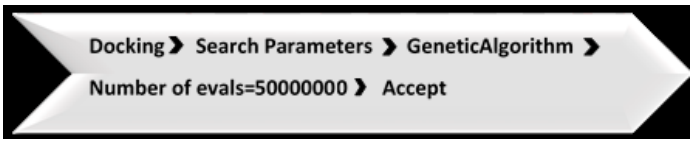

Molecular docking parameters: adjustable according to the experiment. Here they were set automatically (by default).

Importing the parameter library: the program will use individual parameters using the file AD4.1_bound.dat contained in this file in order to optimize the accuracy of the calculation.

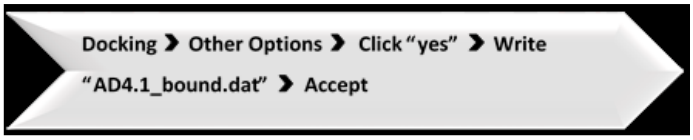

Save the AutoDock file: this file contains part of the parameters of the force field which are related to the intramolecular actions and must be saved after it will be used during the execution of the program.

Run AutoDock

At this point the "RunAutoDock" tab is opened in order to run the program.

Program path name: select the file that the program needs to run. Define the file that the program needs to run AutoDock.

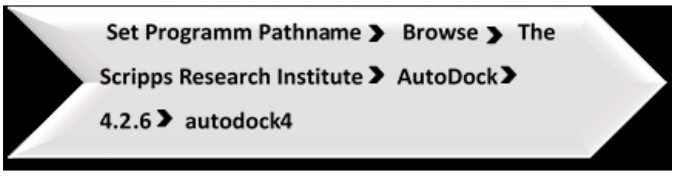

Define the file that the program needs to run AutoDock.

- Launch starts the calculation.

Visualization of AutoDock results

- Import the results (".dlg" file) after the end of the molecular docking process (one of the ligand configurations will appear on the surface of the program)

Insertion of the macromolecule into the program surface (the .pdbqt file that was saved during the preparation of the AutoGrid file)

Check the ligand conformations in the active site of the receptor: this option enables observation of ligand conformations by clicking on the arrows left and right number of each configuration.

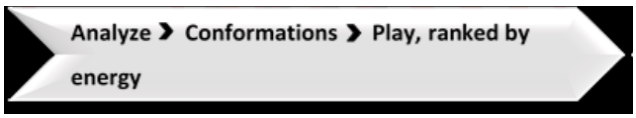

Visualization of the interactions formed between receptor and ligand.

1.2.7. AutoDock4Zn

It is a well-known fact that zinc is present in a wide variety of proteins. These proteins are metalloenzymes and their metallocentre is important in the metabolism of most organisms. In a lot of cases, drug molecules target these proteins, in a way that creates interactions with the zinc ion. AutoDock4Zn is an improved AutoDock Force Field for small-molecule docking to zinc metalloenzymes and accurate prediction of the interaction of ligands with that. This new force field was calibrated on a data set of 292 crystal complexes containing zinc and improved the coordination geometry and the interaction strength. The authors of AutoDock4Zn use a pseudo atom for the possible location of the atom that has the coordination bond with Zn. There were improvements in both free energy of binding estimation as well as in root-mean-square deviation from the crystal structure pose. This method has limitations since the number of complexes used at that time was relatively small, so it does not always reproduce the experimental pose. The images developed by that program show a superposition of the docking pose and the crystallographic structure. In that case, the zinc atom (dark gray) has a coordination bond with the nitrogen (blue) of the ligand. PyMOL represents this interaction as a bond (stick) due to the bond distance at which the prediction is made (pseudo atom

TZ). Before inserting a ligand in the spike protein, according to the *in silico* models, Zn interacts with three amino acids (*i.e.* HIS A 374, HIS A 378 and GLU A 402) in a square planar geometry. [66,67]

Complex	Amino acids involved in metal complexation and distance (A°)
6LZG chain A / Zn square planar	HIS 374 A: (2.09) HIS 378 A: (2.10) GLU 402 A: (2.76) GLU 402 A: (2.00)

Table 2: Interactions of COVID-19 Angiotensin-converting enzyme 2 (6LZG chain A) amino acid residues with the Zn^{II} metallocentre.

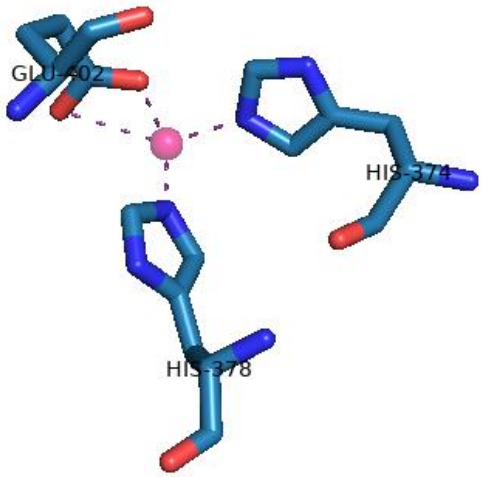

Figure 11: Depictions of interactions of Zn^{II} metallocentre incorporated in a cavity of Angiotensin-converting enzyme 2 (chain A of 6LZG) of SARS-CoV-2 Coronavirus using crystallographic grid.

1.2.8 AutoDock4Zn - User Guide / Experimental Procedure

- Step 1 – Preparation of the receptor and ligand (as in the standard AutoDock protocol), addition of polar hydrogens, Gasteiger charges and set atom types:

%MGLROOT%\python prepare_receptor4.py -r protein.pdb -o protein.pdbqt
%MGLROOT%\python prepare_ligand4.py -l ligand.mol2 -o ligand.pdbqt -A hydrogens

- Step 2 – Addition of Tetrahedral Zinc Pseudo Atoms (TZ) to the receptor. TZ atoms represent the preferred position for tetrahedral coordination by the ligand.

$MGLROOT/bin/pythonsh zinc_pseudo.py -r protein.pdbqt -o protein_tz.pdbqt

- Step 3 - Use of the modified forcefield (AD4Zn.dat)

The AutoDock4Zn forcefield is mostly defined by non-bonded pairwise potentials which are written to the grid parameter file (*.gpf) in the form of npb_r_eps keywords. The file AD4Zn.dat includes the definition of the TZ atom type for the AutoDock forcefield. The keyword parameter_file in the .gpf specifies AD4Zn.dat as the forcefield to be used, so AutoGrid requires a local copy of it in the working directory. Alternatively, the keyword parameter_file in the .gpf file can point to the full or relative path where AD4Zn.dat is located.

- Step 4 – Generation of the Grid Parameter File (.gpf)

The preparation script will be executed to generate the GPF to configure the grid calculation:

%MGLROOT%\python prepare_gpf4zn.py -l ligand.pdbqt -r protein_tz.pdbqt \
-o protein_tz.gpf -p npts = 60, 60, 60 -p gridcenter = -25, 12, -18 \ –p parameter_file=AD4Zn.dat

The -p flag is used to set the box center (gridcenter) and size (npts) along with the parameter_file specific for this case.

- Step 5 – Running of AutoGrid4

The code that supports user defined pairwise potentials (npb_r_eps keyword) from the .gpf file was restored from an old version of the software and added to the modified AutoGrid4 binary provided in this tutorial. These changes will be included in next release of the standard AutoDock binaries.

autogrid4 -p protein_tz.gpf -o protein_tz.glg

At this stage, all forcefield information has been encoded in the maps (*.map), and the remaining steps are the same as in the standard AutoDock protocol.

- Step 6 – Generation of the Docking Parameter File (.dpf)

The preparation script will be executed to generate the DPF to configure the actual docking calculation:

%MGLROOT%\python prepare_dpf42.py -l ligand.pdb -r protein_tz.pdbqt \ -o ligand_protein_tz.dpf

- Step 7 – Running of AutoDock autodock4 -p ligand_protein_tz.dpf -o ligand_protein_tz.dlg

1.3. Results - Discussion

Hydrogen bond is defined by maximum distance and minimum angle cutoffs. If the default cutoff values are different in different programs, the number of hydrogen bonds reported by the programs may be different. The typical lengths of H-bonds in proteins are: 2.2 - 2.5 Å (strong), 2.5 - 3.2 Å (moderate strength) and 3.2 - 4.0 Å (weak). Good hydrogen bonds (as determined by PyMOL) are shown in yellow. PyMOL guesses bonding connectivity based on proximity, based on the empirical observation that two atoms of a given radius will not be generally closer than a certain distance unless they are bonded. PyMOL does not have sufficient information to rigorously determine hydrogen bonds, since typical PDB files are ambiguous with respect to charge states, bonds, bond valences, and tautomers. As it stands, all those things are guessed

heuristically. In the Plip case, the maximum distance between acceptor and donor in hydrogen bonds is 4.1 Å, so it shows weak interactions as well.
In a ligand-protein complex in each database, it will always have the same van der Walls, electrostatic and other type of interactions, regardless the software. Some tools show less or more contacts, based on their settings and setup of the package. *e.g* some packages may not show you pi-pi and cation-pi bonds but that does not mean that these contacts do not exist. In order for us to understand the interface better, we use 2 or 3 tools and summarize the interacting residues with the ligand. As a result, the bond energies calculated by different tools may differ. Plip is the most analytical of the above-mentioned tools and shows the most interactions.[26,64,65]

1.3.1. N3 inhibitor

In the previous chapters, reference was made to the experimental procedure followed by molecular docking calculations. For this thesis, over 100 molecules including already known drugs but also natural products, were tested, in order to find effective ligands for hindering the development and transmission of the SARS-CoV-2 virus. We run all the compounds using Autodock Vina 4.0 and identified the lowest binding energy orientation of the ligand in the receptor. This chapter presents the *in silico* results of these calculations as well as images of the compounds complexes obtained using the PyMOL program and the Plip program. Coronavirus main protease is also known as COVID-19 coronavirus 3CL hydrolase (Mpro). Initially, we tested the binding affinity of the crystal structure of COVID-19 main protease (Mpro) in complex with its inhibitor (N3 peptidomimetic inhibitor). Yang *et. al.* identified a mechanism-based inhibitor, known as N-[(5-Methyl-1,2-oxazol-3-yl)carbonyl]-L-alanyl-L-valyl-N-{(2S,3E)-5-(benzyloxy)-5-oxo-1-[(3S)-2-oxo-3-pyrrolidinyl]-3-penten-2-yl}-L-leucinamide (Figure 12), by computer-aided drug design, and then determined the crystal structure of Mpro of SARS-CoV-2 in complex with this compound. It is important to run that molecule and confirm the literature results, in order to accurately compare the new potential inhibitors. Mpro is a key enzyme of coronaviruses and has a pivotal role in mediating viral replication and

transcription, making it an attractive drug target for SARS-CoV-2. As a result, it is of great importance to find efficient ligands to bind at this enzyme. The molecular docking calculation for each potential ligand was repeated three times according to the procedure analyzed in the previous chapter and the docking scores are derived from the average of the values of the three experiments.[39,68]

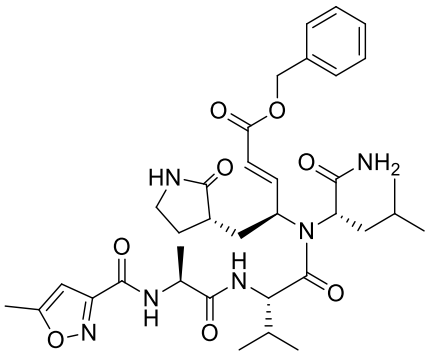

Figure 12: Structural depiction of the N3 inhibitor

Based on the binding at the active site of the protein, the N3 inhibitor forms one hydrogen bond with HIS 41 and showed a binding energy of -8.05 kcal / mol as well as an inhibition constant of 64.2 uM. After visualization on PyMOL there were also nine potential hydrogen bonds, one with HIS 41, one with HIS 164, two with GLU 166, four with GLN 189 and one with THR 190. Using Plip, it forms six hydrogen bonds, two with TYR 54, two with GLU 166, one with GLN 189 and one with ALA 191, four hydrophobic bonds with ASN 142, MET 165, GLU 166 and GLN 189. Lastly, it seems that a salt bridge with HIS 41 also exists as it can be seen below (Figure 13).

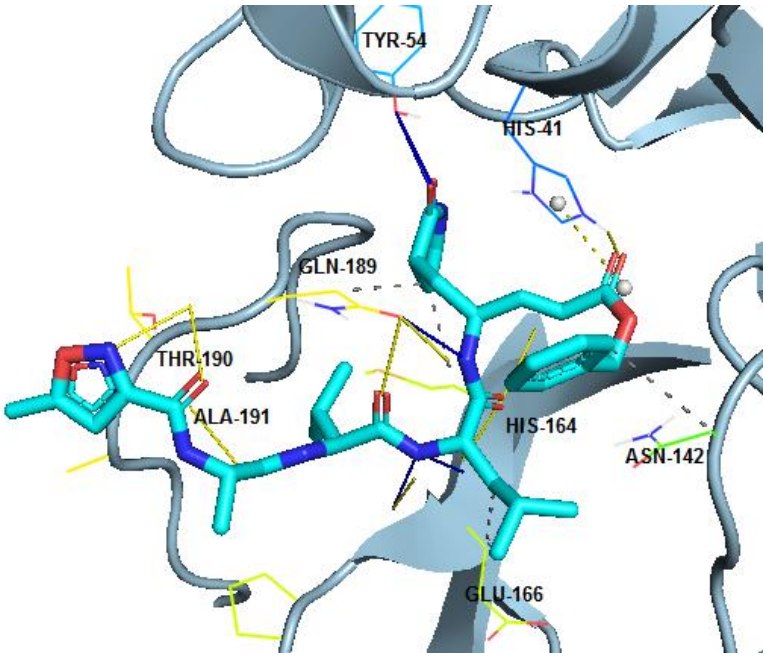

Figure 13: N3 inhibitor incorporated in a cavity of Mpro (6LU7) of SARS-CoV-2 Coronavirus using crystallographic grid.

1.3.2. Sartans

Initialy, we tested both in the Mpro and Spike protein several new ligands by starting with sartans. AT1-receptor antagonists or sartans, are a group of pharmaceuticals which modulate the renin-angiotensin-aldosterone system.

Our focus was mostly the sartans containing a tetrazole group because it is a group which forms usually strong hydrogen bonds.[69,70] (Figure 14).

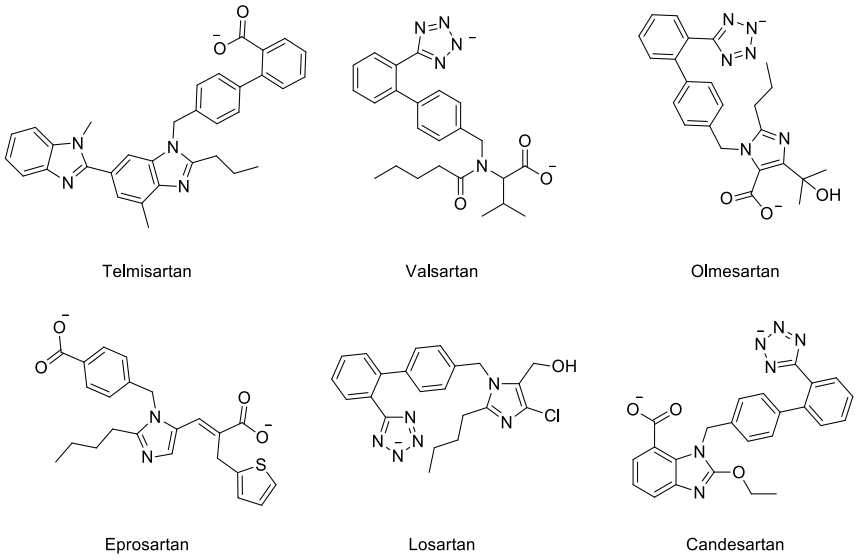

Figure 14: Structural depiction of Telmisartan, Valsartan, Olmesartan, Eprosartan, Candesartan and Losartan

In the case of The Mpro, Losartan seems to bind the strongest with binding energy of -10.41 kcal / mol. For losartan based on Autodock there are two hydrogen bonds with GLU 166 and GLN 189 and on PyMOL there also two hydrogen bonds with GLU 166 and PHE 140. After using Plip, losartan has three hydrophobic interactions with GLU 166, GLN 189 and two hydrogen bonds with GLU 166 and GLN 189 (Table 3 & Table 4).

For the Spike protein, we can observe the same pattern. On the lead is again losartan with a binding energy of -10.36 kcal / mol. According to Autodock for losartan, one hydrogen bond is formed with ASN 277 and on PyMOL there are five hydrogen bonds with ASN 277, TYR 279, SER 280 and ASN 290. After using Plip, it seems that there are three hydrophobic interactions, two with TYR 279 and one with VAL 283 (Table 4) (Figures 15 & 16).

Ligands	Binding affinity for proteins ΔG (Kcal / mol)	
	Mpro	Spike protein (chain A)
Candesartan	-8.28	-6.00
Olmesartan	-7.2	-5.25
Eprosartan	-7.76	-5.77
Telmisartan	-7.95	-7.42
Valsartan	-8.68	-4.88
Losartan	-10.41	-10.36

Table 3: The average values of binding affinity for the complexes of Telmisartan, Valsartan, Olmesartan, Eprosartan, Candesartan and Losartan with COVID-19 receptors

Ligands	Interactions of ligands with amino acids	
	Mpro	Spike protein (chain A)
Candesartan	**Autodock** CYS 145, GLU 166 **PyMOL** HIS 41, GLN 189, CYS 145, ASN 142, GLU 166 **Plip** GLY 143, CYS 145, GLU 166 MET 165, ASP 187, GLN 189 HIS 41	**Autodock** LYS 441 **PyMOL** ALA 153, ASN 277, THR 276, GLY 268, PHE 274, LYS 441 **Plip** ASN 154, ASP 269, THR 276 (2), ASN 277 (2) ASP 269, PHE 274, THR 276 LYS 441
Olmesartan	**Autodock**	**Autodock**

	THR 26, GLY 143, GLU 166 **PyMOL** THR 26, LEU 141, GLY 143, GLU 166 **Plip** THR 26, GLY 143, SER 144, CYS 145, GLU 166 THR 25, GLU 166, GLN 189	LYS 441 **PyMOL** ASN 154, ASN 277, LYS 441 **Plip** ASN 154, ASP 269, THR 276, ASN 277 (2), LYS 441 LEU 248, LEU 266, TYR 279, LEU 281 LYS 441
Eprosartan	**Autodock** CYS 145, HIS 41 **PyMOL** HIS 41, GLY 143, SER 144, CYS 145, HIS 164 **Plip** GLY 143, SER 144 (2), CYS 145, HIS 163 THR 26, PHE 140, MET 165, GLU 166	**Autodock** LYS 441 **PyMOL** ALA 153, SER 155, ARG 161, THR 276, LYS 441 **Plip** ASN 277, SER 280 LEU 156, TYR 252, LEU 266, ASN 277, LEU 278, TYR 279

	HIS 41 (2) HIS 41	ARG 161, LYS 441
Telmisartan	**Autodock** GLY 143 **PyMOL** THR 26, LEU 141, GLY 143 **Plip** THR 26, ASN 119, GLY 143, SER 144 THR 25, THR 26, LEU 27, TYR 118 (2), ASN 142, GLU 166	**Autodock** LYS 441 **PyMOL** SER 155, LYS 441 **Plip** LEU 156, LEU 248, LEU 266, THR 276, LEU 278, TYR 279, LEU 281 LYS 441
Valsartan	**Autodock** HIS 41, CYS 145 **PyMOL** HIS 41, SER 144, CYS 145, GLU 166, GLN 189 **Plip**	**Autodock** ASN 154, LYS 441 **PyMOL** ASN 154, THR 276 **Plip** ASN 154, TYR 279

	TYR 54, GLY 143, SER 144, CYS 145 THR 25, MET 165, GLU 166, GLN 189 HIS 41	ALA 153, LEU 156, TYR 279 LYS 441
Losartan	**Autodock** GLU 166, GLN 189 **PyMOL** GLU 166, PHE 140 **Plip** GLU 166, GLN 189 GLU 166, GLN 189 (2)	**Autodock** ASN 277 **PyMOL** ASN 277, SER 280, ASN 290, TYR 279 **Plip** TYR 279, SER 280 (2), ASN 290, LYS 441 TYR 279 (2), VAL 283

Table 4: Interactions of amino acid residues of COVID-19 receptors in Mpro and Spike protein with Telmisartan, Valsartan, Olmesartan, Eprosartan, Candesartan and Losartan. (H-Bonds, Hydrophobic bonds, π-Stackings, π-Cation interactions, Halogen bonds and Salt bridges).

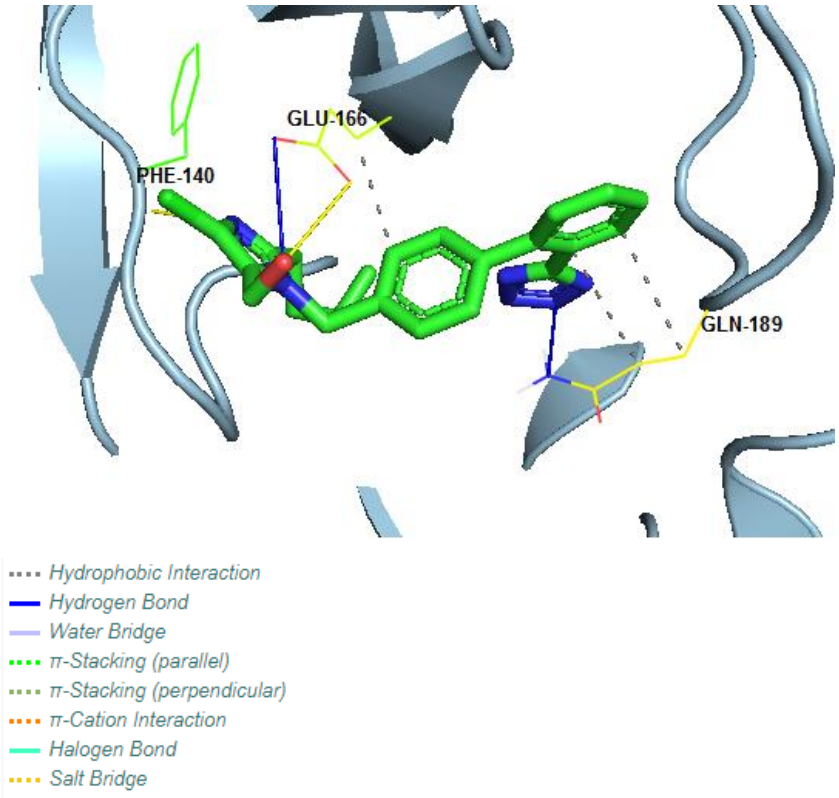

Figure 15: Losartan incorporated in a cavity of Mpro (6LU7) of SARS-CoV-2 Coronavirus using crystallographic grid.

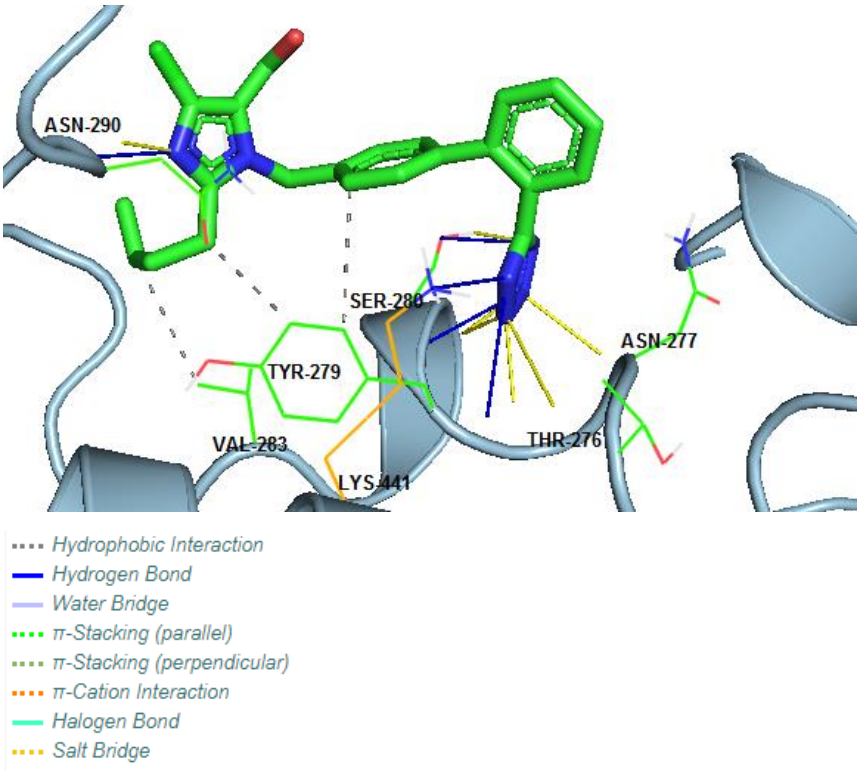

Figure 16: Losartan incorporated in a cavity of the Spike protein's Receptor binding domain (6LZG) of SARS-CoV-2 Coronavirus using crystallographic grid.

After testing the binding of sartans in the Mpro and Spike protein, we received interesting results. The presence of tetrazoles allows strong binding with amino acids like GLN 189. Also, presence of $-COO^-$ allows also the formation of hydrogen bonds with GLU 166 and HIS 41. Sartans, also have a lot of heteroatoms (N, S, O) in their molecular frame, allowing them to bind with amino acids like GLY 143, SER 144 and CYS 145. HIS 41 also forms salt bridges with the $-COO^-$ groups. In the case of the chain A of the Spike protein, LYS 441 forms salt bridges with the $-COO^-$ groups. Also, there are a lot of hydrogen bonds with ASN 154, THR 276, ASN 277 and LYS 441 due to the tetrazoles existence.

1.3.3. BV6 and its derivatives, EXP-3174 and DIZE

Diminazene diaceturate (DIZE) is an N-acetylglycinate salt resulting from the reaction of diminazene with 2 eq. of N-acetylglycine. It has a role as an

antiparasitic agent and a trypanocidal drug. It is approved by the US Food and Drug Administration and is used not only to treat human trypanosomiasis, but it has been shown to have antifibrotic properties by enhancing ACE2 activity too. This drug is also used to treat human trypanosomiasis and appears to have no major toxicity.

Losartan carboxylic acid (EXP-3174), an active carboxylic acid metabolite of Losartan, which is a non-peptide angiotensin II receptor antagonist that effectively blocks the angiotensin II-induced responses in vascular smooth muscle cells (VSMC). EXP-3174 elevates plasma renin activities and reduces mean arterial pressure. EXP-3174 is more effective than losartan in blocking the angiotensin II-induced increase in Egr-1 mRNA.

BV6 is a symmetrically bis-substituted imidazole analogue bearing at N-1 and N-3 two biphenyl moieties *ortho*-substituted either with tetrazole. It showed superior antagonistic activity and receptor affinity to that of losartan. Based on that Matsoukas *et. al.* provided BV6 derivatives for docking, as well (Figure 17).[71–80]

.

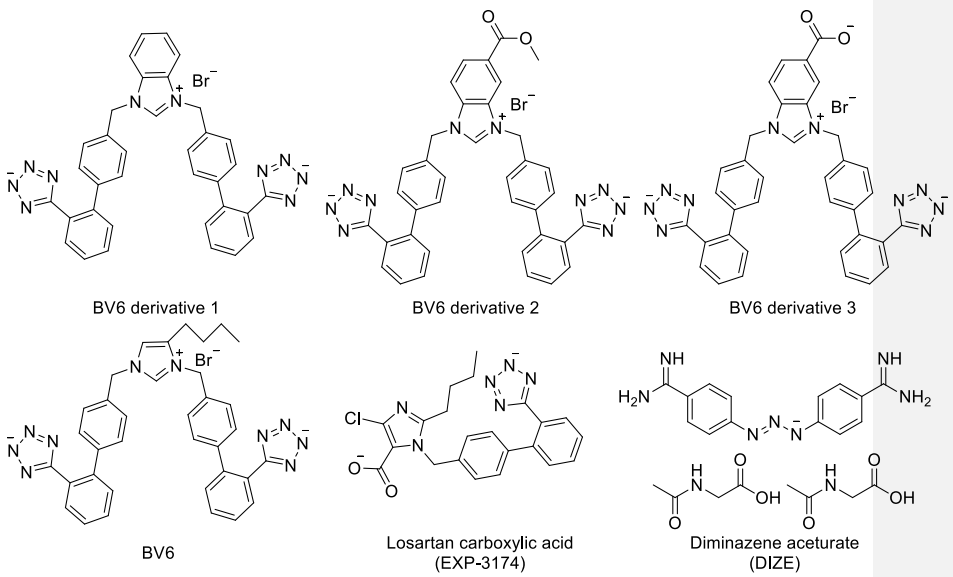

Figure 17: Structural depiction of BV6 and its derivatives, EXP-3174 and DIZE.

All these compounds showed exceptionally promising results in almost all cases. DIZE had the poorest results in most receptors. For Mpro, EXP-3174 has the highest score of -11.4 Kcal / mol followed by -11.06 Kcal / mol from the BV6 docking and -9.53 Kcal / mol from BV6 derivative **1** docking. After running Autodock, EXP-3174 forms three hydrogen bonds with MET 162, TYR 161, ASN 142 and on PyMOL two with HIS 41 and GLY 143. On Plip, it forms three hydrogen bonds with HIS 41, GLY 143 and CYS 145 and one hydrophobic bond with MET 165. BV6 showed on Autodock two hydrogen bonds with MET 162, GLN 189 but on PyMOL there are four different hydrogen bonds with CYS 145, LEU 141, GLU 166 and HIS 163. On Plip, BV6 forms four hydrogen bonds with SER 144 (2), CYS 145 and HIS 163, as well as seven hydrogen bonds with LEU 27 (2), MET 165, GLU 166, PRO 168, GLN 189 and ALA 191. Lastly, BV6 derivative **1** forms on Autodock, two hydrogen bonds with ASN 119 and GLU 166 and on PyMOL two hydrogen bonds with GLU 166 and GLN 189. On Plip, the hydrogen bonds are the same as on Autodock (*i.e*. ASN 119 and GLU 166), but it also forms four hydrophobic bonds with THR 25, LEU 27, MET 165 and GLN 189 and one π-stacking with HIS 41. (Table 5 & Table 6).

For the Spike protein (chain A), again EXP-3174 has a score of -11.2 Kcal / mol, BV6 a score of -9.56 Kcal / mol. On Autodock, EXP-3174 forms no bonds but on PyMOL, it forms two hydrogen bonds with ASN 154 and ASN 277. Also, on Plip, EXP-3174 forms three hydrogen bonds with ALA 153, ASN 154 and ASN 277 and four hydrophobic with LEU 156, LEU 278 and LEU 281 (2). In addition, BV6 on Autodock forms one hydrogen bond with LEU 156 and on PyMOL five hydrogen bonds with ASN 154, GLY 268, ASN 277 and PHE 274 (2). Lastly, on Plip, BV6 forms four hydrogen bonds with ASN 154, ASP 269, THR 276 and ASN 277, but also five hydrophobic bonds with ASN 149, ALA 153, LEU 156, ASP 269 and ASN 277 (Table 5 & Table 6).

For the Spike protein (chain B), BV6 seems to be the most efficient molecule with a score of -10.06 Kcal / mol, followed by BV6 derivative 1 with a score of -9.45 Kcal / mol. In fact, BV6 on Autodock shows four hydrogen bonds with ARG 357, ASN 343, ASP 398 and ASN 450 and on PyMOL, it shows four hydrogen bonds with ARG 346, ASN 450, ARG 357 and ARG 355. On Plip, BV6 shows five hydrogen bonds with ARG 346 (2), LYS 356, ARG 357 and ASN 450, as

well as four hydrophobic bonds with ALA 352, ASN 354 and ARG 355 (2). The BV6 derivative **1** forms on Autodock, two hydrogen bonds with SER 349 and ARG 357, but on PyMOL with SER 349 and PHE 347. Also, on Plip, the BV6 derivative **1** showed five hydrogen bonds with SER 349, LYS 356, ARG 357 (2) and ASN 450 and four hydrophobic bonds with ALA 344, ALA 348, ALA 352 and LYS 356 (Table 5 & Table 6).

For the RBD the BV6 derivatives showed excellent scores, specifically BV6 derivative **1** had a score of -11.3 Kcal / mol, BV6 derivative **2** had a score of -10.48 Kcal / mol and BV6 derivative **3** had a score of -9.96 Kcal / mol. After running Autodock, BV6 derivative **1** forms one hydrogen bond with LYS 353 but after running PyMOL, it forms one hydrogen bond with TYR 449. On Plip, BV6 derivative **1** forms four hydrogen bonds with four amino acids (*i.e.* LYS 353, SER 494, GLY 496 and TYR 505), nine hydrophobic bonds with HIS 34, GLU 37 (2), ASP 38, TYR 449, LEU 452, PHE 490, GLN 493 and TYR 505 and a π-cation bond with LYS 353, too. For BV6 derivative **2**, as well as BV6 derivative **3** on Autodock and on PyMOL they form the same bonds as BV6 derivative **1**. On Plip they also have the same π-cation bonds and almost the same hydrogen bonds, except the lack of the bond with SER 494 for BV6 derivative **3.** BV6 derivative **2** and BV6 derivative **3** have the same hydrogen bonds as BV6 derivative **1** with the exception of the absence of TYR 449 for BV6 derivative 3 and BV6 derivative **2** and BV6 derivative **3** have two additional bonds with LEU 452 and PHE 490 (Table 5 & Table 6).

For the Metallocenter, all the compounds had excellent scores. In detail, BV6, BV6 derivative **1**, BV6 derivative **2**, BV6 derivative **3** and EXP-3174 had scores of -11.42 Kcal / mol, -12.05 Kcal / mol, -11.79 Kcal / mol, -10.56 Kcal / mol and -9.46 Kcal / mol respectively. The metal complexation interaction in the above cases were with the tetrazole of each molecule and DIZE binds with the Zn^{II} with the azene (Table 5).

Except from the interactions with Zn^{II} there are also different types of bonds, formed with the ligands and the amino acids. In the case of BV6, it forms on PyMOL four hydrogen bonds with ASN 51, GLU 402, HIS 374 and PRO 346 and on Plip three hydrogen bonds with SER 47, ASN 51 and HIS 345, eleven

hydrophobic bonds with ASN 51, VAL 343, HIS 345, THR 347, ALA 348, TRP 349, LEU 359, PHE 504 and TYR 510 (3) but also a π-stacking interaction with HIS 378 (Table 6).

The BV6 derivative **1** forms on PyMOL two hydrogen bonds with PRO 346 and GLU 402 and on Plip four hydrogen bonds with ALA 348, ASP 350 (2) and GLU 402, three hydrophobic bonds with ASP 350, GLU 402 and TYR 515 but also a π-stacking interaction with HIS 374 and a salt bridge with ARG 514 (Table 6).

The BV6 derivative **2** forms on PyMOL four hydrogen bonds with GLU 406, GLU 357, PRO 346 and GLU 402 and on Plip, two hydrogen bonds with GLU 402 and GLU 406, six hydrophobic bonds with PHE 274, HIS 378, THR 449, PHE 504 and TYR 515 (2), three π-stacking interactions with PHE 274, HIS 401 and TYR 515 two π-cation interactions with ARG 273 and ARG 518, but also a salt bridge with HIS 505 (Table 6).

The BV6 derivative 3 forms on PyMOL four hydrogen bonds with ARG 514, ALA 348, ASP 350 and GLU 402 and on Plip, it forms four hydrogen bonds with HIS 345, PRO 346, GLU 398, GLU 402 and ARG 518, six hydrophobic bonds with PRO 346 (2), THR 371, HIS 401, GLU 402 and PHE 504 and two π-cation interactions with HIS 505 (2) (Table 6).

Lastly, EXP-3174 doesn't form bonds on PyMOL, but on Plip, it forms five hydrogen bonds with PRO 346, GLU 398, GLU 402 and ARG 514 (2), a hydrophobic bond with THR 347 and a salt bridge with ARG 518 (Table 6) (Figures 18-31).

Ligands	**Binding affinity for proteins ΔG (Kcal / mol)**				
	Mpro	**Spike protein (chain A)**	**Spike protein (chain B)**	**Receptor binding domain**	**Metallocenter**
BV6	-11.06	-9.56	-10.06	-6.71	-11.42
BV6 derivative 1	-9.53	-6.15	-9.45	-11.3	-12.05
BV6 derivative 2	-8.45	-7.8	-8.26	-10.48	-11.79
BV6 derivative 3	-8.1	-5.73	-8.53	-9.96	-10.56

DIZE	-6.75	-7.05	-5.3	-7.67	-6.22
EXP-3174	-11.4	-11.2	-7.45	-4.47	-9.46

Table 5:The average values of binding affinity for the complexes of BV6 and its derivatives, EXP-3174 and DIZE with COVID-19 receptors

Ligands	**Interactions of ligands with amino acids**				
	Mpro	**Spike protein (chain A)**	**Spike protein (chain B)**	**Receptor binding domain**	**Metallocenter**
BV6	**Autodock** MET 162, GLN 189 **PyMOL** CYS 145, LEU 141, GLU 166, HIS 163 **Plip** SER 144 (2), CYS 145, HIS 163 LEU 27 (2), MET 165, GLU 166, PRO 168, GLN 189, ALA 191	**Autodock** LEU 156 **PyMOL** ASN 154, GLY 268, ASN 277, PHE 274 (2) **Plip** ASN 154, ASP 269, THR 276, ASN 277 ASN 149, ALA 153, LEU 156, ASP 269, ASN 277	**Autodock** ARG 357, ASN 343, ASP 398, ASN 450 **PyMOL** ARG 346, ASN 450, ARG 357, ARG 355 **Plip** ARG 346 (2), LYS 356, ARG 357, ASN 450 ALA 352, ASN 354, ARG 355 (2)	**Autodock** - **PyMOL** ALA 397, SER 399 **Plip** ASN 354 (2), SER 399 (2), ARG 466 ALA 344, ALA 352, ARG 355, LYS 356 ARG 466	**PyMOL** ASN 51, GLU 402, HIS 374, PRO 346 **Plip** SER 47, ASN 51, HIS 345 ASN 51, VAL 343, HIS 345, THR 347, ALA 348, TRP 349, LEU 359, PHE 504, TYR 510 (3) HIS 378
BV6 derivative 1	**Autodock**	**Autodock**	**Autodock**	**Autodock**	**PyMOL**

	ASN 119, GLU 166 **PyMOL** GLU 166, GLN 189 **Plip** ASN 119, GLU 166 THR 25, LEU 27, MET 165, GLN 189 HIS 41	SER 280 **PyMOL** ASN 149, ASN 277 **Plip** ASN 149, MET 270, TYR 279, SER 280 ALA 153, LEU 156, ASP 269, TRP 271, PHE 274 (2)	SER 349, ARG 357 **PyMOL** SER 349, PHE 347 **Plip** SER 349, LYS 356, ARG 357 (2), ASN 450 ALA 344, ALA 348, ALA 352, LYS 356	LYS 353 **PyMOL** TYR 449 **Plip** LYS 353, SER 494, GLY 496, TYR 505 HIS 34, GLU 37 (2), ASP 38, TYR 449, LEU 452, PHE 490, GLN 493, TYR 505 LYS 353	PRO 346, GLU 402 **Plip** ALA 348, ASP 350 (2), GLU 402 ASP 350, GLU 402, TYR 515 HIS 374 ARG 514
BV6 derivative 2	**Autodock** ASN 119 **PyMOL** ASP 18, ASN 119, TYR 54	**Autodock** ASP 269, ARG 273 **PyMOL** THR 276, ASP 269,	**Autodock** LYS 356, SER 399 **PyMOL** THR 353, ALA 352, ASN 354,	**Autodock** LYS 353 **PyMOL** TYR 449 **Plip**	**PyMOL** GLU 406, GLU 357, PRO 346, GLU 402 **Plip** GLU 402,

	Plip TYR 54 (2), ASN 119, ASN 142 THR 26, TYR 118, ASN 142, MET 165, GLN 189	PHE 274 **Plip** ARG 273, THR 276, LYS 441 ASN 149, ALA 153, ASP 269, TRP 271, PHE 504 TRP 271 LYS 441	SER 399, VAL 341 **Plip** ALA 344, ARG 355, LYS 356, SER 399 ALA 344, ALA 348, LYS 356, ILE 468 ARG 466	LYS 353, SER 494, GLY 496, TYR 505 HIS 34, GLU 37 (2), ASP 38, TYR 449, LEU 452 (2), PHE 490 (2), GLN 493, TYR 505 LYS 353	GLU 406 PHE 274, HIS 378, THR 449, PHE 504, TYR 515 (2) PHE 274, HIS 401, TYR 515 ARG 273, ARG 518 HIS 505
BV6 derivative 3	**Autodock** HIS 164, ASN 119 **PyMOL** SER 46, ASN 119, GLN 189, GLY 143, HIS 164, THR 26 **Plip** THR 24, SER 46,	**Autodock** ASN 277, LYS 441 **PyMOL** LYS 441, ASN 290 **Plip** ASN 277, SER 280, ASN 290	**Autodock** ARG 357, SER 399 **PyMOL** ARG 346, SER 399, ASN 354, VAL 341, THR 353, ARG 357 **Plip** ARG 355 (2), LYS 356,	**Autodock** LYS 353 **PyMOL** TYR 449 **Plip** LYS 353, GLY 496, TYR 505 HIS 34, GLU 37 (2),	**PyMOL** ARG 514, ALA 348, ASP 350, GLU 402 **Plip** HIS 345, PRO 346, GLU 398, GLU 402, ARG 518 PRO 346 (2), THR 371, HIS 401, GLU 402, PHE 504

	ASN 119 (2) THR 25, LEU 27, TYR 118 (2), ASN 142	ASN 149, ALA 153, LEU 156 (2), TYR 279 LYS 441	ARG 357 (2), SER 399 ALA 344, ALA 348, ALA 352, ASN 354, LYS 356, ILE 468	ASP 38, LEU 452 (2), PHE 490 (2), GLN 493, TYR 505 LYS 353	HIS 505 (2)
DIZE	**Autodock** GLU 166 **PyMOL** THR 25, SER 46, GLU 166, ARG 188 **Plip** HIS 41, CYS 44, SER 46, GLU 166(2),) ARG 188, GLN 189, THR 190 MET 165, GLN 189	**Autodock** SER 155, LEU 156 (2), ASN 277, GLU 150, ALA 153 **PyMOL** LEU 156, TYR 252, SER 155, ASN 277, ALA 153 **Plip** SER 155, LEU 156, ARG 161, TYR 252, ASN 277 LEU 156 (2), ALA 251, TYR 252 (2)	**Autodock** ASN 343, ASP 364, PHE 338, THR 345 **PyMOL** GLU 340, LYS 336 **Plip** PHE 338, GLY 339, GLU 340 (2), TYR 365, LEU 368 PRO 337, PHE 338 (2), LEU 368	**Autodock** LYS 353, GLU 35, GLY 496, GLU 37, ARG 403, TYR 505 **PyMOL** GLU 35, GLU 37, TYR 505, SER 494 **Plip** GLU 35, GLU 37 (2), ASP 38 (2), LYS 353, ARG 403, GLN 493, SER 494 (3), TYR 505 GLU 37, ASP 38, TYR 449,	**PyMOL** ARG 393, ASP 350, ALA 348, GLU 375, GLU 402 **Plip** ALA 348 (3), ASP 350, GLU 375, TYR 385, ARG 393, GLU 402 THR 347, ASP 350

				TYR 505	
EXP-3174	**Autodock** MET 162, TYR 161, ASN 142 **PyMOL** HIS 41, GLY 143 **Plip** HIS 41, GLY 143, CYS 145 MET 165	**Autodock** - **PyMOL** ASN 154, ASN 277 **Plip** ALA 153, ASN 154, ASN 277 LEU 156, LEU 278, LEU 281 (2)	**Autodock** LYS 356, ARG 357, ARG 346 **PyMOL** ARG 355, ARG 357, ILE 358 **Plip** ARG 355 (2), ARG 357 ARG 357 ARG 355, ARG 357 ASN 354 LYS 356	**Autodock** PHE 464 **PyMOL** PHE 464, ARG 466 **Plip** ASN 354, ARG 355, PHE 464, ARG 466 ARG 355 ARG 355, ARG 466 (2) ARG 466	**PyMOL** - **Plip** PRO 346, GLU 398, GLU 402, ARG 514 (2) THR 347 ARG 518

Table 6: Interactions of amino acid residues of COVID-19 receptors in Mpro and Spike protein with BV6 and its derivatives, EXP-3174 and DIZE. (H-Bonds, Hydrophobic bonds, π-Stackings, π-Cation interactions, Halogen bonds and Salt bridges).

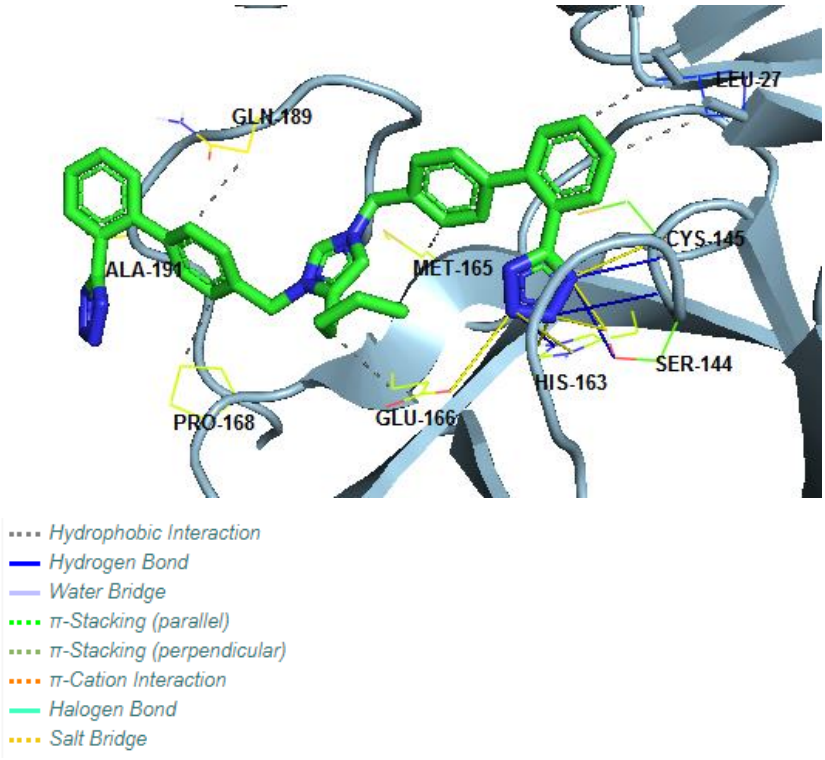

Figure 18: BV6 incorporated in a cavity of Mpro (6LU7) of SARS-CoV-2 Coronavirus using crystallographic grid.

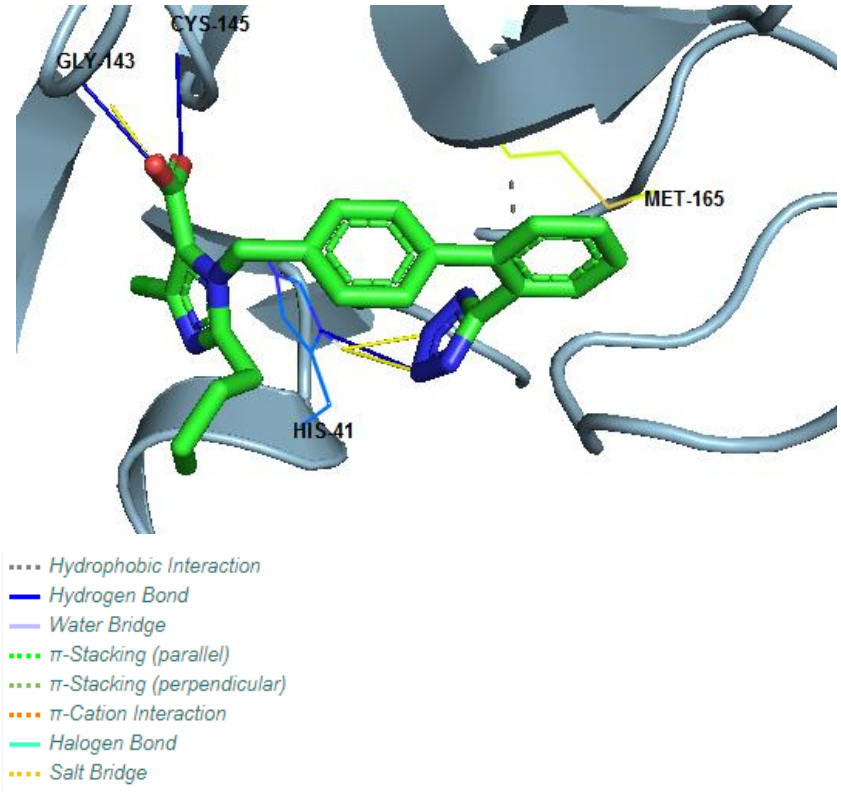

Figure 19: EXP-3174 incorporated in a cavity of Mpro (6LU7) of SARS-CoV-2 Coronavirus using crystallographic grid.

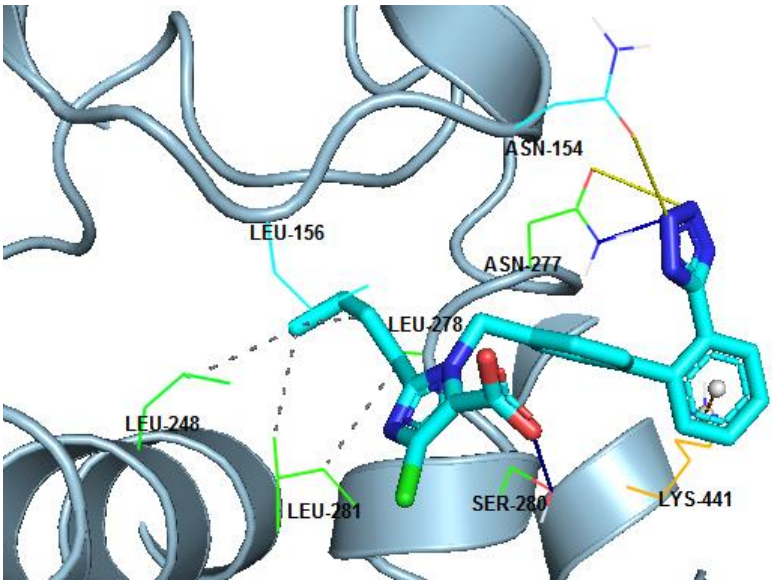

Hydrophobic Interaction
Hydrogen Bond
Water Bridge
π-Stacking (parallel)
π-Stacking (perpendicular)
π-Cation Interaction
Halogen Bond
Salt Bridge

Figure 20: EXP-3174 incorporated in a cavity of with Angiotensin-converting enzyme 2 (chain A of 6LZG) of SARS-CoV-2 Coronavirus using crystallographic grid.

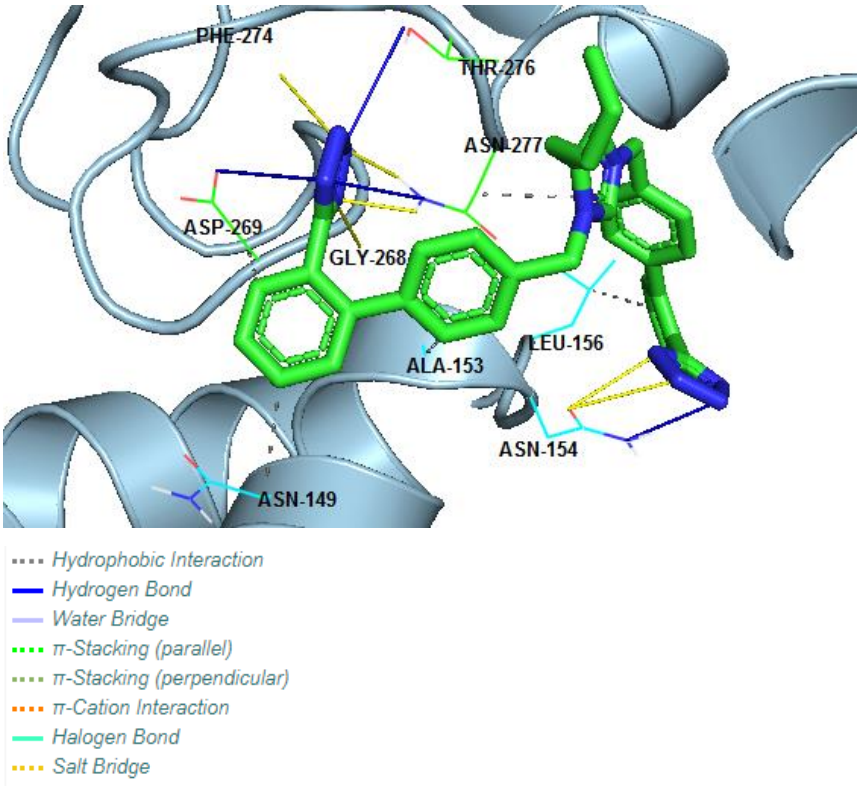

Figure 21: BV6 incorporated in a cavity of with Angiotensin-converting enzyme 2 (chain A of 6LZG) of SARS-CoV-2 Coronavirus using crystallographic grid.

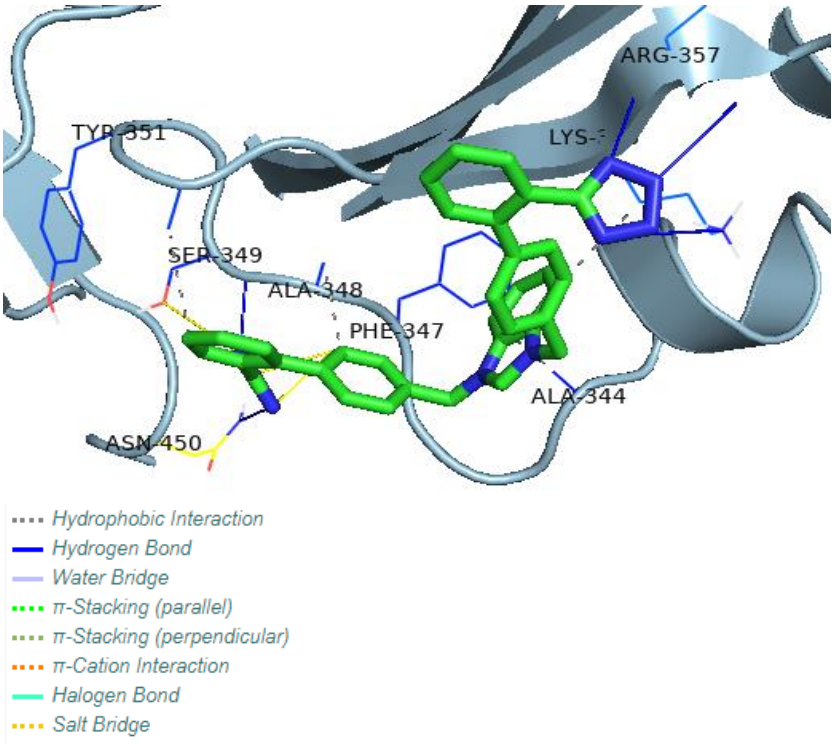

Figure 22: BV6 derivative 1 incorporated in a cavity of with Spike glycoprotein (chain B of 6LZG) of SARS-CoV-2 Coronavirus using crystallographic grid.

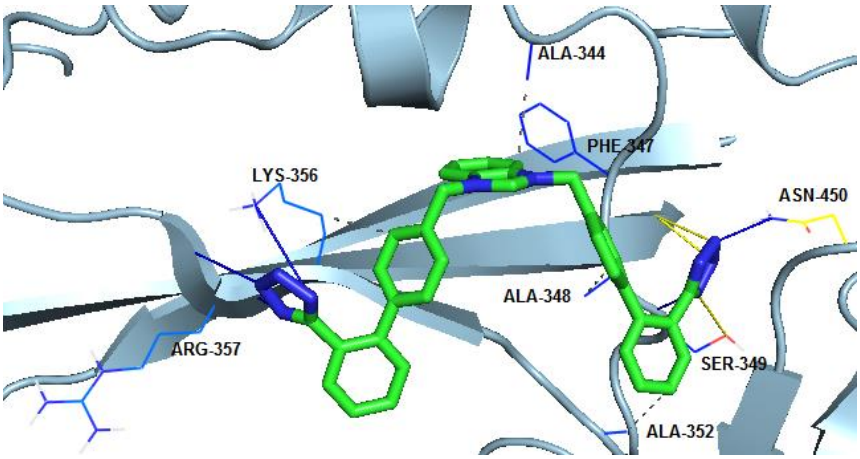

Hydrophobic Interaction
Hydrogen Bond
Water Bridge
π-Stacking (parallel)
π-Stacking (perpendicular)
π-Cation Interaction
Halogen Bond
Salt Bridge

Figure 23: BV6 incorporated in a cavity of with Spike glycoprotein (chain B of 6LZG) of SARS-CoV-2 Coronavirus using crystallographic grid.

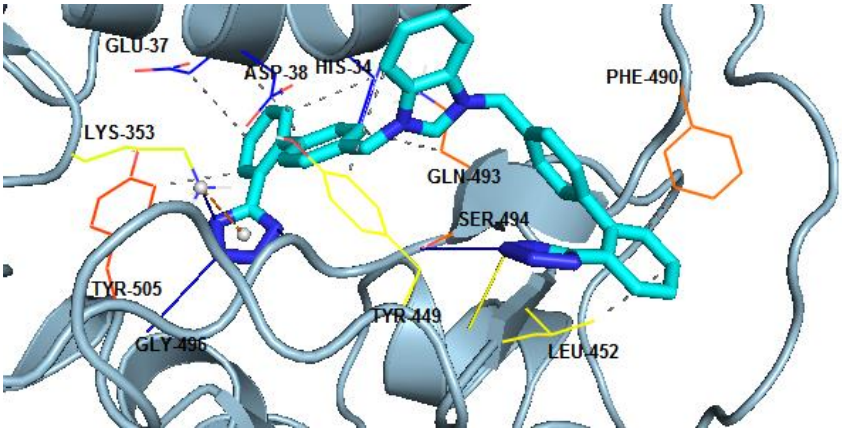

Hydrophobic Interaction
Hydrogen Bond
Water Bridge
π-Stacking (parallel)
π-Stacking (perpendicular)
π-Cation Interaction
Halogen Bond
Salt Bridge

Figure 24: BV6 derivative 1 incorporated in a cavity of the Spike protein's Receptor binding domain (6LZG) of SARS-CoV-2 Coronavirus using crystallographic grid.

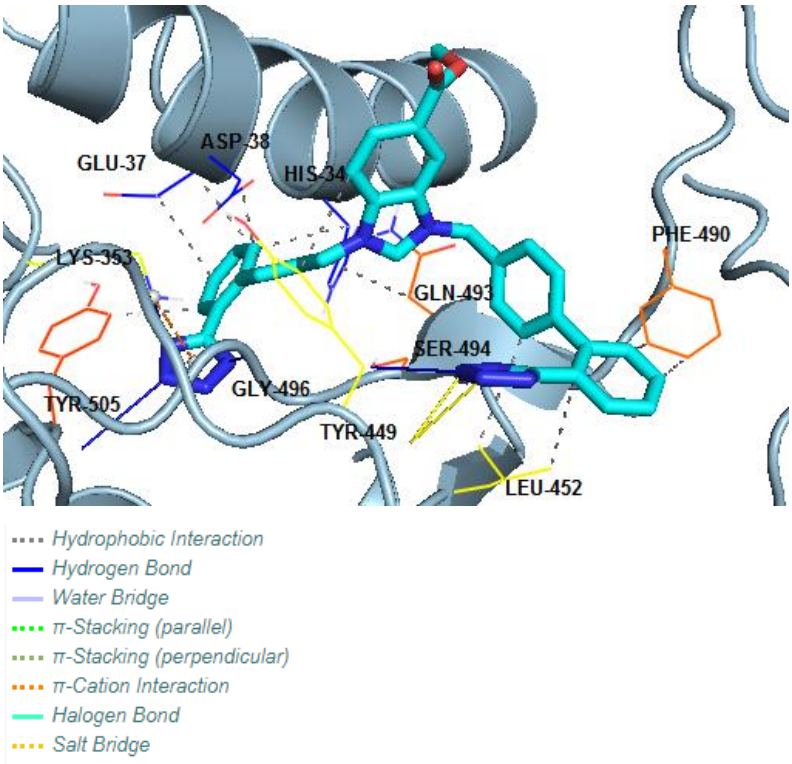

Figure 25: BV6 derivative 2 incorporated in a cavity of the Spike protein's Receptor binding domain (6LZG) of SARS-CoV-2 Coronavirus using crystallographic grid.

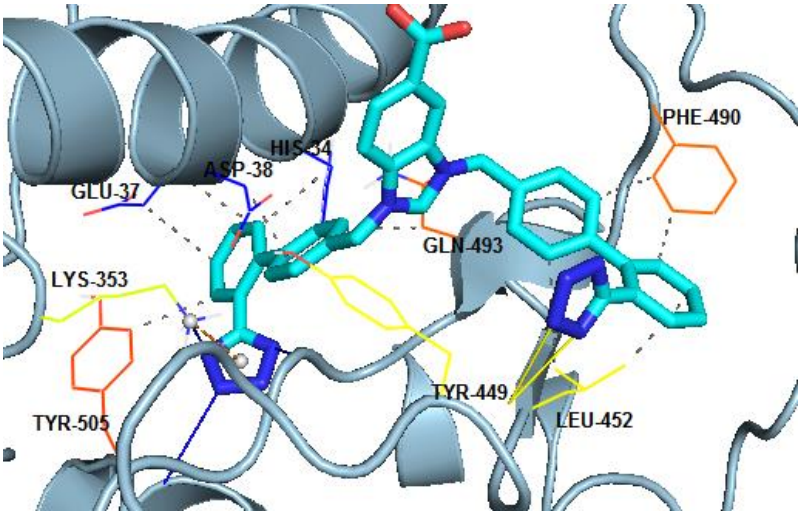

Hydrophobic Interaction
Hydrogen Bond
Water Bridge
π-Stacking (parallel)
π-Stacking (perpendicular)
π-Cation Interaction
Halogen Bond
Salt Bridge

Figure 26: BV6 derivative 3 incorporated in a cavity of the Spike protein's Receptor binding domain (6LZG) of SARS-CoV-2 Coronavirus using crystallographic grid.

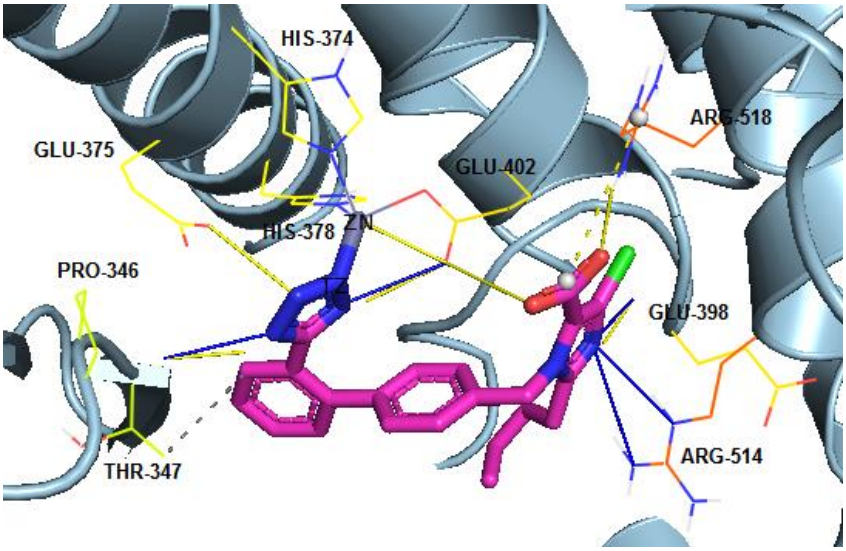

Hydrophobic Interaction
Hydrogen Bond
Water Bridge
π-Stacking (parallel)
π-Stacking (perpendicular)
π-Cation Interaction
Halogen Bond
Salt Bridge

Figure 27: EXP-3174 incorporated in a cavity of the metallocenter of Angiotensin-converting enzyme 2 (chain A of 6LZG) of SARS-CoV-2 Coronavirus using crystallographic grid.

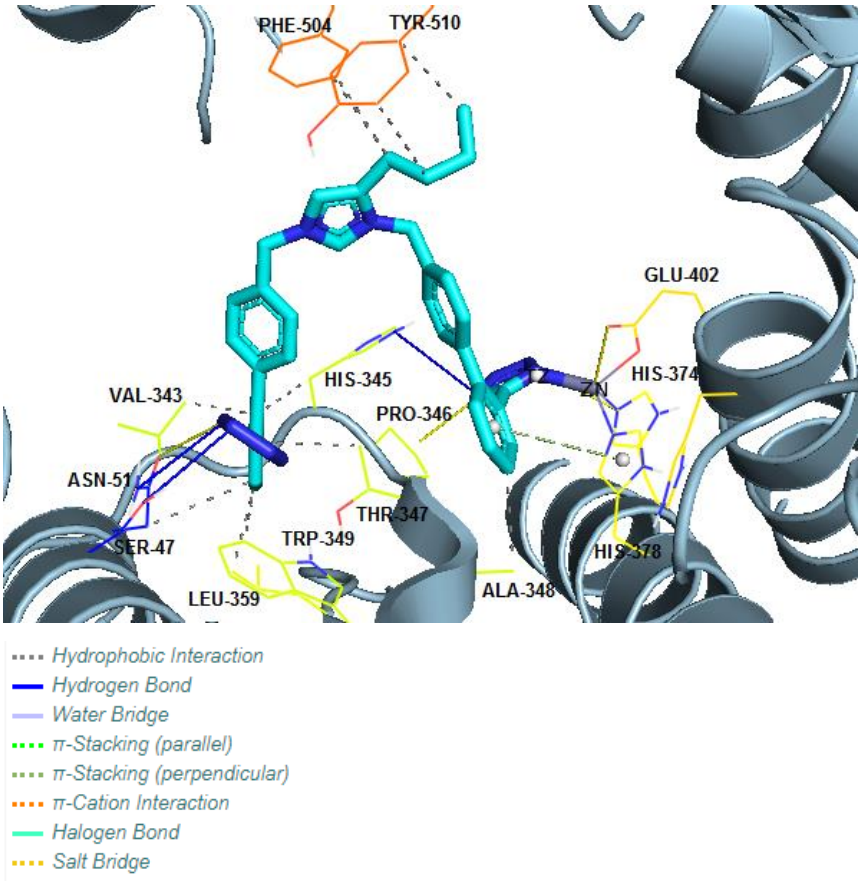

Figure 28: BV6 incorporated in a cavity of the metallocenter of Angiotensin-converting enzyme 2 (chain A of 6LZG) of SARS-CoV-2 Coronavirus using crystallographic grid.

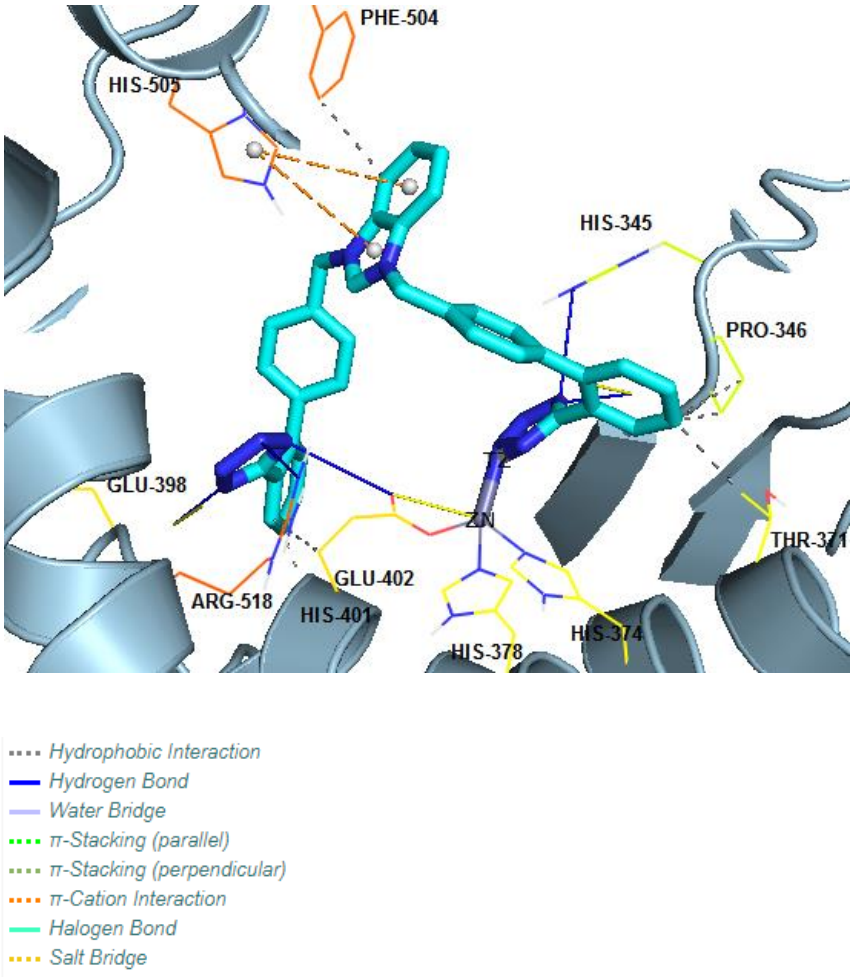

Figure 29: BV6 derivative 1 incorporated in a cavity of the metallocenter of Angiotensin-converting enzyme 2 (chain A of 6LZG) of SARS-CoV-2 Coronavirus using crystallographic grid.

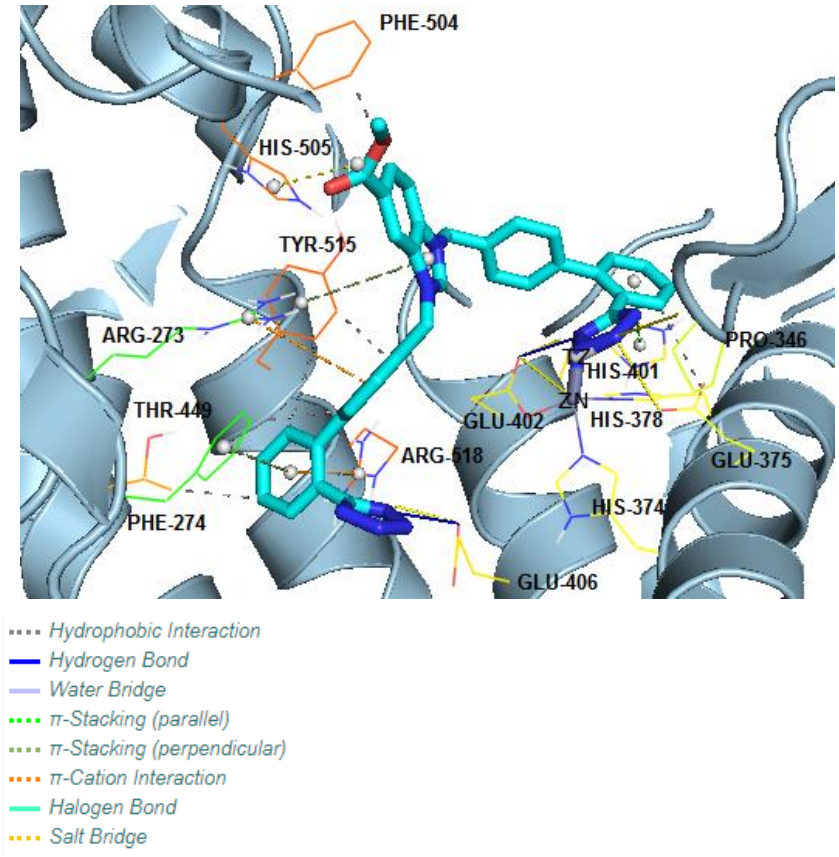

Figure 30: BV6 derivative 2 incorporated in a cavity of the metallocenter of Angiotensin-converting enzyme 2 (chain A of 6LZG) of SARS-CoV-2 Coronavirus using crystallographic grid.

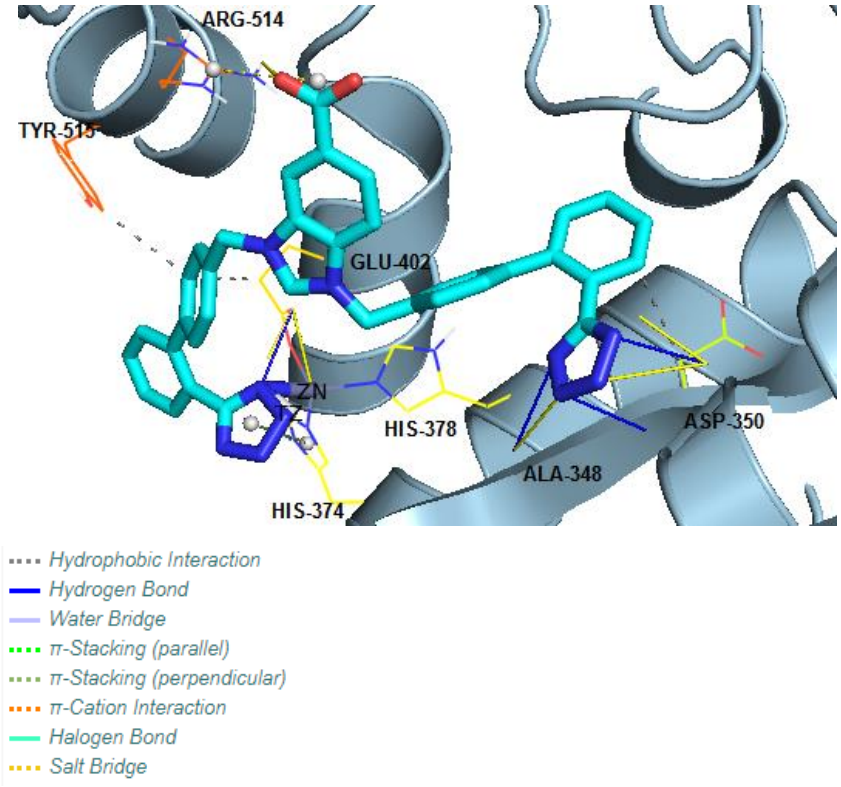

Figure 31: BV6 derivative 3 incorporated in a cavity of the metallocenter of Angiotensin-converting enzyme 2 (chain A of 6LZG) of SARS-CoV-2 Coronavirus using crystallographic grid.

These molecules were assigned at the same binding receptors. DIZE performed the poorest because, it had weak interactions, due to its size and lack of charges and aromatic groups, compared to the other molecules. EXP-3174 is in general very efficient, but that is logical because it is a derivative of losartan, but with an extra negative charge. BV6 and its derivatives have almost the same interactions and that is because of the central imidazole, as well as the two tetrazoles. In the case of Mpro, most of them had hydrogen bonds with HIS 41, ASN 119, GLU 166 and GLN 189, this is because of the presence of tetrazoles. We can also observe hydrophobic interactions with MET 165, due to the aliphatic groups. We also see hydrogen bonds with ASN 154, ASN 277 and THR 276 which were also observed in most of the sartans, in the chain A of the spike protein, because of the tetrazole groups. That is also the case, in

the chain B, where tetrazoles form strong hydrogen bonds with SER 349, ARG 357, LYS 356 and ASN 450. In RBD, due again to the tetrazoles, we observe hydrogen bonds with LYS 353, TYR 449 and GLY 496. Also, the tetrazoles allow the BV6 derivatives and EXP-3174 to bind effectively to the Zn^{II} but besides that they tend to bond to PRO 346, GLU 398 and GLU 402. Lastly, thanks to the aromaticity, the tetrazoles and the extensive size of these molecules, we observe a variation of interactions, besides hydrogen bonds and hydrophobic interactions.

1.3.4. Compounds from natural sources

Another class of compounds tested was the natural products, isolated by plants (*i.e.* fruits, vegetables, leaves, seeds, and grains). Quercetin is a plant flavonol from the flavonoid group of polyphenols. It has antioxidant and anti-inflammatory effects which might help reduce inflammation, kill cancer cells, control blood sugar, and help prevent heart disease. Rosmarinic acid is a polyphenol constituent of many culinary herbs, including rosemary. It is a caffeic acid ester, with tyrosine providing another phenolic ring *via* dihydroxyphenyl-lactic acid. Rosmarinic acid has a wide range of pharmacological effects, including anti-oxidative, anti-apoptotic, anti-tumorigenic, and anti-inflammatory effects. Its anti-inflammatory effects have been also revealed through *in vitro* and *in vivo* studies of various inflammatory diseases like arthritis, colitis, and atopic dermatitis. Caffeic acid is a polyphenol that is classified as a hydroxycinnamic acid. It has phenolic and acrylic functional groups and is found in all plants because it is an intermediate in the biosynthesis of lignin, one of the principal components of woody plant biomass and its residues. Caffeic acid is an antioxidant *in vitro* and also *in vivo* and in addition, it shows immunomodulatory and anti-inflammatory activity and antiviral abilities. It has also a variety of potential pharmacological effects in *in vitro* studies and in animal models, and the inhibitory effect of caffeic acid on cancer cell proliferation by an oxidative mechanism in the human HT-1080 fibrosarcoma cell line has recently been established. Salvianic acid is a 2-hydroxy monocarboxylic acid and a member

of catechols. It derives from a rac-lactic acid. It is a conjugate acid of a 3-(3,4-dihydroxyphenyl)lactate. It is used for antioxidation, anti-apoptosis, and anti-inflammation in various diseases. It also has anti-inflammatory, antioxidant and anti-acute myocardial ischemia effects and could protect against acute myocardial ischemia by blocking the formation of six-helix bundle core of Spike protein of SARS-CoV-2. Curcumin is a diarylheptanoid, belonging to the group of curcuminoids, which are natural phenols. It aids in the management of oxidative and inflammatory conditions, metabolic syndrome, arthritis, anxiety, and hyperlipidemia. Curcumin blocks the formation of reactive-oxygen species, possesses anti-inflammatory properties because of inhibition of cyclooxygenases (COX) and other enzymes involved in inflammation; and disrupts cell signal transduction by various mechanisms including inhibition of protein kinase C. These effects may play a role in the agent's observed antineoplastic properties, which include inhibition of tumor cell proliferation and suppression of chemically induced carcinogenesis and tumor growth in animal models of cancer (Figure 32). [71,81–92]

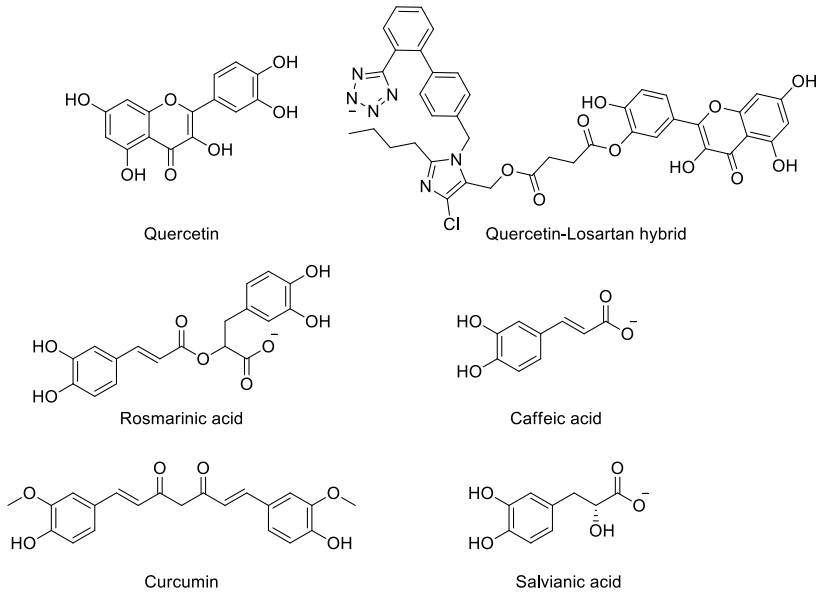

Figure 32: Structural depiction of Quercetin-Losartan complex, Quercetin, Rosmarinic acid, Caffeic acid, Curcumin and Salvianic acid

For all the receptors, it seems that Rosmarinic acid binds the strongest of all the studied compounds. Specifically, the scores are -13.97 kcal / mol for the Mpro, -10.21 kcal / mol for the Spike protein (chain A) and -10.09 kcal / mol for the Spike protein (chain B). After using Autodock, Rosmarinic acid seems to form nine hydrogen bonds with Mpro and specifically with LEU 141 (2), HIS 172, GLU 166, SER 144, MET 162, HIS 164, TYR 161 and GLN 192. For PyMOL there are six hydrogen bonds with GLN 192, GLN 189, GLU 166, HIS 163, SER 144 and CYS 145. Finally, in Plip there are eleven hydrogen bonds with LEU 141 (2), GLY 143, SER 144, CYS 145, HIS 163, GLN 189, THR 190 (2) and GLN 192 (2), but also two hydrophobic bonds with GLU 166 and PRO 168 (Table 7 & Table 8).

In the case of the Spike protein (chain A), with Autodock, four hydrogen bonds with ASN 277, SER 280, ASN 154 and LYS 441 exist and with PyMOL the same bonds exist. An additional hydrogen bond is observed with THR 276. After using Plip, Rosmarinic acid forms eight hydrogen bonds with ASN 154, TYR 252 (2), THR 276, TYR 279, SER 280 (2) and LYS 441, but also three

hydrophobic bonds with three different amino acids LEU 156, LEU 278 and LEU 281 (Table 8).

Lastly, we used Autodock with the Spike protein (chain B), and observed five hydrogen bonds with SER 399, ASN 450 (2), ALA 348 and ASP 398. For PyMOL, Rosmarinic acid bonds with SER 339, VAL 341, ALA 348, ARG 346 and THR 345 to form five hydrogen bonds. In addition, after using Plip, it seems that Rosmarinic acid forms eight hydrogen bonds with four different amino acids THR 345 (2), ARG 346 (2), ALA 348 and SER 399 (3), three hydrophobic bonds with ALA 344, ARG 346 and ASN 354 and one salt bridge with ARG 346 (Table 8) (Figures 33-35).

Ligands	**Binding affinity for proteins ΔG (Kcal / mol)**		
	Mpro	**Spike protein (chain A)**	**Spike protein (chain B)**
Quercetin-Losartan complex	-8.32	-5.55	-3.72
Quercetin	-9.53	-8.82	-7.0
Rosmarinic acid	-13.97	-10.21	-10.09
Caffeic acid	-8.91	-9.17	-6.12
Curcumin	-7.13	-4.91	-4.35
Salvianic acid	-9.51	-8.58	-7.42

Table 7: The average values of binding affinity for the complexes of Quercetin-Losartan complex, Quercetin, Rosmarinic acid, Caffeic acid, Curcumin and Salvianic acid with COVID-19 receptors

Ligands	**Interactions of ligands with amino acids**		
	Mpro	**Spike protein (chain A)**	**Spike protein (chain B)**
Quercetin-Losartan complex	**Autodock** TYR 161, GLN 192, HIS 164	**Autodock** LEU 156, SER 280	**Autodock** THR 345, ARG 346

	PyMOL ASN 142, CYS 145, HIS 164, GLU 166, GLN 192, ARG 188 **Plip** THR 25, THR 26, HIS 164, GLU 166, LEU 167, GLN189, THR 25, THR 26, LEU 27, GLU 166, GLN 189 HIS 41	**PyMOL** ASN 149, ASN 277, TYR 279, SER 280 **Plip** ASN 154, SER 155, TYR 252, ASN 277 (2), ASN 290 LEU 156 (2), ASN 277, TYR 279 (2)	**PyMOL** TYR 351, ARG 346, THR 345 **Plip** THR 345, ARG 346 (2), TYR 351 ALA 344, ALA 352, ILE 468 (2), THR 470, LEU 492 TYR 351
Quercetin	**Autodock** LEU 141, HIS 164, SER 144, LEU 141, TYR 161 **PyMOL** HIS 163, HIS 164, SER 144, GLY 143, CYS 145 **Plip** LEU 141, GLY143, SER 144 (2), CYS 145, HIS 163, GLU 166 (2), GLN 189 (2)	**Autodock** ASN 154 **PyMOL** ASN 154, ASN 277 ALA 153 **Plip** ASN 154 (2), TYR 252 (3) LEU 156, ASN 277, LEU 278	**Autodock** ASP 398, ASP 364 (2), GLY 339, LEU 335, ASP 442, TYR 451 **PyMOL** ASP 364, PHE 338, CYS 336 **Plip** LEU 335, GLY 339, ASN 343, ASP 364 (3), LEU 368

	GLU 166		PHE 338, LEU 368
Rosmarinic acid	**Autodock** LEU 141 (2), HIS 172, GLU 166, SER 144, MET 162, HIS 164, TYR 161, GLN 192 **PyMOL** GLN 192, GLN 189, GLU 166 HIS 163, SER 144, CYS 145 **Plip** LEU 141 (2), GLY 143, SER 144, CYS 145, HIS 163, GLN 189, THR 190 (2), GLN 192 (2) GLU 166, PRO 168	**Autodock** ASN 277, SER 280, ASN 154, LYS 441 **PyMOL** ASN 154, ASN 277, THR 276, SER 280, LYS 441 **Plip** ASN 154, TYR 252 (2), THR 276, TYR 279, SER 280 (2), LYS 441 LEU 156, LEU 278, LEU 281	**Autodock** SER 399, ASN 450 (2), ALA 348, ASP 398 **PyMOL** SER 339, VAL 341, ALA 348, ARG 346, THR 345 **Plip** THR 345 (2), ARG 346 (2), ALA 348, SER 399 (3) ALA 344, ARG 346, ASN 354, ARG 346
Caffeic acid	**Autodock** LEU 141, TYR 161 SER 144, GLN 189, HIS 164, MET 162, GLU 166 **PyMOL**	**Autodock** GLU 150, ASN 277 **PyMOL**	**Autodock** PHE 347 (2), ASN 450, GLY 339, ASP 398 **PyMOL**

	HIS 163, HIS 41, GLU 143 CYS 145, SER 144 **Plip** LEU 141 (2), SER 144 (2), CYS 145, HIS 163 HIS 41	TYR 252, SER 280, ASN 277 LEU 278, ALA 153 **Plip** ASN 154, TYR 252 (3), ASN 277, SER 280 LEU 156	TYR 351, ARG 346, ASN 450 **Plip** ARG 346, PHE 347 (2), TYR 351, ASN 450 ALA 352
Curcumin	**Autodock** MET 162, HIS 164, GLN 192 **PyMOL** GLN 192 **Plip** THR 190, GLN 192 HIS 41, LEU 167, ASP 187, GLN 189, GLN 192	**Autodock** ALA 153, LEU 156, GLU 150, LYS 441 **PyMOL** SER 280, LYS 441, ASN 277, ASN 154, ALA 163 **Plip** ALA 153, THR 276, ASN 277, TYR 279, SER 280, LYS 441 ASN 154, LEU 156, TYR 279	**Autodock** GLY 339, ASP 442, THR 345, VAL 367 **PyMOL** VAL 341, THR 345, SER 399, ARG 346 **Plip** THR 345 (2), LYS 356, SER 399 GLU 340, ASN 354, LYS 356
Salvianic acid	**Autodock**	**Autodock**	**Autodock**

	LEU 141, HIS 163, GLU 166, SER 144, HIS 172 **PyMOL** HIS 163, GLN 189 SER 144, CYS 145, GLU 166 **Plip** GLY 143, SER 144 (4), CYS 145, HIS 163, GLU 166 (2), GLN 189 GLU 166	GLU 150, GLY 268 **PyMOL** LEU 266, TYR 252, LEU 281, SER 280 **Plip** TYR 252 (2), GLY 268, ASN 277(2), SER 280 (2), LEU 281 LEU 156, LEU 278	ARG 346, ASN 450 (2), ASN 150, ASP 398 **PyMOL** TYR 351, ARG 346, ASN 450 **Plip** ARG 346, PHE 347 (2), TYR 351 (2), ASN 450 ALA 352

Table 8: Interactions of amino acid residues of COVID-19 receptors in Mpro and Spike protein with Quercetin-Losartan complex, Quercetin, Rosmarinic acid, Caffeic acid, Curcumin and Salvianic acid. (H-Bonds, Hydrophobic bonds, π-Stackings, π-Cation interactions, Halogen bonds and Salt bridges).

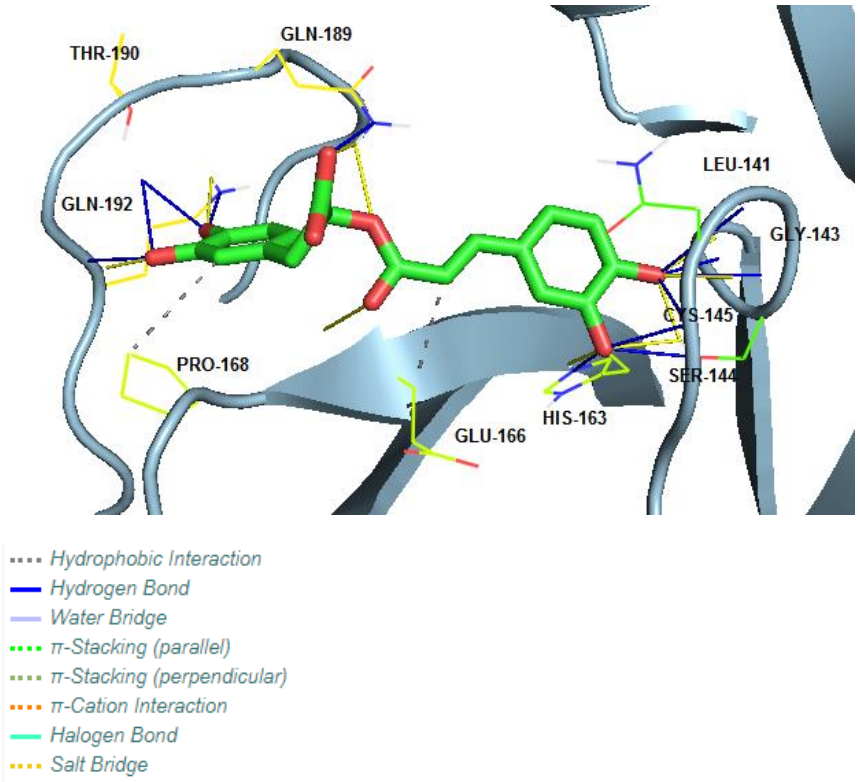

Figure 33: Rosmarinic acid incorporated in a cavity of Mpro (6LU7) of SARS-CoV-2 Coronavirus using crystallographic grid.

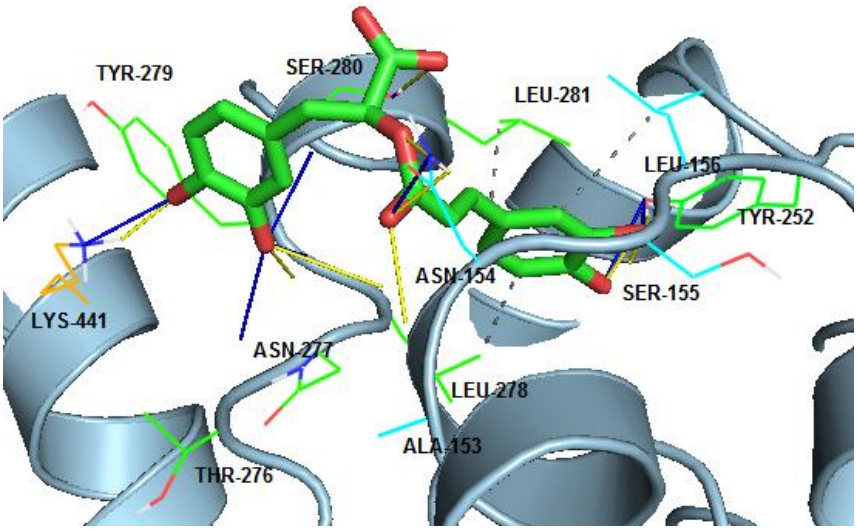

Hydrophobic Interaction
Hydrogen Bond
Water Bridge
π-Stacking (parallel)
π-Stacking (perpendicular)
π-Cation Interaction
Halogen Bond
Salt Bridge

Figure 34: Rosmarinic acid incorporated in a cavity of with Angiotensin-converting enzyme 2 (chain A of 6LZG) of SARS-CoV-2 Coronavirus using crystallographic grid.

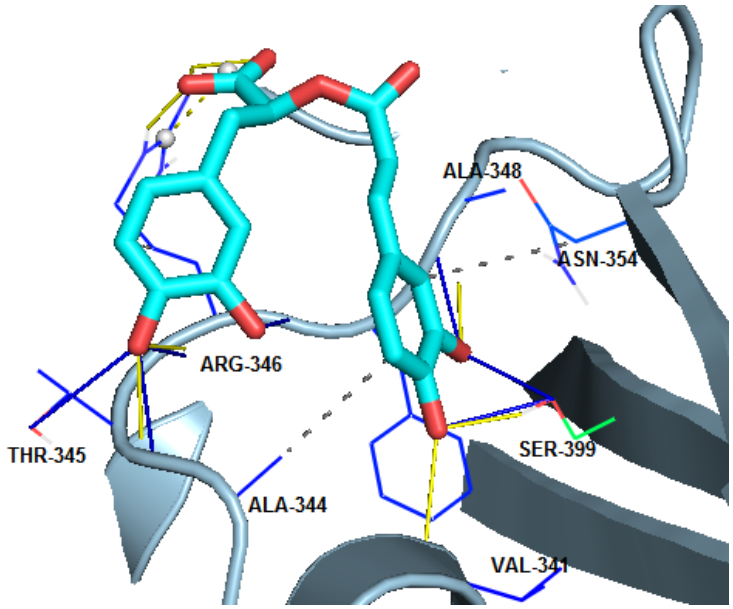

Hydrophobic Interaction
Hydrogen Bond
Water Bridge
π-Stacking (parallel)
π-Stacking (perpendicular)
π-Cation Interaction
Halogen Bond
Salt Bridge

Figure 35: Rosmarinic acid incorporated in a cavity of with Spike glycoprotein (chain B of 6LZG) of SARS-CoV-2 Coronavirus using crystallographic grid.

These molecules were tested at the same binding pockets. We can observe the same interactions with the exception of the Quercetin-Losartan complex, due

to its size also interacts in the Mpro with THR 25, THR 26, LEU 27. In Mpro, GLU 166 and GLN 189 are once again common amino acids that interact *via* hydrogen bonds as well as SER 144 and CYS 145. CYS 145, SER 144 and GLN 192, bind strongly due to the alcohols and GLN 189 interacts with the -COO^- group present in Rosmarinic acid, as well as the other molecules. For the chain A of the Spike protein, ASN 154, ASN 277 and SER 280 hydrogen bonds are mostly observed and rarer the LYS 441 hydrogen bonds, though they still are observed, especially interacting with molecules who have alcohols. That is also the case for ASN 154 and ASN 277 and SER 280 interacts strongly with -COO^-. In the chain B of the Spike protein, the most common interactions are with SER 399, ARG 346 and THR 345 due to the presence of the alcohol groups, and ASP 398 and ASN 450 with the aromatic groups.

1.3.5. Curcumin derivatives

Based on the interesting and promising results of the natural products, we collaborated with Professor Tzakos, who provided a range of curcumin derivatives, to be tested *in silico* (Figure 36). After testing those molecules, we observed that D-4 and B-37 have excellent scores for the Mpro and the Spike protein (chain A) and good scores for the Spike protein (chain B). In detail, the score for D-4 for the Mpro was -10.76 kcal / mol, for the Spike protein (chain A) -10.61 kcal / mol and -7.66 kcal / mol for the Spike protein (chain B). Similarly, for the B-37 the score for the Mpro was -10.61 kcal / mol, for the Spike protein (chain A) -9.07 kcal / mol and -7.94 kcal / mol for the Spike protein (chain B) (Table 9).

In the case of Mpro, based on Autodock, D-4 forms a hydrogen bond with TYR 161 and on PyMOL forms two hydrogen bonds with ASN 142 and GLN 189. On Plip, the hydrogen bond exists with GLN 189, as well as six hydrophobic bonds with PHE 140, MET 165, GLU 166, PRO 168, ASP 187 and GLN 189. For the Spike protein (chain A) on Autodock, D-4 forms three hydrogen bonds with ASN 154, ALA 153, ASN 277 and on PyMOL there are the same bonds except for ASN 277. Based on Plip, D-4 forms three hydrogen bonds with ASN 154, ASN 277, SER 280 and eight hydrophobic bonds with LEU 156 (2), LEU 248, TYR 252 (2), LEU 266, ASN 277 and LEU 278. (Table 10).

For the B-37 molecule, it seems that on Mpro, by using Autodock, that it forms two hydrogen bonds with TYR 161 and HIS 163 and on PyMOL, two different

hydrogen bonds with LEU 141 and HIS 164. On Plip, B-37 binds with four amino acids (*i.e.* GLY 143, SER 144, HIS 163 and GLN 189), forming four hydrogen bonds, with three amino acids (*i.e*. HIS 41, MET 165, PRO 168) forming three hydrophobic bonds and with one amino acid *(i.e.* HIS 41) forming a π-stacking bond. For the Spike protein (chain A) on Autodock, B-37 forms three hydrogen bonds with TYR 252, LEU 156 and SER 280 but no hydrogen bonds were formed using PyMOL. Finally, on Plip, there were three hydrogen bonds with ASN 154, TYR 252, SER 280, six hydrophobic bonds with LEU 156, LEU 248, TYR 252, LEU 266, ASN 277, LEU 278 and with one amino acid *(i.e*. LYS 441) forming a π-stacking bond (Table 10) (Figues 37-40).

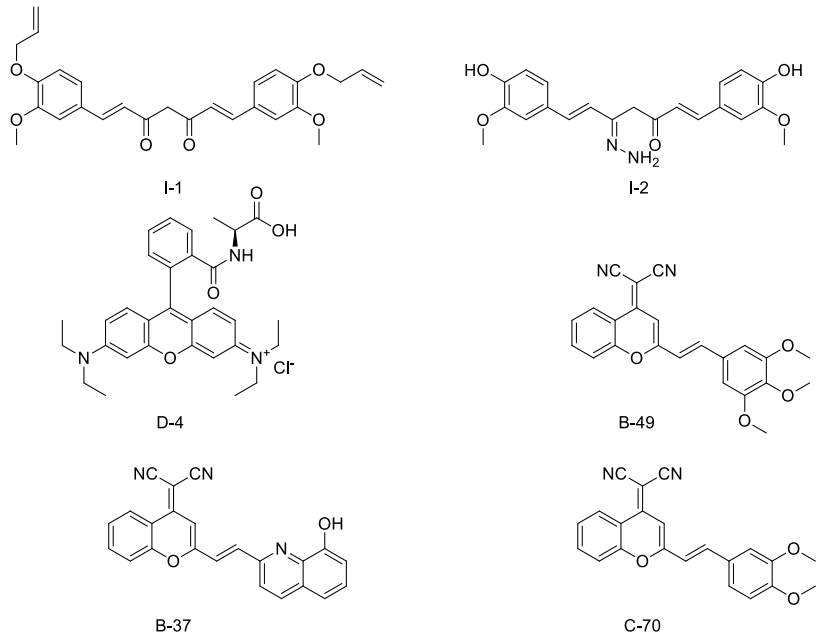

Figure 36: Structural depiction of I-1, I-2, D-4, B-49, B-37 and C-70

Ligands	**Binding affinity for proteins ΔG (Kcal / mol)**		
	Mpro	**Spike protein (chain A)**	**Spike protein (chain B)**
I-1	-6.98	-6.62	-5.1
I-2	-8.35	-7.88	-6.35

D-4	-10.76	-10.61	-7.66
B-49	-8.97	-7.9	-6.38
B-37	-10.61	-9.07	-7.94
C-70	-9.3	-8.89	-6.9

Table 9:The average values of binding affinity for the complexes of I-1, I-2, D-4, B-49, B-37 and C-70 with COVID-19 receptors

Ligands	**Interactions of ligands with amino acids**		
	Mpro	**Spike protein (chain A)**	**Spike protein (chain B)**
I-1	**Autodock** TYR 161, HIS 163, THR 26 **PyMOL** THR 26, ASN 142, LEU 141, HIS 163, GLN 189 **Plip** THR 26, HIS 163, GLN 189 THR 25, GLU 166, LEU 167, GLN 189	**Autodock** LEU 281 **PyMOL** LEU 278, PRO 263, VAL 244 **Plip** LEU 248, TYR 252, LEU 281 TYR 158, ALA 251, TYR 255, ILE 256, LEU 262, LEU 278	**Autodock** ARG 355, ASP 398, ASN 450 **PyMOL** ASN 354, ARG 346, ASN 450 **Plip** ARG 346 (2), SER 349, ASN 450 ALA 344, ARG 346, ALA 348, ALA 352
I-2	**Autodock** TYR 161, HIS 163, GLN 189 **PyMOL**	**Autodock** ASN 290, LEU 156, TYR 252, LYS 441, SER 280 **PyMOL**	**Autodock** SER 399, ARG 466 **PyMOL** ARG 346, SER 399, VAL 341,

	GLU 166, THR 190, GLN 192 **Plip** GLU 166, THR 90, GLN 192 (2) MET 165, PRO 168, GLN 189	ASN 290, LYS 441, ALA 153, SER 280, LEU 266 **Plip** ALA 153, ASN 154, ARG 161 (2), GLY 268, ASN 277, SER 280, ASN 290, LYS 441 LEU 156 (2), LEU 266, TYR 279, LEU 281 (2) ARG 161	ARG 355, ARG 466 **Plip** ARG 346, ARG 355 (3), LYS 356, SER 399, ARG 466 (2) VAL 341 (2) ARG 355 (2)
D-4	**Autodock** TYR 161 **PyMOL** ASN 142, GLN 189 **Plip** GLN 189 PHE 140, MET 165, GLU 166, PRO 168, ASP 187, GLN 189	**Autodock** ASN 154, ALA 153, ASN 277 **PyMOL** ASN 154, ALA 153 **Plip** ASN 154, ASN 277, SER 280 LEU 156 (2), LEU 248, TYR 252 (2), LEU 266, ASN 277, LEU 278	**Autodock** SER 399, ASP 264, ASP 398, ARG 355, ASN 354, THR 345, ARG 346 **PyMOL** ALA 348, SER 399, ASN 354 **Plip** ALA 348, ASN 354, SER 399 (4) ALA 344, ALA 348, ALA 352 LYS 356
B-49	**Autodock** - **PyMOL** THR 190, GLU 166 **Plip**	**Autodock** ASN 154 **PyMOL** ASN 277, LEU 156 **Plip**	**Autodock** ARG 346, TYR 351, ASP 442, ASN 450 **PyMOL** ASN 450, ARG 346, PHE 347,

	HIS 41, GLU 166 (2), GLN 189 GLU 166, GLN 189	ASN 154 ASN 154, LEU 156 (2), LEU 266, LEU 278, LEU 281 (2)	ALA 352, ASN 354, ARG 355 **Plip** SER 349, ARG 355, ASN 450 ALA 348, ALA 352, ILE 468 ARG 355, LYS 356
B-37	**Autodock** TYR 161, HIS 163 **PyMOL** LEU 141, HIS 164 **Plip** GLY 143, SER 144, HIS 163, GLN 189 HIS 41, MET 165, PRO 168 HIS 41	**Autodock** TYR 252, LEU156, SER 280 **PyMOL** - **Plip** ASN 154, TYR 252, SER 280 LEU 156, LEU 248, TYR 252, LEU 266, ASN 277, LEU 278 LYS 441	**Autodock** SER 399, ALA 348, ARG 346, ASP 442 **PyMOL** ALA 348, ASN 450, SER 349, TYR 351, SER 399 **Plip** ALA 348, SER349 (2), TYR 351, SER 399, ASN 450 ALA 344, ALA 348, ALA 352 LYS 356
C-70	**Autodock** TYR 161, HIS 163 **PyMOL** THR 190 **Plip** HIS 41, GLU 166 (2),	**Autodock** GLU 150, ASN 154 **PyMOL** SER 280, ALA 251, ALA 153 **Plip** TYR 252, ASN 277, SER 280	**Autodock** ARG 355, ASP 398 **PyMOL** ARG 346 **Plip** ASN 354, ALA 344

	GLN189, GLN 192 (2) MET 165, GLU 166	ALA 251, TYR 252 (2), LEU 266, ASN 277, LEU 278, LEU 281	ALA 348 PHE 347

Table 10: Interactions of amino acid residues of COVID-19 receptors in Mpro and Spike protein with I-1, I-2, D-4, B-49, B-37 and C-70. (H-Bonds, Hydrophobic bonds, π-Stackings, π-Cation interactions, Halogen bonds and Salt bridges).

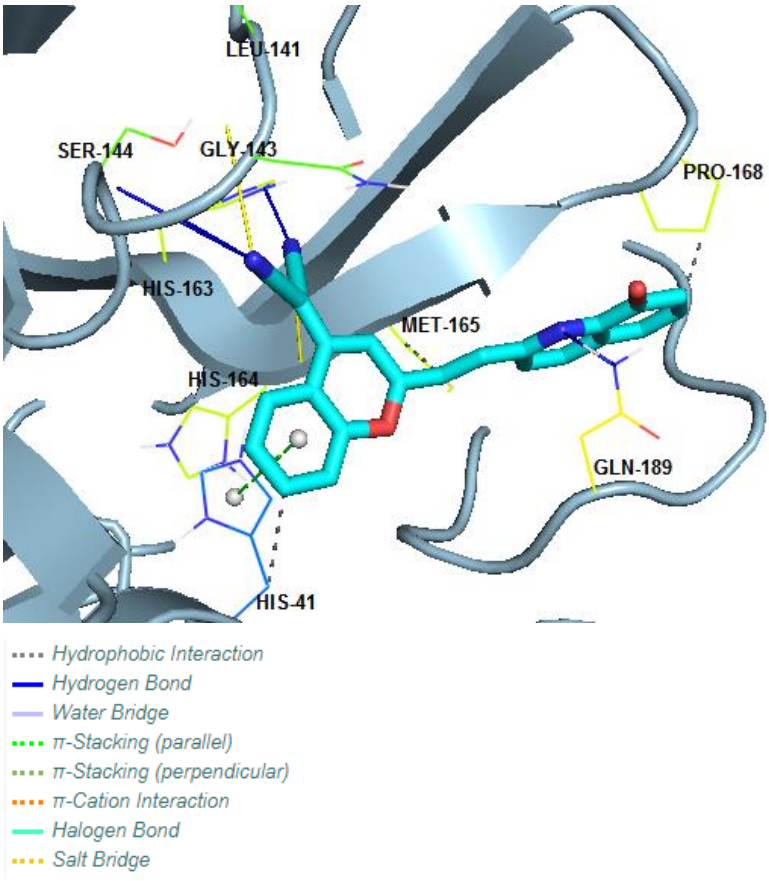

Figure 37: B-37 incorporated in a cavity of Mpro (6LU7) of SARS-CoV-2 Coronavirus using crystallographic grid.

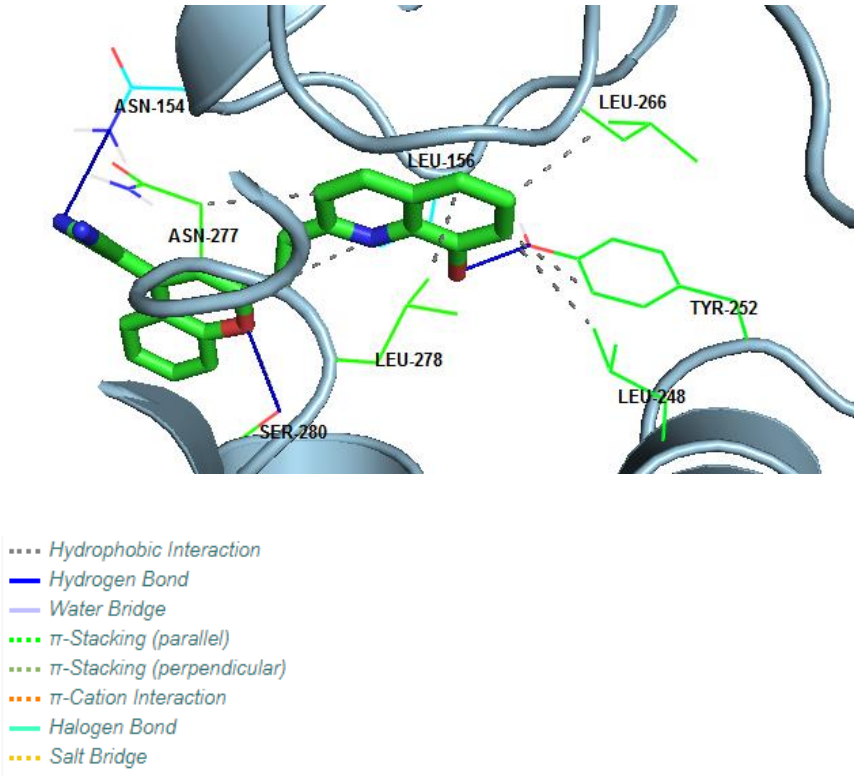

Figure 38: B-37 incorporated in a cavity of with Angiotensin-converting enzyme 2 (chain A of 6LZG) of SARS-CoV-2 Coronavirus using crystallographic grid.

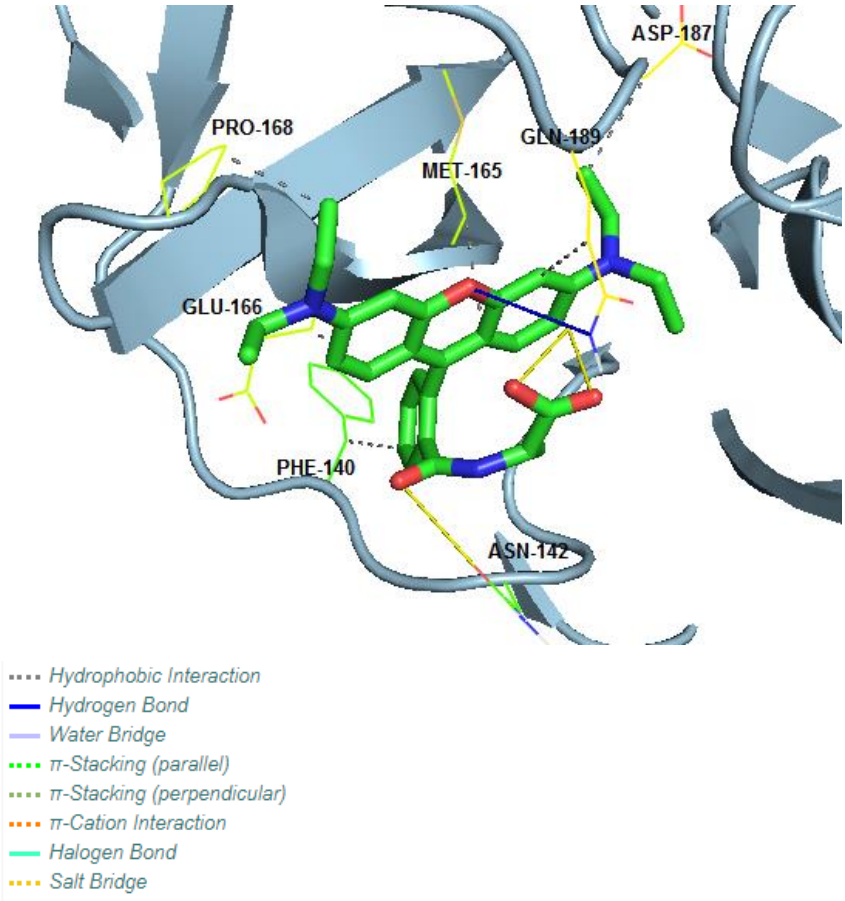

Figure 39: D-4 incorporated in a cavity of Mpro (6LU7) of SARS-CoV-2 Coronavirus using crystallographic grid.

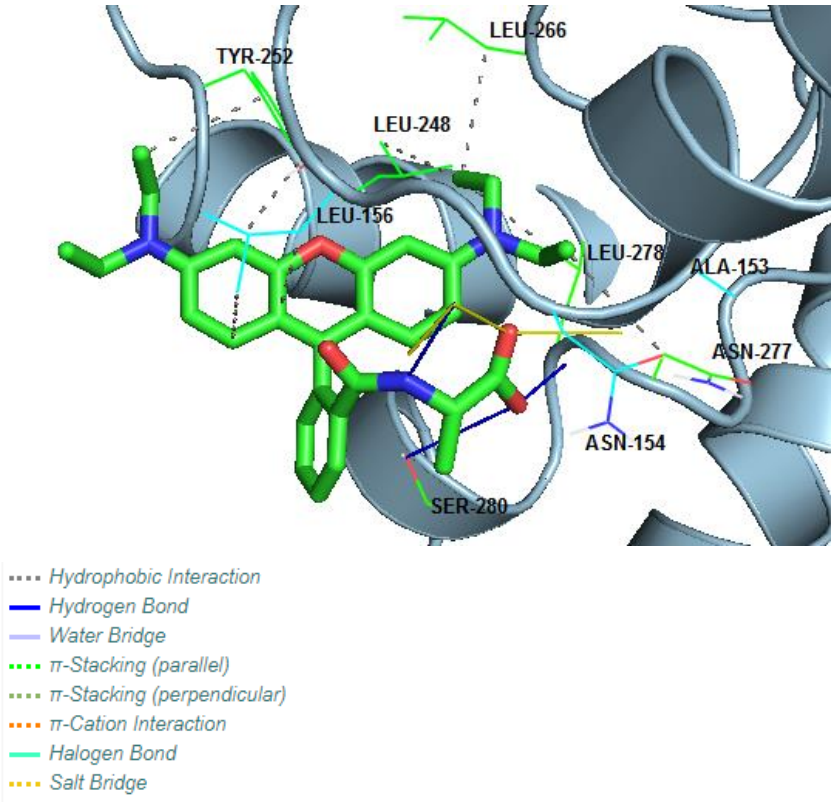

Figure 40: D-4 incorporated in a cavity of with Angiotensin-converting enzyme 2 (chain A of 6LZG) of SARS-CoV-2 Coronavirus using crystallographic grid.

Again, all these molecules were assigned to interact with the same receptors. For Mpro, the most usual hydrogen bonds were with GLU 166, GLN 189 and GLN 189, as well as HIS 41 and HIS 163, that are almost abundant due to presence various heteroatoms. For the chain A of the Spike protein, we observed hydrogen bonds with ASN 154 and heteroatoms, with SER 280, ASN 277 and $-COO^-$ and a lot of hydrophobic interactions due to the presence of aliphatic groups, in these molecules. In the case of chain B of the Spike protein, were observed mostly interactions with ARG 346 and other ARG groups, as well as SER 399 and ASN 354. ARG groups seem to interact mostly with -CN groups, but SER 399 and ASN 354, interact with $-COO^-$ groups.

1.3.6. Pfizer drugs

In Greece, more than 95% of the vaccinated population, preferred the Pfizer vaccine. According to the data of the European Organization for Special Diseases (ECDC), a total of 4,653,520 doses of vaccine against Covid-19 have been distributed in Greece and 3,109,127 have been administered. Of this amount, 2,95 million doses have been distributed by BioNTech-Pfizer, 1.22 million by AstraZeneca, 442,800 by Moderna and 30,000 by Johnson & Johnson. Based on the statistics, we found it necessary to test the new antiviral drugs on clinical trials, created by Pfizer. Last year, Pfizer reported PF-07304814, a small molecule inhibitor of SARS-CoV-2's main protease. Pfizer chemists first discovered the active compound, PF-00835231, which was designed to target the 3CL protease of SARS-CoV, during the 2002–2003 outbreak of severe acute respiratory syndrome (SARS). The 3CL protease of SARS-CoV is very similar to that of SARS-CoV-2, and the two proteases' active sites are identical, so Pfizer scientists and their collaborators decided to examine how it fared in cellular tests against SARS-CoV-2. PF-07304814 contains a phosphate group that makes the compound soluble and gets cleaved by alkaline phosphatase enzymes in tissue, releasing the active antiviral PF-00835231.The precursor molecule can only be given intravenously. Recently, Pfizer also came up with an oral SARS-CoV-2 inhibitor to avoid this difficulty and to make a drug, that is more accessible and easier to use. This antiviral candidate administered compound in the clinic that targets the 3CL protease of SARS-CoV-2. By inhibiting the main protease, PF-07321332, just like PF-00835231, prevents the virus from cleaving long protein chains into the parts it needs to reproduce itself. It's a reversible covalent inhibitor that reacts with one of the main protease's cysteine residues (Figure 41).[44,93,94]

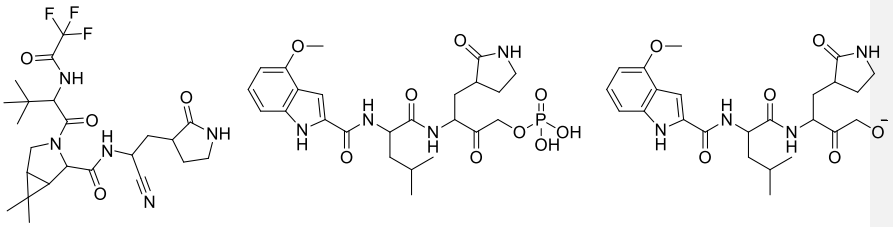

Figure 41: Structural depiction of PF-07321332, PF-07304814 and PF-00835231

From the molecules, developed by Pfizer, PF-00835231 is the most efficient compound compared to the others in binding on Mpro and on Spike protein (chain B) but for the Spike protein (chain A), the inactive form of it, PF-07304814, had the best score. Specifically, PF-00835231 has a score of -8.07 Kcal / mol for the Mpro and -6.94 Kcal / mol for the Spike protein (chain B). (Table 11).

From Autodock, we could observe that PF-00835231 forms a hydrogen bond with CYS 145, from PyMOL there were two additional hydrogen bonds formed with SER 144, HIS 164 and from Plip, were seven hydrogen bonds in total with GLY 143, SER 144, CYS 145, HIS 163, HIS 164, GLU 166, GLN 189 and one hydrophobic bond with GLN 189. For the Spike protein (chain A), PF-07304814 had a decent score of -6.00 Kcal / mol and forms one hydrogen bond, based on PyMOL with ASN 154, and two additional hydrogen bonds, based on Autodock with ALA 153 and ASN 277. Lastly, from Plip, we could observe seven hydrogen bonds in total with ALA 153, ASN 154 (2), TYR 252, ASN 277, SER 280 and LYS 441, in addition to four hydrophobic bonds with ASN 154, LEU 156, LEU 266 and LEU 278 (Table 12) (Figures 42-44).

Ligands	**Binding affinity for proteins ΔG (Kcal / mol)**		
	Mpro	**Spike protein (chain A)**	**Spike protein (chain B)**
PF-07321332	-7.26	-4.42	-6.22
PF-07304814	-6.08	-6.00	-6.04
PF-00835231	-8.07	-3.67	-6.94

Table 11:The average values of binding affinity for the complexes of PF-07321332, PF-07304814 and PF-00835231 with COVID-19 receptors

Ligands	Interactions of ligands with amino acids		
	Mpro	**Spike protein (chain A)**	**Spike protein (chain B)**
PF-07321332	**Autodock** - **PyMOL** LEU 141, GLU 166 **Plip** PHE 140, SER 144, HIS 163, GLU 166, GLN 189 MET 165, GLN 189	**Autodock** ASN 154, LEU 156 **PyMOL** ASN 277, PHE 274 **Plip** ASP 269, ARG 273, THR 276, THR 276, ASN 277, SER 280 ASN 149, ALA 153, PHE 274, THR 276	**Autodock** ARG 346, ARG 357, ASN 354 **PyMOL** ASN 354, ARG 346, ARG 355 **Plip** ARG 346, ASN 354 (2), ARG 355 (2), ARG 357 VAL 341 (2), ALA 344, LYS 356 (2)
PF-07304814	**Autodock** GLY 143 **PyMOL** PRO 168, LEU 167, HIS 41, GLY 143, GLN 189, GLU 166 **Plip**	**Autodock** ALA 153, ASN 154, ASN 277 **PyMOL** ASN 154 **Plip**	**Autodock** ASN 354 (2), ARG 355 (2), ASP 398 (2) **PyMOL** ALA 348, ARG 346, ASN 354 **Plip**

	ASN 142, GLY 143, GLU 166 (2), ARG 188, GLN 189 MET 165, GLU 166	ALA 153, ASN 154 (2), TYR 252, ASN 277, SER 280, LYS 441 ASN 154, LEU 156, LEU 266, LEU 278	ARG 346, SER 349, ASN 354 (3), SER 399 (2) ALA 348, LYS 356 ARG 346
PF-00835231	**Autodock** CYS 145 **PyMOL** SER 144, CYS 145, HIS 164 **Plip** GLY 143, SER 144, CYS 145, HIS 163, HIS 164, GLU 166, GLN 189 GLN 189	**Autodock** ASN 154 **PyMOL** SER 280, ASN 277, ASN 154, ALA 153 **Plip** ASN 154, THR 276, ASN 277, SER 280 (4), LEU 281	**Autodock** ASP 398 **PyMOL** ASN 345, ARG 346, PHE 347 **Plip** ASN 343, THR 345 (2), ARG 346 (5) GLU 340, ALA 344

Table 12: Interactions of amino acid residues of COVID-19 receptors in Mpro and Spike protein with PF-07321332, PF-07304814 and PF-00835231. (H-Bonds, Hydrophobic bonds, π-Stackings, π-Cation interactions, Halogen bonds and Salt bridges).

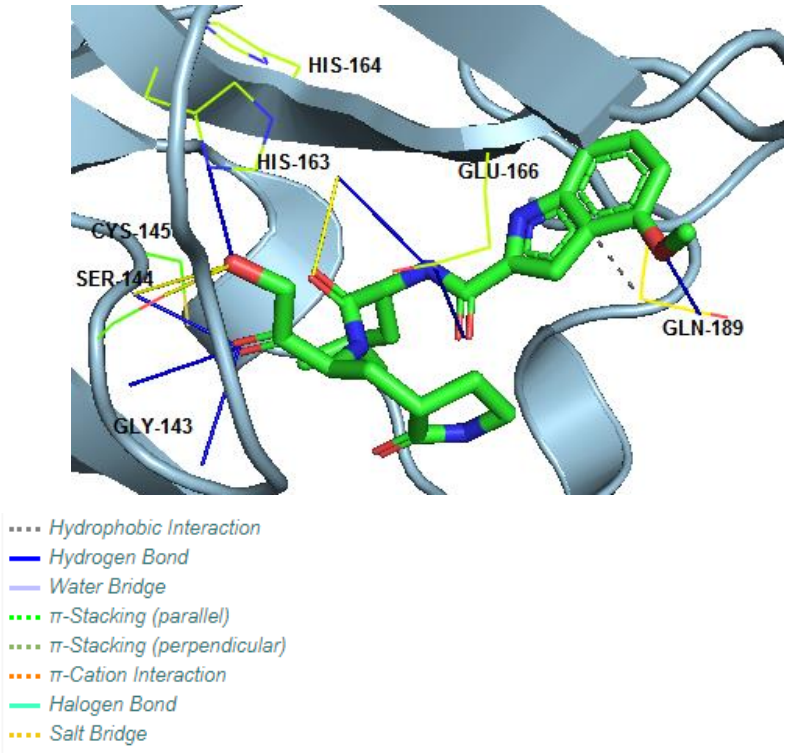

Figure 42: PF-00835231 incorporated in a cavity of Mpro (6LU7) of SARS-CoV-2 Coronavirus using crystallographic grid.

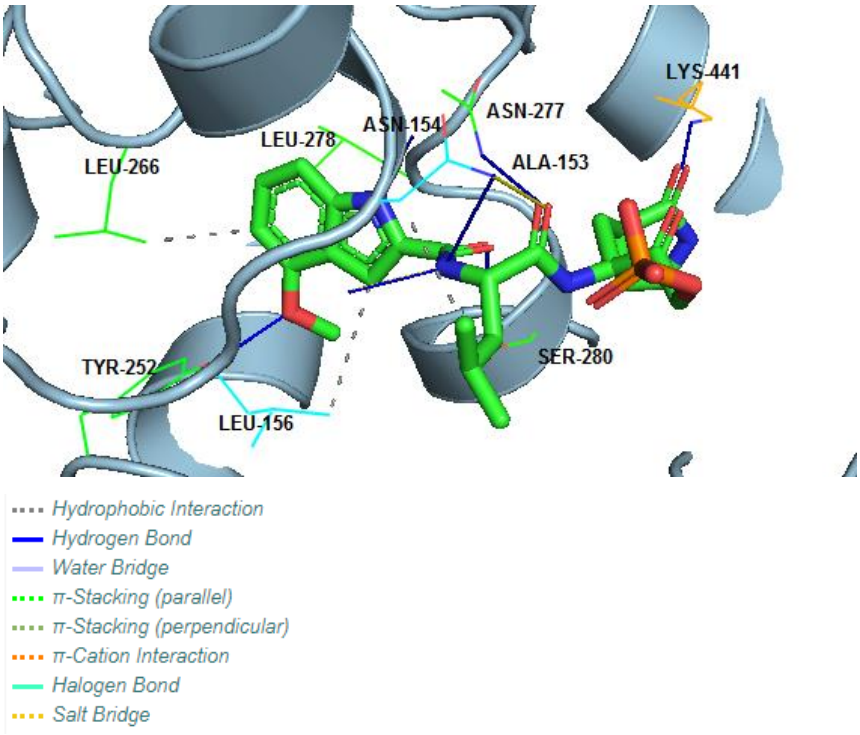

Figure 43: PF-07304814 incorporated in a cavity of with Angiotensin-converting enzyme 2 (chain A of 6LZG) of SARS-CoV-2 Coronavirus using crystallographic grid.

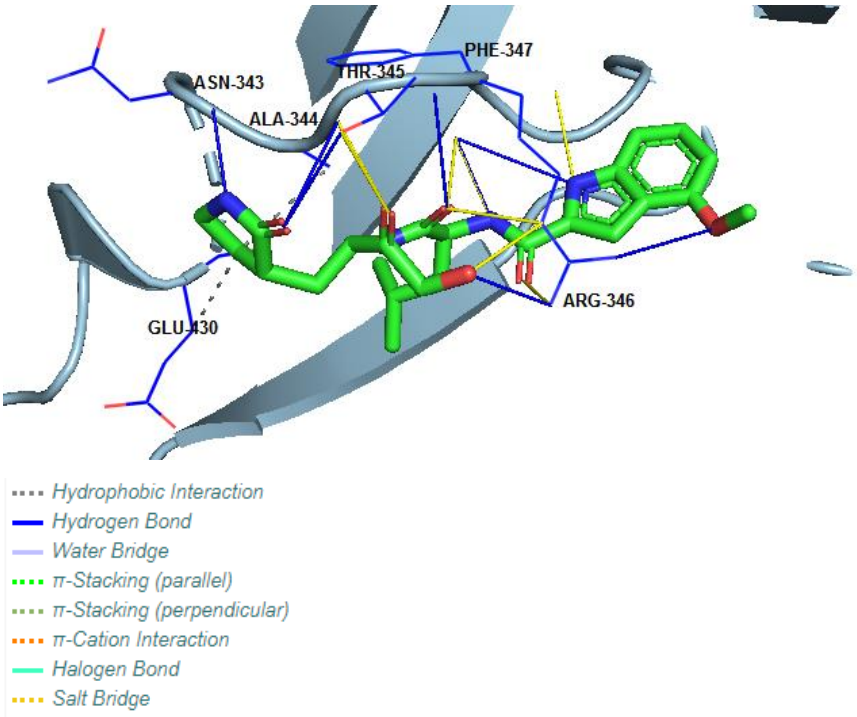

Figure 44: PF-00835231 incorporated in a cavity of with Spike glycoprotein (chain B of 6LZG) of SARS-CoV-2 Coronavirus using crystallographic grid.

After testing this series of molecules, we observed mostly in the case of Mpro, hydrogen bonds with GLU 166 and GLN 189, due to the -NH groups of their molecular frame. Also, there were hydrophobic interactions with MET 165 and aliphatic groups. For the chain A of the spike protein, we can observe, hydrogen bonds with SER 280 and the oxygen of the acetamide like group and hydrogen bonds with the -NH groups and ASN 154 and ASN 277. Lastly, in the chain B of the Spike protein, we observe hydrogen bonds with all the molecules and ARG 346. This is because, it interacts with the heteroatoms of the molecular framework. For the same reason there are also bonds here with other ARG but also ASN amino acids.

1.3.7. Drugs against Covid-19

It is important to also include the *in silico* results on Mpro of already applied components, which were used against SARS-CoV-2 or were planned to. Some of them seem to bind strongly to the receptor but that doesn't mean that these molecules cannot cause side effects. Most of these molecules show good results in *in vitro* studies, therefore it is important to test them *in silico* too.

Utilization of programs established by the FDA to allow clinicians to gain access to investigational therapies during the pandemic has been essential. As of October 22, 2020, remdesivir, an antiviral agent, is the only drug fully approved for treatment of COVID-19.

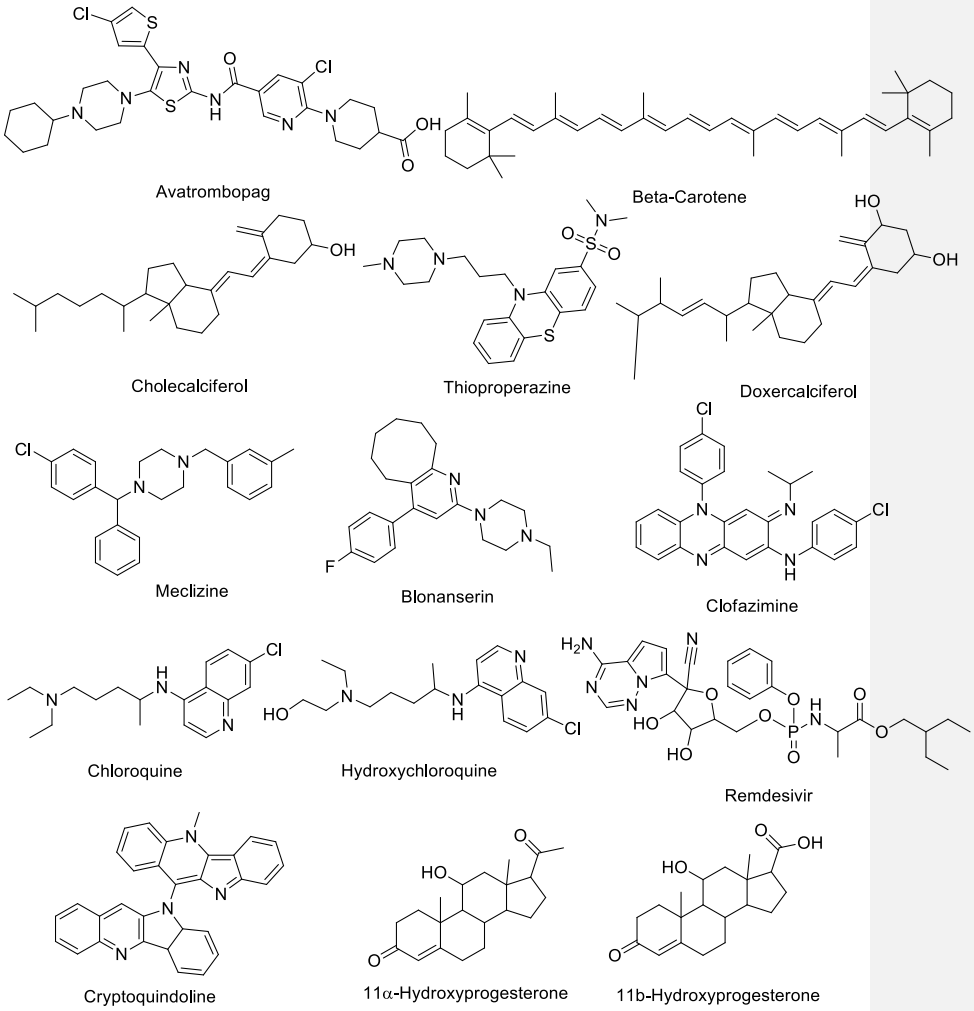

Figure 45: Structural depiction of Cryptoquindoline, Clofazimine, Avatrombopar, Blonanserin, Betacarotene, Cholecalciferol, Thioproperazine, Meclizine, Doxecalciferol, Chloroquine, Hydroxychloroquine, Remdesivir, 11α-Hydroxyprogesterone and 11β-Hydroxyprogesterone

From the above molecules (Figure 45), cryptoquindoline, clofazimine and 11α-Hydroxyprogesterone had excellent scores, avatrombopar, blonanserin, betacarotene, cholecalciferol, thioproperazine, meclizine and doxecalciferol very good scores and chloroquine, hydrochloroquine, remdesivir and 11β-Hydroxyprogesterone relatively good scores. Cryptoquindoline has a score of -11.19 Kcal / mol and is the molecule with the lowest binding affinity, followed by clofazimine with -10.61 Kcal / mol and 11α-Hydroxyprogesterone with -10.09 Kcal / mol. After running Autodock, cryptoquindoline seems to form one hydrogen bond with GLU 166, but based on PyMOL, there is one with ARG 188. On Plip it appears one hydrogen bond with GLU 166 and three hydrophobic bonds with HIS 41, GLU 166 and GLN 189. Clofazimine showed on Autodock, one hydrogen bond with GLU 166, but none on PyMOL. In addition, on Plip, it formed three hydrogen bonds with two amino acids (*i.e*. GLU 166, GLN 189 (2)), four hydrophobic bonds with MET 49, PHE 140, MET 165, GLU 166 and two halogen bonds with THR 26 and GLN 192. Finally, 11a-Hydroxyprogesterone, showed on Autodock, two hydrogen bonds with the amino acid GLU 166 (2), on PyMOL three hydrogen bonds with GLU 166, GLN 189 and THR 190 and on Plip seven hydrogen bonds with GLU 166 (2), GLN 189, THR 190 (2) and GLN 192 (2), as well as five hydrophobic bonds with PHE 140, MET 165, GLU 166, ASP 187 and GLN 189 (Table 13 & Table 14) (Figures 46-48).

Ligands	**Binding affinity for proteins ΔG (Kcal / mol)**
	Mpro
Cryptoquindoline	-11.19
Clofazimine	-10.61
Avatrombopar	-9.11
Blonanserin	-9.34
Betacarotene	-9.52
Cholecalciferol	-9.43
Thioproperazine	-9.04

Meclizine	-9.4
Doxecalciferol	-9.66
Chloroquine	-6.59
Hydroxychloroquine	-7.1
Remdesivir	-6.56
11α-Hydroxyprogesterone	-10.09
11β-Hydroxyprogesterone	-7.72

Table 13: The average values of binding affinity for the complexes of Cryptoquindoline, Clofazimine, Avatrombopar, Blonanserin, Betacarotene, Cholecalciferol, Thioproperazine, Meclizine, Doxecalciferol, Chloroquine, Hydroxychloroquine, Remdesivir, 11α-Hydroxyprogesterone and 11β-Hydroxyprogesterone with Mpro.

Ligands	**Interactions of ligands with amino acids**
	Mpro
Cryptoquindoline	**Autodock** GLU 166 **PyMOL** ARG 188 **Plip** GLU 166 HIS 41, GLU 166, GLN 189
Clofazimine	**Autodock** GLU 166

	PyMOL - **Plip** GLU 166, GLN 189 (2) MET 49, PHE 140, MET 165, GLU 166 THR 26, GLN 192
Avatrombopar	**Autodock** THR 26 **PyMOL** GLN 189, GLU 166, THR 26 **Plip** THR 26 PRO 168, ALA 191 HIS 41
Blonanserin	**Autodock** GLU 166

	PyMOL GLU 166 **Plip** MET 165, LEU 167, PRO 168, GLN 189 (2) GLU 166
Betacarotene	**Autodock** - **PyMOL** - **Plip** GLN 107, PRO 108, PHE 134, VAL 202, GLU 240, ILE 249 (2), PRO 252, PRO 293 (2), PHE 294
Cholecalciferol	**Autodock** GLU 166 **PyMOL** PHE 140 **Plip** GLU 166 PHE 140, MET 165, GLU 166, LEU 167, GLN 189, GLN 192

Thioproperazine	**Autodock** HIS 163, GLU 166 **PyMOL** GLU 166 **Plip** HIS 163, GLU 166 HIS 41, MET 49, GLN189 GLU 166
Meclizine	**Autodock** - **PyMOL** - **Plip** THR 25, LEU 27, HIS 41, MET 49, MET 165, ASP 187, GLN 189 (2) HIS 41
Doxecalciferol	**Autodock** SER 144, HIS 163, GLU 166 **PyMOL** PHE 140, HIS 163, GLU 166

	Plip LEU 141, HIS 163, GLU 166 PHE 140, MET 165, LEU 167, GLN 189, GLN 192
Chloroquine	**Autodock** HIS 164 **PyMOL** HIS 164 **Plip** HIS 163, HIS 164 MET 165, GLU 166 HIS 41 THR 190 GLU 166
Hydroxychloroquine	**Autodock** SER 144, HIS 163, HIS 164 **PyMOL**

	LEU 141, HIS 163, HIS 164 **Plip** SER 144, HIS 163, HIS 164 HIS 41, MET 49, MET 165, GLU 166, GLN 189 HIS 41 GLU 166
Remdesivir	**Autodock** GLN 189 (2) **PyMOL** GLU 166 (2), GLN 189 (2) **Plip** SER 46, ASN 142, GLU 166 (3), GLN 189 (2) HIS 41 HIS 163
11α-Hydroxyprogesterone	**Autodock** GLU 166 (2)

	PyMOL GLU 166, GLN 189, THR 190 **Plip** GLU 166 (2), GLN 189, THR 190 (2), GLN 192 (2) PHE 140, MET 165, GLU 166, ASP 187, GLN 189
11β-Hydroxyprogesterone	**Autodock** GLY 143, GLU 166 **PyMOL** LEU 141, GLY 143, GLU 166 **Plip** LEU 141, GLY 143, SER 144, CYS 145, GLU 166

Table 14: Interactions of amino acid residues of COVID-19 receptors in Mpro with Cryptoquindoline, Clofazimine, Avatrombopar, Blonanserin, Betacarotene, Cholecalciferol, Thioproperazine, Meclizine, Doxecalciferol, Chloroquine, Hydroxychloroquine, Remdesivir, 11α-Hydroxyprogesterone and 11β-Hydroxyprogesterone. (H-Bonds, Hydrophobic bonds, π-Stackings, π-Cation interactions, Halogen bonds and Salt bridges).

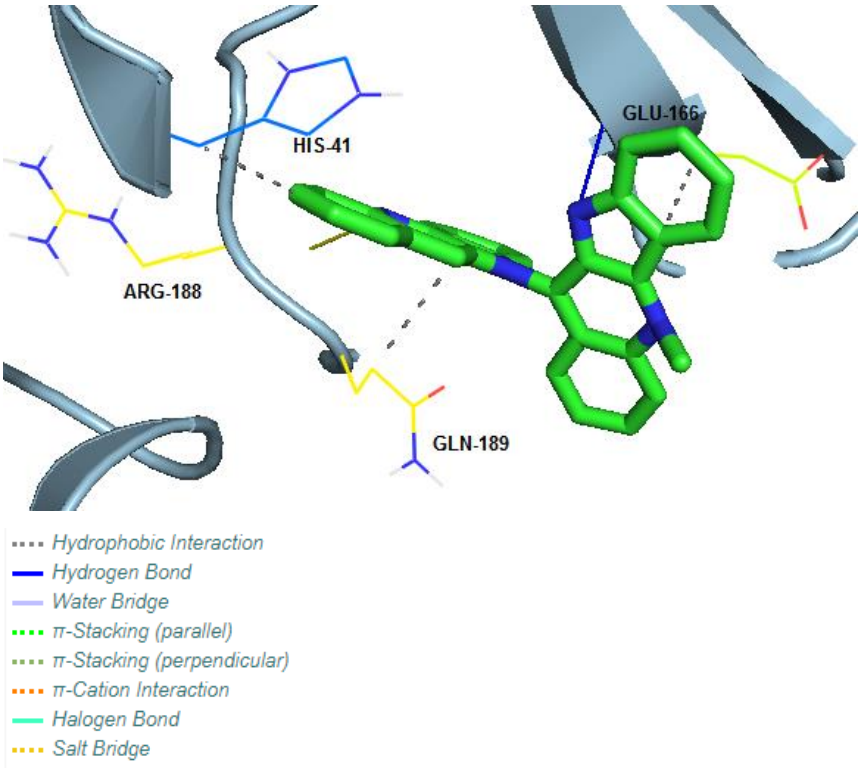

Figure 46: Cryptoquindoline incorporated in a cavity of Mpro (6LU7) of SARS-CoV-2 Coronavirus using crystallographic grid.

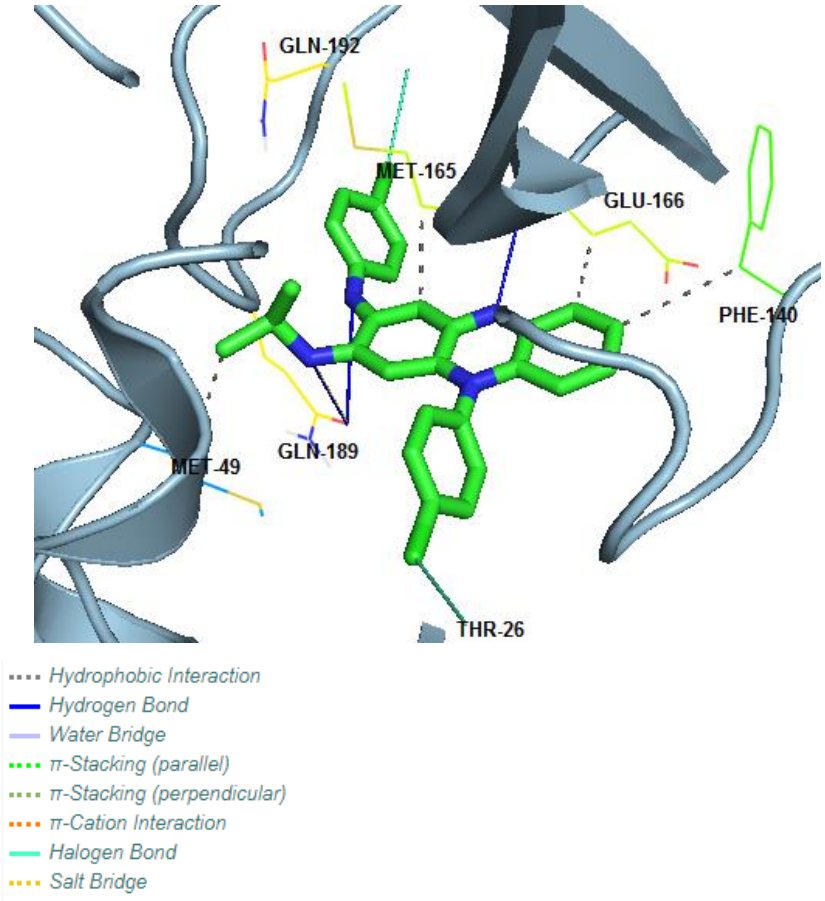

Figure 47: Clofazimine incorporated in a cavity of Mpro (6LU7) of SARS-CoV-2 Coronavirus using crystallographic grid.

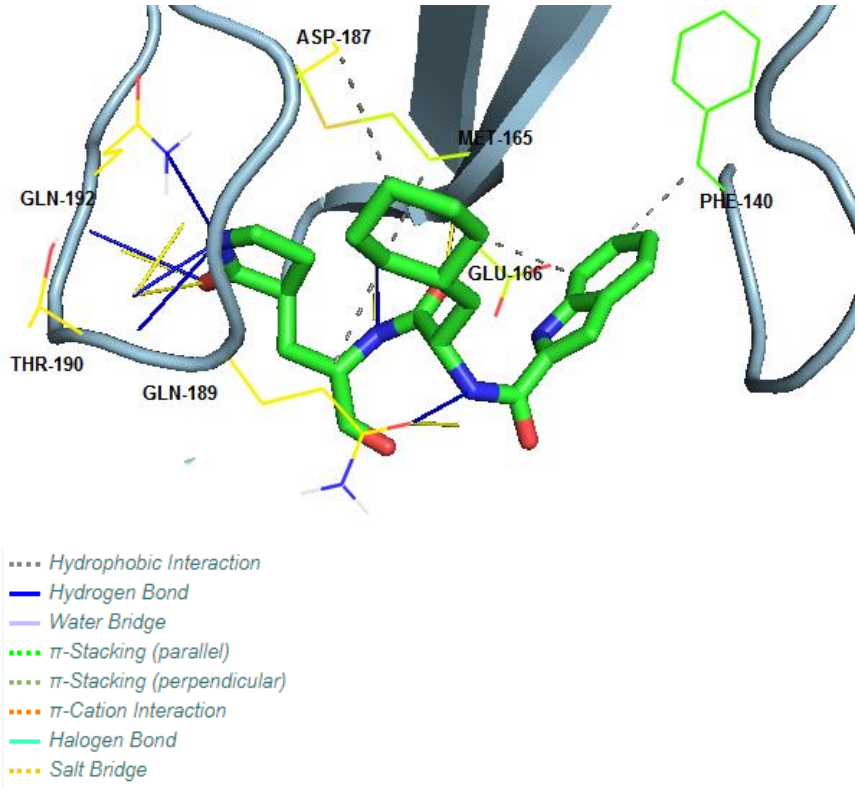

Figure 48: 11α-Hydroxyprogesterone incorporated in a cavity of Mpro (6LU7) of SARS-CoV-2 Coronavirus using crystallographic grid.

By testing, already known drugs, we gained interesting results for their interaction with Mpro. It is logical for Betacarotene, to not show any bond other than hydrophobic interaction, due to its lipidic nature and as a result, it binds with an allosteric center. Meclizine binds with the correct receptor, but it only forms strong hydrophobic interactions and one π-Cation interaction with HIS 41. All the other molecules bind to the receptor mostly again with hydrogen bonds with GLU 166, GLN 189 and GLN 192.

1.4. Experimental conclusions and future goals

Evaluating the results of the molecular docking calculations of the potential ligands in the various receptors, the following conclusions emerged:

For Mpro, losartan, D-4, B-37, BV6, EXP-3174, Cryptoquindoline, Clofazimine, 11α-Hydroxyprogesterone and Rosmarinic acid showed excellent scores, from which Rosmarinic acid has the lowest score (-13.97 kcal / mol). The most common hydrogen bonds were observed with HIS 41, PHE 140, GLY 143, SER 144, CYS 145, GLU 166, GLN 189 and GLN 192.

For the RBD of the Spike protein, losartan, BV6 derivative **1**, BV6 derivative **2**, BV6 derivative **3** have excellent scores, from which BV6 derivative **1** has the lowest score (-11.3 kcal / mol). The most common hydrogen bonds were observed with SER 349, LYS 356, ARG 357 and ASN 450.

For the chain A of the Spike protein, Rosmarinic acid, D-4 and EXP-3174 have excellent scores, from which EXP-3174 has the lowest score (-11.2 kcal / mol). The most common hydrogen bonds were observed with ASN 154, ASN 277, SER 280 and LYS 441.

For the chain B of the Spike protein, Rosmarinic acid and BV6 have excellent scores, from which Rosmarinic acid has the lowest score (-10.9 kcal / mol). The most common hydrogen bonds were observed with THR 345, ARG 346, ASP 398 and SER 399.

Lastly, for the metallocenter of the Spike protein BV6 and its derivatives have excellent scores, from which BV6 derivative **1** has the lowest score (-12,05 kcal / mol). The most common hydrogen bonds were observed with PRO 346, GLU 398 and GLU 402.

The next steps include doing Molecular dynamics calculations with the most efficient ligands, and also run *in vitro* and animal testing with our partners in Turkey and Australia.

It's an emergency, that scientists need to come up or develop new drugs against SARS-CoV-2. The virus has increased its resistance in drugs in use and some of these drugs have side effects, so it is important that new medicines need to arrive at the market. Also, there should be development not only for a cure against the virus, but also medicine to relieve symptoms, to prevent the virus from entering the host or reproducing and with minimal side effects and cost. This virus has the ability to mutate rapidly, and it seems that the newest

mutation strains (*i.e.* mutation Δ and mutation Mu) are spreading ferociously and are dangerous.

Chapter 2: Synthesis of Co^{II} Complexes in Environment of Pincer Ligands with NHC Donors and Their Use in Ketone Hydrogenation Reactions

2.1. Introduction

2.1.1. 3d metals

Today, there is an ongoing quest to replace the platinum group metals (PGMs), frequently used in catalytic reactions, which are precious metals with high price volatility, with more Earth-abundant metals. In general, heavier metals were initially of strong interest due to specific catalytic applications, like C−C and C-heteroatom cross coupling (Pd), alkene metathesis (Ru), transfer hydrogenation (Rh, Ir), and various carbonylations (Rh, Ir). Despite their effectiveness, those metals can be harmful and are prohibitively expensive when required in large quantities. The study of catalytic reactions with abundant 3d metals in the earth's solid crust is a modern direction of chemistry aimed at the long-term viability of catalytic transformations and the synthetic processes associated with them. Homogeneous catalysis with Earth-abundant, first-row transition metals is receiving increasing attention as a potentially cost-effective and sustainable methodology. Furthermore, first row transition metals provide platforms to explore catalysis in a new chemical space. The kinetically and thermodynamically accessible oxidation and spin states may enable new mechanistic pathways, substrate scope and reactivity. Thus, there is a strong interest on inexpensive and highly abundant first-row transition metals notably nickel, iron, and cobalt. [95–101]

Several cobalt complexes, not only well-defined but also *in situ*-formed, are gaining considerable popularity. Importantly, the stability and reactivity of the complexes have been based on multidentate ligands imposing steric and/or

electronic influences. Consequently, non-noble metal catalysts based on pincer type ligands are of special interest in organometallic chemistry and homogeneous catalysis.

The precious metal catalysts technology has relied on the metal centre supported by strong field ligands to enable highly predictable two-electron steps redox chemistry that accompany the key bond breaking and forming steps during turnover. Since 3d metals commonly feature stable oxidation states differing by one electron, concepts encompassing metal ligand cooperation in catalysis to accommodate the two electron changes necessary for the catalytic steps have been devised and developed; they include *e.g.* the use of redox active, non-innocent and/or proton responsive ligands. [96,99,100,102]

2.1.2. Cobalt

The peculiarities of 3d metals (*e.g.* relative stabilities of oxidation states, reduced strength of metal-heteroatom bonds, chemical (lability), electronic configurations with open shells and paramagnetic character require the optimization of existing ligands for catalytic functionality and / or the design and synthesis of new types of ligands. Some relevant objectives of the research endeavors in this area are: (i) stabilization of well-defined metal complex substructures at the catalytic center, (ii) stabilization of functional oxidative states of relevance to the catalytic cycle, (iii) occassional use of non-innocent ligands, (iv) bi-functional architectures with dual, synchronous activation of the substrate by the metal and ligand.[97]

Cobalt (Co), has atomic number Z = 27 and atomic weight A_r = 58.93320. Its electronic configuration is $[Ar]3d^74s^2$ and the only natural isotope is ^{59}Co. Despite that, the man-made ^{60}Co constitutes an important γ-ray source, widely used in cancer treatment, as a tracer, and for radiotherapy. Co is air-stable and is not affected by water. It was isolated by N. - L. Vanquelin (France, 1780) and its name is of German origin: "kobald" which means evil demon of mines. This name was given by miners since its presence was associated with accidents in the mines. Cobalt is a transition element and belongs to the 4th period and to

group VIIIB (or 9). Of relevance to the previous discussion, the earth abundance of Co is 0.0029% of mass in earth crust, so it is placed 33rd in order of abundance and its average content in the Earth's crust is approximately 25–30 ppm, albeit widely distributed. The current price is *ca.* 24,000 USD / ton and its toxicity (LD_{50} for $CoCl_2$ = 766 mg / kg) is low. The common oxidation states are: 0, +1, +2, +3, +4 with more stable +2 and +3 states. Co(I) and Co(0) are stabilized as complexes with π-acceptor ligands, while few Co(IV) complexes have been documented. More specifically, the +2 state is -absence of complexing factors- much more stable than that of +3, especially for simple compounds. Co^{III} (aq) is a powerful oxidant that it oxidizes water to oxygen (Figure 49)

$$Co^{3+}(aq) + e^- \rightarrow Co^{2+}(aq) \qquad E^0_1 = 1.82\ V$$

$$Co^{2+}(aq) + 2e^- \rightarrow Co(s) \qquad E^0_2 = -0.28\ V$$

Figure 49:Typical reduction potentials of cobalt. [103,104]

Co^{II} forms tetrahedral and octahedral complexes but there are also examples of complexes with planar T-shaped, trigonal-planar, trigonal-pyramidal, square-pyramidal, square-planar geometries as well as distorted and/or distorted geometries. Co^{II} centers are paramagnetic: the high-spin (d^7, S = 3/2) and low spin (d^7, S = 1/2). Octahedral complexes and tetrahedral complexes are high spin, while square planar complexes are low spin. Co^{III} appears to adopt mostly octahedral and rarely tetrahedral or square-pyramidal coordination geometries, almost invariably of low spin (*i.e.* diamagnetic). An interesting exception is the high spin paramagnetic CoF_6^{3-} (Figure 50).

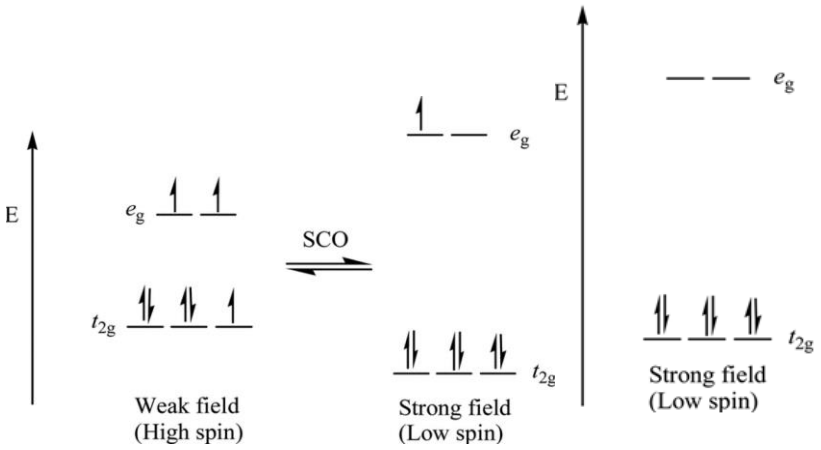

Figure 50:Electronic arrangement for d^6 Co^{III} (right) and of d^7 Co^{II} in weak field and in strong fields (left).[103,104]

Our focus is Co^{II} complexes, and the strong and weak field cases are differentiated from the spectrochemical series of the donors in the ligand. This series orders the ligands on the basis of their field strength, *i.e*. the splitting between the non-bonding and the antibonding orbitals in the complex that they cause as shown in Figure 51. Ligands that have low field strength, promote high spin electronic configurations, and are listed first in the series, followed by ligands of higher field strength, that promote low spin configurations. Strong-field ligands, such as CN^- and CO, increase the Δ splitting and are more likely to result in low-spin complexes whereas weak-field ligands, such as I^- and Br^- cause a smaller Δ splitting and are more likely to be high-spin.

(weak) $I^- < Br^- < S^{2-} < SCN^- < Cl^- < NO_3^- < N_3^- < F^- < OH^- < C_2O_4^{2-} \approx H_2O <$

$NCS^- < CH_3CN < py < NH_3 < en < bipy < phen < NO_2^- < PPh_3 < CN^- \approx CO$ *(strong)*

Figure 51: The spectrochemical series of ligands

The thermodynamic stability of metal complexes depends on the properties of the ligand and the metal ion and on the type of bonding. Metal–ligand interaction can be viewed as Lewis acid–base interactions. Lewis bases (the donors of the ligand) can be divided into two categories:

- Hard, containing small, relatively nonpolarizable donor atoms (such as N, O, and F), and
- soft containing larger, polarizable donor atoms (such as P, S, and Cl).

Metal ions with the highest affinities for hard bases are hard acids (also classified along similar lines of size and polalizability), whereas metal ions with the highest affinity for soft bases are soft acids.

Conversely, soft acids tend to be cations of less electropositive metals; consequently, they have lower charge-to-radius ratios and are more polarizable. Based on the principle that hard acids prefer to bind to hard bases, and soft acids prefer to bind to soft bases, stable complexes are formed. Co^{II} is soft and Co^{III} is hard due to their size and charge difference. [103–108]

2.1.3. Carbenes

The term "carbene" is used when describing a molecule containing a neutral carbon atom with six valence electrons, two of which are non-bonding. In general, carbenes are neutral molecules with a divalent carbon atom and a general formula **:**CR_2. The geometry of carbenes can be either linear or bent depending on the hybridization of carbon center. In the case of sp hybridization linear geometry whereas in the sp^2 hybridization bent geometry is adopted; carbenes frequently adopt bent geometry when the carbon substituents include heteroatoms (N, O, S *etc*). The energy of one of the pπ orbitals does not change during the transition of linear (sp) to bent (sp^2) hybridization. The newly formed sp^2 hybrid orbital denotes as sigma orbital which is energetically stabilized by the partial s character from its sp^2. Based on the orbital distribution of the non-bonding electrons the carbene moieties are divided into two categories: The singlet state singlet and the triplet state carbenes (Figure 52). In the former the non-bonded electrons occupy the non-bonding sp^2 orbital with antiparallel spins, forming a pair. In the latter, the non-bonded electrons occupy two different orbitals and have parallel spins.[109–112]

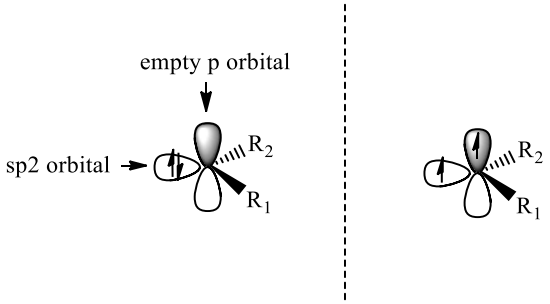

Figure 52: Singlet (left) and Triplet (right) carbenes.

Carbene chemistry is constantly evolving and is now is a topical area of chemistry. One major factor for the progress witnessed is the availability of techniques and equipment to study reactive species. [113]

Initially, the views of the scientific community on the validity of the existence of carbenes were divided. That changed after the conduction of studies on methylene and daxomethane derivatives in the early 20th century. Eduard Buchner had first conducted cyclopropanation studies of ethyl diazoacetate with toluene in 1903. In 1912 Hermann Staudinger also converted alkenes to cyclopropanes with diazomethane and CH_2 as an intermediate and a few decades later Doering in 1954 demonstrated with dichlorocarbene synthetic utility by synthesizing Tropolone derivatives and adding dialogonemethylene to olefins (cyclopropanation). Since then, the interest of the scientific community in carbenes flourished, with several references to cyclopropane reactions, methylene inserting and ring expanding promoted by an intermediate type: CX_2 (Figure 53).[109,114–119]

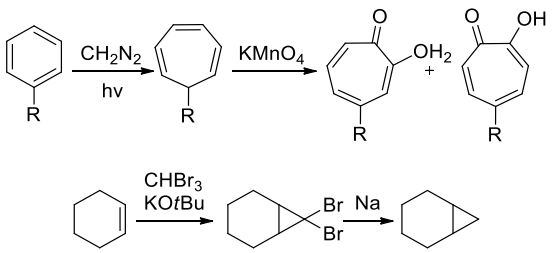

Figure 53: Methylene interfering and cyclopropanation reactions via intermediate carbene.[117,119]

The first metal complex structure containing carbene ligand was mentioned in the literature by Tschugaeff in 1925, when he synthesized a complex with diamino ligand and from the starting material Potassium hexachloroplatinate. This product which is also known as "Tschugajeff's salt" was initially described structurally incorrectly. The accurate structure was finally depicted some decades later in the 1970s.[120,121]

Significant contributors to the field of coordinated carbenes, but also to the related organometallic chemistry, were Fisher and Schrock. The first fully characterized carbene-metal complex was reported in the literature by Fischer in 1964. That complex was a W^0 pentacarbonyl complex and had a carbene ligand. A decade later, Schrock synthesized another type of carbene complex using Ta^V, a high oxidation state metal. It is also important to add that in the 1970s Michael F. Lappert first showed the existence of transient monomeric in solution acyclic carbene analogs that exist in equilibrium with dimeric electron rich olefins. Although the synthesis and isolation of free carbenes had not yet been achieved, the remarkable efforts by Fischer and Schrock showed that carbenes could be effective on metal transitions to form stable complexes (Figure 54). [122–124]

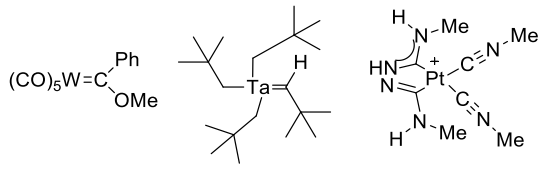

Figure 54: the Fischer complex (left), the Schrock complex (middle) and the Tschugajeff salt (right) [122–124]

2.1.4. N-heterocyclic carbenes

N-heterocyclic carbenes, where the carbene carbon is integrated into a heterocyclic ring (usually imidazol, Figure 55) are singlet state carbenes *i.e.* the non-bonding electrons of the carbon occupy a $\sigma(sp^2)$ orbital in the ground state. Their unique stability can be attributed to a range of electronic and stereochemical factors including: (i) the inductive attraction of electron density from the carbenic centre to the more electronegative heteroatoms, which

reduces the energy of the σ(sp^2) orbital; (ii) the supply of π-electron density from the neighboring nitrogen to the empty p-orbital of the carbene carbon. The formation of an aromatic ring (6 e^-), given that carbon has a double bond between C4 and C5, offers additional stability to the system, although the uptake of electrons from nitrogen into the carbene is negligible. [125,126]

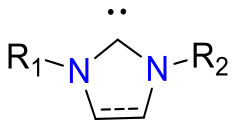

Figure 55: General type N-heterocyclic carbene

Common N-heterocyclic carbenes or named sometime as Arduengo carbenes and abbreviated as NHCs are heterocyclic compounds of great importance due to their rich chemistry and their use as ligands in metal complexes, but also for their applications in organometallic catalysis and material chemistry. They are electron-rich nucleophilic species. [125,127]

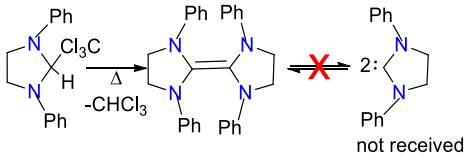

Figure 56: Attempt to synthesize N-heterocyclic carbenes from Wanzlick.[127,128]

Wanzlick and Öfele where the first to prove the transient existence of N-heterocyclic carbenes based on the imidazolin-2-ylidenes. Sadly, the isolation and characterization of this type of carbenes was relatively difficult and was achieved many years later. In the early 1960s Wanzlick attempted to synthesize a free carbene from an imidazolidine derivative by thermal abstraction of chloroform (Figure 56). Instead, he isolated a colorless crystalline solid, an electron rich olefin, which resulted from dimeriation of the carbene product. The first N-heterocyclic carbene metal complexes were reported independently in 1968 by both Wanzlick and Öfele, who reported the synthesis of Hg^{II} and Cr^0 complexes, respectively, with in situ deprotonation of imidazole salts and subsequent complexation (Figure 57).[125,127–130]

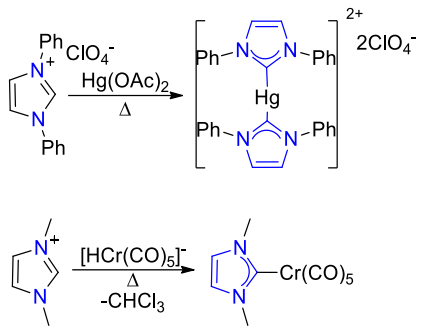

Figure 57: The first complexes of N-heterocyclic carbenes [129,130]

The first stable, in the absence of oxygen and moisture, free N-Heterocyclic carbene was synthesized a few decades later in 1991 by Arduengo *et al.* Till then N-heterocyclic carbene research remained fruitless until this discovery.

This N-heterocyclic carbene with adamantyl ligands, also known as IAd 1,3-bis(adamantyl)imidazol-2-ylidene, was isolated as a colorless crystalline solid by deprotonation of 1,3-di(adamantyl)imidazolium salt with sodium hydride in the presence of catalytic amount of DMSO in THF. This work by Arduengo and his collaborators was very important to the scientific community as it paved the way for further research into this class of chemical compounds and eventually to their increasing use in organic and organometallic materials chemistry (Figure 58). [131–133]

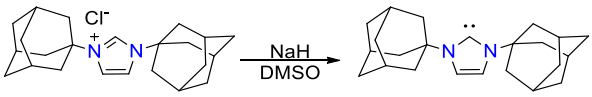

Figure 58: The synthesis of the first N-heterocyclic carbene [131]

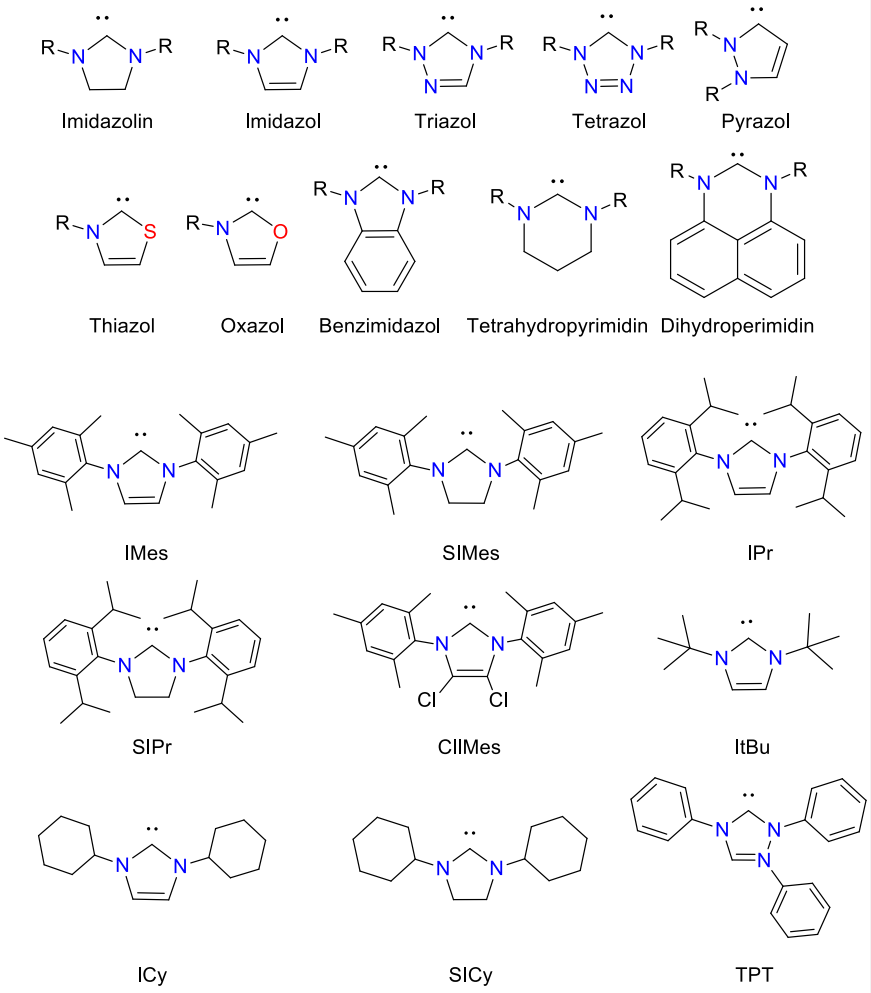

Figure 59: Most commonly used imidazolium salts [134]

NHCs form a group of versatile donor ligands with unique stereoelectronic properties that assist in the stabilization of metal complexes, which display low coordination numbers and/or unusual oxidation states endowed with unique catalytic, physical or medicinal properties. Some of the most commonly imidazolium salts are depicted at Figure 59. NHCs are spectator ligands that are usually very strong sigma donors, often drawing comparisons to phosphines. Since the metal-NHC bond is generally stronger than the metal-phosphorus bond they impart high stability and enhanced activity to their complexes with transition metals. Their steric properties are also very tuneable.

Several attempts have been made to quantify these properties to determine a reliable model of the stereochemical parameter corresponding to the electronic parameter. Tolman suggested a way to evaluate the stereochemical demands of a conical phosphine ligand from the angle of the cone with apex at the metal, the P atom at 2.28 Å from the metal and apex angle defined by tangents encompassing the van der Waals radii of substituent atoms considered as spheres. Tolman also proposed a method for evaluating the electronic properties of the phosphines known as Tolman electronic parameter (TEP) based on the positions of the IR absorption of $[NiL(CO)_3]$ complexes. Analogously, the σ-donation from a N-heterocyclic carbene to a metal center is described by the vibrational frequency of a carbonyl ligands with IR spectroscopy in complexes $LNi(CO)_3$ or $RhL(CO)_2CI$, $IrL(CO)_2CI$, where L = NHC. This means that due to the increased back-bonding from the metal orbitals to the carbonyl π*-orbitals results in a reduction in the frequency of vibration of the carbon-oxygen bond. In general, the better σ-donor the ligand is, the more electronically rich the metal center becomes, reducing the bond strength between carbon and oxygen to the carbonyl ligand.

N-heterocyclic carbenes do not have conical symmetry but have an umbrella shape enclosing the metal center, raising the need for alternative models to quantify ligand sterics. Some of these methods that have been developed are (i) the "% buried volume" stereochemical parameter (% V_{bur}), developed by Nolan and Cavallo. This parameter is calculated based on the volume percentage of a sphere centered on the metal with a diameter of 3 Å that is occupied by the ligand atoms. The distance between the metal and the ligand is considered 2 Å. A useful feature of % V_{bur} is that it can also be applied to phosphines, allowing them to be compared with N-heterocyclic carbenes using the same parameter. [108,125,135–139]

NHC carbenes form complexes with almost all transition metals. Due to their use in catalysis and synthesis, as well as due to their special properties in the field of organometallic chemistry they are being studied extensively by the scientific community. They have also been used for the development of metal catalysts, used in cycloaddition, hydroamination, hydroformylation, polymerization of unsaturated substrates, cross coupling, and other reactions,

with very good results. Some of the most well-known complexes are the ruthenium second-generation Grubbs catalysts and the Hoveyda-Grubbs catalysts, which are widely used in olefin metathesis reactions (Figure 60). Justified for their contribution to the field of organometallic chemistry Grubbs, Schrock and Chauvin were awarded with the Nobel Prize in Chemistry in 2005. [133,140–146]

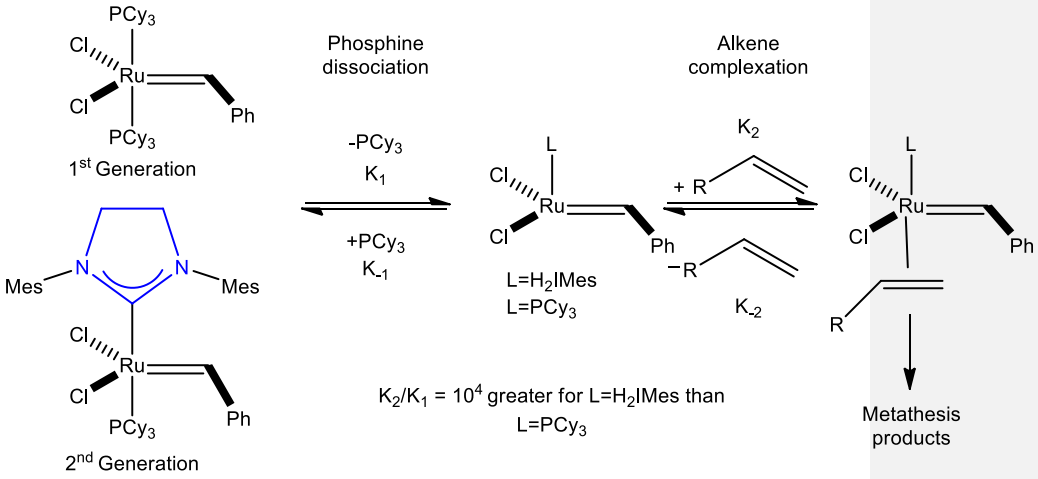

Figure 60: First and second generation of Grubbs olefin metathesis catalysts [125,147]

2.1.5. N-heterocyclic carbene complexes with Co^{II}

The NHC chemistry of cobalt is somewhat comparable to that of iron. The synthesis of cobalt NHC complexes is a challenging procedure. In general, the synthetic strategies leading to these complexes can be categorized into three methods depending on NHC providing entity employed. Firstly, the free carbenes can be produced *via* the deprotonation of imidazolium salts using a strong base and subsequent treatment with metal precursors. Secondly, a direct metallation of an imidazolium salt with a metal containing basic amide groups such as $Co[N(SiMe_3)_2]_2$ known as aminolysis. Lastly, a very popular method of receiving cobalt NHC complexes is *via* transmetallation from silver or even copper NHC complexes (Figure 61). [148,149]

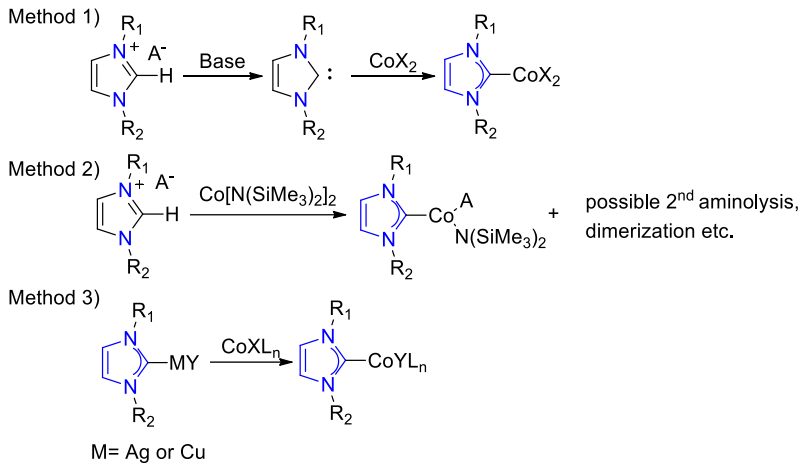

Figure 61: General synthetic methods for cobalt-NHC complexes. [148,149]

NHC-complexes with cobalt, are accessible in three oxidation states Co^{I}, Co^{II} and Co^{III}, with rarer examples of the highly oxidized complexes (formally Co^{IV} or Co^{V}). In 2014, Deng's group reported the synthesis of a Co^{IV} imido complex, (depicted below Figure 62) by reaction of the Co^{0} alkene complex with 2 eq. of the bulky $DiPPN_3$ azide. In the solid state the complex is trigonal-planar with an overall C_{2v} symmetry. It is stable in solution and in the solid state at room temperature. After CV experiments took place, it was hypothesized, that the Co^{V} analogue can be isolated too. In fact, by performing chemical oxidation of the Co^{IV} with $[FeCp_2](BAr^{F}_4)]$, resulted in the formation of Co^{V} analogue, which was isolated in 88% yield. The ^{1}H and ^{13}C NMR spectra of this diamagnetic Co^{V} complex suggest a C_{2v} symmetric $[Co(NDiPP)_2(IMes)]^{+}$ cation in solution. The crystal structure of the Co^{V} complex, revealed a trigonal-planar geometry around the Co center, similar to one of the Co^{IV} precursor complex. [103–108]

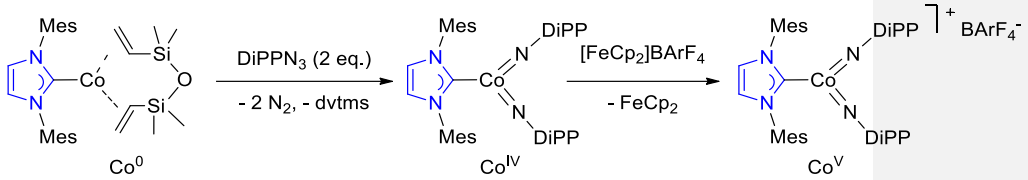

Figure 62: Synthesis of the NHC-complexes Co^{IV} and Co^{V}.[107,108]

Due to all these peculiarities, cobalt is particularly attractive for use in metalocentered catalysis to achieve various chemical transformations. These characteristics of cobalt are reflected in a multitude of applications, which have been developed in both heterogeneous and homogeneous catalysis. Its use has already been established in a multitude of diverse transformations (*e.g.* cyclotrimerizations, Pauson-Khand reactions, carbonylations, hydrogenations, water oxidation *etc.*) based on its great affinity towards carbon-carbon and carbon-nitrogen π-bonds and the accessibility of reactive organometallics (alkides, acyls, hydrides etc.) with closed- or open-shell electronic structures. Historically, most important applications of cobalt in homogeneous catalysis are in hydroformylation and hydrosilyation reactions. The Classical example of cobalt catalyzed reactions, the synthesis of aldehydes from alkenes *via* an addition process using $HCo(CO)_4$. In 1960, dicobalt dicarbonyl was used as catalyst in hydrosilyation reaction. Despite these studies, cobalt catalyzed organic transformations are still way behind than platinum group metals.[150–156]

An early example with promising results was in the hydroformylation of 1-octene using the hydrido cobalt complex $[(IMes)Co(CO)_3H]$ by Llewellyn *et al*. The unusual high selectivity for the branched hydroformylation product versus linear 1-nonanal seems to indicate that the [(NHC)Co] complex catalyzes alkene isomerization prior to hydroformylation. Also it is interesting to describe the only example of a homoleptic Co^{II} NHC complex of the type $[Co(NHC)_4]^{2+}(A^-)^2$. This complex has been obtained in 52% yield by reaction of ^{Me2}IEt with $[CoCl(PPh_3)_3]$ and $NaBF_4$, followed by one-electron oxidation with $[FeCp_2](BF_4)$. The solution magnetic moment of it, μ_{eff} = 2.4 μ_B, is consistent with a low-spin four-coordinate Co^{II} center. A square-planar coordination geometry for the Co center was established by X-ray crystallography, and the complex was further characterized by EPR spectroscopy. This complex can engage in one-electron

redox reactions, as evidenced by its reaction with aryl Grignard reagents (p-tolylmagnesium bromide), which led to the reduction of the metal center. is a privileged platform for one-electron redox reactions (Figure 63). [157,158]

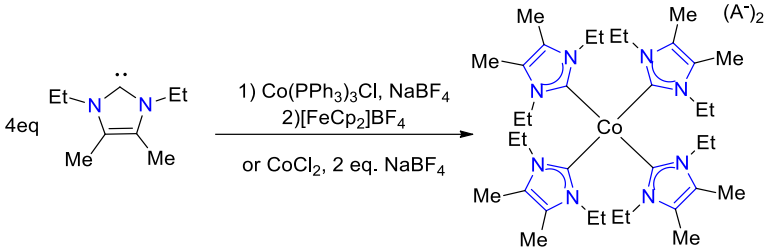

Figure 63:The only example of homoleptic Co^{II} NHC Complex [157,158]

2.1.6. Pincer ligands

The term pincer ligands emerged in the late 1970s based on the studies of Shaw and van Koten (Figure 64). They were the pioneers, who first described organometallic complexes containing this type of ligands. Initially that term referred to tridentate ligands with a central anionic carbon and two flanking binding units that enforce a meridional coordination about the metal center. The term pincer has greatly broadened since then, to include any chelating agents that bind tightly to three adjacent coplanar sites. Ligands with 'pincer' architecture are versatile and precise tools. Because of the steric and electronic tunability of pincer ligands the stability and reactivity of the complexes can be tuned and optimized. The donor groups are immobilized in mer stereochemistry at desired positions of the spherical sphere, while the sub-structures of the formed complexes in which the pincer is involved have increased stability (chelating effect). Many pincer ligands contain phosphines but pincers which contain carbenes are now studied at an accelerating pace.[159–164]

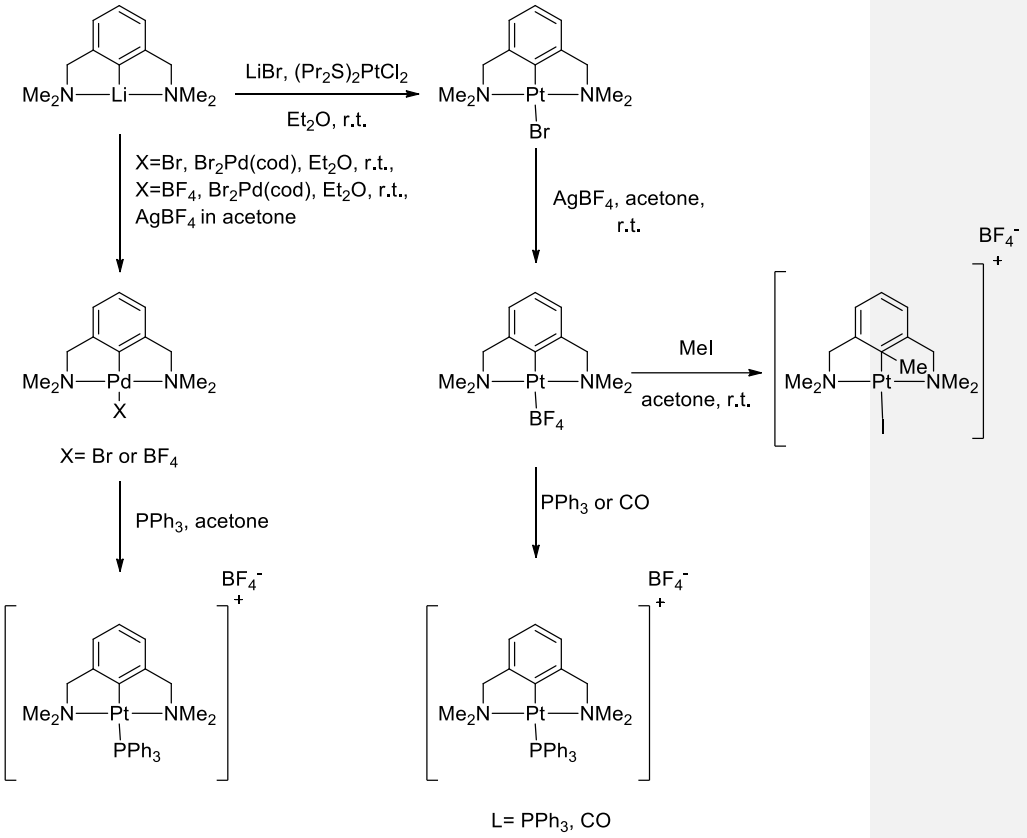

Figure 64: The pincer (NCN) complexes by van Koten et al [161]

The interest of the scientific community for the development of pincer ligands was initially focused on organometallic complexation, wherein a terdentate pincer ligand with rigid or semirigid conformation, was bound to the metal centre *via* at least one metal–carbon σ bond. Usually, the synthesis of a complex with pincer ligands results in the formation of two five-membered metallocyclic rings although, there are cases where six-membered metallocyclic rings are formed. Pincer ligands are also distinguished by the ability to "tune" electronic properties of the complexes formed, for example the enhancement of the thermal stability of the metal complex systems and, in some cases, in the stabilization of unusual and unstable oxidation states of the metal center in the course of formation of chelate metal cycles and in general the chemical stability

avoiding dissociation of the metal. Some of the most commonly used pincer ligands are depicted below (Figure 65) [159–161,165–169]

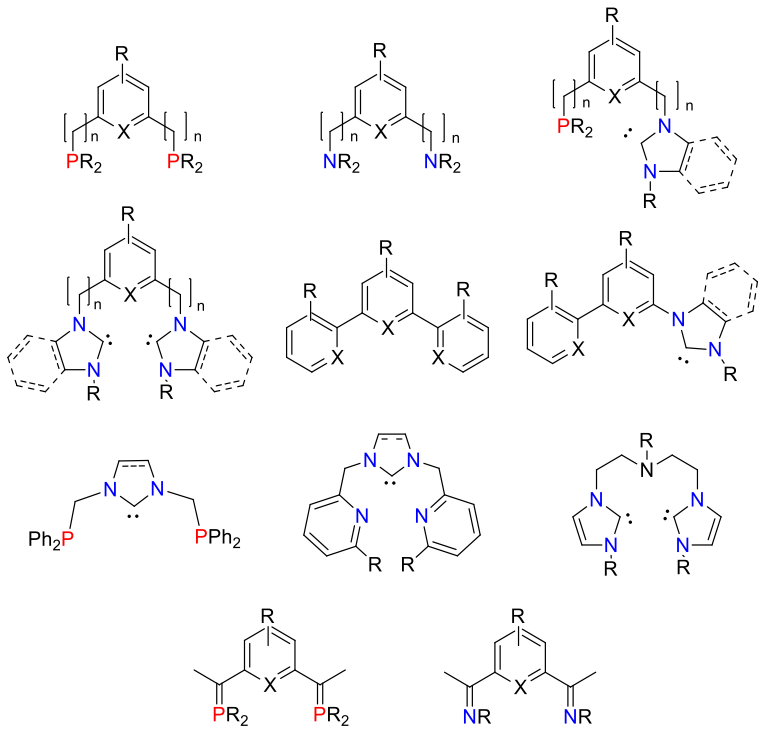

Figure 65: Examples of commonly used pincer ligands [134]

Given the plethora of the pincer ligands synthesized in the recent years, it is of great importance to discuss the various structural modifications of them. The general abbreviation of a pincer ligand is {YXY} with Y as the neutral two-electron donating groups (—$N(R)_2$, —$P(R)_2$, —SR, —$As(R)_2$, or —OR, R=alkyl, aryl), which are located at the side arms and X as the central donor group. The Y donor groups are connected by linker units (Z) , which are very usually alkyl chains of various lengths. Pincer ligands can be characterized as symmetrical, when $L^1=L^2$ or nonsymmetrical, when $L^1\neq L^2$. For practical synthetic reasons however, the symmetrical systems tend to be more popular. Additionally, the

size of the donor ligands as well as the introduction of various functional groups into the benzylic positions strongly affect the steric and electronic properties of the formed pincer complex. Lastly, the OCO ligands (in which the oxygen-containing group acts as L^1, L^2) and their complexes are rarer, and examples of their application are nearly absent. General structures and model frameworks of pincer NHC ligands are shown in Figure 66. [170–172]

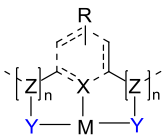

M: metal
n: 0, 1, 2
X: N, NH, C, B, S, P
Y: PR_2, NR_2, SR, OR, NHC
Z: CH_2, NR, O
R= H, alkyl, aryl

Figure 66: General structure of 'pincer' ligands

X represents the central part of the ligand and it can be a nonanionic or an anionic group. Most frequently L is a 2,6-disubstituted phenylene ring or with the anionic carbon atom in position 1. This carbon atom forms the C—M covalent bond with the metal atom (M) in the complex. In addition, neutral nitrogen-containing (pyridines) and some other organic fragments can also be used as X. The nature of the central donor atom (typically C^- or N) may also have an important electronic impact, particularly through the variation of the trans influence. It is possible that the electronic properties can be altered by changing the substituents in the aromatic ring. Zero electron centers such as trivalent boron may provide strikingly different ligand environments, particularly when these centers are located in the central element of the pincer where their coordination is enforced by the wingtip groups. These modifications are the most common as well as variations of substituents on the ring (donor, acceptor groups) or even the elimination of the ring. [160,173–176]

Finally, the modifications of the bridging fragment between L and L^1, L^2 also affects the properties of the produced complex thus controlling the accessibility of the metal center for attack by certain substrates or for the formation of a chiral cavity for asymmetric catalysis. The size of the linker arms determines the ring size and therefore influences the bite angle, a factor that also affects the

reactivity of the complex. When using flexible linkers the fac binding or even fluxionality between the two forms take place.[177,178]

The rigidity of the pincer ligands plays a big role in how efficient they are in asymmetric catalysis. The lateral, mutually trans donors, known as pincer 'wingtips' cooperate with the bridgehead in the functionality of the 'pincer' complexes with 3d metals. Rigidity is not only affected by bridging fragment but also by the wingtips. If the wingtip groups are not very rotatable, they may instead maintain a geometry in which suitable ligands project into the active site area of the catalyst where they help enantio-differentiation of the relevant transition states. The more rigid pincers can give exceptionally efficient ligands for asymmetric catalysis by preventing the wingtip groups from rotating, thus holding them in a geometry that directs ligands into the active site area of the catalyst. [134,178,179]

Except from the numerous examples, where the usage of this type of ligands gives efficient catalytic results, they also give a range of emissive complexes, in which the pincer coordination is preferred over bidentate chelation. In a pincer complex the metal ion is conformationally constrained, the number of distortions that may provide pathways for non-radiative decay to the ground-state are minimized, and this produces clear benefits on the efficiency of the luminescent properties of the complex. [176,178]

2.1.7. Pincer ligand complexes with Co^{II}

The synthesis of Co- pincer complexes can be a crucial step because the formation of a metal-C bond(s) can be difficult. In general, it is achievable *via* the binding of two electron donor moieties. Four general methods exist for the synthesis of the pincer Co complexes. Firstly, those complexes can be produced *via* a direct metalation with a metal containing basic amide groups such as $Co[N(SiMe_3)_2]_2$ known as aminolysis (already described in the complexation of cobalt and NHC carbenes). Secondly the metal can be introduced *via* oxidative addition which results in a different oxidation state. Again, the transmetalation method can be applied here using metal transfer

agents and lastly *via* transcyclometalation routes. Consequently, metalation of these pincer ligands may occur *via* electrophilic aromatic substitution. All these methods must involve a metalation reaction of the corresponding pincer ligands creating a new metal-carbon σ bond in the final step (Figure 67).[134,180–183]

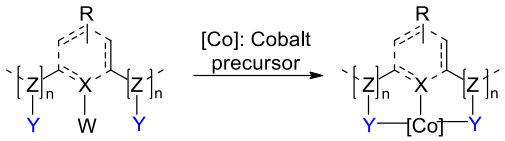

1st method W=H
2nd method W=Cl, Br, I *etc.*
3rd method W=Li, SiR_3, SnR_3, *etc.*

Figure 67: Synthetic strategies for pincer complexes. [134,180–183]

Since 2004 a variety of Co pincer complexes were created. Notably, Danopoulos *et al,* reported the first air-sensitive Co^{II} pincer complex based on the 2,6- bis(arylimidazol-2ylidene) pyridine ($C^{NHC}NC^{NHC}$) ligand. It was obtained by the aminolysis reaction of $[Co\{N(SiMe_3)_2\}_2]$ with the pincer imidazolium salt proligand (Figure 68). [184]

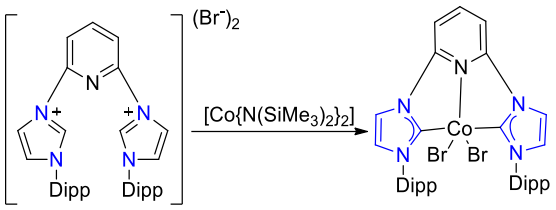

Figure 68: The first pentacoordinated Co^{II} pincer complex [184]

2.2. Results - discussion

2.2.1 Paramagnetic NMR

It is well-known that chemical entities with unpaired electron(s) are paramagnetic. Many transition metal complexes have unpaired electrons being paramagnetic. In organometallic chemistry, these metal ions are complexed with organic ligands resulting in complexes with interesting characteristics. The NMR spectra of paramagnetic complexes can sometimes (but not always) provide valuable information and aid the characterization of paramagnetic complexes. Observable peaks are usually broad and shifted dramatically downfield or upfield depending on the position of the proton nuclei responsible for the resonance relative to the paramagnet (*i.e.* metal). Excessive broadening (related to the rate of relaxation of electron spin momentum, coordination geometry and dynamic processes) makes resonance lines unobsevable. In favourable cases, information about the number and the type of the protons can be extracted from the spectrum. Therefore, the width of the signal depends on the electron relaxation There can be also some broad lines, which may lie in the diamagnetic range that may be misinterpreted as baseline distortions or not be identified at all. On the other hand, the routine signal ranges of diamagnetic compounds, henceforth called diamagnetic shift ranges (*e.g.*, 20 >δ >0 for protons), were checked, while most often the relevant paramagnetic signals appear far outside. Other issues related to paramagnetic NMRs is accurate signal integration due to distorted baselines and overlapping peaks. The stereochemical information of complexes can be retrieved, based on the fact that coupling constants depend on the relative orientation of the interacting partners. Of course, the proton position in the paramagnetic center plays an important role. By integrating the peaks, we can tentatively assign them to specific protons, but coupling patterns cannot be observed. Other magnetic heteronuclei (*e.g.* ^{31}P, ^{13}C *etc.*) in paramagnetic complexes are usually not observable. [185–187]

In our case, the paramagnetic NMR spectra, did not provide sufficient information. Thankfully, crystalline complexes that were tested *via* NMR, were also analyzed with X-ray.

2.2.2. Aminolysis of $Co[N(SiMe_3)_2]_2$ as a methodology to prepare Co-NHC complexes

In order to achieve the desired framework, we chose an aminolysis method to synthesize the cobalt-NHC complexes.

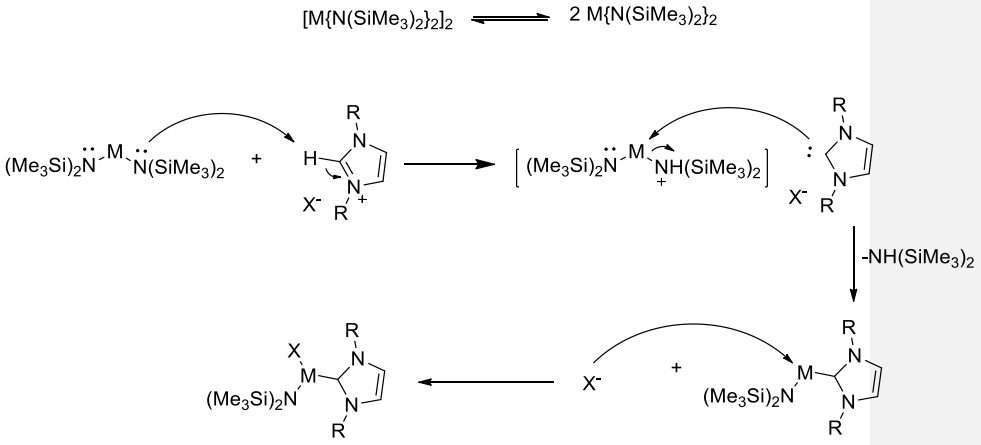

Figure 69: General aminolysis reaction

This method is based on the acidity of the C2-imidazolium proton and the basicity of a bis-silylamide coordinated on certain metals (Fe^{II}, Co^{II}, Mn^{II} *etc*.). The aminolysis product is the volatile $HN(SiMe_3)_2$ and the corresponding NHC which is trapped and coordinates to the metal; finally, the counteranion of the imidazolium (mainly halide) can also enter the metal coordination sphere. In the case of cobalt the aminolysis reagent is $Co[N(SiMe_3)_2]_2$. The ligand precursors (*i.e.* imidazolium salts) were dried prior use due to the air and moisture sensitive nature of the aminolysis reagent $Co[N(SiMe_3)_2]_2$. In the recent years, a wide range of Co^{II} complexes with NHCs including chelating bis-NHCs have been obtained by the aminolysis of $Co[N(SiMe_3)_2]_2$. The aminolysis of the Co silylamide, by suitable imidazolium halides cleanly affords, as well as “pincer” complexes and therefore we applied this methodology. Needless to say, that

the controlled aminolysis of mono-imidazolium complexes with $[Co[N(SiMe_3)_2]_2]$ in a stoichiometry 1:1 should lead to selective reaction of one bis-silylamide only.

It is possible that, if the free NHC ligands are not stable under the substitution reaction conditions they can be introduced in the metal coordination sphere since the isolation of the reactive/unstable NHC is not necessary, making this method useful for the stabilization of reactive organometallics. However, aminolysis with $Co[N(SiMe_3)_2]_2$ to some pincer ligands is sensitive to its exact nature and the experimental conditions. The $[Co\{N(SiMe_3)_2\}_2]_2$ exists in a monomer−dimer equilibrium in benzene solution. In the dimer $[(Me_3Si)_2NCo\{\mu\text{-}N(SiMe_3)_2\}_2CoN(SiMe_3)_2]$, the two three-coordinate Co^{II} centers are bridged by two $-N(SiMe_3)_2$ ligands, and are also bonded to a terminal $-N(SiMe_3)_2$ amido group. The dimer $[Co\{N(SiMe_3)_2\}_2]_2$ (**Co1**) was synthesized *via* the addition of $LiN(SiMe_3)_2$ to a suspension of $CoCl_2$ in diethyl ether, which afforded a dark olive-green solution. Removal of the solvent followed by extraction with hexanes, filtration, concentration, and distillation of the residue afforded $[Co\{N(SiMe_3)_2\}_2]_2$ as an intensely colored dark green vapor, which solidified to a red/brown solid. It is important to say that in the presence of a donor solvent, the dimer can break.

In the present work, the aminolysis method was used to synthesize some of the cobalt NHC complexes *i.e.* **Co2-Co6**, **Co10, Co11** and **Co13** by reacting $Co[N(SiMe_3)_2]_2$ with their corresponding imidazolium salts. Similarly, Danopoulos and coworkers have reported a series of Co^{II} NHC complexes with other bulky ligands such as N,N'-diarylimidazolin-2-ylidene, N.N'-diphosphanylimidazolin-2-ylidene (PCP), N-phosphanyl-N'-2,6-diisopropylphenyl (PCC) and cyclic amino carbene analogues, so this method is quite versatile. In conclusion, the methodology is particularly advantageous in cases where the generation and/or stability of the NHCs are problematic. [100,149,184,188–196]

2.2.3. Quaternization reactions for the preparation of imidazolium salts

In order to receive the imidazolium salts without linkers for the ligand synthesis, we mainly used quaternization of N-substituted imidazoles.

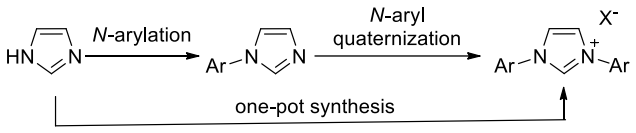

Figure 70: N-arylation, N-aryl quaternization and one pot synthesis of imidazolium salts

In this case we used DiPP- or Mes-imidazoles combined with an electrophile (*i.e.* 2,6-dibromo-3,5-lutidine, 2,6-dibromopyridine, *etc.*), stirring for a few days at room or elevated temperatures in the presence or absence of solvent (in the latter case in the melt). However, quaternization can be troublesome because it needs durable glassware in high temperatures, (in some cases >150 °C). It is also possible, despite the precise amounts of the reagents and the correct conditions to obtain the di-quaternized, that only the monoquaternized product can be obtained. Finally, there are also cases where the received product is not completely clean due to the creation of thermal decomposition products. When we wanted to receive *the* imidazolium *salts with linkers* for the ligand synthesis, we had no problem using the nucleophilic substitution reaction. In fact, the benzylic primary halides that we used to obtain those salts *(i.e.* 2,6-bis(bromomethyl)pyridine) react with imidazolium salts at room temperatures in polar solvents. The work up of the reaction mixture consisted of solvent removal (if solvent was used), and the product residue was washed with diethyl ether, then dried under vacuum; the products were pure enough to use in the complex formation steps. [178,183,197,198]

The ligands **L12a, L12b, L13** and **L17** were synthesized *via* quaternization and **L6a** and **L6b** were synthesized *via* SN2.

2.2.4. Syntheses of Substituted Imidazoles

Of great importance in order to build the pincer ligand framework is obtaining imidazoles starting material which after quaternization and deprotonation of the resulting imidazolium salts acted as NHC sources. There are several ways, with which the substituted imidazoles are obtainable.

The first synthesis is a direct 1-pot alkylation of the imidazol with electrophilic alkyl halides. The method works well for aliphatic ligands. (Figure 70)

Alternatively, the imidazol heterocycle is built from suitable precursors. This method also works well with alkyl substituted imidazoles, however, there are examples, where it can also be applied to a limited number of aromatic amines (*i.e.* 2,6-dichloroaniline). This method involves except of the amines, glyoxal, NH_4Cl, H_2CO, H_2O, pH=2, heated in 90 ^oC for 3-6 hours.

Another one-step route to the synthesis of N-imidazoles is the N-Arylation. That approach works well for unhindered aromatic amines, but problems arise, when scaling-up because 1 eq. of 1,10-phenanthroline is used. This basic heterocycle can be difficult to separate from the imidazole product. As a result, to receive the product free from impurities, a column is required. This method involves except of the ArBr and the 1*H*-imidazole, CuO*Tf*, Cs_2CO_3, dba, 1,10-phenanthroline, xylene, heated in 125 ^oC for 36 hours.

A different one-step approach for the synthesis of 1-arylimidazoles is *via* nucleophilic displacement of labile aromatic halogen, by imidazole using Na_2CO_3 and DMF. Although this method is relatively simple, it has low yields, tedious isolation procedure and failure when there are no electron-withdrawing groups on the aromatic ring.

The last route that was used involves multiple steps and is only applicable mostly to hindered aromatic amines. This approach works well for scale-up purposes, as the obtainable product is clean, so it doesn't require chromatographic separations. This is a four-step Marckwald synthesis which is a ring closure-oxidation-reduction sequence furnishing reaction. The isothiocyanates can be prepared by the reaction of thiophosgene with the corresponding anilines and the intermediate aryldiethoxyethylthioureas are usually cyclized without purification to the crystalline 1-aryl-2-mercaptoimidazoles using hot 10% HCl. The mercapto group is readily oxidized

with hot 20% HNO_3 and the overall yields of 1-arylimidazoles are usually <50%. It is important to say that the Mes-imidazole can be obtained also by the 1-pot condensation because Mes-aniline in not as hindered as DiPP-aniline. To prepare the ligands, we used this method, and we obtained the products clean and in a good yield based on the literature.

With this methodology, addition of an aromatic group can be achieved on the nitrogen of the imidazole. If we wanted to add an alkyl group, we should proceed *via* an electrophilic attack.

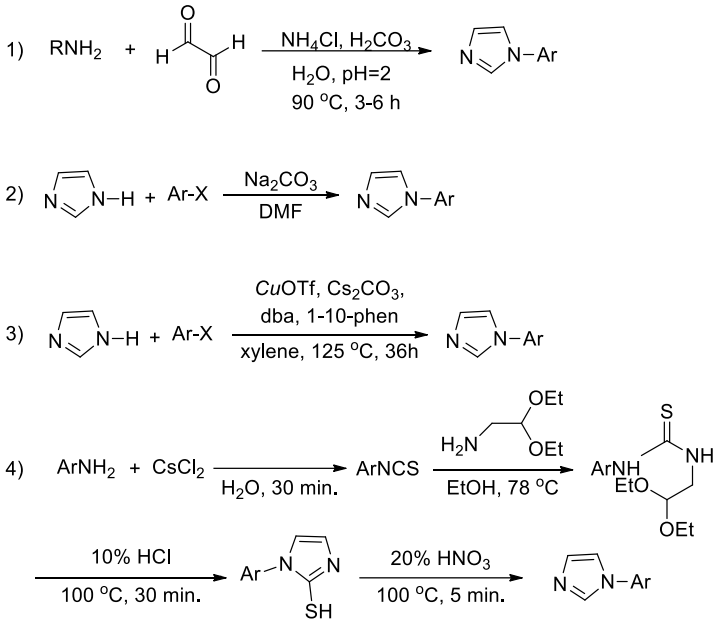

Figure 71: Syntheses of 1-Arylimidazoles

L5a and **L5b** were synthesized with the last synthesis, giving good yields, based on the literature. [199–203]

2.2.5. Ligand syntheses

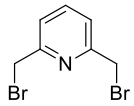

L1

L1 was obtained according to the known protocol by bromination of the commercially available 2,6-dihydroxymethylpyridine 1 with PBr_3 at 0 °C, affording 2,6-dibromomethylpyridine **L1** in the same yield as the literature (89% compared to 95%).

The absolute absence of water is necessary in order to avoid the side reaction:

$PBr_3 + 3H_2O \rightarrow H_3PO_4 + 3HBr$

In this procedure, we have witnessed problems with the stirring, so maybe it is better to use more DMF. [204]

Molecular Weight: 264.95

Yield: 89%

Mp: 82 ºC

Colour: white

Chemical formula: $C_7H_7Br_2N$

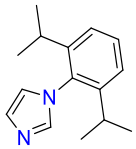

L5a

L5a was synthesized according to the already published protocol and gave similar yields to the literature (75% compared to 80%). During the final step of the addition of HNO_3, large amounts of gases are evolved, and as e result, it is advised, to lower the scale. Because imidazole supports only a monocationic charge but the reaction under acidic conditions consumes two cations, imidazole formation liberates protons to the reaction medium and thus the pH changes. The side reactions of the imidazole synthesis are suppressed in an

acidic environment; thus, the possible by-products are formed mainly during the first stages of the process. Hence, a pH =1 should be close to optimum for imidazole synthesis. We repeated the procedure with 10 g, 15 g, 20 g, 25 g of mercaptane. We realized that it is more efficient, after the addition of NH_3 to remove the excess of HNO_3, to cool down the solution using running water at the exterior. Then we filter the precipitate, and we reduce the volume by 50%. Later, we put it in the fridge to receive more precipitate. The recrystallization occurred with n-hexane trituration. Then we dry solids in rotavapor and we use the vacuum line, to be sure that the product is free of solvent. [199–203]

Molecular Weight: 228.33

Yield: 75%

Mp: 124 ºC

Colour: beige

Chemical formula: $C_{15}H_{20}N_2$

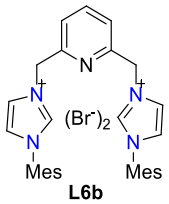

L6b

L6b was originally synthesized according to the protocol developed in the Danopoulos laboratory and gave similar yields (79% compared to 80%). To increase the efficiency of this reaction we add a slight excess of imidazole (2.2 eq. instead of 2 eq.). After we tested the progress of the reaction in aliquots using NMR, we saw that there was part of the starting salt remaining. In an effort to clean the product, we used various solvents and we let it precipitate, overnight. In order to remove the starting material salt, we add ether and let it precipitate overnight. After precipitation in the fridge, we received the product as brown oil. We thought that there is moisture and maybe some staring material. Therefore, we removed the solvent mixture with the help of a pipette

and then dried it in rotavapor followed by azeotropic drying. Toluene was used as a solvent due to its high boiling point. The final product was obtained after removing the moisture and the solvent under reduced pressure and washed with pentane. [198,205]

Molecular Weight: 637.45

Yield: 79%

Mp: 250 ºC

Colour: beige

Chemical formula: $C_{31}H_{35}N_5$*2Br

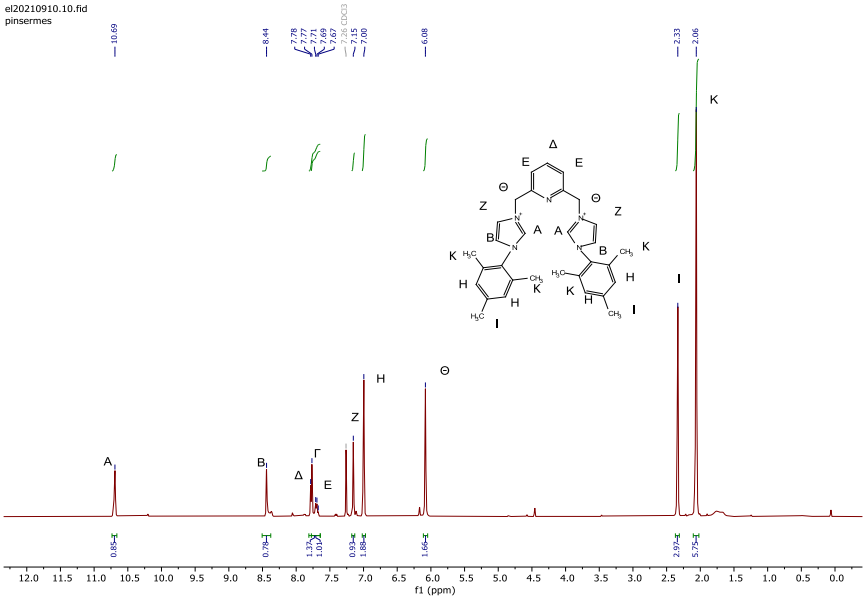

*Figure 72: [1]H-NMR spectrum of **L6b** in $CDCl_3$*

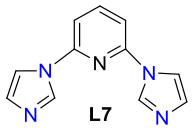

L7 was generated effectively from an Ullmann-type coupling reaction in relatively good yield (76% compared to 96%). We tried three different synthetic routes to access L7. In the first procedure, we used 1*H*-imidazole, K_2CO_3, CuI, 2,6-dibromopyridine and L-proline. The mixture was heated at 90 ºC and after 12h, the reaction was cooled and participated between 250 mL water and 250 mL CH_2Cl_2. Because of the low yield we used a different procedure, using 1*H*-imidazole, K_2CO_3, CuI and 2,6-dibromopyridine in dry DMF. The mixture was heated at 130 ºC for 24h. Then CH_2Cl_2 was added and washed with H_2O, by solvent extraction procedure and was recrystallized. Lastly, in a third procedure 50 mL round bottom flask, provided with a condenser, we added 1*H*-imidazole, KOH and TBAB were stirred at r.t. for 15 min, then 2,6-dibromopyridine was added and the mixture was stirred for 2 h at 80 °C. The residue was extracted with EtOH but it was not clean. [206–208]

Molecular Weight: 210.23

Yield: 76%

Mp: 135 ºC

Colour: white

Chemical formula: $C_{12}H_{10}N_4$

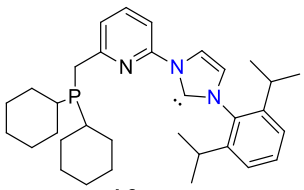

L8

L8 was synthesized following the protocol with a relatively good yield, 73%. The $^{R}PNC^{NHC}$ free carbene was synthesized by the selective deprotonation of the imidazolium, phosphonium salt precursor using 2 equiv of $KN(SiMe_3)_2$. This reaction can be tricky, in order to stop the deprotonation at that stage and not proceed any further in dearomatization of the pyridine or formation of the

complex, directly obtained by transmetalation (K(^{Cy}P*N$_a$C^{NHC})). Using dry ice is an essential step in order to kinetically control the reaction as well as to make sure we receive the correct product. The goal is that with the replacement of one P-donor arm of the standard ^{R}PN^{R}P by an NHC donor, we could obtain the nonsymmetrical ligand ^{R}PNC^{NHC}.[100,209]

Molecular Weight: 515.71

Yield: 73%

Colour: beige

Chemical formula: $C_{33}H_{45}N_3P$

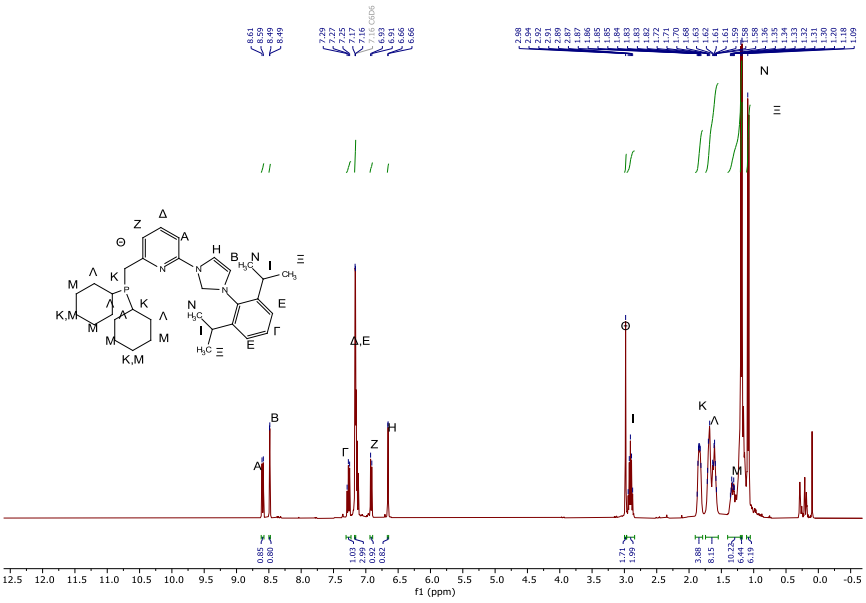

*Figure 73: ^{1}H-NMR spectrum of **L8** in C_6D_6*

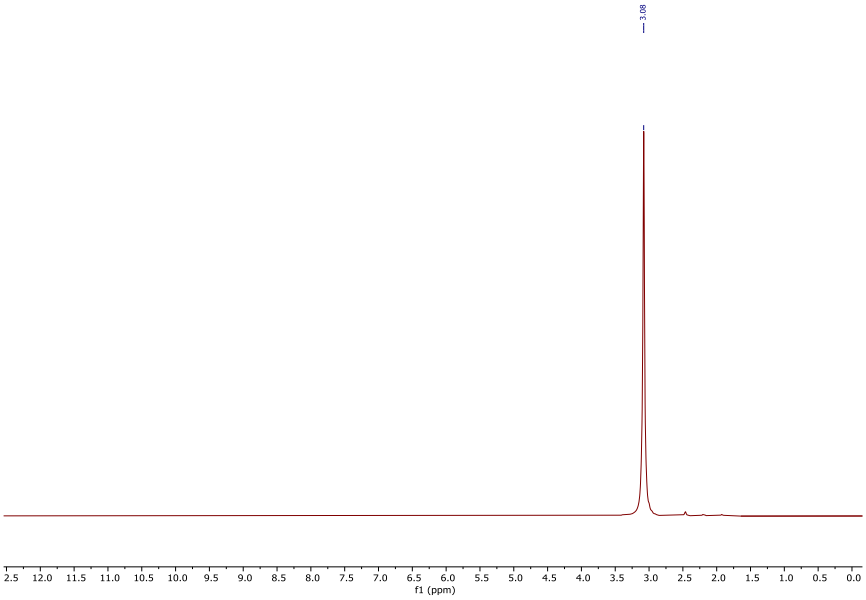

*Figure 74: ^{31}P-NMR spectrum of **L8** in C_6D_6*

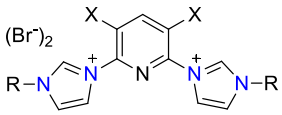

L12a, L12b

R=DiPP, X=H, **L12a**
R=DiPP, X= CH_3, **L12b**

L12b was synthesized according to an adaptation of the literature route to ligand 2-(DiPP-imidazolium)-6-bromo-3,5-pyridine (**L12a**), with yield close to the literature (73% compared to 77%). The first step is halogen exchange of 2,6-dibromo-3,5-dimethylpyridine, which is extremely important in order to replace the external anions Br^- with I^-. Unexpectedly, double deprotonation of the iodide salt afforded poor yields of the ligand. However, exchange of the iodides for bromides, gave good yields. When quaternisation of compound **L10**

with 2 equivalents of DiPP-imidazole (**L5a**) was attempted, after 7 days at 140 °C a mixture of mono- and di-quaternised products was identified in the ^{1}H NMR spectrum of the reaction product. The presence of two imidazolium peaks at 10.83 and 10.45 ppm in a 1:2 ratio indicated that more forcing conditions were required to drive the reaction to completion. Increasing the amount of DiPP-imidazole to 3 molar equivalents and also increasing the reaction temperature to 190 °C resulted in clean conversion to the di-quaternised product **L12b** after 7 days. [210,211]

Molecular Weight: 721.61

Yield: 89%

Colour: cream

Chemical formula: $C_{37}H_{47}N_5$*2Br

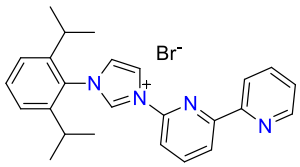

L13

L13 was synthesized following the lab protocol in the same yield as the literature (82%). Quaternisation of 6-bromo-2,2-bipyridine and with the 1-(2,6-diisopropylphenyl)imidazole proceeds smoothly in the melt at 160 °C, giving moderate yields of the desired imidazolium bromide after purification and azeotropic drying. [198]

Molecular Weight: 463.41

Yield: 89%

Mp: 160 °C

Colour: beige

Chemical formula: $C_{25}H_{27}N_4$*Br

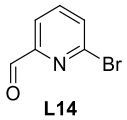

L14

L14 was synthesized based on the literature, affording the product at the same yield (65%). The *n*-BuLi in hexanes solution was added dropwise because it reacts violently with di-bromopyridine and that is the reason why the solution was cooled using dry ice, in advance. This reaction is a mono-lithiation of 2,6-dibromo- pyridine, which was followed by DMF quenching afforded known aldehyde **L14**. The yield was improved when the procedure was repeated using a slight excess (5% mol) of DMF solution. [212,213]

Molecular Weight: 186.01

Yield: 89%

Mp: 80 °C

Colour: beige

Chemical formula: C_6H_4NOBr

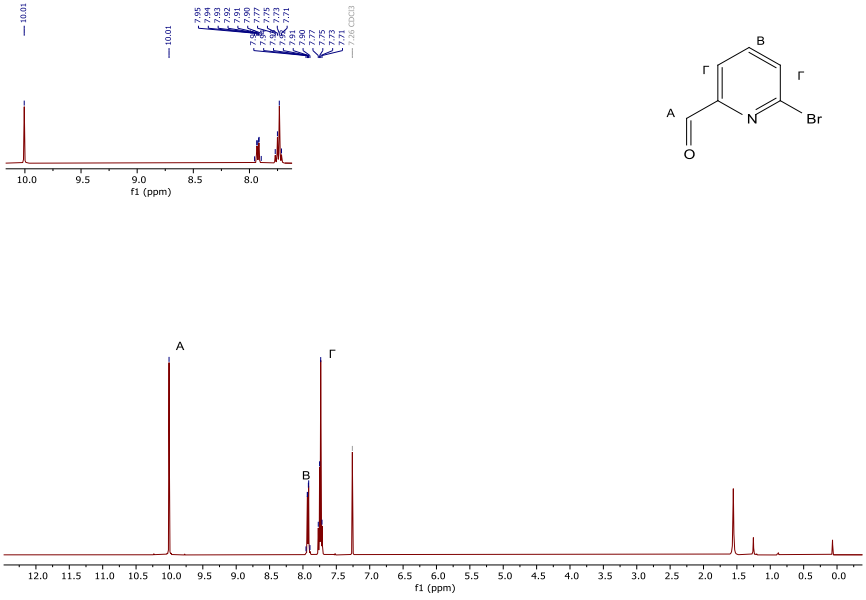

*Figure 75: [1]H-NMR spectrum of **L14** in $CDCl_3$*

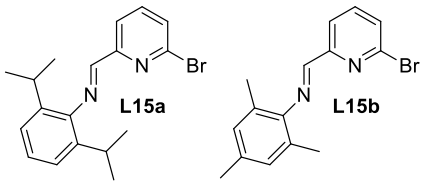

L15a, L15b were synthesized as described in the literature, with slight variations. The aldimine synthesis took place in EtOH with typically one drop of formic acid as catalyst. The yields were 89% and 72% respectively, compared to the literature 78% and 98%. The product was dissolved in hexane, with the help of heat gun. The solution was then transferred in a new spherical flask and put in the freezer for several hours. The formation of yellow crystals was observed, and the solution was orange. We filter it through Buchner and reduce the volume with the help of rotavapor. We repeat the crystallization process until we stop receiving crystals. The NMR showed once, excess of the desired product, but there was also a part of the Z product, which probably will not react in the next step with $ZnCl_2$. However, we also noticed traces of hydrolysis when checking the NMR, especially when using "old" wet $CDCl_3$. What made us think it could come from the solvent was that amount of aldehyde in the ^1H NMR spectrum (easily seen from the -C(O)H signal) is the same as the amount of $ArNH_2$. When we started using dry and degassed $CDCl_3$, stored in a Schlenk over 3A, we didn't have this issue anymore. In order to be sure that the hydrolysis came from the solvent, we used more pushing conditions like Dean-Stark conditions, using toluene or benzene. When we tried the Dean-Stark procedure the temperature in toluene was set to 140 ^oC and in benzene in 110 ^oC. The Dean-Stark run firstly overnight because there was still monohaldehyde and during that we added more catalyst and aniline. Using this procedure, we could reach full conversion and separate the product from the catalyst by extracting with Et_2O and filtering off the white powder formed. The imine is soluble but the $ArNH_3^+$/*p*-tol-SO_3^- salt formed is not. Other ways that we tried to reduce that problem was column chromatography, but the silica affected our mixture or adding more catalyst *p*-tol-SO_3H (around 3 drops), but

the Dean-Stark conditions, worked the best. We also checked by IR the presence of water in the desired products, and there was none. It seems that the problem was indeed the quality of the $CDCl_3$. Now the NMR spectrums seem clearer after using $CDCl_3$ with sieves. [197]

L15a

Molecular Weight: 345.28

Yield: 89%

Mp: 105 ^{o}C

Colour: yellow

Chemical formula: $C_{18}H_{21}BrN_2$

L15b

Molecular Weight: 303.20

Yield: 72%

Colour: yellow-orange

Chemical formula: $C_{15}H_{15}BrN_2$

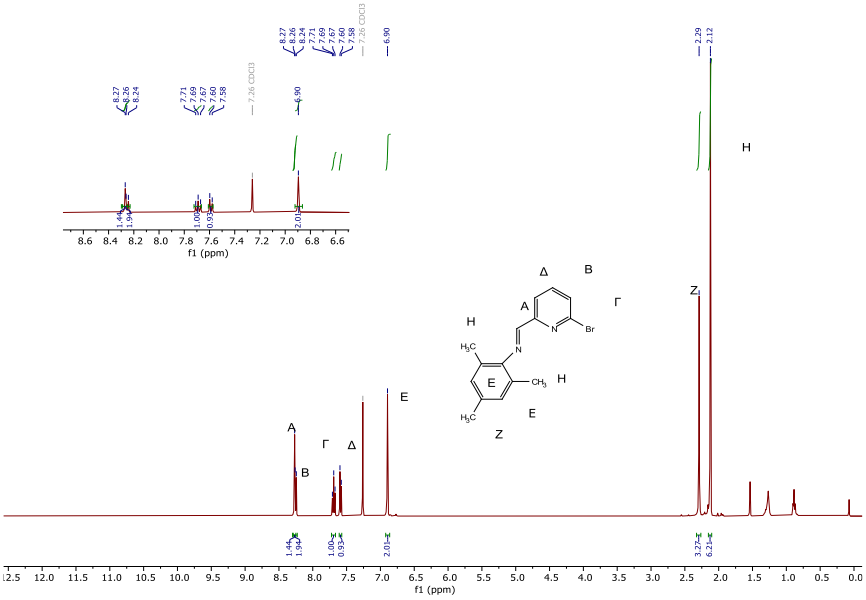

*Figure 76: ^{1}H-NMR spectrum of **L15b** in $CDCl_3$*

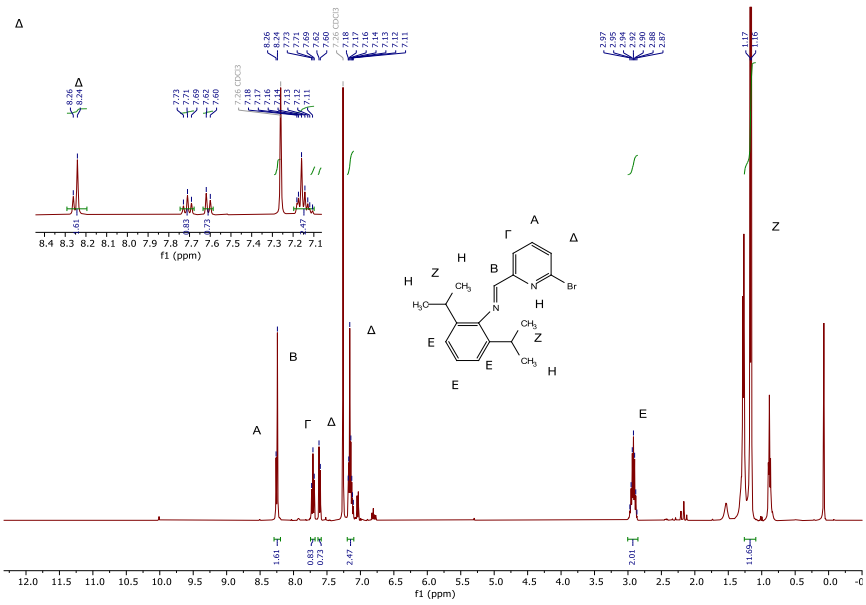

*Figure 77: ^{1}H-NMR spectrum of **L15a** in $CDCl_3$*

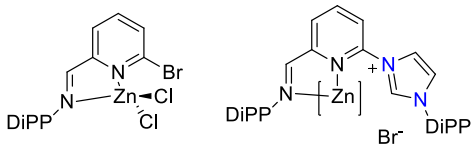

L16 **L17**

L16 was synthesized, according to the literature and with the same yield 90%.

Molecular Weight: 481.55

Yield: 90%

Colour: yellow

Chemical formula: $C_{18}H_{21}BrCl_2N_2Zn$

L17 was received *in situ* and was not tested *via* NMR.

Molecular Weight: 559.09

Colour: yellow

Chemical Formula: $C_{33}H_{42}N_4Zn$

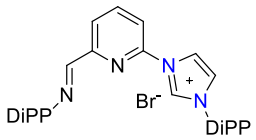

L18

L18 was synthesized, when a mixture of **L16** (1eq.) and imidazole **L5a** (2.5eq.) was heated in a sealed flask at 150-160 ºC for 4d. The yield was 69% compared to 76% of the literature. We tried three different imidazoles namely, 1-methyl-1*H*-imidazole, 1-(4-(tert-butyl)-2,6-dimethylphenyl)-1*H*-imidazole and 1-(2,6-diisopropylphenyl)-1*H*-imidazole. The first two trials based on the NMRs were not successful, especially in the second case. Our hypothesis is that the use of DMAC in that reaction harmed the final product, and as a result we could not observe it on the spectrum. In all the cases, it is important to retrieve the excess of the imidazole, in the form of crude. We have repeated the process by adding more excess of the imidazole and by mixing the two starting materials with mortar and pestle, inside the glove box, in order to be equally distributed, inside the flask. After receiving the product, we check its purity *via* NMR, but the product seems impure. Then we tried trituration with hot toluene, but the quality of the product didn't seem to change. We have also washed the solid with copious amounts of Et_2O, but no improvement has been observed. Later we tried to clean it with column chromatography (97.5% CH_2Cl_2 and 2.5% MeOH). We repeated column chromatography with the addition of Et_3N. Although, after that, the TLC plates have only one spot, the NMR is not better. The cause of that might be the heating in such temperatures. We have repeated the same procedure with lower temperatures and/ or fewer days, but we witness the same problem. The product seems soluble in acetone and acetonitrile, so we tried took NMR in acetonitrile, but we still don't have a clear image. Another problem is that we can not see the peak at 11.58 ppm, so we maybe we have not received the desired product or can not see it because we used MeCN as the solvent and therefore observe fast dynamic processes. To check it clarity, we also tested the product with ESI-MS and it seems that maybe we have received some product, but it is not clean. [197]

Molecular Weight: 572.60

Yield: 69%

Colour: beige

Chemical formula: $Br^*C_{33}H_{41}N_4$

MS (ESI) m/z: 493,52 ($[M+H]^+$

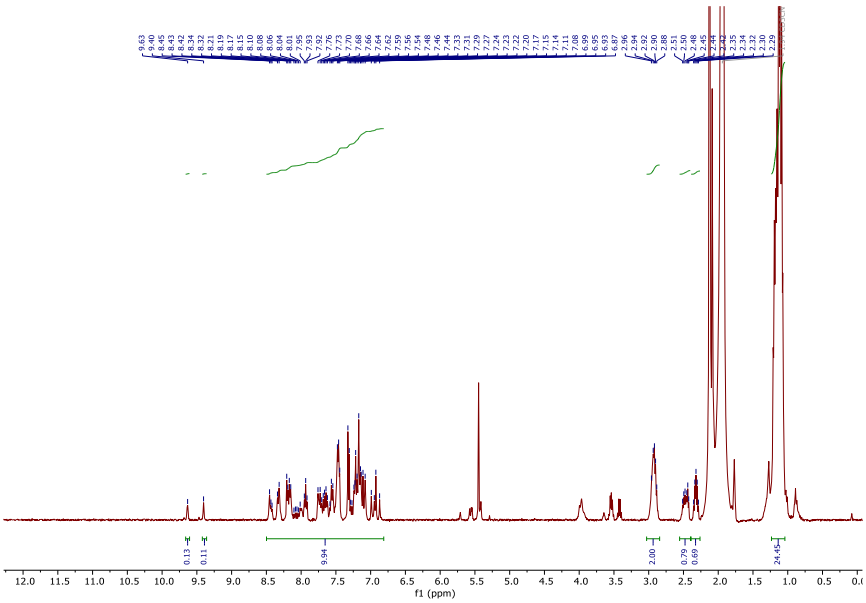

*Figure 78: ^{1}H-NMR spectrum of **L18** in MeCN*

2.2.6. Complex syntheses

$[Co\{N(SiMe_3)_2\}_2]_2$

Co1

Co1 was synthesized according to the literature, in the same yield 75%. It was used in the rest complex formations as a staring material. [191]

Molecular Weight of the monomer: 379.70

Yield: 75%

Melting point: 90°C

Chemical formula: $C_{12}H_{36}CoN_2Si_4$

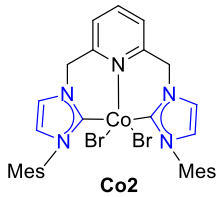

Co2

Co2 was synthesized with 1eq. **Co1** into a solution of 1eq. **L6b** in 15 mL of precooled THF, inside the glove box. When the THF is added at r.t. the solution turns green but precooled at -30 ºC, the solution is purple. The solution was filtrated, then the volatiles were removed and the solid was dissolved in THF and layered with Et_2O. Pink crystals were formed, but they are not of good quality.

Molecular Weight: 696.38

Yield: 95%

Colour: Pink

Chemical formula: $C_{31}H_{35}Br_2CoN_5$

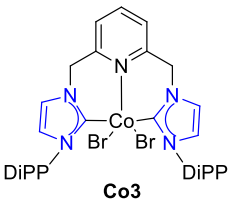

Co3

Co3 was synthesized with 1eq. **Co1** into a solution of 1eq. **L6a** in 15 mL precooled THF, inside the glove box. The next day we discovered that the mother liquid is dark red, and the precipitate is blue. We removed manually some liquid and place it in a new glassware with a smaller diameter and tried to crystallize by layering THF / ether. After having no luck, we used the slow

vapour diffusion techniques of THF into pentane. Finally, we received dark purple crystals which were analyzed by X-ray diffraction and the crystal structure was determined. After many efforts, we also tried to recrystallize the blue precipitate but with no success. We removed the solid from the glove box and we dissolved it in CH_2Cl_2. The solution was not completely transparent, so we used a frit-canula covered in filter paper and Teflon tape, with no success. Then we used a frit Schlenk glassware, but the problem remained. We then reduced the volume, layered it with Et_2O and store it in the fridge. In the next days, we received crystal nuclei, but not of satisfactory quality for X-ray crystallography. As a result, we decided to redissolve the crystals but again the result is not better. As a last resort, we attempted anion exchange by adding 2 eq. of sodium tetrakis[3,5-bis(trifluoromethyl)phenyl]borate (NaBARF) to establish whether the low solubility/porr crystallinity could be attributed to the presence of salt (complex cation and bromide anion) with size mismatch between cation and anion. Anion exchange would alleviate this problem. After the addition, the complex was destroyed. In next synthetic procedures, where the blue precipitate was again received, we tried to dissolve it in MeOH, H_2O, *i*-PrOH without success. We also tried MeCN or DMF as a solvents, which dissolved the complex but the next day, it turned green, presumably decomposed. After repeating the same synthesis, we received the blue precipitate in the form of small crystals, that may be have a chance to be used successfully for structural determination.

Molecular Weight: 780.54

Yield: 95%

Colour: Purple

Chemical formula: $C_{37}H_{47}Br_2CoN_5$

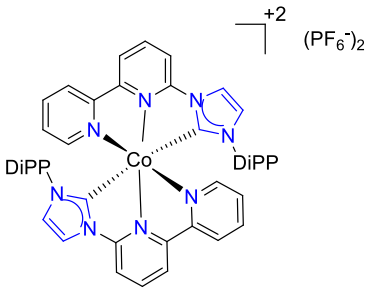

Co4

Co4 was synthesized with 1eq. **Co1** into a solution of 2eq. **L13** in 10 mL THF. One of our goals was to also synthesize the 1:1 complex, which means that only one ligand **L13**, would attach to the metal. By decreasing the temperature to -30 ºC, we could still only get the 2:1 complex. In order to receive a 1:1 analogue complex, we could try using a more sterically hindered ligand or another starting material instead of $[Co\{N(SiMe_3)_2\}_2]_2$. We obtained crystals of the 2:1 complex (**Co4**), by applying the solvent layering method outside the glove box, using CH_2Cl_2 and pentane. This method was applied after adding added 2 eq. of sodium tetrakis[3,5-bis(trifluoromethyl)phenyl]borate (NaBARF) for the reasons outlined above. The crystals were of excellent quality, therefore the crystal structure, was obtained. Interestingly, sometimes we observed the formation of yellow crystals instead of the black cube like crystals, we normally get. We believe that based on their color there may be a Co^{III} complex, is also formed. The yellow crystals were obtained again with CH_2Cl_2 and pentane solvent system by they were not of sufficient quality to give us a structural data.

Molecular Weight: 1128.9

Colour: reddish black

Chemical formula: $C_{51}H_{57}CoN_8P_2F_{12}$

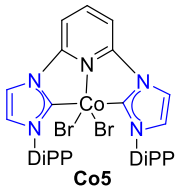

Co5

Co5 was synthesized with 1 eq. **Co1** into a solution of 1 eq. of the bis(imidazolium) salt (CH-N-CH)Br_2, **(L12a)** in THF gave quantitative yields of **Co5** as a red-purple, microcrystalline, moderately air-sensitive solid. The reaction has been successfully scaled up (10-15 g of imidazolium salt). This complex was already characterized in 2003 by Danopoulos lab but X-ray diffraction studies need to be repeated. However, after we resynthesized this complex, we decided to test it as a precatalyst for hydrogenation and transfer hydrogenation of ketones. The yield was the same as reported (95%). [184]

Molecular Weight: 752.49.

Yield: 95%

Colour: red

Chemical Formula: $C_{35}H_{43}Br_2CoN_5$

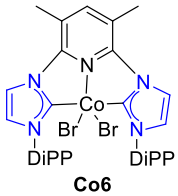

Co6

Co6 was synthesized with the same protocol as **Co5**. 1eq. **Co1** into a solution of 1 eq. of the corresponding bis(imidazolium) salt, (**L12b**) in THF gave quantitative yields of **Co6** as a dark red, microcrystalline, moderately air-sensitive solid. This complex has not been characterized *via* X-ray diffraction studies, because crystals of satisfactory quality, were not formed. This procedure will be repeated. This complex was used as a precatalyst for hydrogenation and transfer hydrogenation of ketones as described in this work. [184]

Molecular Weight: 780.54

Yield:

Colour: dark red

Chemical Formula: $C_{37}H_{47}Br_2CoN_5$

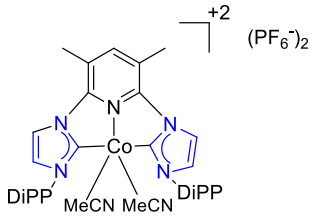

Co7

Co7 was synthesized with 1eq. **Co6** and 2 eq. KPF_6, dissolved in MeCN and stirred overnight, giving a red solution. Crystallisation attempts did not produce crystals of X-ray quality. These attempts will be repeated in the future.

Molecular Weight: 992.766

Colour: red

Chemical Formula: $C_{41}H_{55}CoN_7P_2F_{12}$

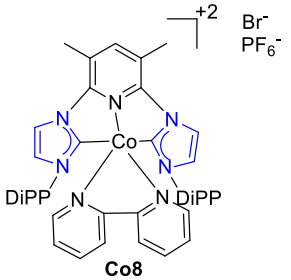

Co8

Co8 was obtained by the reaction of 1eq. **Co6** and 1eq. bipyridine, which were dissolved in 10 mL THF. 2eq. of KPF_6 were dissolved in MeCN and the solution was added to the reaction mixture shortly after and the orange mixture was stirred overnight. After evaporating the solvent, the brown residue was washed with ether in order to remove any unreacted excess bipyridine. Co8 dissolves

in CH_2Cl_2 may be with partial decomposition as inferred by the formation of a white powder. This complex is characterized *via* X-ray diffraction studies because crystals of satisfactory quality, were formed but instead of two PF_6^- we only received one and one Br^- in the exterior layer of the crystal structure. This procedure will be repeated with layering MeCN / Et_2O.

Molecular Weight: 1001.78

Colour: orange

Chemical formula: $C_{47}H_{55}CoN_7BrPF_6$

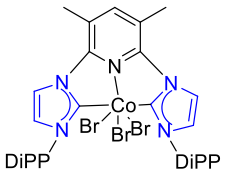

Co9

We tried to synthesize **Co9** using 1eq. **Co6**, which was dissolved in 10 mL THF. In the first case, we used 2-3 drops of Br_2 (2 – 3 eq.) and in the second trial, we used 1 eq. of NBS. In both cases, the solution does not change colour, thus we assume that the reaction did not occur. The NBS procedure, seems more promising, but it is necessary to repeat it, in the future.

Molecular Weight: 860.45

Colour: red

Chemical formula: $C_{37}H_{47}Br_3CoN_5$

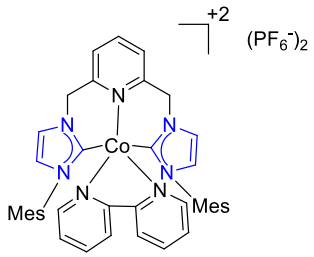

Co10

Co10 was synthesized using 1 eq. **Co1**, and 1 eq. **L6b** and 1 eq. bipyridine in 15 mL of THF at r.t. 2 eq. KPF_6 were also dissolved in MeCN, then added to the THF solution and was let to stir overnight, receiving a brown solution. Then the volatiles were removed and was washed with Et_2O, in order to remove the excess amount of bipyridine. This complex will be characterized *via* X-ray diffraction studies because crystals of satisfactory quality, were formed, using layering with MeCN / Et_2O.

Molecular Weight: 982.68

Colour: brown

Chemical formula: $C_{41}H_{43}CoN_7P_2F_{12}$

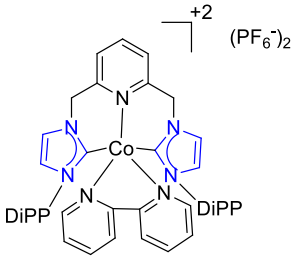

Co11

Co11 was synthesized, with the same procedure as **Co11**. **Co11** was synthesized using 1 eq. **Co1**, and 1 eq. **L6a** and 1 eq. bipyridine in 15 mL of THF at r.t.. 2 eq. KPF_6 were also dissolved in MeCN, then added to the THF solution and was let to stir overnight, receiving a brown solution. Then the volatiles were removed and was washed with Et_2O, in order to remove the

excess amount of bipyridine. This complex was not characterized *via* X-ray diffraction studies because crystals of satisfactory quality, were not received despite layering with MeCN / Et_2O.

Molecular Weight: 1066.84

Colour: brown

Chemical Formula: $C_{47}H_{55}CoN_7P_2F_{12}$

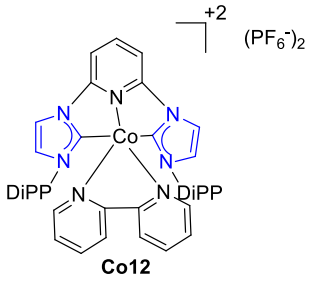

Co12

Co12 was synthesized, with the same procedure as **Co8**. **Co12** was received after the reaction of 1eq. **Co5** and 1eq. bipyridine, which were dissolved in 10 mL THF. 2eq. of KPF_6 were dissolved in MeCN was added shortly after and let stir overnight. It is important to wash the brown solid before the layering, in order to remove the excess bipyridine. **Co12** seems to dissolve in CH_2Cl_2, but because of a presence of a white powder there, it is possible that destroys the complex. This complex will be characterized *via* X-ray diffraction studies because crystals of satisfactory quality were received *via* layering MeCN / Et_2O.

Molecular Weight: 1198.56

Colour: brown- orange

Chemical formula: $C_{45}H_{51}CoN_7P_2F_{12}$

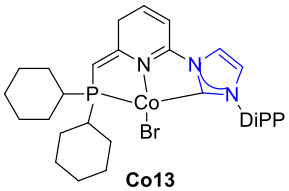

Co13

Co13 was synthesized, with 1 eq. **L9** in THF precooled at - 78 °C, which was added dropwise to a cold solution of 1 eq. **Co1**. After extraction with toluene, filtration and evaporation of the toluene solution afforded we received **Co13** as a dark purple solid. This procedure was repeated in the past, therefore, no characterization is needed, and this complex will be tested as a catalyst, in comparison with **Co5** and **Co6**.

Molecular Weight: 655.56

Colour: purple

Chemical formula: $C_{21}H_{30}BrCoN_3P$

2.2.7. Crystallography

The structure of **Co3** revealed a 5-coordinated square pyramidal geometry at the Co. (Figure 79)

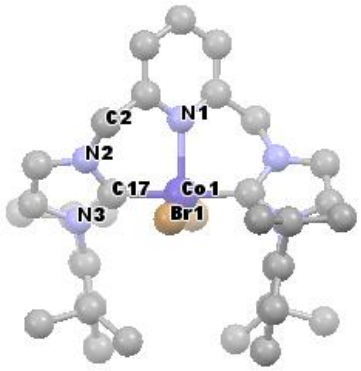

*Figure 79: ORTEP representation of the structure of **Co3** showing 50% probability ellipsoids with hydrogen atoms and solvents omitted for clarity.*

Atom 1	Atom 2	Bond lengths (A˚)
Co1	Br1	2.441
Co1	N1	2.105

Co1	C17	1.930
N2	C17	1.359
N2	C2	1.465
N3	C17	1.381

*Table 15: Selected bond lengths (A˚) of **Co3** structure.*

Atom 1	Atom 2	Atom 3	angles (◦)
C17	Co1	C17'	178.29
C17	Co	N1	88.07
Br1	Co	Br1'	150.30

*Table 16: Selected angles (◦) of **Co3** structure*

The structure of the **Co4** revealed a distorted 6-coordinated octahedral geometry at the Co. (Figure 80)

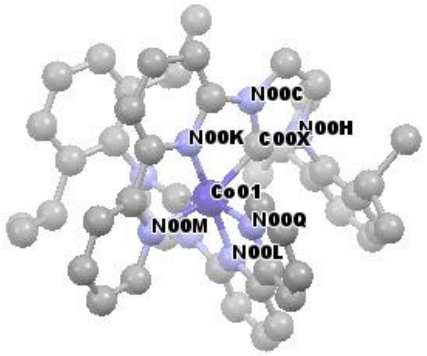

*Figure 80: ORTEP representation of the structure of **Co4** showing 50% probability ellipsoids with hydrogen atoms, solvents and PF_6^- omitted for clarity.*

Atom 1	Atom 2	Bond lengths (A˚)
Co01	N00Q	2.092
Co01	N00L	1.925

Co01	C00S	2.008
C00S	N001	1.315
C00S	N00E	1.363
Co01	N00M	2.069
Co01	N00L	1.923
Co01	C00X	2.009
C00X	N00H	1.338
C00X	N00C	1.371

*Table 17: Selected bond lengths (A˚) of **Co4** structure.*

Atom 1	Atom 2	Atom 3	angles (◦)
N00K	Co01	N00L	173.5(2)
N00K	Co01	N00M	82.1(2)
N00K	Co01	N00Q	92.4(2)
N00K	Co01	C00S	110.1(2)
N00K	Co01	C00X	76.3(2)
N00L	Co01	N00M	94.3(2)
N00L	Co01	N00Q	81.9(2)
N00L	Co01	C00S	75.3(2)
N00L	Co01	C00X	107.2(2)
N00M	Co01	N00Q	85.8(2)
N00M	Co01	C00S	92.8(2)
N00M	Co01	C00X	158.4(2)
N00Q	Co01	C00S	157.0(2)
N00Q	Co01	C00X	94.1(2)
C00S	Co01	C00X	95.4(2)
C00W	N00C	C00X	113.8(4)
C00W	N00C	C015	130.0(4)
C00X	N00C	C015	116.2(4)
N00K	Co01	N00M	82.1(2)
N00K	Co01	N00Q	92.4(2)
N00K	Co01	C00S	110.1(2)

N00K	Co01	C00X	76.3(2)
N00L	Co01	N00M	94.3(2)
N00L	Co01	N00Q	81.9(2)
N00L	Co01	C00S	75.3(2)

*Table 18: Selected angles (◦) of **Co4** structure*

2.2.8. Hydrogenation of ketones

Homogeneous catalytic hydrogenation of carbonyl compounds is a pivotal organic transformation for the synthesis of alcohols in synthetic chemistry. Hydrogenation in general is one of the fundamental transformations in organic synthesis, and its industrial applications extend from the synthesis of pure chemicals to the pharmaceutical composition. To improve sustainability, more ecofriendly, inexpensive, and earth-abundant base metals should be employed to replace the precious metals that currently dominate the development of hydrogenation catalysts. As a result, cobalt, the 3d metal congener of rhodium and iridium, has attracted increasing interest in the development of hydrogenation catalysts. In fact, regarding the hydrogenation of ketones and aldehydes, the groups of Hanson, Kempe and Li have each reported well-defined pincer cobalt catalyst (Figure 81). However, the above-mentioned catalysts include amino-phosphine ligands. In the recent years, efforts have been made, in order to replace that type of ligands with more inexpensive NHC ligands. Liu on the other hand focused on the hydrogenation of ketones and aldehydes, using mostly catalysts formed *in situ*. The disadvantages with that method are that is not as predictable as using well defined complexes nor it is always easy to understand, which is the complex that catalyzes the reaction. We hope that our cobalt based catalysts will enable efficient and stereoselective hydrogenation of C=O bonds. [214–219]

Selected Examples of Hydrogenation of Ketones using Cobalt pincer Complexes

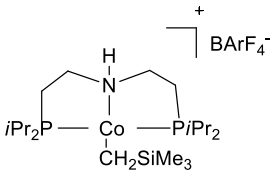

Hanson 2012

2 mol% cat.
THF, 4 bar H_2, 25-60 °C

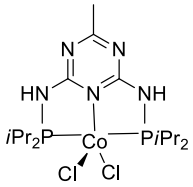

Kempe 2015

0.25-3 mol% cat.
THF, 20 bar H_2, 25 °C

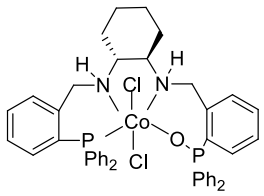

Li 2016

2 mol% cat.
THF, 60 bar H_2, 100 °C

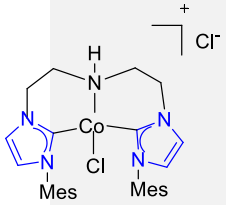

Liu 2019

0.033-5 mol% cat.
THF, 5- 50 bar H_2
60 °C

Transfer Hydrogenation of Ketones using Cobalt pincer Complexes

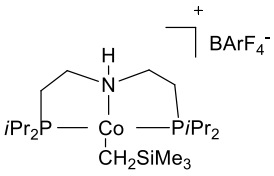

Hanson 2013

2 mol% cat.
THF, *i*PrOH, r.t., 24h

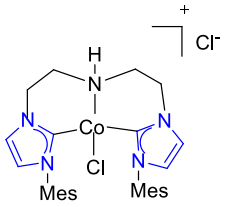

Yang 2019

0.033-5 mol% cat.
*i*PrOH, 5- 50 bar H_2
60 °C

Figure 81: Cobalt-catalyzed hydrogenation/transfer hydrogenation of ketones. [214–220]

In our laboratory, we synthesized two well defined Co^{II} pincer complexes, that we believe may act as good catalyst for the hydrogenation of ketones. They were synthesized according to the literature and are described further in the experimental section. (Figure 82) [184]

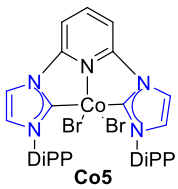

Co5

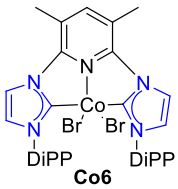

Co6

Figure 82: Co^{II} pincer complexes synthesized by Danopoulos group. [184]

2.2.8.1. General hydrogenation procedure

The reactions took place in 8 mL tubes, equipped with a magnetic stir bar. In an argon filled glove box, the cobalt catalysts **Co5** and **Co6** were inserted in the tubes with a specific catalytic load and in the cases of $NaO(CF_3)_2$, $NaO(CH_3)_2$, they were also added inside the glove box. Outside the glove box, acetophenone was used as the initial substrate (0.5 mmol, 59 μl). Initially, the catalyst was added, followed by the substrate and the base and 2 mL of solvent. The solvents that we used were previously distilled and degassed and the bases were freshly prepared. The reactions firstly took place in a vacuum line, with an argon atmosphere before inserting the tubes in the autoclave. The tubes were placed into a Parr Instruments autoclave, purged with argon which was then sealed, and purged with hydrogen gas. During the purging, the autoclave was cooled with the assistance of ice and salt, in order to avoid solvent leaks, with the sudden pressure that the H_2 atmosphere creates. The autoclave was heated then to 75 ^oC, with the assistance of an oil bath. After 16 hours, the autoclave was again cooled down to 0 ^oC before releasing the hydrogen gas. After removal of the volatiles, Et_2O was added and the solution was filtrated, through celite, in order to remove the catalyst and the access amount of base. The yield of the product compared to the starting material was determined by NMR.

2.2.8.2. Catalytic experiment design of hydrogenation

For the selection of the optimal reaction conditions, acetophenone was selected as the starting substrate. For the initial study time of the reaction, 16 h were selected, according to the literature. [214–219] The initial solvent that we tried was dry THF. The catalytic system was first examined, in the absence of a catalyst and a base, to see if atmosphere of 30 bar H_2, would cause partial hydrogenation. No change was observed *via* control in NMR, so we tried the same system, but different bases were added, but again no change was observed. (Table 19)

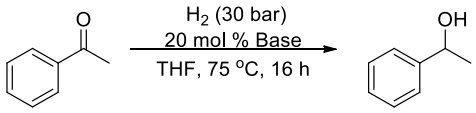

Entry	Catalyst	Solvent	Base	Time (h)	Temperature (°C)	(%)[a] NMR yield
1	-	THF	K_3PO_4	16	75	n.p.
2	-	THF	KOH	16	75	n.p.
3	-	THF	NaOMe	16	75	n.p.
4	-	THF	$NaO(CH_3)_2$	16	75	n.p.
5	-	THF	tBuOK	16	75	n.p.

Table 19: Hydrogenation experiments without catalytic loading, reaction conditions: 0.5 mmol acetophenone, 20 mol % base, 2 mL of THF under 30 bar H_2 at 75 °C for 16 h. n.p., no product

a: The (%) NMR yield was calculated by comparing the integrals of the substrate with the product.

We initially prepared two types of pincer NHC complexes on the basis of pyridene- and lutidine-derived pincer motifs that involve metal-ligand cooperation functionality (**Co5**, **Co6**). So, then we tried to add 5% catalytic loading of **Co5**, in the absence of bases, which have an activating role. A NMR yield of 3% product is observed. **Co5** was then studied for their catalytic activity at a low catalytic loading of 4%, in 2 mL of dry THF, with various bases. It seems that the optimal base is the strong base KOH. Then we compared the catalytic activity of **Co5** and **Co6**. It seems that **Co6** is better because in 20 mol % KOH, the NMR yield (%) was 32% compared to 28% of the **Co5**. (Table 20)

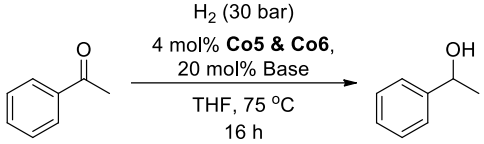

Entry	Catalyst	mol%	Solvent	Base	Time (h)	Temperature (°C)	NMR yield (%)[a]
1	**Co5**	4	THF	-	16	75	n.p.
2	**Co5**	4	THF	K_3PO_4	16	75	n.p.
3	**Co5**	4	THF	K_2CO_3	16	75	n.p.
4	**Co5**	4	THF	KOAC	16	75	n.p.

5	**Co5**	4	THF	tBuOK	16	75	6%
6	**Co5**	4	THF	$NaO(CF_3)_2$	16	75	2%
7	**Co5**	4	THF	$NaO(CH_3)_2$	16	75	13%
8	**Co5**	4	THF	NaOMe	16	75	23%
9	**Co5**	4	THF	KOH	16	75	28%
10	**Co6**	4	THF	KOH	16	75	32%

Table 20: Hydrogenation experiments with a variety of bases, reaction conditions: 0.5 mmol acetophenone, 4 mol % catalytic loading, 20 mol % base, 2 mL of THF under 30 bar H_2 at 75 °C for 16 h. n.p., no product

a: The (%) NMR yield was calculated by comparing the integrals of the substrate with the product.

In order to increase the efficiency and with the shortest possible reaction times, we increased the catalytic loading. The reactions were then carried out in the presence of 7.5 mol % cobalt catalyst under 30 bar H_2 and 75 °C. We also tried to change the solvents, in order to check if THF, was indeed the optimal solvent. The lutidine-pincer complex **Co6** performed the best with a 70% NMR ratio, in THF confirming that it is indeed the best solvent. (Table 21)

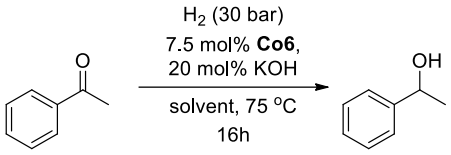

Entry	Catalyst	mol%	Solvent	Base	Time (h)	Temperature (°C)	NMR yield (%)[a]
1	**Co6**	7.5	toluene	KOH	16	75	15%
2	**Co6**	7.5	tert-butyl methyl ether	KOH	16	75	35%
3	**Co6**	7.5	2-methyl-THF	KOH	16	75	50%
4	**Co6**	7.5	THF	KOH	16	75	70%

Table 21:Hydrogenation experiments with a variety of solvents, reaction conditions: 0.5 mmol acetophenone, 7.5 mol % catalyst, 20 mol % KOH, 2 mL of solvent under 30 bar H_2 at 75 °C for 16 h.

a: The (%) NMR yield was calculated by comparing the integrals of the substrate with the product.

More experiments need to take place in order to optimize the reaction. In addition to that type of hydrogenation, we also prepared some experiments for transfer hydrogenation. Direct hydrogenation with pressurized H_2 gas and atomic transfer hydrogenation are the two applicable hydrogenation techniques. Transfer hydrogenation refers to the technique of adding hydrogen to a molecule from a source other than the H_2 gas and is a powerful and convenient technique for producing various hydrogenated compounds. It is an attractive alternative to direct hydrogenation and has recently become the focus of research as far as hydrogenation is concerned. The main reasons for this are: a) hydrogen transport does not require potentially hazardous H_2 compressed gas hazardous experimental devices b) atomic hydrogen donors are readily available, inexpensive and easy and safe to use. In fact, transfer hydrogenation of ketones and aldehydes, has been achieved by the groups of Hanson and Yang using well-defined pincer cobalt catalysts and *i*-PrOH as the hydrogen source (Figure 81). [102,211,214,217,219–221]

2.2.8.3. General transfer hydrogenation procedure

In an argon filled glove box, the cobalt catalyst (**Co5**) was inserted inside two-neck round bottom flasks, along with a stirring bar. **Co5** was inserted with 3% catalytic loading and in the cases of $NaO(CF_3)_2$, $NaO(CH_3)_2$, they were also added inside the glove box. After removing the flask from the glove box, acetophenone was used as the initial substrate (0.5 mmol, 59 μl). Initially, the catalyst was added, followed by the substrate and the base and 5 mL of *i*-PrOH. The isopropanol used was previously distilled and degassed and the bases were freshly prepared. The reactions firstly took place in a vacuum line, with an

argon atmosphere. The flasks were heated then to 75 ºC, with the assistance of an oil bath. After 24 hours, the flask was let to cool down to r.t.. After removal of the volatiles, Et_2O was added and the solution was filtrated through celite, in order to remove the catalyst and the access amount of base. The yield of the product compared to the starting material was determined by NMR.

2.2.8.4. Catalytic experiment design of transfer hydrogenation

For the selection of the optimal reaction conditions, acetophenone was selected again as the starting substrate. For the initial study time of the reaction, 24h were selected, according to the literature. The solvent and the source of hydrogen that we tried was dry *i*-PrOH. The catalytic system was first examined, in the absence of a catalyst and a base, to see if *i*-PrOH alone, would cause partial hydrogenation. No change was observed *via* control in NMR, so we tried the same system, but different bases were added, but again no change was observed. (Table 22)

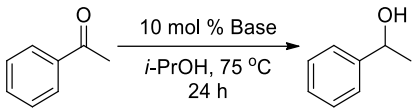

Entry	Catalyst	Solvent	Base	Time (h)	Temperature (ºC)	NMR yield (%)[a]
1	-	*i*-PrOH	K_3PO_4	24	75	n.p.
2	-	*i*-PrOH	KOAC	24	75	n.p.
3	-	*i*-PrOH	KOH	24	75	n.p.
4	-	*i*-PrOH	$NaO(CF_3)_2$	24	75	n.p.
5	-	*i*-PrOH	$NaO(CH_3)_2$	24	75	n.p.
6	-	*i*-PrOH	NaOMe	24	75	n.p.

Table 22: Transfer hydrogenation experiments without catalytic loading, reaction conditions: 0.5 mmol acetophenone, 10 mol % base, 5 mL of i-PrOH at 75 °C for 24 h. n.p., no product

a: The (%) NMR yield was calculated by comparing the integrals of the substrate with the product.

Then we tried to add 3% catalytic loading of **Co5**, in the absence of bases, which again is assumed that they create in situ the active catalyst, but no product was observed. **Co5** was then studied for its catalytic activity at a low catalytic loading of 3%, in 5 mL of dry *i*-PrOH, with various bases. It seems that the optimal base is the strong base NaOMe. Most of the bases didn't give any product or only traces of it, with the exception of $NaO(CH_3)_2$ that gave 25% NMR yield and NaOMe, which gave the very promising result of 85% NMR yield. More experiments need to be done in order to understand the nature of our catalyst as well as its mechanism. (Table 23)

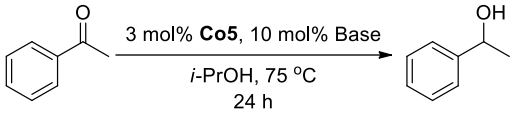

Entry	Catalyst	mol%	Solvent	Base	Time (h)	Temperature (°C)	NMR yield (%)[a]
1	**Co5**	5	*i*-PrOH	-	24	75	n.p.
1	**Co5**	3	*i*-PrOH	K_3PO_4	24	75	n.p.
2	**Co5**	3	*i*-PrOH	K_2CO_3	24	75	n.p.
3	**Co5**	3	*i*-PrOH	KOAC	24	75	n.p.
4	**Co5**	3	*i*-PrOH	$NaO(CF_3)_2$	24	75	4%
5	**Co5**	3	*i*-PrOH	tBuOK	24	75	5%
6	**Co5**	3	*i*-PrOH	KOH	24	75	6%
7	**Co5**	3	*i*-PrOH	$NaO(CH_3)_2$	24	75	25%
8	**Co5**	3	*i*-PrOH	NaOMe	24	75	85%

Table 23: Transfer hydrogenation experiments with a variety of bases, reaction conditions: 0.5 mmol acetophenone, 3 mol % catalyst, 10 mol % base, 5 mL of i-PrOH at 75 °C for 24 h. n.p., no product

a: The (%) NMR yield was calculated by comparing the integrals of the substrate with the product.

In summary, we synthesized two phosphine-free Co-NHC pincer complexes **Co5** and **Co6**, which showed promising results in both hydrogenation and transfer hydrogenation of ketones. A broad set of ketones including aromatic,

aliphatic, and heterocyclic ones need to be tested in order to have a full picture.

2.2.8.5. Proposed mechanism

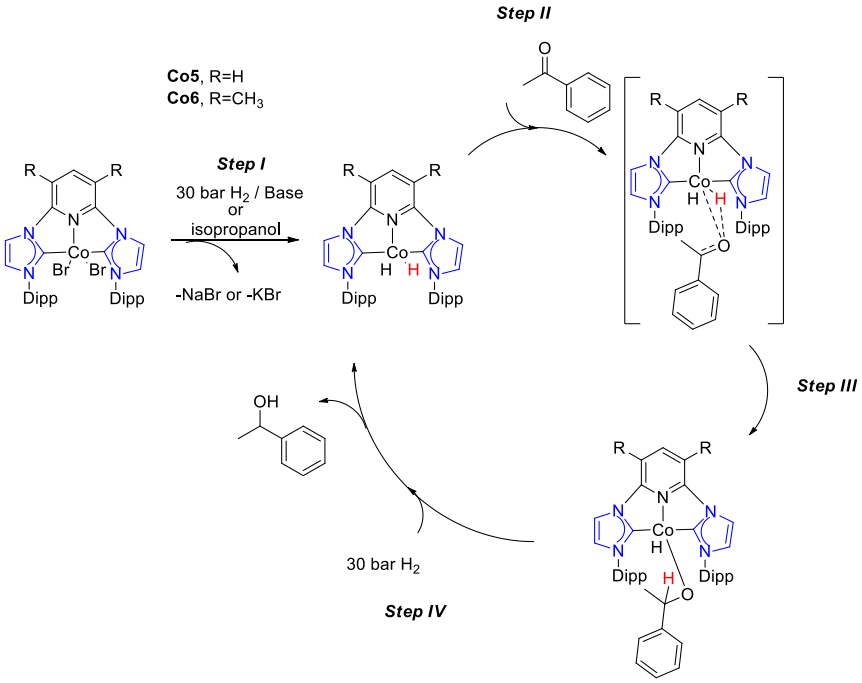

*Figure 83: Proposed Inner sphere mechanism of homogenous catalyzed hydrogenations using **Co5** and **Co6** as precatalysts.* [215,217,222]

The figure shows a proposed catalytic cycle for the catalytic system developed in the context of this work, based on previous literature on hydrogenation. In step I, the Co^{II} complex is the activated by replacing one or both of its two halides with hydrides, with the assistance of Bases. In hydrogenation, the source of hydrogen is H_2 gas and in the transfer hydrogenation, it is *i*-PrOH. In step II, the oxygen of the carbonyl forms a bond with the Co^{II} complex, forming in situ a Co^{III} intermediate complex. In step III, eventually one of the Co-H bonds breaks and the Hydride allows the substrate to reduce its carbonyl group. In

step IV, the Co^{II} complex, which is considered to be the active catalyst, is regenerated, in the presence of a continuous source of hydrogen, due to the outputs of the substrate in the form of antistatic hydrogenated alcohol. Due to the lack of mechanistic experiments, our hypothesis is that those complexes, with the assistance of bases, replace their -Br groups to form *in situ* the active catalyst, that is maybe the corresponding hydride, based on the experiments by the Kempe group (Figure 83).[215,222]

2.3. Perspectives

In conclusion, a series of cobalt-based complexes were synthesized bearing pincer type ligands, which are of synthetic, magnetic, and catalytic interest. The study of catalytic reactions with abundant 3d metals in the earth's solid crust is a modern direction of chemistry aimed at the long-term viability of catalytic transformations and the synthetic processes associated with them. In recent years there has been an increase in the use of 3d first-row metals for catalytic processes. A large part of these reactions involves the hydrogenation of alkenes or alkynes and rarer ketones, aldehydes, nitriles, esters and imines. In the complexes that we synthesized, it is assumed that an amount of base, helps to activate the catalyst by creating the corresponding hydride in situ. Our catalysts gave promising results, both towards hydrogenation using H_2 gas, as well as in transfer hydrogenation, but optimization in both cases is needed, as well as calculation of the isolated yield of the products. The development of new catalytic protocols is necessary for the recognition of the possibilities, but also the limitations of these reactions. We also plan to use other complexes that we synthesized in the above catalytic reactions. In addition, the utilization of these complexes in hydrogenation opens the way for further research with the aim of developing its enantioselective version, possibly with the use of asymmetric complexes. For example, the use of **Co13** which has both a NHC and a phosphine, could be interesting in these types of reactions. One of our future goals is to test how effective they are with the hydrogenation of other ketones, as well as testing different, more challenging substrates, like esters. Comparative study of different 3d metal catalytic complexes (*i.e.* Fe, Mn) in an

Με σχόλια [GV1]: ΤΙ ΣΧΕΣΗ ΕΧΟΥΝ ΑΥΤΑ ΤΑ ΣΥΜΠΛΟΚΑ ΜΕ ΑΣΥΜΜΕΤΡΗ ΣΥΝΘΕΣΗ??? ΥΠΑΡΧΕΙ ΚΑΠΟΙΑ ΑΣΥΜΜΕΤΡΙΑ??? ΕΑΝ ΟΧΙ ΠΡΕΠΕΙ ΝΑ ΑΦΑΙΡΕΘΕΙ ΑΥΤΗ Η ΠΡΟΤΑΣΗ…

environment of pincer type ligands with NHC donors needs also to take place. Except from the hydrogenation reactions, according to the recent literature (*i.e*. Chirik, Thomas and Hout group) there are similarities of our complexes with catalysts that were used in hydrosilylation, hydroborylation, borylation, C-H activation, as well as C-C coupling. In addition, three of our synthesized complexes (**Co4, Co6, Co8)** are being studied *via* electrochemistry in order to confirm their potential electrocatalytic efficiency. It is also a possibility that these molecules have biological activity. Lastly, the synthesized complexes need to be crystallized, in order to have the full picture of their structures, thus their properties.

2.4. Experimental Section General Considerations

2.4.1. General experimental part

General information on reactions and solvents

All of the reagents and solvents used were recently purchased from Sigma-Aldrich, Fluka, Merck, Fluorochem and Alfa Aesar. All metal salts used were anhydrous and their purity was equal to or higher than 98%.

Unless otherwise stated, all reactions and subsequent manipulations were performed under inert atmosphere (dinitrogen) atmosphere using standard Schlenk line or glovebox techniques. Solvents were obtained water- and oxygen-free stored over molecular sieves 3 Å under nitrogen atmosphere. Concentrations of the solvents were made under reduced pressure in a rotary concentrator.

NMR spectra were recorded on a Bruker Avance 200 (^{1}H-NMR, 199.9 MHz; ^{13}C-NMR, 50.3 MHz), Bruker Avance DPX 400 (^{1}H-NMR, 400.13 MHz; ^{13}C-NMR, 100.53 MHz; ^{31}P-NMR, 162 MHz) in 298K and chemical shifts are reported relative to the residual signal of the deuterated solvent. The chemical displacements of the NMR spectra are expressed in ppm, while the order of presentation of the chemical displacement data in the ^{1}H-NMR spectra is as

follows: chemical displacement, multiplicity (s, simple, d, double, t, triple, q, quadruple, q, quadruple multiple), coupling constants in Hertz (Hz), and number of protons. Data from published literature were used to identify the peaks in the ^{1}H-NMR spectra, comparisons were made with precursors, and calculations were made using NMR spectrum prediction programs. Particularly in the ^{1}H-NMR spectra, peaks were identified for which this was possible, while the remaining peaks could not be correctly identified without the presence of additional spectroscopic data. An important observation is that, especially in the ^{1}H-NMR spectra, peaks occurring at 0.86 and 1.25 ppm in some ^{1}H-NMR spectra are attributed to grease protons, and / or petroleum ether residues, which are difficult to remove due to oily and increased viscosity of some compounds.^{13}C-NMR spectra are broad-band proton-decoupled (^{13}C{^{1}H}) Assignment of the ^{13}C-NMR data was supported by ^{13}C,^{1}H correlation experiments. Chemical shifts are listed in parts per million (ppm) and were determined relative to internal C_6D_5H (^{1}H, δ = 7.16; C_6D_6) and natural-abundance carbon resonances C_6D_6 (^{13}C, δ = 128.1; C_6D_6).

For High Resolution Mass spectrometry (HRMS), the samples were taken on a QTOF maxis Impact spectrometer (Bruker), in which the ionization of the compounds was done by electrospray ionization (ESI). GC / MS spectra were obtained on a Shimadzu R GCMS-QP2010 Plus Gas Chromatograph Mass Spectrometer using a MEGA R column (MEGA-5, FT: 0.25mm, ID: 0.25mm, L: 30m, T max: 350oC, Column ID # 11475).

2.4.2. Thin layer chromatography

The control of the progress of the various reactions, as well as the investigation of the elution sequence of the substances during the column chromatography, was carried out with Thin Layer Chromatography (TLC), for which aluminum sheets with 60 mm silicon and 0.2 mm silica gel were used, bearing fluorescent indicator F254 (Merck, Art.5714). The thin layer chromatography technique was additionally used to confirm the purity of various products (in combination with ^{1}H, ^{13}C-NMR, GC / MS and HRMS assays). UV lamps (λ = 254 nm and 365

nm) and / or aqueous potassium permanganate solution were used to display the chromatograms.

2.4.3. Column chromatography

The prepared products were purified by column chromatography. For effective elution of the compounds, air column pressure (flash column chromatography) was applied. Merck silica gel 60 (230-400 mesh) was used as a filler in the chromatographic columns. For the chromatographic separation of the various products, gradient column chromatography was performed.

2.4.4. FT-IR

Infrared (FT-IR) spectra were recorded as a function of the wavelength on an IRAffinity-1 spectrophotometer, SHIMADZU, in the range 4000 – 400 cm^{-1} using Nujol oil.

2.4.5. X-ray crystallography

The X-ray crystallography method is a basic tool for the identification and determination of both inorganic metal complexes and large biomolecules, organic or pharmaceutical solid compounds. It is an analytical technique that uses X-rays to determine the position of atoms in a crystalline solid with precision and consequently the overall structure of the system to be studied.
A monocrystal being studied consists of a number of atoms, among which there is a finite number of them, which is repeated and can be a molecule or a part of an extended structure. The basic structural element is the unit cell which is characteristic and different for each structure. The unit cell is a geometric "box" in which atoms are in specific positions. Repetition of the unit cell in space, without rotation and gaps, results in the creation of a perfect single crystal which is also desirable for measurement for X-ray diffraction. The shape that the unit cell of the crystalline solid can have can be as follows in order of decreasing symmetry: cubic, square, orthorombic, triangular, hexagonal, single and triple.

Diffraction is the phenomenon in which an elastic scattering takes place, which means that the energy of the incident radiation is the same as the energy of the diffused radiation. From 1912 it became known by the physicist Laue that monocrystals diffuse X-rays. X-ray radiation is an electromagnetic radiation with a wavelength ranging between 100−0.01 nm and thus is suitable for investigating atomic information. This wavelength corresponds to frequencies 1015 - 1019 Hz or photon energies 10 - 100 KeV. Wave-shaped radiation is an electric field oscillator, causing oscillation in charged particles located in the environment that radiates. Thus, in turn, the electrons behave as oscillators of the incoming radiation, thus acting as a source of radiation, scattering a part of it. According to electromagnetic theory, a pulsating dipole acts as a source of electromagnetic waves. Therefore, each electron in the crystal acts as a source of radiation with the scattered beams being recorded by the film or detector as visible spots, thus defining a point diffraction pattern as the crystal gradually rotates. Thus, the radiation that strikes at a certain angle at the positions of the atoms of the crystal, is diffracted by the electron density of the atoms in different directions and is recorded. The amplitude of the diffused radiation is proportional to the number of electrons in the cloud of their electron density. The final result of an experimental measurement by the method of crystallography is not a real picture of the atoms, but a map of the distribution of electronic density in the space corresponding to each atom.

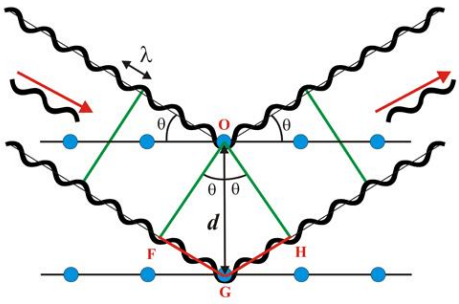

Figure 84: Reflection of Bragg's law. The diffracted X-rays will exhibit an amplifying contribution when the distance between the waves has a phase difference an integer multiple of the wavelength.

When the phase difference of the electron oscillation is an integer multiple of the wavelength then we say that we have a constructive interference. If the phase difference is 180º then we have a destructive interference. The

contribution between the waves increases and decreases depending on the scattering angle.

Due to the periodicity between the atoms, only the reflections that are in the same phase with each other will appear. These are displayed at specific angles for a given relative arrangement of crystal and incident radiation. Based on the above characteristics, the law of crystallography, known as Bragg's law, was formulated as follows:

$$n\lambda = 2 \times d \times \sin\vartheta$$

In general, for each lattice family of levels (each having a unique distance d between adjacent planes) corresponds to a Bragg reflection, thus collecting different values of the Bragg reflection from different scattering angles 2ϑ of the single crystal. Then it is said that the reflection is indexed. The indexing gives the parameters of the unit cell, its lengths and angles, as well as the space group it belongs to. The solution of the structure will require data from many reflections at different angles. The data is ultimately captured as an image through a mathematical analysis called the Fourier transform.[223–225]

The data were collected on a X-Ray single crystal diffractometer by Associate Professor Bethanis at the Agricultural University of Athens.

2.4.6. Syntheses of salts

Synthesis of sodium isopropoxide

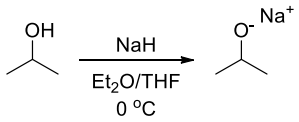

In a suspension of NaH (0.288 g, 0.012 mol) in Et_2O (5 mL) in 0 °C, dry isopropanol was added dropwise (1 mL). After gas evolution stops, THF was added till the suspension becomes clear. The volatiles were removed under reduced pressure, and the white solid was washed with copious amounts of pentane. (Yield: 0.613 g, 61%)

Synthesis of sodium 1,1,1,3,3,3-hexafluoropropan-2-olate

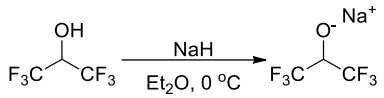

In a suspension of NaH (0.553 g, 5.26 mmol) in Et_2O (5 mL) in 0 °C, dry sodium 1,1,1,3,3,3-hexafluoropropan-2-ole was added dropwise (0.55 mL, 5.26 mmol). After gas evolution stops the solution becomes clear. The volatiles were removed under reduced pressure, and the oily residue was triturated with pentane to become a white solid. (Yield: 0.690 g, 69%)

2.4.7. Syntheses of organic ligands

Synthesis of 2,6-bis(bromomethyl)pyridine (L1)

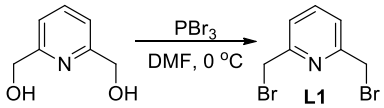

To a solution of 2,6-dihydroxymethylpyridine (2.80 g, 2.01 mmol) in DMF (15 mL) was added dropwise at 0 °C, PBr_3 (4.35 mL, 46.3 mmol). The mixture was stirred at room temperature overnight and then water was added (20 mL). After extraction with Et_2O (3 × 100 mL), the organic layer was dried with $MgSO_4$ and the solvent was removed under reduced pressure. 2,6-dibromomethylpyridine **L1** was obtained as a pure white solid (Yield: 4.73 g, 89%).[204]

L1: ^{1}H-NMR (400 MHz, $CDCl_3$): δ= 7.64 (t, *J* = 7.7 Hz, 1H), 7.31 (d, *J* = 7.7 Hz, 2H), 4.47 (s, 4H) ppm. ^{13}C-NMR ($CDCl_3$, 100.63 MHz): δ = 156.73,138.11, 122.79, 33.45 ppm.

Synthesis of 2,6-diisopropylphenylimidazole (L5a)

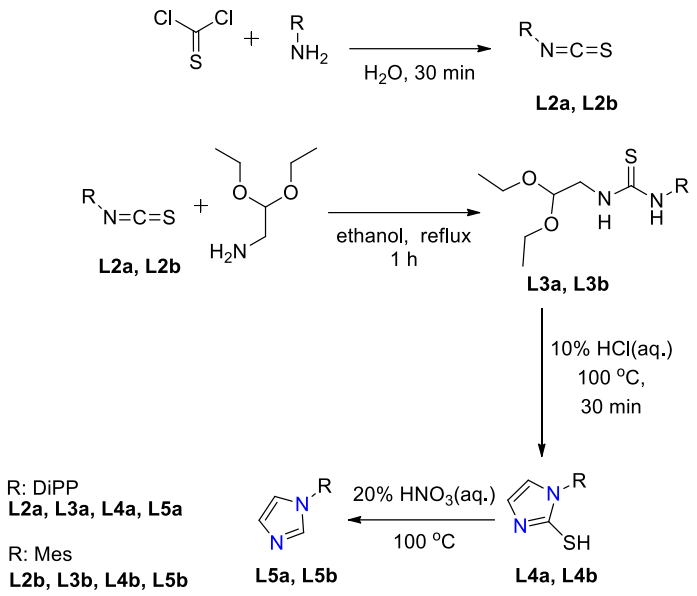

In a two-liter, two neck, round bottom flask, 2,6 diisopropylamine (18.8 mL, 0.1 mmol) was slowly added over a period of 30 minutes into a mixture of thiophosgene (9.2 mL, 0.11 mmol) and water at room temperature with rigorous mechanical stirring. After the completion of addition, the stirring continued for 30 minutes. The resulting solution was extracted with $CHCl_3$ (3 × 30 mL) and the solvent was removed under reduced pressure to get a crude isothiocyanate (**L2a, L2b**). The crude isothiocyanate was used for the next step without further purification.

The formed crude isothiocyanate (**L2a, L2b**) was slowly added into a solution of aminoacetaldehyde diethyl acetal (14.5 mL, 0.1 mmol) and ethanol (100 mL) was added dropwise over the period of 30 min. The reaction mixtures were heated up to reflux until the isocyanate disappeared (approximately 1h, monitored by TLC). After that we let the solution to cool to room temperature. The solvent was evaporated to obtain the crude aryl diethoxyethylthioureas (**L3a, L3b**). Then the oily product was mixed with HCl (1 N, 30 mL) solution. The reaction mixture warmed to 100 °C and stirred for 30min and let to reflux. The formed precipitate was collected from filtration, inserted in a one-liter round bottom flask and then treated with 20% of HNO_3 solution at 100 °C for 10 mins.

The reaction mixture was cooled down to room temperature till the production of brown gas stops. Then it is treated with an aqueous solution of NH_3 until it reaches to pH 10. A fraction of each imidazole product precipitated at this stage and was collected by filtration. The filtrates were extracted with CH_2Cl_2 (3 × 50 mL), dried over $MgSO_4$ to obtain the rest of the material. The combined solid portions were purified by recrystallization of ethyl acetate and/or hexanes. (Yield: 17 mg, 75%). [199,200]

L5a: ^{1}H-NMR (400 MHz, $CDCl_3$): δ = 7.49–7.36 (m, 2 H), 7.28–7.14 (m, 3 H), 3.44 (s, 1 H), 2.45–2.32 (m, 2 H), 1.11 (d, *J* = 6.9 Hz, 12 H) ppm.

^{13}C-NMR (100.63 MHz, $CDCl_3$): δ 146.5, 138.4, 129.8, 129.3, 123.7, 121.5, 28.1, 24.3.

Synthesis of α,α'-bis-[3-(mesityl)imidazolium]lutidine dibromide (L6b)

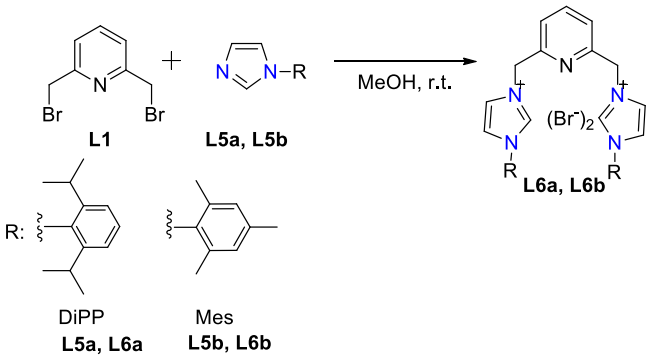

In a 2-neck flask were weighed 2,6-bis(bromomethyl)pyridine (**L1**) (0.485 g, 1.8 mmol) and 1-mesityl-*1H*-imidazole (0.750 g, 4 mmol) in 20 mL of MeOH at room temperature. 2,6-bis(bromomethyl)pyridine was neutralized with an aqueous solution of sodium carbonate, the neutralized solution was extracted using diethyl ether (3 × 50 mL) at 0 °C, dried with magnesium sulfate and filtered. The filtrate was added slowly into the solution of 1-mesitylimidazole (3.5 g, 17.5 mmol) in methanol (100 mL) at 0 °C. In order to remove the starting material salt, we add ether and let it precipitate overnight. After precipitation in the fridge,

we received the product as brown oil. We thought as we mentioned before that there is moisture and maybe some staring material. Therefore, we removed the solvent mixture with the help of a pipette and then dry it in rotavapor and followed by azeotropic drying due to the presence of moisture. Toluene was used as a solvent due to its high boiling point. The final product was obtained after removing the moisture and the solvent under reduced pressure and wash with pentane. (Yield: 0.9 g, 79%)[198,205]

L6b: ^{1}H-NMR (400 MHz, $CDCl_3$): δ = 10.57 (s,1H, 2-imidazolium H), 8.58 (s, 1H, 4-imidazolium H), 7.69 (s, 2H, 4-imidazol-2-ylidene H), 7.65 and 7.86 (d, 2H, and t, 1H, pyridine ring protons), 7.18 (s, 2H, 5-imidazol-2-ylidene H), 6.97 (s, 4H, $C_6H_2Me_3$), 6.07 (s, 2H, CH_2), 2.15 (s, 3H, *p*-CH_3), and 2.03 (s, 6H, *o*-CH_3) ppm.

^{13}C-NMR (100.63 MHz, $CDCl_3$): δ 153.1, 141.2, 138.98, 137.83, 133.9, 130.5, 129.75, 124.6, 123.8, 123.19, 53.40, 20.98, and 17.55 ppm.

Synthesis of 2.6-di(*1H*-imidazol-1-yl)pyridine (L7)

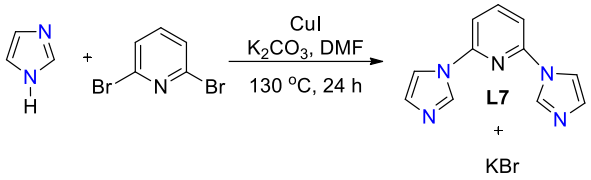

A mixture of CuI (100 mg, 0.52 mmol), K_2CO_3 (1153 mg, 8.34 mmol), imidazole (431 mg, 6.33 mmol) and 2.6-dibromopyridine (500 mg, 2.1 mmol) in dry DMF 5 mL was stirred at r.t. for 30 min, in a two-neck 100 mL bottom flask and allowed to be stirred at 130 °C for 24 h. After completion, it was let to cool to r.t. Later CH_2Cl_2 (40 mL) added and washed with water (2 x 20 mL) by solvent extraction procedure. The organic layer was collected and concentrated under reduced pressure. In the resulting solution we add a non-polar solvent and we let it in fridge overnight. The next morning, the white solid was collected. (Yield: 337 mg, 76%) [206,207]

L7: ^{1}H-NMR (400 MHz, $CDCl_3$,) δ = 41 (s, 2H), 8.00 (t, J = 8.0 Hz, 1H), 7.70 (s, 2H), 7.32 (d, J = 8.0 Hz, 2H), 7.26 (s, 2H) ppm.

^{13}C-NMR (100.63 MHz, $CDCl_3$) δ: 148.2, 142.0, 134.9, 131.0, 116.0, 109.5 ppm.

Deprotonation of ligand (^{Cy}PNC^{im})Br·HBr (L8 & L9)

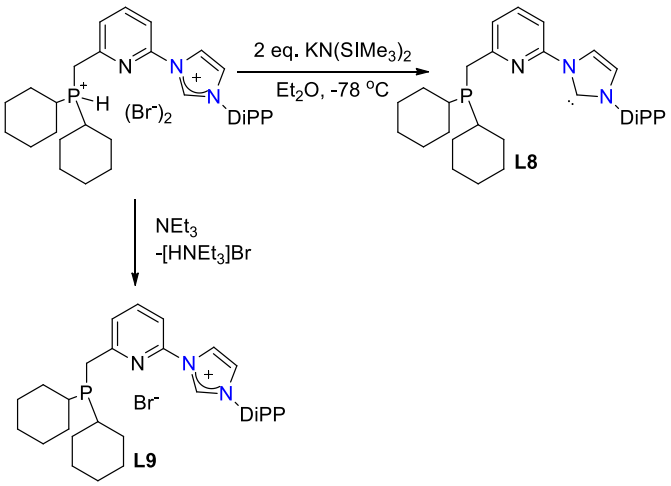

To a suspension of (^{Cy}PNC^{im})Br·HBr (200 mg, 0.30 mmol) in Et_2O precooled at -78 °C, using dry ice, was added a solution of 2 eq. $KN(SIMe_3)_2$ (119.7 mg, 0.60 mmol) in Et_2O. The resulting suspension was allowed to reach r.t. and was stirred for several hours, giving a yellow solution. Removal of volatiles under reduced pressure, extraction of the resulting solid with toluene filtration and evaporation of the solvent gave a yellow solid. Total conversion was confirmed by ^{31}P and the product was obtained. (Yield: 113.2 mg, 73%) [100,209]

L8: ^{1}H-NMR (400.13 MHz, C_6D_6): δ =8.61 (d, J = 8.1 Hz, 1H, $CH_{pyr.}$), 8.49 (d, J= 1.3 Hz, 1H, $CH_{imid.}$), 7.27 (t, J = 7.7 Hz, 1H, CH_{DiPP}), 7.17-7.10 (m, 3H, $CH_{pyr.}$ + CH_{DiPP}), 6.91 (d, J = 7.6 Hz, 1H, $CH_{pyr.}$), 6.65 (d, J = 1.3 Hz, 1H, $CH_{imid.}$), 2.98 (s, 2H, CH_2P), 2.90 (sept, 2H, $CH(CH_3)_2$), 1.89-1.78 (m, 4H, Cy), 1.74-1.55 (m,

8H, Cy), 1.39-1.10 (m, 10H, Cy), 1.19 (d, *J* = 6.9 Hz, 6H, $CH(CH_3)_2$), 1.08 (d, *J* = 6.9 Hz, 6H, $CH(CH_3)_2$) ppm.

^{13}C-NMR (100.62 MHz, C_6D_6): *δ*= 219.8 (C_{NHC}), 160.0 (d, $C_{arom.}$), 153.6 ($C_{arom.}$), 146.3 ($C_{arom.}$), 138.8 ($C_{arom.}$), 138.5 ($CH_{arom.}$), 129.2 ($CH_{arom.}$), 123.8 ($CH_{arom.}$), 122.8 ($CH_{arom.}$), 121.1 (d, $CH_{arom.}$), 116.4 ($CH_{arom.}$), 111.5 ($CH_{arom.}$), 34.1 (d, CH Cy), 32.3 (d, CH_2P), 30.3 (d, CH_2 Cy), 29.6 (d, CH_2 Cy), 28.6 ($CH(CH_3)_2$), 27.7 (d, CH_2 Cy), 27.6 (d, CH_2 Cy), 26.9 (CH_2 Cy), 24.4 ($CH(CH_3)_2$), 24.1 ($CH(CH_3)_2$).

^{31}P-NMR (161.98 MHz, C_6D_6): δ 3.3 ppm

L9: ^{1}H-NMR (400 MHz, $CDCl_3$,): δ= 11.28 (t, 1H, $CH_{imid.}$), 9.16 (t, 1H, $CH_{imid.}$), 8.95 (d, 1H, $CH_{pyr.}$), 7.98 (t, 1H, $CH_{pyr.}$), 7.63 (t, 1H, *p*-CH_{DiPP}), 7.45 (d, 1H, $CH_{pyr.}$), 7.41 (t, 1H, $CH_{imid.}$), 7.40 (d , 2H, *m*-CH_{DiPP}), 3.05 (d, 2H, CH_2P), 2.44 (sept, 2H, $CH(CH_3)_2$), 1.84-1.72 (m, 8H, Cy), 1.71-1.58 (m, 4H, Cy), 1.33-1.06 (m, 10H, Cy),1.28 (d ,6H, $CH(CH_3)_2$),1.20 (d, 6H, $CH(CH_3)_2$), *J* =6.8 Hz).

^{13}C-NMR ($CDCl_3$, 100.63 MHz): δ= 162.4 (d, $C_{arom.}$), 145.63 ($C_{arom.}$), 145.58 ($C_{arom.}$), 141.0 ($CH_{arom.}$), 136.2 ($CH_{arom.}$), 132.4 ($CH_{arom.}$),130.5 ($C_{arom.}$), 125.8 (d ,$CH_{arom.}$), 125.4 ($CH_{arom.}$), 125.1 ($CH_{arom.}$), 120.8 ($CH_{arom.}$), 112.9 (d, $CH_{arom.}$), 34.0 (d, CH Cy), 32.0 (d, CH_2P), 30.3 (d, CH_2 Cy), 29.6 (d, CH_2 Cy), 29.2 ($CH(CH_3)_2$), 27.64 (d, CH_2 Cy), 27.56 (d, CH_2 Cy), 26.9 (d, CH_2 Cy), 24.4 ($CH(CH_3)_2$), 24.3 ($CH(CH_3)_2$).

^{31}P-NMR (161.98 MHz, CD_2Cl_2): δ 6.4 (s).

Synthesis of L12a and L12b

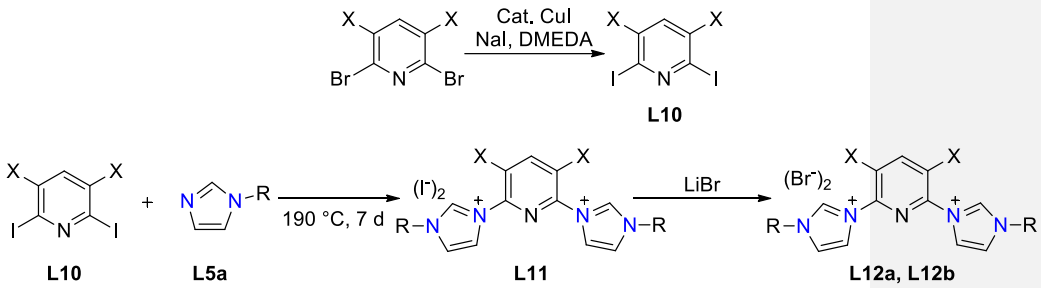

R = DiPP

X=H, **L12a**,
X= CH_3, **L12b**

In a Schlenk flask we add NaI, DMEDA in the presence of catalytic amount of CuI in order to achieve halogen exchange of 2,6-dibrobo-3,5-dimethylpyridine (1 g, 3.77 mmol) (**L10**) (Yield: 1,13 g, 83%). Quaternisation of compound **L10** with 3 molar equivalents of DiPP-imidazole (**L5a**) (2.15 g, 9.39 mmol) resulted in clean conversion to the di-quaternised product **L11** after 7 days at 190 °C. Compound **L11** was isolated as a hygroscopic pale grey powder by precipitation with Et_2O from a DCM solution of the reaction product. Then after addition of LiBr, product **L12b** was received as a beige powder. (Yield: 1.6 g, 73%)[210]

L12b: ^{1}H-NMR (400 MHz, $CDCl_3$) δ = 10.95 (2H, s, imidazolium CH), 9.14 (s, 2H), 7.24 (br s, 4H, Ar), 2.62 (s, 6H, py-Me), 2.33 (septet, 4H, Ar), 7.97 (s, 1H, Ar), 7.47 (t, 2H, *J* = 6.0 Hz, Ar), 7.33 (2H, s, Pr CH), 1.18 and 1.12 (d, each 12H, J = 6.5 Hz, iPr CH_3) ppm.

^{13}C-NMR (100.63 MHz, $CDCl_3$,): 147.51 (CH, Ar), 144.79, 141.82 (C, Ar), 138.24, 131.83 (CH, Ar), 130.97, 129.53, 128.71, 127.91 (C, Ar), 124.90, 124.46, 124.01 (CH, Ar), 28.56 (CH, iPr), 24.22, 23.82 (CH3, iPr), 18.06 (CH3, py-Me) ppm.

Synthesis of 3-([2,2'-bipyridin]-6-yl)-1-(2,6-diisopropylphenyl)-*1H*-imidazol-3-ium bromide (L13)

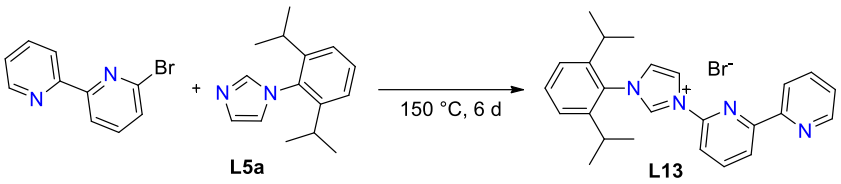

L5a L13

6-Bromo-2,2-bipyridine (1.40 g, 5.95 mmol) and 1-(2,6-diisopropylphenyl)imidazole (1.46 g, 6.38 mmol) were placed in a glass ampoule which was sealed under vacuum. This was completely immersed in an oil bath at 150 °C for 6 d. After cooling to r.t, the ampoule was opened, and the brown residue was dissolved in dichloromethane. After evaporation of the solvent, the product was stirred with diethyl ether at 0 °C for several hours, the solvent removed by filtration and the solid dried in vacuo. This gave the product **(L13)** as a brown solid (Yield: 2.27 g, 82%).[198]

L13: ^{1}H-NMR (300 MHz, C_6D_6): δ = 8.66 (d, *J* = 8.2 Hz, 1 H, aromatic CH), 8.48–8.56 (m, 3 H, aromatic CH), 8.28 (d, *J* = 1.7 Hz, 1 H, imidazole backbone CH), 7.19–7.32 (m, 5 H, aromatic CH), 6.74 (ddd, *J* = 1.1, 4.7, 7.4 Hz, 1 H, aromatic CH), 6.66 (d, *J* = 1.6 Hz, 1 H, imidazole backbone CH), 2.94 [sept, *J* = 6.9 Hz, 2H, $CH(CH_3)_2$], 1.22 (d, *J* = 6.8 Hz, 6 H, Me), 1.13 (d, *J* = 6.9 Hz, 6 H, Me), ppm.

^{13}C-NMR (75.45 MHz, C_6D_6): δ = 22.82 (Me), 23.17 (Me), 27.36 [$CH(CH_3)_2$], 113.80 (aromatic CH), 115.13 (aromatic CH), 117.63 (aromatic CH), 119.61 (aromatic CH), 121.56 (aromatic CH), 122.55 (aromatic CH), 127.07 (aromatic CH), 127.98 (aromatic CH), 135.19 (aromatic CH), 138.07 (aromatic CH), 145.01 (aromatic C), 148.27 (aromatic CH), 152.34 (aromatic C), 153.46 (aromatic C), 154.98 (aromatic C) ppm.

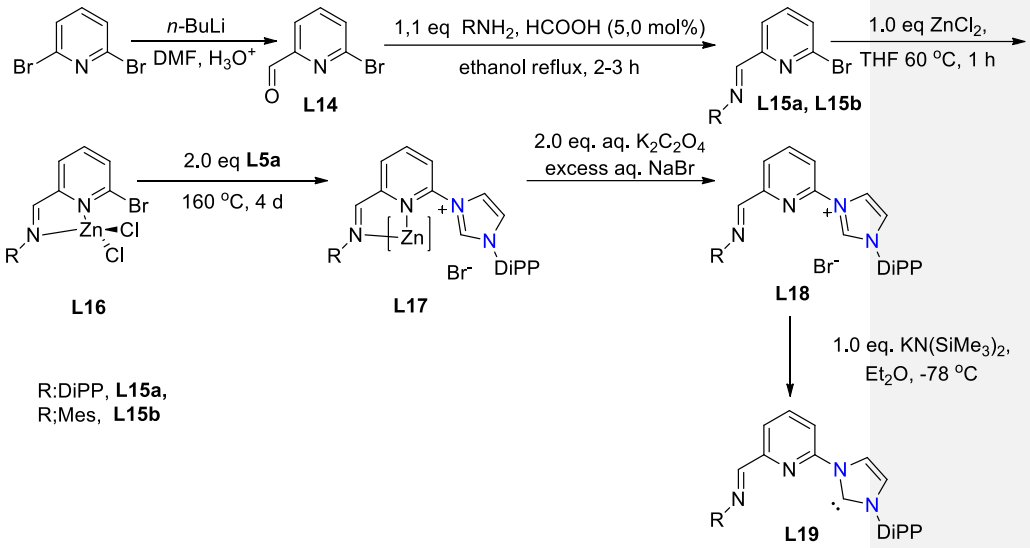

Synthesis of 6-bromopyridine-2-carbaldehyde

To a solution of 2,6-dibromopyridine (5 g, 21.1 mmol) in Et_2O (100 mL), cooled at −78 °C, was added dropwise a solution of *n*-BuLi in hexane (21.1 mmol, 8.45 mL of 2.5 M solution) over 15 min. After a period of 10 minutes, a solution of DMF (25.8 mmol, 2.00 mL in 10 mL of Et_2O) was slowly added. The resulting mixture was stirred at −78 °C for 20 min, allowed to warm up to −10 °C and quenched by the addition of 10% aqueous HCl until the mixture became acidic. The resulting solution was made alkaline by the addition of aqueous saturated K_2CO_3 solution. The crude product partitioned between $CHCl_3$ and water. The aqueous layer was separated and washed with $CHCl_3$ (3 × 20 mL). The combined organic layers were washed with brine and dried over $MgSO_4$. Removal of the volatiles under reduced pressure gave the crude product as an oil. Recrystallization from warm hexane afforded the **L14** as colourless prisms by letting the flask in the freezer, overnight. (Yield: 2.5 g, 64%).

L14: ^{1}H-NMR (400 MHz, $CDCl_3$): δ = 9.98 (d, *J* = 0.7 Hz, 1H, CHO), 7.91 (dd, *J* = 1.8 Hz, 1H, $CH_{pyr.}$), 7.78–7.68 (m, 2H, $CH_{pyr.}$) ppm.

^{13}C-NMR ($CDCl_3$, 100.63 MHz): δ= 191.7 (CHO), 153.6 (C_{pyr}), 142.7 ($C_{pyr.}$), 139.5 ($CH_{pyr.}$), 132.8 ($CH_{pyr.}$), 120.5 ($CH_{pyr.}$) ppm.[212,213]

Synthesis of 1-(6-bromopyridin-2-yl)-*N*-mesitylmethanimine (L15b)

A mixture of **L14** (1.65 g, 8.87 mmol), 2,4,6-trimethylaniline (1.37 mL, 9.75 mmol) and formic acid (17 µL, 0.444 mmol, 5.0 mol%) in ethanol was heated to reflux for 2–3 h. All volatiles were evaporated under reduced pressure to dryness and the resulting solid was recrystallized from hexane to afford **L15b** as yellow prisms. Yield: 1.95 g, 72%.[226]

^{1}H-NMR (400.13 MHz, $CDCl_3$): δ= 8.27 (s, 1H, NCH), 8.25 (dd, 1H, $CH_{pyr.}$), 7.69 (t, 1H, $CH_{pyr.}$), 7.59 (dd, 1H, $CH_{pyr.}$), 6.90 (s, 2H, $CH_{mes.}$), 2.29 (s, 3H, *p*-CH_3 mes.), 2.13 (s, 6H, *o*-$CH_{3\ mes.}$) ppm.

^{13}C-NMR (100.63 MHz, $CDCl_3$): δ =162.0 (*C*HN), 155.9 ($C_{arom.}$), 147.5 ($C_{arom.}$), 141.9 ($C_{arom.}$), 139.1 (*C*H$_{arom.}$), 133.9 ($C_{arom.}$), 129.8 (*C*H$_{arom.}$), 129.0 (*C*H$_{arom.}$), 126.9 ($C_{arom.}$), 119.9 (*C*H$_{arom.}$), 20.9 (*p-C*$H_{3\ mes.}$), 18.4 (*o-C*$H_{3\ mes.}$) ppm.

Synthesis of 1-(6-bromopyridin-2-yl)-N-(2,6-diisopropyl-phenyl)methanimine (L15a)

A mixture of **L14** (1.065 g, 5.72 mmol), 2,6-diisopropylaniline (1.2 mL, 6.29 mmol) and formic acid (11 µL, 0.29 mmol, 5.0 mol%) in ethanol was heated to reflux for 2–3 h. All volatiles were evaporated to dryness and the resulting solid was recrystallized from hexane to afford **L15a** as yellow-green prisms. (Yield: 1.763 g, 89%)[226]

L15a :^{1}H-NMR (400.13 MHz, $CDCl_3$): δ = 8.26 (dd, 1H, $CH_{pyr.}$), 8.25 (d, *J* = 0.6 Hz, 1H, NCH), 7.71 (m, 1H, $CH_{pyr.}$), 7.61 (dd, 1H, $CH_{pyr.}$), 7.20–7.13 (m, 3H, CH_{DiPP}), 2.92 (sept, 2H, $CH(CH_3)_2$), 1.17 (d, *J* =6.9 Hz, 12H, $CH(CH_3)_2$) ppm.

^{13}C-NMR (100.62 MHz, $CDCl_3$,): *δ* 161.6 (*C*HN), 155.6 ($C_{arom.}$), 148.0 ($C_{arom.}$), 142.0 ($C_{arom.}$), 139.1 ($C_{arom.}$), 137.2 ($C_{arom.}$), 130.0 ($CH_{arom.}$), 124.8 (*C*H$_{arom.}$), 123.2 ($CH_{arom.}$), 120.0 ($CH_{arom.}$), 28.1 ($CH(CH_3)_2$), 23.6 ($CH(CH_3)_2$).

Synthesis of [{1-(6-bromopyridin-2-yl)-*N*-(2,6-diisopropyl-phenyl)methanimine}$ZnCl_2$] (L16)

To a solution of **L15a** (1.5 g, 4.33 mmol) in dry THF (20 mL) was added anhydrous $ZnCl_2$ (0.59 g, 4.33 mmol). The mixture was heated for 1 h to 60 °C, during which time a yellow precipitate appeared from the light brown solution. After cooling down to rt, Et_2O (20 mL) was added and the formed precipitate was collected by filtration, washed with Et_2O and dried *in vacuo*, affording **L16**·THF as a yellow powder (THF adduct based on the NMR data). Heating the THF adduct at 100 °C under vacuum for several hours afforded **L16** as a yellow powder. Single crystals suitable for X-ray diffraction analysis were obtained by slow diffusion of pentane in a dilute solution of the complex. Yield: 2.15 g, 90%. [226]

^{1}H-NMR (400.13 MHz, $CDCl_3$): δ= 8.22 (d, *J* = 7.7 Hz, 1H, $CH_{pyr.}$), 8.21 (s, 1H, NCH), 7.95 (t, 1H, $CH_{pyr.}$), 7.85 (d, *J* = 7.8 Hz, 1H, $CH_{pyr.}$), 7.17 (2 overlapping d, *J* = 8.4, 6.4 Hz, 2H, *m*-CH_{DiPP}), 7.11 (dd, 1H, *p*-CH_{DiPP}), 2.84 (sept, 2H, $CH(CH_3)_2$), 1.11 (d, *J* = 6.9 Hz, 12H, $CH(CH_3)_2$) ppm.

^{13}C-NMR (400.13 MHz, $CDCl_3$): *δ*= 161.6 (*C*HN), 154.6 ($C_{arom.}$), 147.7 ($C_{arom.}$), 141.4 ($C_{arom.}$), 140.6 ($CH_{arom.}$), 136.4 ($C_{arom.}$), 130.4 ($CH_{arom.}$), 124.6 ($CH_{arom.}$), 122.9 ($CH_{arom.}$), 120.6 ($CH_{arom.}$), 27.5 (*C*H(CH_3)$_2$), 23.2 (CH(*C*H_3)$_2$) ppm.

Synthesis of L18

Με σχόλια [GV2]: ΕΔΩ ΚΑΤΙ ΛΕΙΠΕΙ

A mixture of **L17** (0.87 g, 1.8 mmol)) and **L5a** (3 equiv.) was heated in a sealed flask at 150–160 °C for 4 d. After cooling to r.t., decoordination of Zn^{II} of was carried out using a slightly modified literature procedure. To a CH_2Cl_2 solution (50 mL) of the crude zinc complex in a separating funnel was added a solution of potassium oxalate monohydrate (*ca.* 3 equiv.) in water. After shaking the mixture for 5–10 min, the aqueous phase, containing a white suspension of $Zn(C_2O_4)$, was separated and the organic phase was washed twice with water

(2 × 25 mL). To avoid a possible mixture of counteranions in the imidazolium salt product, saturated aqueous NaBr solution was added to the organic phase and the resulting biphasic mixture was vigorously stirred for 30 min. The organic phase was separated, dried over anhydrous $MgSO_4$ and evaporated under reduced pressure. The solid residue was triturated with hot hexane (4 × 20 mL), filtered and dried under vacuum to afford **L18** as a yellow solid. (Yield: 0.64 g, 69%)[226]

^{1}H-NMR (400 MHz, $MeCN_,$): δ= 11.58 (t, *J* = 1.5 Hz, 1H, $CH_{imid.}$), 9.46 (dd, 1H, $CH_{pyr.}$), 9.21 (t, 1H, $CH_{imid.}$), 8.46 (dd, 1H, $CH_{pyr.}$), 8.31 (br t, 1H, $CH_{pyr.}$), 8.30 (s, 1H, NCH), 7.64 (t, 1H, *p*-CH_{DiPP}), 7.43 (t, 1H, $CH_{imid.}$), 7.41 (d, *J* = 7.8 Hz, 2H, *m*-CH_{DiPP}), 7.19 (2 overlapping d, *J* = 8.6, 6.6 Hz, 2H, *m*-CH_{DiPP}), 7.14 (dd, *J* = 8.6, 6.6 Hz, 1H, *p*-CH_{DiPP}), 2.95 (sept, 2H, $CH(CH_3)_2$), 2.46 (sept, 2H, $CH(CH_3)_2$), 1.30 (d, *J* = 6.8 Hz, 6H, $CH(CH_3)_2$), 1.20 (d, *J* = 6.8 Hz, 6H, CH(CH3)2), 1.18 (d, *J* = 6.8 Hz, 12H, CH $(CH_3)_2$) ppm.

^{13}C-NMR (100.62 MHz, MeCN,): δ= 161.4 (NCH), 153.9 ($C_{arom.}$), 148.5 ($C_{arom.}$), 146.4 ($C_{arom.}$), 145.6 ($C_{arom.}$), 141.9 ($CH_{arom.}$), 137.5 ($C_{arom.}$), 136.9 ($CH_{arom.}$), 132.5 ($CH_{arom.}$), 130.4 ($C_{arom.}$), 125.5 ($CH_{arom.}$), 125.21 ($CH_{arom.}$), 125.17 ($CH_{arom.}$), 123.5 ($CH_{arom.}$), 123.0 ($CH_{arom.}$), 120.9 ($CH_{arom.}$), 118.4 ($CH_{arom.}$), 29.3 ($CH(CH_3)_2$), 28.4 ($CH(CH_3)_2$), 24.43 ($CH(CH_3)_2$), 24.37 ($CH(CH_3)_2$), 23.6 ($CH(CH_3)_2$) ppm.

2.4.8. Syntheses of complexes

Synthesis of $[Co\{N(SiMe_3)_2\}_2]_2$ (Co1)

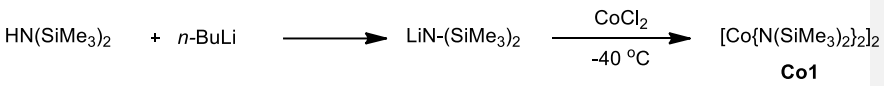

A diethyl ether suspension of $LiN\text{-}(SiMe_3)_2$ was synthesized in situ by adding through a syringe *n*-BuLi (18 mL, 2.5 M solution in hexanes, 0.044 mol) dropwise to $HN(SiMe_3)_2$ (8.4 mL, 0.040 mol) in diethyl ether (40 mL), cooled in an ice bath. The solution was allowed to come to room temperature and stirring

was continued overnight. The resulting opaque suspension was added dropwise *via* cannula to a diethyl ether (40 mL) slurry of $CoCl_2$ (2.86 g, 22.0 mmol) chilled in an ice bath. An immediate color change of the slurry from blue to dark green was observed. When the addition was complete, the suspension was warmed to ca. 35 °C and stirred for 12 h. The ether was removed under reduced pressure and the resulting dark green solids were extracted with hexanes (40 mL), which resulted in a dark green solution with a gray precipitate. The solution was then filtered through a Celite padded filter-stick to afford a clear dark-green solution. The hexanes were removed under reduced pressure to give a dark green oil. Upon cooling, a brown-dark red solid. The solid was dissolved in hexanes (ca. 30 mL) at 65 °C, which afforded an olive-green solution. Cooling slowly to 0 °C gave **Co1**, in the form of red-olive dichroic crystals. (Yield: 5.70 g, 75%).

^{1}H-NMR (C_6D_6, 400 MHz): 8.97 (br s, −$SiMe_3$, [Co{N($SiMe_3$)$_2$}$_2$)], 0.51 (s, −$SiMe_3$ (terminal), [Co{N-($SiMe_3$)$_2$}$_2$]$_2$), −4.22 (br s, −$SiMe_3$ (bridging), [Co{N($SiMe_3$)$_2$}$_2$]$_2$) ppm.

Synthesis of Co2

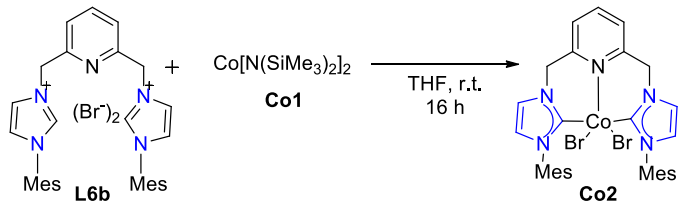

In a Schlenck flask, were weighed solid Co[N($SiMe_3$)$_2$]$_2$ (37.8 mg, 0.1 mmol) slowly was added into a solution of **L6b** (63.8 mg, 0.1 mmol) in 15 mL of THF at room temperature. The THF was inserted in the fridge (-30 °C) beforehand. As the time passes the color changes to brown, then dark green. After letting it stir overnight the mother liquid appears to be purple with dark precipitate. After filtration, it was recrystallized from THF / ether to yield light pink colored crystals. The product is paramagnetic.

Synthesis of Co3

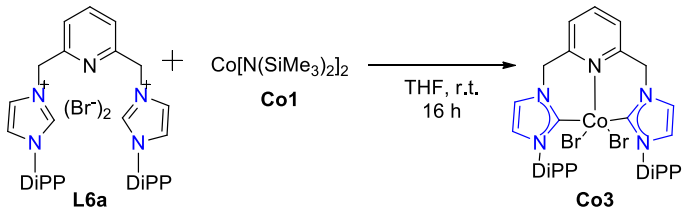

In a Schlenck flask, were weighed solid $Co[N(SiMe_3)_2]_2$ (**Co1**) (37.8 mg, 0.1 mmol) slowly was added into a solution of **L6a** (63.8 mg, 0.1 mmol) in 15 mL of THF at room temperature. The THF was inserted in the fridge (-30 °C) beforehand. As the time passes the color changes to green, then blue-gray. After letting it stir overnight the mother liquid appears to be purple with blue precipitate. After filtration, it was recrystallized from THF/ether to yield light pink colored crystals. The product is paramagnetic.

Synthesis of Co4

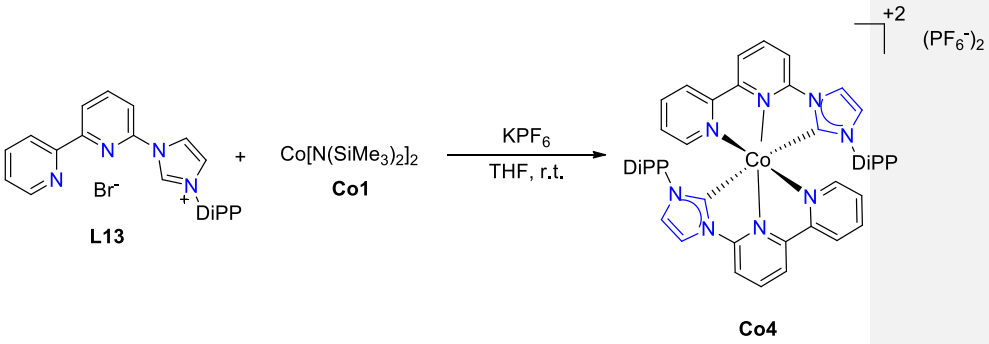

In a Schlenk flask we dissolve 6-(3-(2,6-diisopropylphenyl)-2,3-dihydro-*1H*-imidazol-1-yl)-2,2'-bipyridine (122 mg, 0.54 mmol) in THF. Then we add $Co\{N(SiMe_3)_2\}_2$ (**Co1**) (50 mg, 0.27 mmol) also dissolved in THF, in the solution. We let brown-red mixture stir for 2 h and add KPF_6 (122 mg, 0.54 mmol). The

solution becomes lighter, and we let it stir overnight. The next day we remove the volatiles using the vacuum line. The product is paramagnetic.

Synthesis of Co5

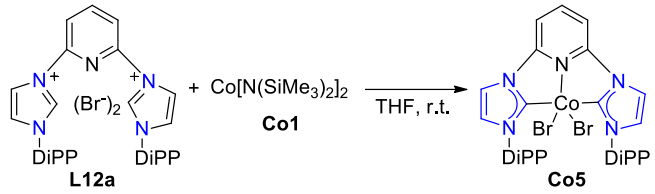

Co[(N(SiMe$_3$)$_2$]$_2$ (**Co1**) (5.0 g, 13.2 mmol) and the bis(imidazolium) salt (9.2 g, 13.2 mmol) (**L12a**), were mixed in a Schlenk tube equipped with a heavy stir bar. This was placed in a dry ice-acetone bath and THF (100 mL) was added slowly *via* syringe. The suspension was allowed to warm up slowly becoming gradually red-orange and finally at room temperature gave rise to a red-purple solution. The reaction mixture was stirred at room temperature for 8 hr; during which time some red precipitate started to form. Removal of the volatiles under vacuum left a red residue, which was washed with ether and dried under vacuum. The product is paramagnetic.

Synthesis of Co6

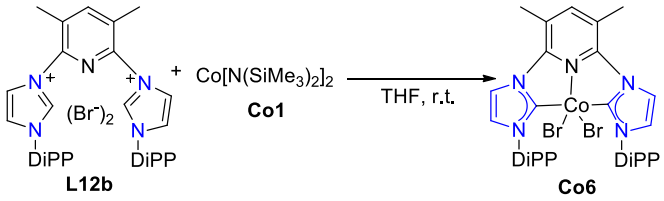

In a Shlenck flask, were weighed solid Co[N(SiMe$_3$)$_2$]$_2$ (507 mg, 1.33 mmol) was added into a solution of **L12b** (1 g, 1.33 mmol) in 15 mL of THF at room temperature. The solution turns red, and we let it stir overnight. The next day the volatiles are removed. The solid is washed with pentane and dried under vacuo. The product is paramagnetic.

Synthesis of Co7

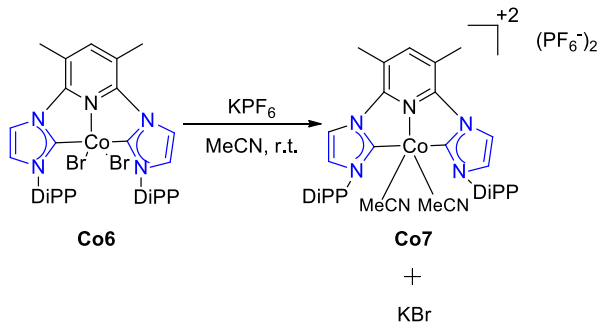

Co6 (20 mg, 0.026 mmol) and KPF_6 (19 mg, 0.052 mmol) were dissolved in MeCN and let stir overnight. The next day we transfer the solution in a clean Schlenk with a fritz canula to remove the precipitate (KBr). Then the solid was dried under vacuo. The product is paramagnetic.

Synthesis of Co8

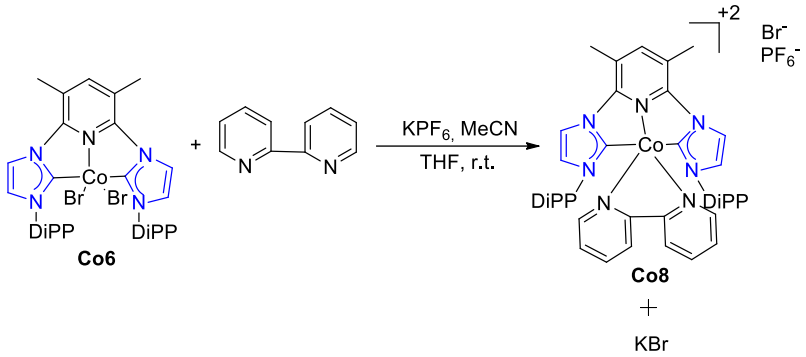

Reaction of **Co6** (50 mg, 0.065 mmol) and bipyridine (10 mg, 0.065 mmol) were dissolved in 10 mL THF. KPF_6 (24 mg, 0.13 mmol) dissolved in MeCN was added shortly after and let stir overnight. The next day we transfer the solution in a clean Schlenk with a fritz canula to remove the precipitate (KBr). Then, the volatiles are removed and the solid is washed with ether and dried under vacuo. The product is paramagnetic.

Synthesis of Co9

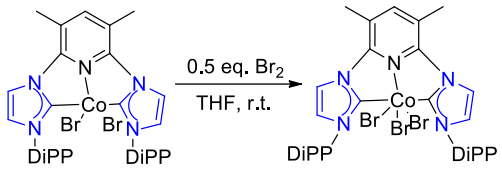

Co6 **Co9**

Co6 (60 mg, 0.078 mmol) was dissolved in 10 mL THF. 2-3 drops of Br_2 (20 - 30mg) are then added to the solution. The resulting solution was stirred at r.t. for 5min and then the volatiles were removed under reduced pressure. The solid was then washed with pentane and the solution was removed with a canula in order to avoid the excess amount of Br_2. Then the solid was dried under vacuo. The product is paramagnetic.

Alternative synthesis of Co9

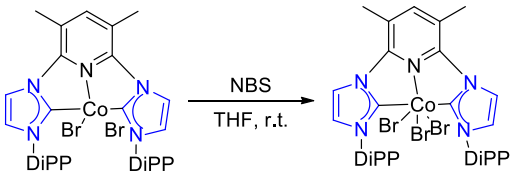

Co5 **Co9**

Co6 (60 mg, 0.078 mmol) and NBS (14 mg, 0.078 mmol) were dissolved in 10 mL THF. The resulting solution was stirred at r.t. until we see a color change and then the volatiles were removed under reduced pressure. The solid was then washed with ether and the solution was removed with a canula in order to avoid the excess amount of NBS. Then the solid was dried under vacuo. The product is paramagnetic.

Synthesis of Co10

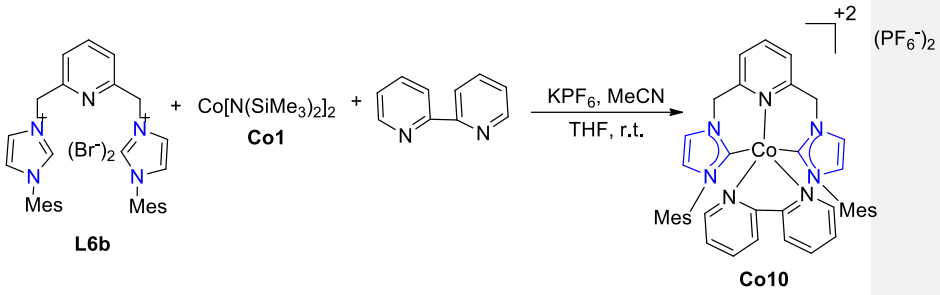

In a Shlenck flask, were weighed the solids $Co[N(SiMe_3)_2]_2$ (63 mg, 0.166 mmol) **L6b** (126 mg, 0.166 mmol) and bipyridine (26 mg, 0.166 mmol) in 15 mL of THF at room temperature. KPF_6 (61 mg, 0.33 mmol) were dissolved in MeCN, then added to the THF solution and was let to stir overnight. As the time passes the color changes from red to brown. The next day, the volatiles are removed and the solid was with ether and dried under vacuo. The product is paramagnetic.

Synthesis of Co11

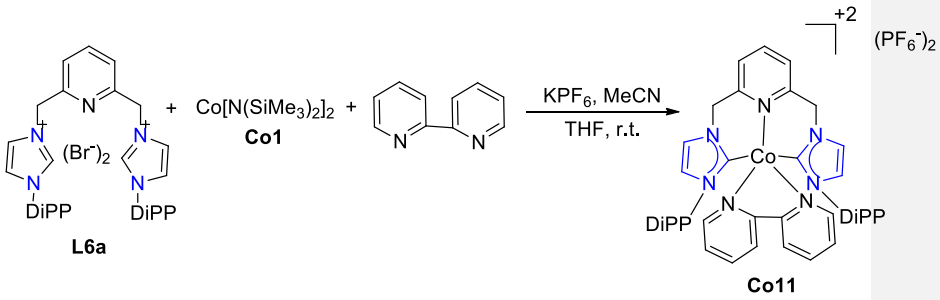

In a Shlenck flask, were weighed the solids $Co[N(SiMe_3)_2]_2$ (63 mg, 0.166 mmol) **L6a** (126 mg, 0.166 mmol) and bipyridine (26 mg, 0.166 mmol) in 15 mL of THF at room temperature. KPF_6 (61 mg, 0.33 mmol) were dissolved in

MeCN, then added to the THF solution and was let to stir overnight. As the time passes the color changes from red to brown. The next day, the volatiles are removed and the solid was with ether and dried under vacuo. The crude product was recrystallized from CH_2Cl_2 . The product is paramagnetic.

Synthesis of Co12

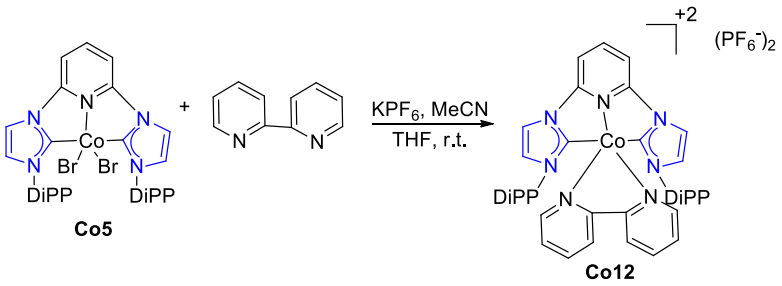

In a Shlenck flask, were weighed the solids **Co5** (38 mg, 0.05 mmol) and bipyridine (8 mg, 0.05 mmol) in 5 mL of THF at room temperature. KPF_6 (30 mg, 0.25 mmol) were dissolved in MeCN, then added to the THF solution and was let to stir overnight. As the time passes the color changes from red to brown-orange. The next day, the volatiles are removed and the solid was with ether and dried under vacuo. The crude product was recrystallized from CH_2Cl_2 . The product is paramagnetic.

Synthesis of Co13

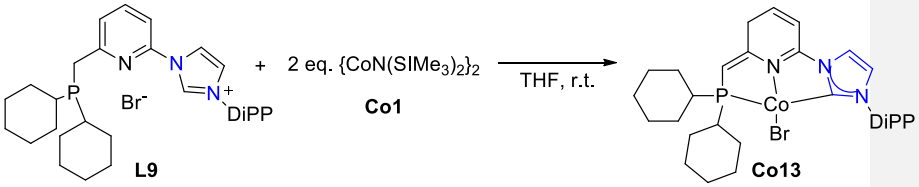

To a suspension of (^{Cy}PNC^{im})Br (106 mg, 0.181 mmol) in THF precooled at -78°C was added dropwise a cold solution of [Co{N(SiMe$_3$)$_2$}$_2$] (**Co1**) (70 mg, 0.181 mmol) in THF. The resulting dark-red solution was allowed to reach room temperature, stirred for 2 h and briefly heated to reflux. All the volatiles were evaporated under reduced pressure and the resulting brown-red solid was extracted with toluene. Filtration and evaporation of the toluene solution afforded **Co13** as a dark purple solid. The product is paramagnetic.

Appendix of Chapter 1

6LU7

Compound	Binding score (kcal / mol)
Ibuprofen	-5.59
Warfarin	-7.62
Denopamine	-6.77
Naminterol	-7.79
Rotigaptide	-4.72
Bometelol	-8.04
Benzquercin	-8.59
Gastgeiger	-6.72
Rotigaptide	-6.07
5,7,3',4'-Tetrahydroxy-2'-(3,3-dimethylallyl)isoflavone	-8.48
Favipiravir	-4.49
2oxo1Hpyrazine3carboxamide	-4.43
6amino3oxo3_4dihydropyrazine2carboxamide	-4.58
3aminomethyl5fluoropyrazin2_1H_one	-5.45
6fluoro2oxo1Hpyrazine3carboxamide	-4.59
Nmethyl3oxo3_4dihydropyrazine2carboxamide	-4.65
(-)-Catechin	-7.87
(-)-Catechin_gallate	-6.24
(-)-epicatechin	-6.45
epicatechin(2β-O-7, 4β-8)-epicatechin	-4.53
epicatechin-(4β-8)-epicatechin	-7.96
Chloroquine	-6.59
Hydroxychloroquine	-7.01
Darunavir	-7.16
Arbidol	-7.2
Azithromycin	-4.22
Lopinavir	-5.54
Sofosubir	-5.91
Remdesivir	-6.56
Ribavirin	-5.75
Ritonavir	-2.91
Remdesivirtriphosphate	-1.99
Oxycodone	-7.56
Cinnamic acid	-5.11
Paracetamol	-5.16
Proparacetamol	-5.82
Ascorbic acid	-3.93
Retinol	-7.84
betacarotene	-9.52
Cholecalciferol	-9.43
Riboflavin	-6.44
Biotin	-5.0

Vitamink	-7.15
VitaminB1	-8.2
VitaminE	-7.7
glucosiduronate	-8.83
Nicotinicacid	-4.39
Folicacid	-5.37
Pyridoxalphosphate	-4.48
Pyridoxine	-4.66
Pantothenicacid	-4.61
Nicotinamide	-4.56
Tigecycline	-7.07
Fenoterol	-6.9
Montelukast	-7.21
reproterol	-6.32
oxytetracycline	-6.63
cefpiramide	-6.1
Demeclocycline	-5.64
doxycycline	-8.75
lymecycline	-3.9
Pheneticillin	-7.1
Saquinavir	-7.34
Thymidine	-6.05
Sulfasalazine	-7.52
Valganciclovir	-5.91
dieckol	-6.13
Indinavir	-5.73
Tipranavir	-7.9
Faldaprevir	-6.24
10-Hydroxyusambarensine	-10.56
6-oxoisoiguesterin	-8.99
Cryptoquindoline	-11.19
Eszopiclone	-8.2
22-Hydroxyhopan-3-one	-8.32
Simeprevir	-6.49
Avatrombopag	-9.11
22Oxacalcitriol	-8.34
Blonanserin	-9.34
Bromocriptine	-9.73
Buclizine	-9.03
Canagliflozin	-8.09
Dalfopristin	-6.71
Clofazimine	-10.61
Conivaptan	-9.42
Dihydrotachysterol	-8.86
Doxazosin	-8.67
Doxercalciferol	-9.59
Empagliflozin	-8.09
Ergoloidmesylate	-8.18

Ergotamine	-8.02
Meclizine	-9.4
Nilotinib	-9.27
Terfenadine	-8.37
Thioproperazine	-9.04
Tolvaptan	-8.98
Zafirlukast	-8.01

6LZG

Zafirlukast	-8.08
Warfarin	-7.24
Denopamine	-6.46
Naminterol	-5.68
Rotigaptide	-5.56
Bometelol	-5.0
Benzquercin	-8.75
5,7,3',4'-Tetrahydroxy-2'-(3,3-dimethylallyl)isoflavone	-7.78
Favipiravir	-4.84
2oxo1Hpyrazine3carboxamide	-4.83

Appendix of Chapter 2

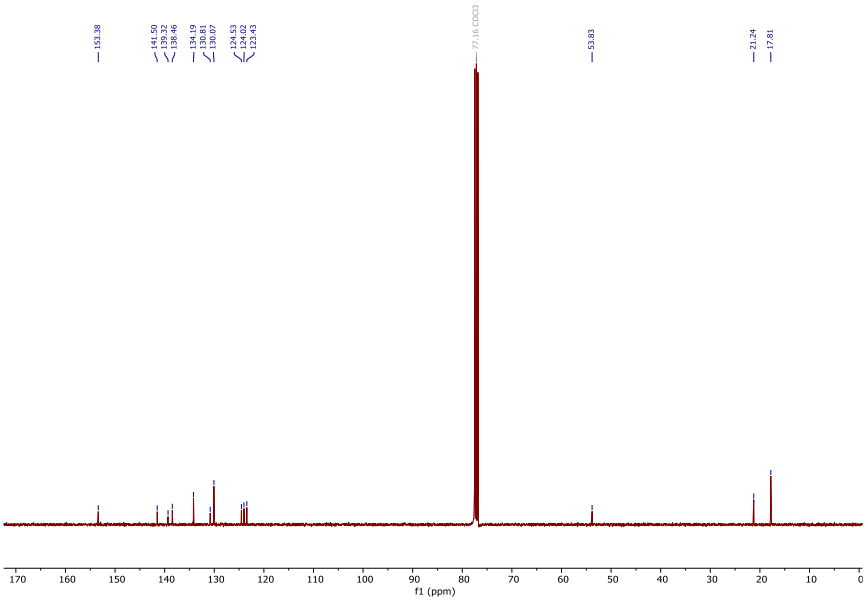

*Figure 85: ^{1}H-NMR spectrum of **L6b** in $CDCl_3$*

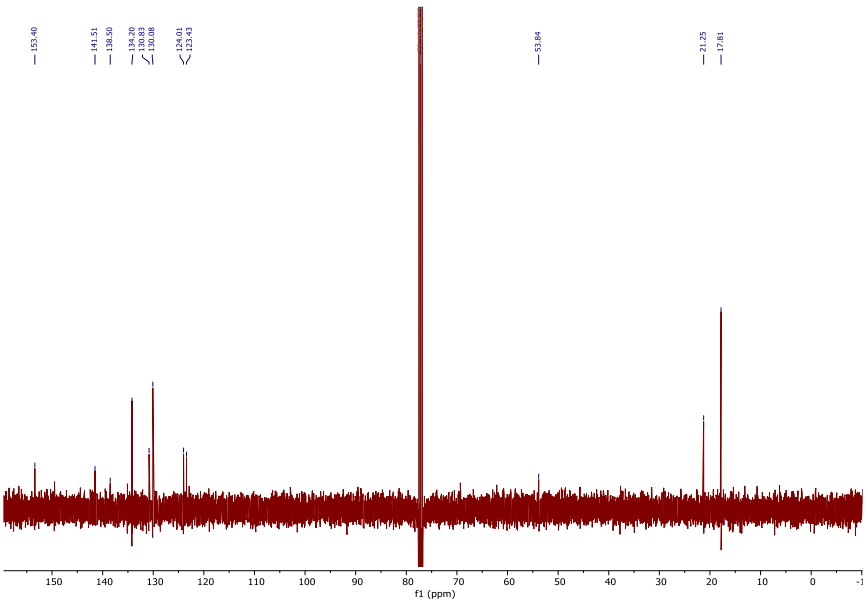

*Figure 86: ^{13}C-NMR spectrum of **L6b** in $CDCl_3$*

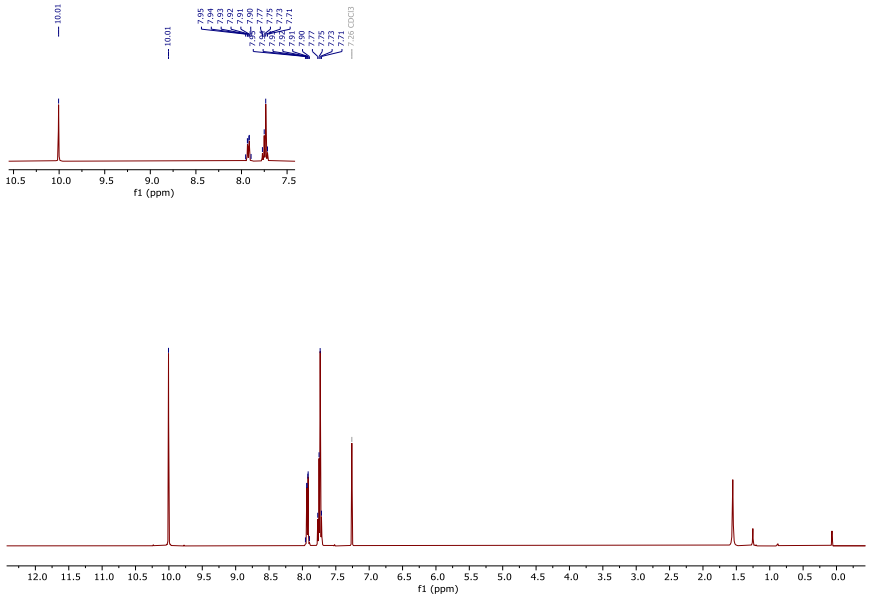

*Figure 87: ^{1}H-NMR spectrum of **L14** in $CDCl_3$*

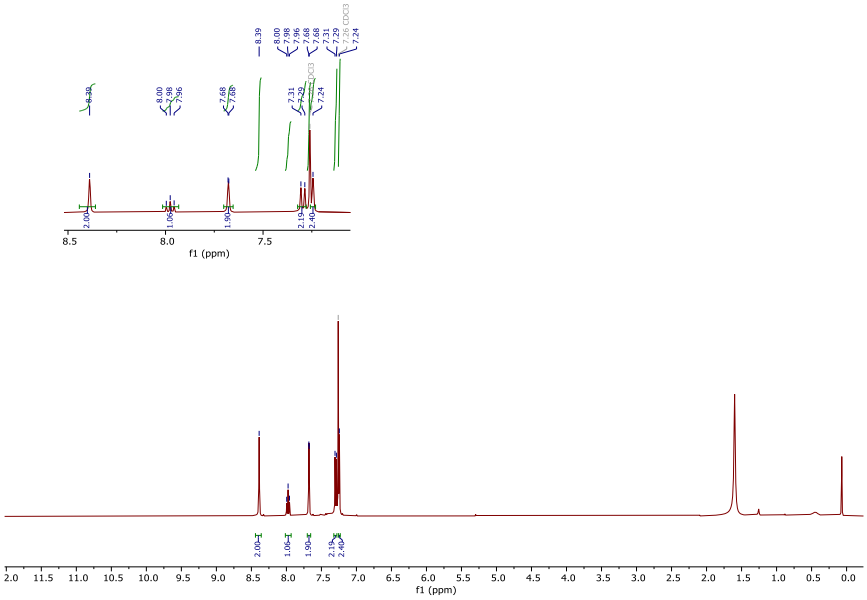

*Figure 88: ^{1}H-NMR spectrum of **L7** in $CDCl_3$*

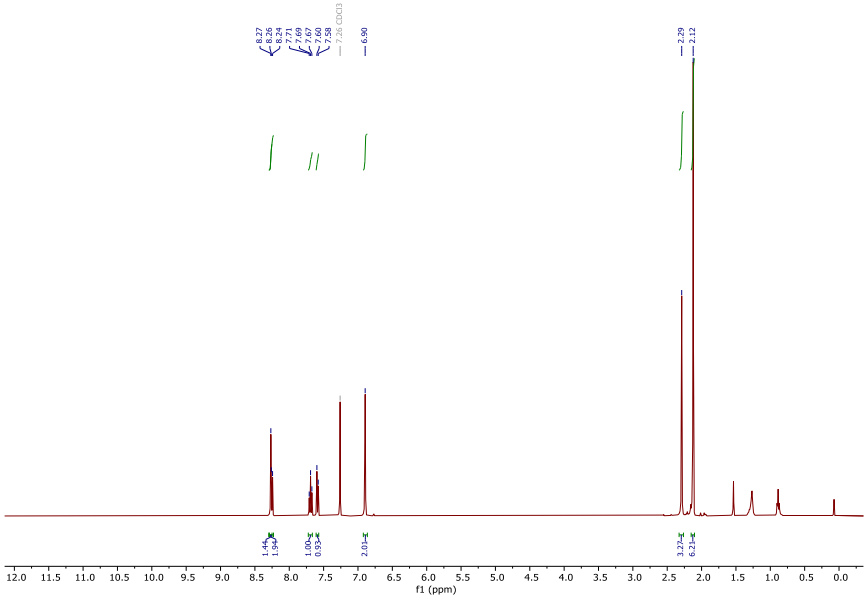

*Figure 89: ^{1}H-NMR spectrum of **L15b** in $CDCl_3$*

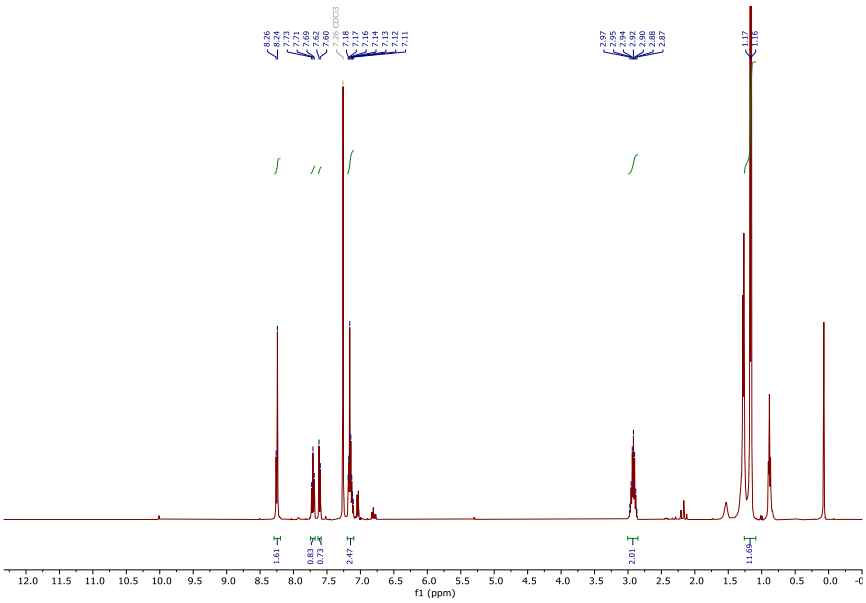

*Figure 90: ^{1}H-NMR spectrum of **L15a** in $CDCl_3$*

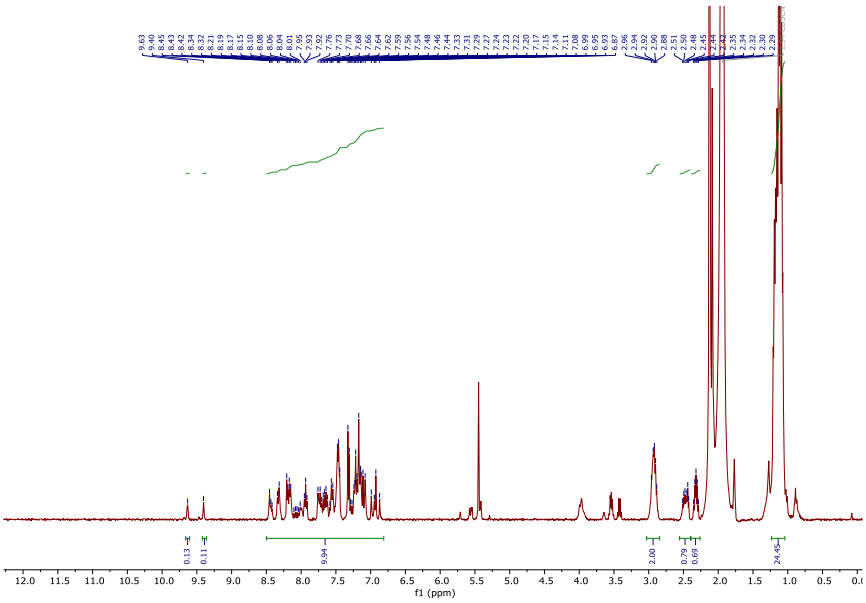

*Figure 91: ^{1}H-NMR spectrum of **L18** in $CDCl_3$*

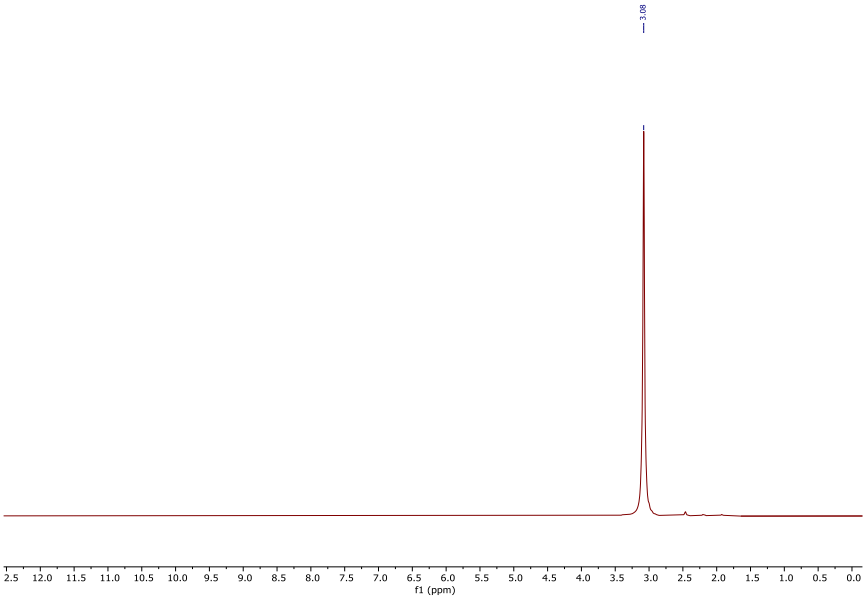

*Figure 92: ^{31}P-NMR spectrum of **L8** in C_6D_6*

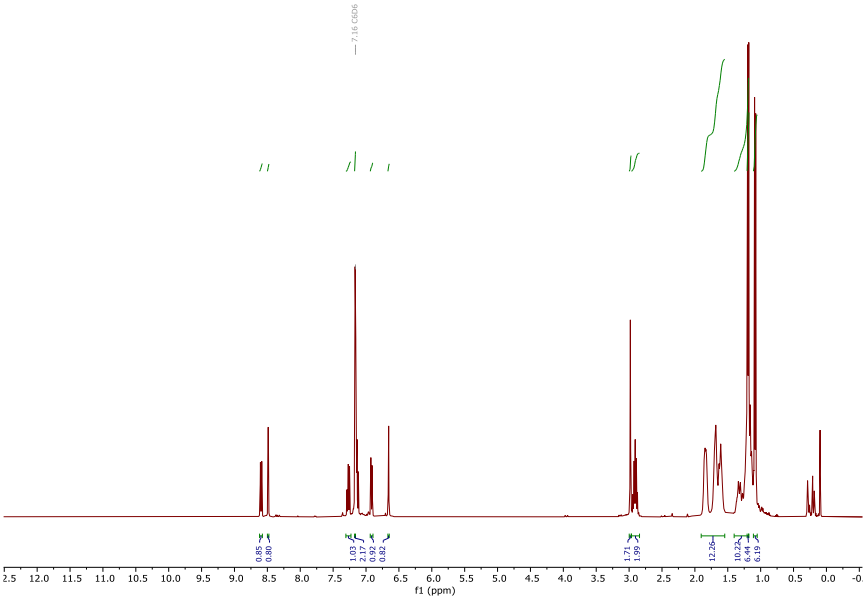

*Figure 93: ^{1}H-NMR spectrum of **L8** in C_6D_6*

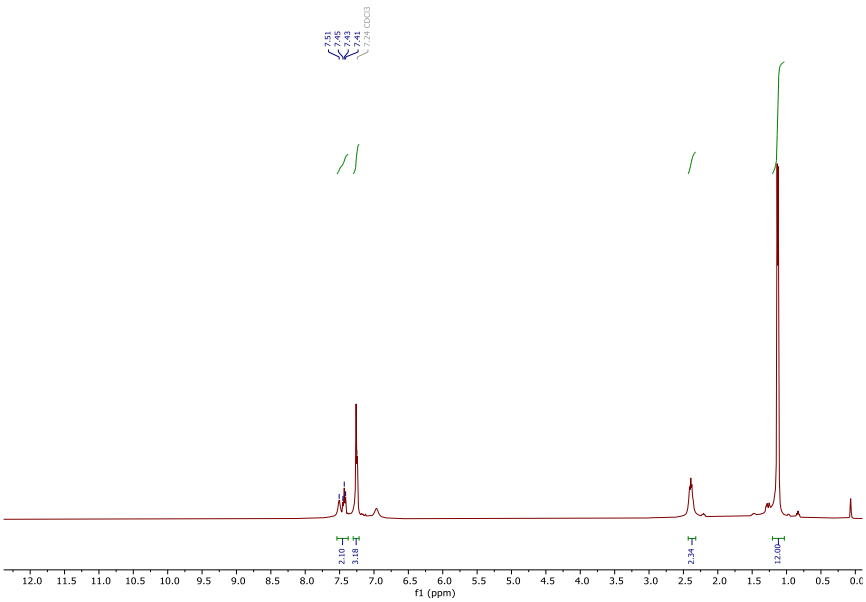

*Figure 94: ^{1}H-NMR spectrum of **L5a** in $CDCl_3$*

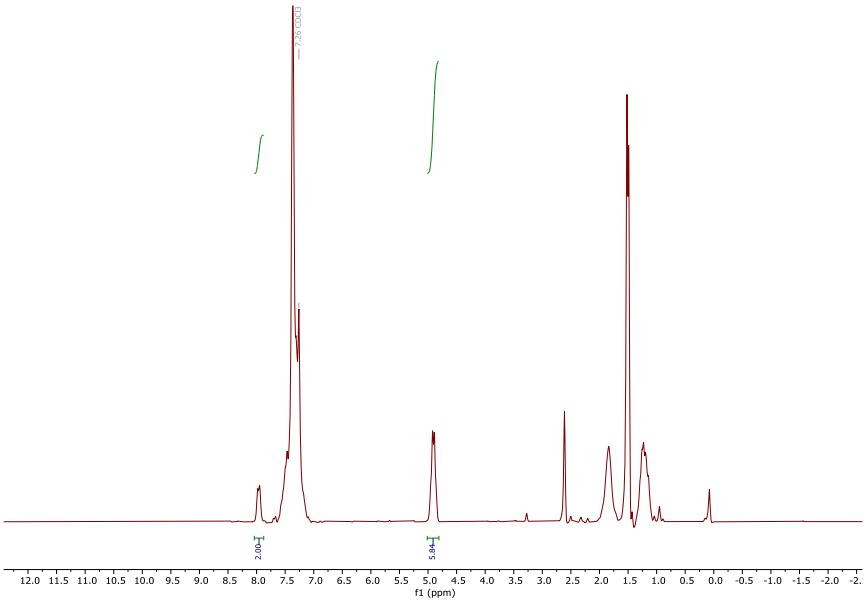

*Figure 95: Best ^{1}H-NMR yield of 85% in transfer hydrogenation, using **Co5** in $CDCl_3$.*

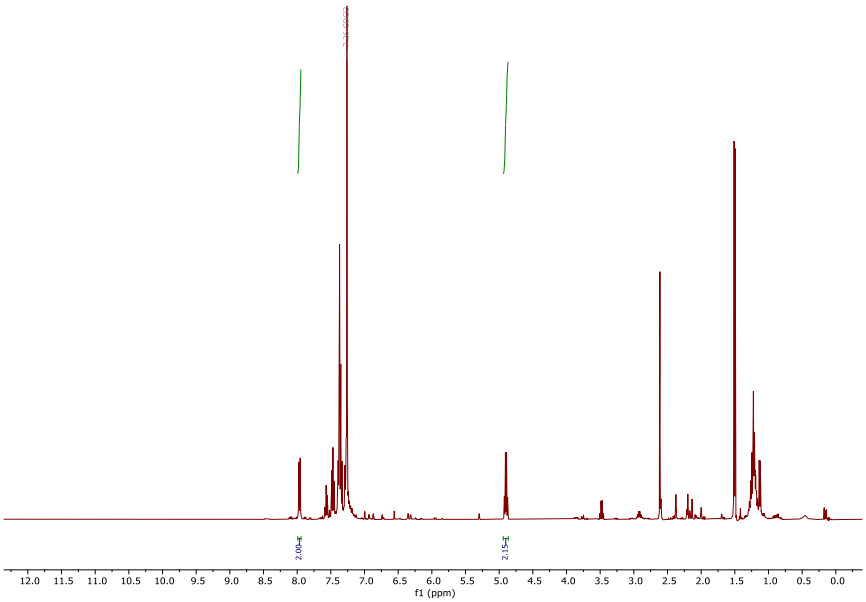

*Figure 96: Best ^{1}H-NMR yield of 70% in hydrogenation, using **Co6** in $CDCl_3$*

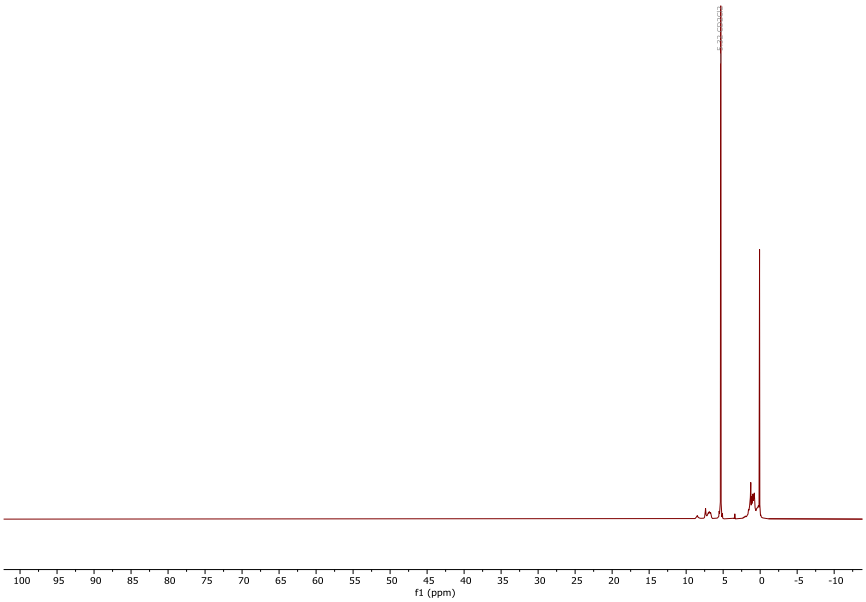

*Figure 97: Paramagnetic ^{1}H-NMR of **Co4** in CD_2Cl_2*

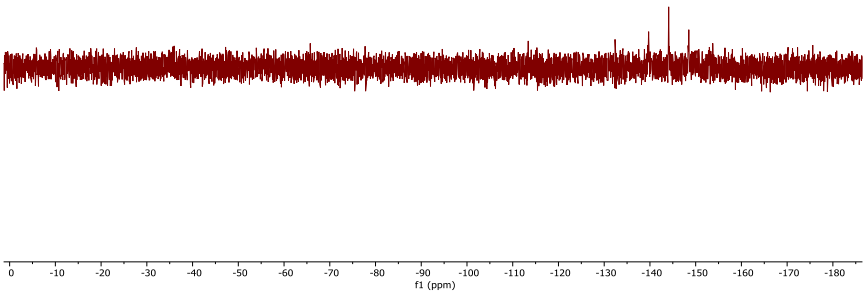

*Figure 98: Paramagnetic ^{31}P-NMR of **Co4** in CD_2Cl_2*

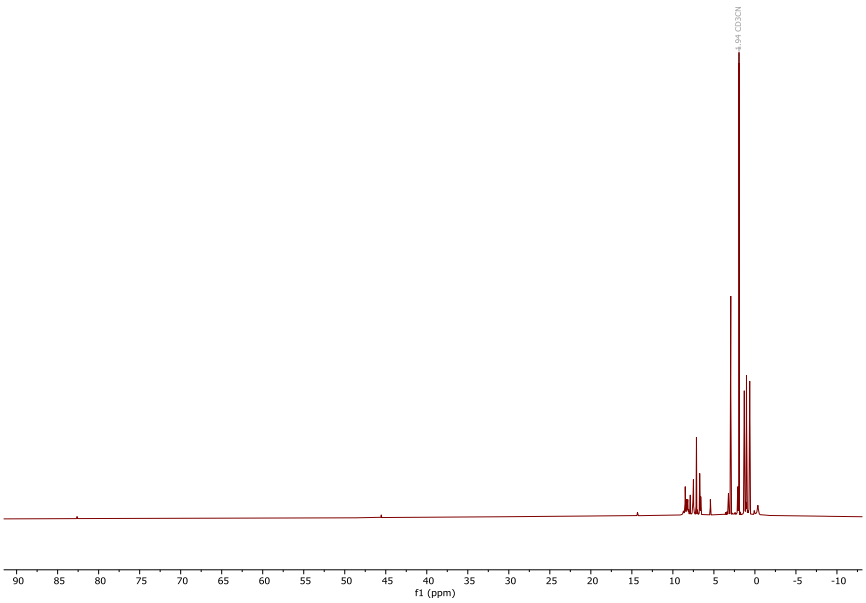

*Figure 99: Paramagnetic ^{1}H-NMR of **Co8** in MeCN.*

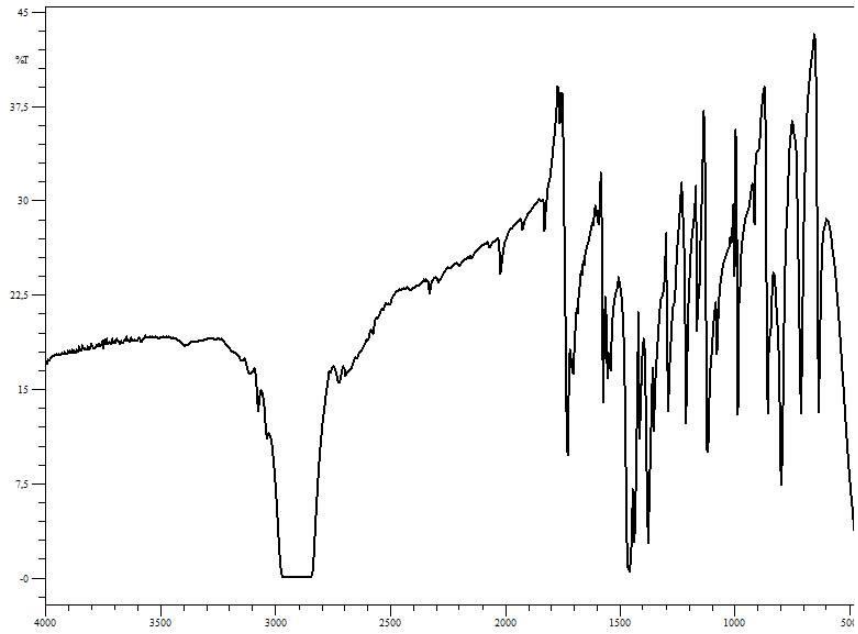

*Figure 100: FT-IT spectrum of **L14** in Nujol*

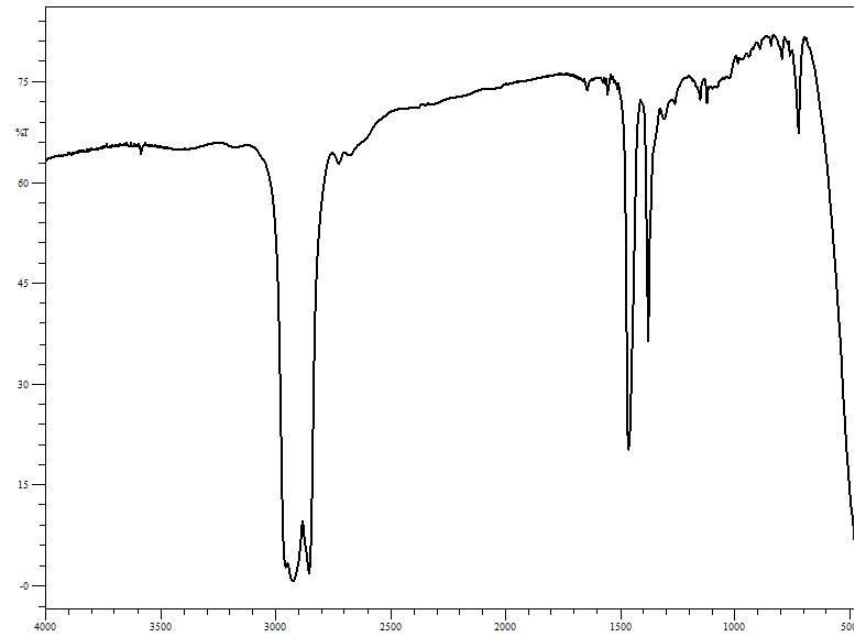

*Figure 101: FT-IT spectrum of **L15a** in Nujol*

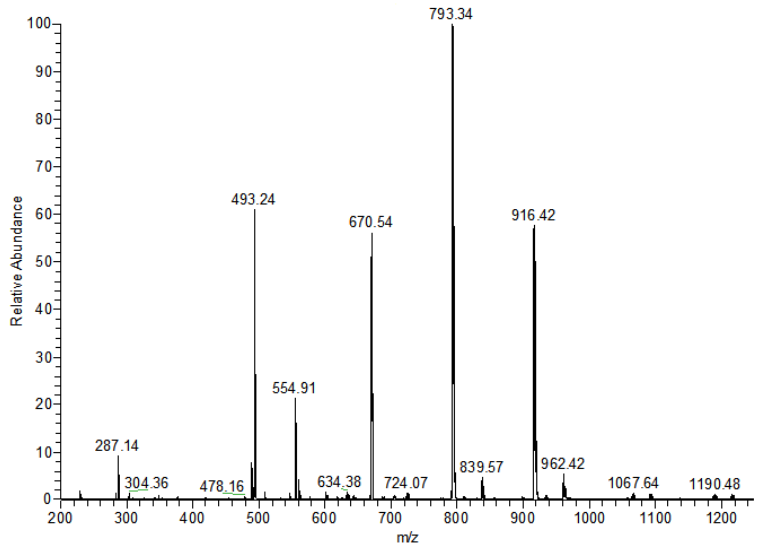

*Figure 102: ESI-MS spectrum of **L18***

Abbreviations

$\%V_{bur}$	percent buried volume
acac	acetylacetonate
ACE2	Angiotensin-converting enzyme 2
ARBs	Angiotensin II receptor blockers
ARDS	Acute respiratory distress syndrome
Ang II	Angiotensin II
BAr^{F}_{4}	tetrakis(3,5-bis(trifluoromethyl)phenyl)borate
bipy	bipyridine
Bn	benzyl
cAAC	cyclic (Alkyl)(Amino)Carbene
CADD	computer-aided drug design
CCSB	Center for Computational Structural Biology
CDC	Center for Disease Control and Prevention
COD	cyclooctadiene
CoVs	Coronaviruses

COX	cyclooxygenases
Cp	cyclopentadienyl
CRP	C-reactive protein
CNS	central nervous system
CV	cyclic voltammetry
Cy	cyclohexyl
^{Cy}cAAC	1-(2,6-diisopropylphenyl)-3-cyclohexyl-5,5-dimethylpyrrolidin-2-ylidene
DFT	density functional theory
DHepP	2,6-di(heptan-4-yl)phenyl
Dba	Dibenzylideneacetone
DiPP	2,6-diisopropylphenyl
DME	1,2-dimethoxyethane
DMF	dimethylformamide
dmfu	dimethylfumarate
DMSO	dimethyl sulfoxide
E	envelope protein
e	electron
eq/equiv.	equivalent
ERGIC	reticulum-Golgi intermediate compartment
ESR	electron spin resonance
ET	electron-transfer
Et	ethyl
ExoN	3′-5′ exoribonuclease
G	Gauss
GISAID	Global initiative on sharing all influenza data
GM CSF	granulocyte macrophage colony stimulating factor
GUI	Graphica lUser Interface
hACE2	human ACE2
Hal	halide
HOMO	highest occupied molecular orbital
HS	high-spin
IAd	1,3-diadamantylimidazol-2-ylidene
*i*Bu	*iso*butyl
I*i*Pr	1,3-diisopropylimidazol-2-ylidene
IL-6	Interleukin-6
Im	imidazol
IMes	1,3-bis(2,4,6-trimethylphenyl)imidazol-2-ylidene
IPr	1,3-bis(2,6-diisopropylphenyl)imidazol-2-ylidene
*i*Pr	*iso*propyl
IPr ^{OMme}	1,3-bis(2,6-dibenzhydryl-4-methoxy-phenyl)imidazol-2-ylidene

IPr*	1,3-bis(2,6-dibenzhydryl-4-methylphenyl)imidazol-2-ylidene
IPr* ^{OMe}	[1,3N,N′-bis(2,6-bis(diphenylmethyl)-4-methoxyphenyl)imidazol-2-ylidene]
IPr*$^{(2\text{-}Np)}$	1,3-bis(2,6-bis(di(naphthalen-2-yl)methyl)-4-methylphenyl)imidazol-2-ylidene
IPr**	1,3-bis(2,6-bis(bis(4-(*tert*-butyl)phenyl)methyl)-4-methylphenyl)imidazol-2-ylidene
IPr* ^{Me}	[1,3N,N′-bis(2,6-bis(diphenylmethyl)-4- methylphenyl)imidazol-2-ylidene]
IPr^{Ph}	1,3-bis(2,6- diisopropylphenyl)-2-phenyl-imidazol-4-ylidene
IR	infrared
I*t*Bu	1,3-di-*tert*-butylimidazol-2-ylidene
IV	intravenous drip, line
LDA	lithium diisopropylamide
LS	low spin
LUMO	lowest unoccupied molecular orbital
M	membrane protein
MD	molecular dynamics
Me	methyl
^{Me2}cAAC	3,3,5,5-tetramethyl-1-(2′,6′-diisopropylphenyl)-pyrrolidin-2-ylidene
^{Me2}IEt	1,3-diethyl-4,5-dimethylimidazol-2-ylidene
^{Me2}I*i*Pr	1,3-diisopropyl-4,5-dimethylimidazol-2-ylidene
^{Me2}IMe	1,3,4,5-tetramethylimidazol-2-ylidene
^{Me2}IMes^{Me}	1,3-bis(2,4,6-trimethylphenyl)-4,5-dimethyl imidazol-2-ylidene
^{Me2}I*t*Bu	1,3-di-*tert*-butyl-4,5-dimethylimidazol-2-ylidene
MeIm	1-methylimidazole
Mes	mesityl
Mpro	main protease
N	Nucleocapsid protein
n.p.,	no product
*n*Bu	*n*-butyl
NHC	N-heterocyclic carbene
NMR	nuclear magnetic resonance
o-tolyl	2-methylphenyl
OTf	triflate, = trifluoromethanesulfonate
p-tolyl	4-methylphenyl
PCET	proton-coupled electron transfer
PDB	Protein Data Bank
PE	polyethylene
Ph	phenyl
phen	phenanthroline
Plip	protein ligand interaction profiler
py	pyridine
QM/MM	quantum mechanics/molecular mechanics

RAAS	Renin-Angiotensin-Aldosterone System
RBD	receptor binding domain
RDRP	RNA-dependent RNA polymerase
RE-NHC	ring expanded NHC
RNA	Ribonucleic acid
r.t.	room temperature
S	spike
S	Spin
SARS-CoV-2	severe acute respiratory syndrome coronavirus 2
SIAd	1,3-diadamantylimidazolidin-2-ylidene
SICy	1,3- dicyclohexylimidazolidin-2-ylidene
SIM	single-ion magnet
SIMe	1,3- dimethylimidazolidin-2-ylidene
SIMes	1,3-bis(2,4,6-trimethylphenyl)imidazolidin-2-ylidene
SIPr	1,3-bis(2,6-diisopropylphenyl)imidazolidin-2-ylidene
$SIPr^{OMe}$	1,3-bis(2,6-dibenzhydryl-4-methoxy-phenyl)imidazolin-2-ylidene
SI*t*Bu	1,3-di-*tert*-butylimidazolin-2-ylidene
SMM	single-molecule magnet
SOMO	singly occupied molecular orbital
ssRNA	single stranded RNA
STD	Saturation Transfer Diffusion
*t*Bu	*tert*-butyl
TEP	Tolman electronic parameter
TLC	Thin Layer Chromatography
TMS	Tetramethylsilane
Tos	tosyl = toluenesulfonyl
trip	2,4,6-triisopropylphenyl
TZ	Tetrahedral Zinc Pseudo Atoms
UV-vis	ultraviolet-visible
WHO	World Health Organization
δ	chemical shifts
ν	frequency
μ_B	Bohr magneton
μ_{eff}	effective magnetic moment

References

1. Smith SJ, Sutcliffe BT. The development of Computational Chemistry in the United Kingdom. *Rev Comput Chem*. **1997**, *10*, 271-316.
2. Boys SF, Cook GB, Reeves CM, Shavitt I. Structure, Automatic fundamental calculations of molecular. *Nature*. **1956**,*178*, 1207-1209.
3. Richards, W. G.; Walker TEH. HRK. A bibliography of ab initio molecular wave functions. *Oxford Clarendon Press*. **1971**.
4. Ng W. Brief history of computation chemistry: Three distinct eras and the relative importance of theoretical insights and computing power in advancing the field. *PeerJ Prepr*. **2014**, 1-2.
5. Allinger NL. Conformational analysis. 130. MM2. A hydrocarbon force field utilizing V1 and V2 torsional terms. *J Am Chem Soc*. **1977**, *99*, 8127-8134.
6. https://www.nobelprize.org/prizes/chemistry/1998/summary/.
7. https://www.nobelprize.org/prizes/chemistry/2013/press-release/.
8. Wang G, Zhu W. Molecular docking for drug discovery and development: A widely used approach but far from perfect. *Future Med Chem*. **2016**, 8
9. Meng X-Y, Zhang H-X, Mezei M, Cui M. Molecular Docking: A Powerful Approach for Structure-Based Drug Discovery. *Curr Comput Aided-Drug Des*. **2011**, *7*, 146-157.
10. McConkey BJ, Sobolev V, Edelman M. The performance of current methods in ligand-protein docking. *Curr Sci*. **2002**, *83*, 845-856.
11. Sperandio O, Miteva M, Delfaud F, Villoutreix BO. Receptor-Based Computational Screening of Compound Databases: The Main Docking-Scoring Engines. *Curr Protein Pept Sci*. **2006**, *7*, 369-393.
12. Bowie J, Luthy R, Eisenberg D. A method to identify protein sequences that fold into a known three-dimensional structure. *Science* **1991**, *253*, 164-170.
13. Khurshid Ahmad MH. Drug Discovery and In Silico Techniques: A Mini-Review. *Enzym Eng*. **2014**, *4*, 1-3.
14. Leelananda SP, Lindert S. Computational methods in drug discovery. *Beilstein J Org Chem*. **2016**, *12*, 2694-2718.
15. Ripphausen P, Nisius B, Peltason L, Bajorath J. Quo vadis, virtual screening? A comprehensive survey of prospective applications. *J Med Chem*. **2010**, *53*, 8461-8467.
16. Sliwoski GR, Meiler J, Lowe EW. Computational Methods in Drug Discovery Prediction of protein structure and ensembles from limited experimental data View project Antibody modeling, Antibody design and Antigen-Antibody interactions View project. *Comput Methods Drug Discov*. **2014**, *66*, 334-395.
17. Kuntz ID, Blaney JM, Oatley SJ, Langridge R, Ferrin TE. A Geometric Approach to Macromolecule-Ligand Interactions. *J Mol Biol*. **1982**, *161*, 269–288.

18. Koshland DE. The Key–Lock Theory and the Induced Fit Theory. *Angew Chemie Int Ed English*. **1995**, *33*, 2375-2378.

19. Thoma JA, D. E. Koshland J. Competitive Inhibition by Substrate during Enzyme Action. Evidence for the Induced fit Theory. *J Am Chem Soc*. **1960**, *82*, 3329-3333.

20. Dastmalchi S, Hamzeh-Mivehroud M, Sokouti B. *Methods and Algorithms for Molecular Docking-Based Drug Design and Discovery,* **2016.**

21. https://riasparklebiochemistry.wordpress.com/2013/03/31/reflection-14lock-key-vs-induced-fit-hypothesis/.

22. Goodsell DS, Sanner MF, Olson AJ, Forli S. The AutoDock suite at 30. *Protein Sci*. **2021**, *30*, 31-43.

23. https://ccsb.scripps.edu/.

24. Trott O, Olson AJ. AutoDock Vina: Improving the speed and accuracy of docking with a new scoring function, efficient optimization, and multithreading. *J Comput Chem*. **2010**, *31*, 455–461.

25. Kitchen DB, Decornez H, Furr JR, Bajorath J. Docking and scoring in virtual screening for drug discovery: Methods and applications. *Nat Rev Drug Discov*. **2004**, *3*, 935-949.

26. Forli W, Halliday S, Belew R, Olson A. AutoDock Version 4.2. *Citeseer*. **2012**,1-66.

27. Morris, G. M., Huey, R., Lindstrom, W., Sanner, M. F., Belew, R. K., Goodsell, D. S., & Olson AJ. AutoDock4 and AutoDockTools4: Automated docking with selective receptor flexibility. *J Comput Chem*. **2009**, *30*, 2785-2791.

28. Hill AD, Reilly PJ. Scoring functions for autodock. *Methods Mol Biol*. **2015**, *1273*, 467-474.

29. Sun P, Lu X, Xu C, Sun W, Pan B. Understanding of COVID-19 based on current evidence. *J Med Virol*. **2020**, *92*, 548-551.

30. Li Y Der, Chi WY, Su JH, Ferrall L, Hung CF, Wu TC. Coronavirus vaccine development: from SARS and MERS to COVID-19. *J Biomed Sci*. **2020**, *27*, 1-23.

31. https://www.who.int/health-topics/coronavirus.

32. https://www.bworldonline.com/no-one-is-safe-unless-everyone-is-safe/.

33. Wang MY, Zhao R, Gao LJ, Gao XF, Wang DP, Cao JM. SARS-CoV-2: Structure, Biology, and Structure-Based Therapeutics Development. *Front Cell Infect Microbiol*. **2020**, *10*, 1-17.

34. Huang Y, Yang C, Xu X feng, Xu W, Liu S wen. Structural and functional properties of SARS-CoV-2 spike protein: potential antivirus drug development for COVID-19. *Acta Pharmacol Sin*. **2020**, *41*, 1141-1149.

35. Hoffmann M, Kleine-Weber H, Schroeder S, et al. SARS-CoV-2 Cell Entry Depends on ACE2 and TMPRSS2 and Is Blocked by a Clinically Proven Protease Inhibitor. *Cell*. **2020**, *181*, 271-280.

36. Beyerstedt S, Casaro EB, Rangel ÉB. COVID-19: angiotensin-converting enzyme 2 (ACE2) expression and tissue susceptibility to SARS-CoV-2

infection. *Eur J Clin Microbiol Infect Dis*. **2021**, *40*, 905-919.

37. Boron Walter F. BEL. *Medical Physiology*.; **2012**.

38. Vander J. Arthur, Sherman James, Luciano Dorothy TM. *Human Physiology - The Mechanisms of Bodily Function*.; **2001**.

39. Jin Z, Du X, Xu Y, et al. Structure of Mpro from SARS-CoV-2 and discovery of its inhibitors. *Nature*. **2020**, *582*, 289-293.

40. Fehr AR, Perlman S. Coronaviruses: An Overview of Their Replication and Pathogenesis. *Methods Mol Biol*. **2015**, 1-23.

41. Burmer G, Burmer M, Pabuwal V. SARS-CoV-2 and COVID-19 Pathogenesis : A Review Biology and Life Cycle of Coronaviruses. **2020**,1-34.

42. Wang M, Cao R, Zhang L, et al. Remdesivir and chloroquine effectively inhibit the recently emerged novel coronavirus (2019-nCoV) in vitro. *Cell Res*. **2020**, *30*, 269-271.

43. Lima de Oliveira MD, Teixeira de Oliveira KM. Comparative docking of SARS-CoV-2 receptors antagonists from repurposing drugs. **2020**, 0-24.

44. Mason SW, Mcgrath ME, Noell S, Obach RS, Matthew NO. Discovery of a Novel Inhibitor of Coronavirus 3CL Protease for the Potential Treatment of COVID-19. *bioRxiv*. **2021**.

45. Amirian ES, Levy JK. Current knowledge about the antivirals remdesivir (GS-5734) and GS-441524 as therapeutic options for coronaviruses. *One Heal*. **2020**, *9*

46. Agostini ML, Andres EL, Sims AC, et al. Coronavirus susceptibility to the antiviral remdesivir (GS-5734) is mediated by the viral polymerase and the proofreading exoribonuclease. *MBio*. **2018**, *9*, 1-15.

47. https://www.youtube.com/watch?v=PXWUDX9C0xw.

48. Yakubu NS, Poyi OC, Afolabi EO. Design, Molecular Docking And In Silico Analysis Of Analogues Of Chloroquine And Hydroxychloroquine Against SARs-COV-2 Target (6w63.pdb). **2020**:1-12.

49. Satarker S, Ahuja T, Banerjee M, et al. Hydroxychloroquine in COVID-19: Potential Mechanism of Action Against SARS-CoV-2. *Curr Pharmacol Reports*. **2020**, *6*, 203-211.

50. Martineau AR, Jolliffe DA, Hooper RL, et al. Vitamin D supplementation to prevent acute respiratory tract infections: Systematic review and meta-analysis of individual participant data. *BMJ*. **2017**; 356.

51. Gombart AF. The vitamin D–antimicrobial peptide pathway and its role in protection against infection. *Future Microbiol*. **2009**, *4*, 1151-1165.

52. Chen, X., Zhao, B., Qu, Y., Chen, Y., Xiong, J., Feng, Y. and Li F. Detectable serum SARS-CoV-2 viral load (RNAaemia) is closely correlated with drastically elevated interleukin 6 (IL-6) level in critically ill COVID-19 patients. Clinical Infectious Diseases. *PMC*. **2020**, *6*, 1-32.

53. Hashemi R, Morshedi M, Jafarabadi MA, Altafi D, Hosseini-Asl SS, Rafie-Arefhosseini S. Anti-inflammatory effects of dietary Vitamin D3 in patients with multiple sclerosis. *Neurol Genet*. **2018**, *4*

54. Fu B, Xu X, Wei H. Why tocilizumab could be an effective treatment for severe COVID-19? *J Transl Med*. **2020**, *18*, 1-5.

55. Xu X, Han M, Li T, et al. Effective treatment of severe COVID-19 patients with tocilizumab. *Proc Natl Acad Sci U S A*. **2020**, *117*, 10970-10975.

56. Villar J, Ferrando C, Martínez D, et al. Dexamethasone treatment for the acute respiratory distress syndrome: a multicentre, randomised controlled trial. *Lancet Respir Med*. **2020**, *8*, 267-276.

57. Peter Horby, Wei Shen Lim, Jonathan Emberson, Marion Mafham, Jennifer Bell, Louise Linsell, Natalie Staplin, Christopher Brightling, Andrew Ustianowski, Einas Elmahi, Benjamin Prudon, Christopher Green, Timothy Felton, David Chadwick, Kanchan Rege, Christ RCG. Dexamethasone in Hospitalized Patients with Covid-19. *N Engl J Med*. **2021**, *384*, 693-704.

58. Islam R, Parves MR, Paul AS, et al. A molecular modeling approach to identify effective antiviral phytochemicals against the main protease of SARS-CoV-2. *J Biomol Struct Dyn*. **2020**

59. Sarma P, Shekhar N, Prajapat M, et al. In-silico homology assisted identification of inhibitor of RNA binding against 2019-nCoV N-protein (N terminal domain). *J Biomol Struct Dyn*. **2020**

60. Prasanth DSNBK, Murahari M, Chandramohan V, Panda SP, Atmakuri LR, Guntupalli C. In silico identification of potential inhibitors from Cinnamon against main protease and spike glycoprotein of SARS CoV-2. *J Biomol Struct Dyn*. **2020**, *3*, 1-15.

61. Manual U. MacroModel 10.8.

62. Harder E, Damm W, Maple J, et al. OPLS3: A Force Field Providing Broad Coverage of Drug-like Small Molecules and Proteins. *J Chem Theory Comput*. **2016**, *12*, 281-296.

63. Wang Q, Zhang Y, Wu L, et al. Structural and Functional Basis of SARS-CoV-2 Entry by Using Human ACE2. *Cell*. **2020**, *181*, 894-904.

64. Salentin S, Schreiber S, Haupt VJ, Adasme MF, Schroeder M. PLIP: Fully automated protein-ligand interaction profiler. *Nucleic Acids Res*. **2015**, *43*, 443-447.

65. DeLano W, Bromberg S. PyMOL User's Guide (Original). *DeLano Sci LLC*. **2004**,1-66.

66. Santos-Martins D, Forli S, Ramos MJ, Olson AJ. AutoDock4Zn: An improved AutoDock force field for small-molecule docking to zinc metalloproteins. *J Chem Inf Model*. **2014**, *54*, 2371-2379.

67. Santos-Martins D, Forli S, Ramos MJ, Olson AJ. AutoDock4Zn - Tutorial. **2014**, 4-5.

68. Keretsu S, Bhujbal SP, Cho SJ. Rational approach toward COVID-19 main protease inhibitors via molecular docking, molecular dynamics simulation and free energy calculation. *Sci Rep*. **2020**, *10*, 1-14.

69. Dhar Y V, Prasad P, Tiwari N, Pankaj V, Bano N, ... An In-Silico Study to Identify Hidden Features of Spike Protein and Main Protease of SARS-Cov2. **2020**

70. Hu J, Zhang X, Zhang X, et al. COVID-19 is more severe in patients with

hypertension; ACEI/ARB treatment does not influence clinical severity and outcome. *J Infect*. **2020**, *81*, 979-997.

71. https://pubchem.ncbi.nlm.nih.gov/.

72. Qaradakhi T, Gadanec LK, McSweeney KR, et al. The potential actions of angiotensin-converting enzyme II (ACE2) activator diminazene aceturate (DIZE) in various diseases. *Clin Exp Pharmacol Physiol*. **2020**, *47*, 751-758.

73. Peregrine AS, Mamman M. Pharmacology of diminazene: a review. **1993**, *54*, 185-203.

74. Shenoy V, Gjymishka A, Jarajapu YP, et al. Diminazene attenuates pulmonary hypertension and improves angiogenic progenitor cell functions in experimental models. *Am J Respir Crit Care Med*. **2013**, *187*, 648-657.

75. Kulemina L V., Ostrov DA. Prediction of off-target effects on angiotensin-converting enzyme 2. *J Biomol Screen*. **2011**, *16*, 878-885.

76. https://www.medchemexpress.com/losartan-carboxylic-acid.html.

77. Kellici TF, Tzakos AG, Mavromoustakos T. Rational drug design and synthesis of molecules targeting the angiotensin II type 1 and type 2 receptors. *Molecules*. **2015**, *20*, 3868-3897.

78. Agelis G, Resvani A, Koukoulitsa C, et al. Rational design, efficient syntheses and biological evaluation of N,N'-symmetrically bis-substituted butylimidazole analogs as a new class of potent Angiotensin II receptor blockers. *Eur J Med Chem*. **2013**, 62, 352-370.

79. Agelis G, Resvani A, Matsoukas MT, et al. Towards non-peptide ANG II AT1 receptor antagonists based on urocanic acid: Rational design, synthesis and biological evaluation. *Amino Acids*. **2011**; *40*, 411-420.

80. Agelis G, Resvani A, Ntountaniotis D, et al. Interactions of the potent synthetic AT1 antagonist analog BV6 with membrane bilayers and mesoporous silicate matrices. *Biochim Biophys Acta - Biomembr*. **2013**; *8*,1846-1855.

81. https://lpi.oregonstate.edu/mic/dietary-factors/phytochemicals/flavonoids.

82. Hewlings SJ, Kalman DS. Curcumin: A review of its effects on human health. *Foods*. **2017**, *6*, 1-11.

83. Zhang J, Zhang Q, Liu G, Zhang N. Therapeutic potentials and mechanisms of the Chinese traditional medicine Danshensu. *Eur J Pharmacol*. **2019**

84. Li Y, Chen H, Yang Y, et al. Danshen formula granule and salvianic acid A alleviate ethanol-induced neurotoxicity. *J Nat Med*. **2020**, *74*, 399-408.

85. Luo C, Zou L, Sun H, et al. A Review of the Anti-Inflammatory Effects of Rosmarinic Acid on Inflammatory Diseases. *Front Pharmacol*. **2020**; *11*, 1-11.

86. Boerjan W, Ralph J, Baucher M. Lignin Biosynthesis. *Annu Rev Plant Biol*. **2003**; *54*, 519-546.

87. Rajendra Prasad N, Karthikeyan A, Karthikeyan S, Venkata Reddy B. Inhibitory effect of caffeic acid on cancer cell proliferation by oxidative mechanism in human HT-1080 fibrosarcoma cell line. *Mol Cell Biochem*. **2011**, *349*, 11-19.

88. https://www.healthline.com/health/caffeic-acid.

89. Olthof MR, Hollman PCH, Katan MB. Chlorogenic acid and caffeic acid are absorbed in humans. *J Nutr*. **2001**, *131*, 66-71.

90. Li L, Liu Y, Zhao X, et al. Salvianic Acid A Sodium Promotes the Recovery of Motor Function After Spinal Cord Injury in Rats by Reducing Microglia Inflammation through Regulating MIP2/Vdac1/Ndufa12 Signaling Axis. *Orthop Surg*. **2020**, *12*, 1971-1979.

91. Ramachandran V, Watts LT, Maffi SK, Chen J, Schenker S, Henderson GI. Ethanol-Induced Oxidative Stress Precedes Mitochondrially Mediated Apoptotic Death of Cultured Fetal Cortical Neurons. *J Neurosci Res*. **2003**, *74*, 577-588.

92. Manolova Y, Deneva V, Antonov L, Drakalska E, Momekova D, Lambov N. The effect of the water on the curcumin tautomerism: A quantitative approach. *Spectrochim Acta - Part A Mol Biomol Spectrosc*. **2014**, *132*, 815-820.

93. https://cen.acs.org/acs-news/acs-meeting-news/Pfizer-unveils-oral-SARS-CoV/99/i13.

94. https://cen.acs.org/pharmaceuticals/drug-discovery/Pfizers-novel-COVID-19-antiviral/98/web/2020/09.

95. Danopoulos AA, Simler T, Braunstein P. N-heterocyclic carbene complexes of copper, nickel, and cobalt. *Chem Rev*. **2019**, *119*, 3730-3961.

96. Duong HA, Wu W, Teo YY. Cobalt-Catalyzed Cross-Coupling Reactions of Arylboronic Esters and Aryl Halides. *Organometallics*. **2017**, *36*, 4363-4366.

97. Arevalo R, Chirik PJ. Enabling Two-Electron Pathways with Iron and Cobalt: From Ligand Design to Catalytic Applications. *J Am Chem Soc*. **2019**, *141*, 23, 9106-9123.

98. Duong HA, Yeow ZH, Tiong YL, Mohamad Kamal NHB, Wu W. Cobalt-Catalyzed Cross-Coupling Reactions of Aryl Triflates and Lithium Arylborates. *J Org Chem*. **2019**, *84*, 12686-12691.

99. Liu W, Sahoo B, Junge K, Beller M. Cobalt Complexes as an Emerging Class of Catalysts for Homogeneous Hydrogenations. *Acc Chem Res*. **2018**, *51*, 1858-1869.

100. Simler T, Braunstein P, Danopoulos AA. Cobalt PNCNHC “pincers”: Ligand dearomatisation, formation of dinuclear and N2 complexes and promotion of C-H activation. *Chem Commun*. **2016**, *52*, 2717-2720.

101. Neely JM, Bezdek MJ, Chirik PJ. Insight into transmetalation enables cobalt-catalyzed Suzuki-Miyaura cross coupling. *ACS Cent Sci*. **2016**, *2*, 935-942.

102. Mukherjee A, Milstein D. Homogeneous Catalysis by Cobalt and Manganese Pincer Complexes. *ACS Catal*. **2018**, *8*, 11435-11469.

103. Κλούρας ΝΔ. *Η Ταυτότητα Των Χημικών Στοιχείων*.; **2007**.

104. Housecroft CE, A. G. Sharpe. *“Inorganic Chemistry” 3rd Edition*.; **2007**.

105. Pourret O, Faucon M-P. Cobalt. In: White WM, ed. *Encyclopedia of Geochemistry: A Comprehensive Reference Source on the Chemistry of the Earth*. Cham: Springer International Publishing; **2017**, 1-4.

106. Lindsay D, Kerr W. Cobalt close-up. *Nat Chem*. **2011**, *3*, 494.

107. Zhang L, Liu Y, Deng L, Zhang L, Liu Y, Deng L. Three-Coordinate Cobalt(IV) and Cobalt(V) Imido Complexes with N-Heterocyclic Carbene Ligation: Synthesis, Structure, and Their Distinct Reactivity in C–H Bond Amination. *J Am Chem Soc*. **2014**, *136*, 15525–15528.

108. Danopoulos AA, Simler T, Braunstein P. N-heterocyclic carbene complexes of copper, nickel, and cobalt. *Chem Rev*. **2019**, *119*, 3730-3961.

109. de Frémont P, Marion N, Nolan SP. Carbenes: Synthesis, properties, and organometallic chemistry. *Coord Chem Rev*. **2009**, *253*, 862-892.

110. Hahn FE, Jahnke MC. Heterocyclic carbenes: Synthesis and coordination chemistry. *Angew Chemie - Int Ed*. **2008**, *47*, 3122-3172.

111. Grasse PB, Brauer BE, Zupancic JJ, Kaufmann KJ, Schuster GB. Chemical and Physical Properties of Fluorenylidene: Equilibration of the Singlet and Triplet Carbenes. *J Am Chem Soc*. **1983**, *105*, 6833-6845.

112. Bourissou, D., Guerret, O., Gabbaï, F. P., Bertrand G. Stable Carbenes. *Chem Rev*. **2000**, *100*, 39-92.

113. Arduengo AJ, Bertrand G. Carbenes introduction. *Chem Rev*. **2009**, *109*, 3209-3210.

114. Parham WE, Reiff HE. Ring Expansion during the Reaction of Indenylsodium and Chloroform. *J Am Chem Soc*. **1955**, *77*, 1177-1178.

115. Parham WE, Twelves RR. Formation of Naphthalenes from Indenes. III. Substituted Methanes as Carbene Precursors. *J Org Chem*. **1957**, *22*, 730-734.

116. Staudinger H, Kupfer O. Über Reaktionen des Methylens. III. Diazomethan. *Berichte der Dtsch Chem Gesellschaft*. **1912**, *45*, 501-509.

117. Doering W von E, Hoffmann AK. The Addition of Dichlorocarbene to Olefins. *J Am Chem Soc*. **1954**, *76*, 6162-6165.

118. Skell PS, Sandler SR. Reactions of 1,1-dihalocyclopropanes with electrophilic reagents. synthetic route for inserting a carbon atom between the atoms of a double bond. *J Am Chem Soc*. **1958**, *80*, 2024-2025.

119. Doering, W. von E., Knox LH. Synthesis of Substituted Tropolones. *J Am Chem Soc*. **1953**, *75*, 297–303.

120. Tschugajeff L, Skanawy-Grigorjewa M, Posnjak A, Skanawy-Grigorjewa M. Über Die Hydrazin-Carbylamin-Komplexe des Platins. *Zeitschrift für Anorg und Allg Chemie*. **1925**, *148*, 37-42.

121. Rouschias G, Shaw BL. A revised structure for Chugaev's salt [PtC8H15N6]xClx. *Chem Commun*. **1970**, *3*, 183.

122. Fischer EO, Maasböl A. Zur Frage eines Wolfram-Carbonyl-Carben-Komplexes. *Angew Chemie*. **1964**, *76*, 645-645.

123. Schrock RR. An "alkylcarbene" complex of tantalum by intramolecular α-hydrogen abstraction. *J Am Chem Soc*. **1974**, *96*, 6796-6797.

124. Cardin DJ, Cetinkaya B, Lappert MF, Manojlović-Muir L, Muir KW. An electron-rich olefin as a source of co-ordinated carbene; Synthesis of trans-PtCl2C(NPhCH2)2PEt3. *J Chem Soc D Chem Commun*. **1971**, *8*, 400-401.

125. Hopkinson MN, Richter C, Schedler M, Glorius F. An overview of N-heterocyclic carbenes. *Nature*. **2014**, *510*, 485-496.

126. Díez-González S, Nolan SP. Stereoelectronic parameters associated with N-heterocyclic carbene (NHC) ligands: A quest for understanding. *Coord Chem Rev*. **2007**, *251*, 874-883.

127. Wanzlick H -W, Schikora E. Ein nucleophiles Carben. *Chem Ber*. **1961**, *94*, 2389-2393.

128. Wanzlick HW. Aspects of Nucleophilic Carbene Chemistry. *Angew Chemie Int Ed English*. **1962**, *1*, 75-80.

129. Wanzlick H -W, Schönherr H -J. Direct Synthesis of a Mercury Salt-Carbene Complex. *Angew Chemie Int Ed English*. **1968**, *7*, 141-142.

130. Öfele K. 1,3-Dimethyl-4-imidazolinyliden-(2)-pentacarbonylchrom ein neuer übergangsmetall-carben-komplex. *J Organomet Chem*. **1968**, *12*, 42-43.

131. Arduengo AJ, Harlow RL, Kline M. A Stable Crystalline Carbene. *J Am Chem Soc*. **1991**, *113*, 361-363.

132. Arduengo AJ, Goerlich JR, Marshall WJ. A Stable Diaminocarbene. *J Am Chem Soc*. **1995**, *117*, 11027-11028.

133. Vougioukalakis GC, Grubbs RH. Ruthenium-Based Heterocyclic Carbene-Coordinated Olefin Metathesis Catalysts. *Chem Rev*. **2010**, *110*, 1746–1787.

134. Pugh D, Danopoulos AA. Metal complexes with 'pincer'-type ligands incorporating N-heterocyclic carbene functionalities. *Coord Chem Rev*. **2007**, *251*, 610-641.

135. Nolan SP. *Asymmetric Organocatalysis Metal-Catalyzed Cross-Coupling Reactions Handbook of Metathesis*.

136. Marion N, Díez-González S, Nolan SP. N-heterocyclic carbenes as organocatalysts. *Angew Chemie - Int Ed*. **2007**, *46*, 2988-3000.

137. Gómez-Suárez A, Nelson DJ, Nolan SP. Quantifying and understanding the steric properties of N-heterocyclic carbenes. *Chem Commun*. **2017**, *53*, 2650-2660.

138. Tolman CA. Steric Effects of Phosphorus Ligands in Organometallic Chemistry and Homogeneous Catalysis. *Chem Rev*. **1977**, *77*, 313-348.

139. Glorius F. *N-Heterocyclic Carbenes in Transition Metal Catalysis. Topics in Organometallic Chemistry.* **2007**

140. Díez-González S, Marion N, Nolan SP. N-heterocyclic carbenes in late transition metal catalysis. *Chem Rev*. **2009**, *109*, 3612-3676.

141. Jacobsen H, Correa A, Poater A, Costabile C, Cavallo L. Understanding the M–(NHC) (NHC = N-heterocyclic carbene) bond. *Coord Chem Rev*. **2009**, *253*, 687-703.

142. Garber SB, Kingsbury JS, Gray BL, Hoveyda AH. Efficient and recyclable monomeric and dendritic Ru-based metathesis catalysts. *J Am Chem Soc*. **2000**, *122*, 8168-8179.

143. Ahmed M, Buch C, Routaboul L, et al. Hydroaminomethylation with novel Rhodium-Carbene complexes: An efficient catalytic approach to

pharmaceuticals. *Chem - A Eur J*. **2007**, *13*, 1594-1601.

144. Duong HA, Louie J. A nickel(0) catalyzed cycloaddition of alkynes and isocyanates that affords pyrimidine-diones. *Tetrahedron*. **2006**, *62*, 7552-7559.

145. Kinder RE, Zhang Z, Widenhoefer RA. Intermolecular hydroamination of allenes with N-unsubstituted carbamates catalyzed by a gold(I) N-heterocyclic carbene complex. *Org Lett*. **2008**, *10*, 3157-3159.

146. Laitar DS, Müller P, Sadighi JP. Efficient homogeneous catalysis in the reduction of CO2 to CO. *J Am Chem Soc*. **2005**, *127*, 17196-17197.

147. Scholl M, Ding S, Lee CW, Grubbs RH. Synthesis and Activity of a New Generation of Ruthenium-Based Olefin Metathesis Catalysts Coordinated with 1,3-Dimesityl-4,5-dihydroimidazol-2-ylidene Ligands. *Org Lett*. **1999**, *1*, 953-956.

148. Zlatogorsky S, Muryn CA, Tuna F, Evans DJ, Ingleson MJ. Synthesis, structures, and reactivity of chelating bis-N-heterocyclic- carbene complexes of iron(II). *Organometallics*. 2011, *30*, 4974-4982.

149. Danopoulos AA, Braunstein P, Stylianides N, Wesolek M. Aminolysis of bis[bis(trimethylsilyl)amido]iron and -cobalt as a versatile route to N-heterocyclic carbene complexes. *Organometallics*. **2011**, *30*, 6514-6517.

150. Karabiyikoglu S, Merlic CA. Transannular [4 + 2] Cycloaddition Reactions of Cobalt-Complexed Macrocyclic Dienynes. *Org Lett*. **2015**, *17*, 4086-4089.

151. Ford A, Miel H, Ring A, Slattery CN, Maguire AR, McKervey MA. Modern Organic Synthesis with α-Diazocarbonyl Compounds. *Chem Rev*. **2015**, *115*, 9981-10080.

152. Giese B, Erdmann P, Göbel T, Springer R. Cobalt-catalyzed carbon-carbon bond formation via radicals. *Tetrahedron Lett*. **1992**, *33*, 4545-4548.

153. Baleizão C, Garcia H. Chiral salen complexes: An overview to recoverable and reusable homogeneous and heterogenous catalysts. *Chem Rev*. **2006**, *106*, 3987-4043.

154. Hess W, Treutwein J, Hilt G. Cobalt-catalysed Carbon-carbon bond-formation reactions. *Synthesis (Stuttg)*. **2008**, *22*, 3537-3562.

155. Murata K, Matsuda A. Applications of Homogeneous Water-gas Shift Reaction. III. A Further Study of the Hydrocarbonylation. A Highly Selective Formation of Diethyl Ketone from Ethene, CO, and H 2 O . *Bull Chem Soc Jpn*. **1981**, *54*, 2089-2092.

156. Cornils B, Herrmann WA, Rasch M. Otto Roelen, Pioneer in Industrial Homogeneous Catalysis. *Angew Chemie Int Ed English*. **1994**, *33*, 2144-2163.

157. Llewellyn SA, Green MLH, Cowley AR. Cobalt N-heterocyclic carbene alkyl and acyl compounds: Synthesis, molecular structure and reactivity. *J Chem Soc Dalt Trans*. **2006**, *3*, 4164-4168.

158. Mo Z, Li Y, Lee HK, Deng L. Square-planar cobalt complexes with monodentate N-heterocyclic carbene ligation: Synthesis, structure, and catalytic application. *Organometallics*. **2011**, *30*, 4687-4694.

159. Moulton BCJ, Shaw BL. Transition metal–carbon bonds. Part XLII. Complexes of nickel, palladium, platinum, rhodium and iridium with the tridentate ligand 2,6-bis[(di-t-butylphosphino)methyl]phenyl. *J. Chem. Soc., Dalton Trans.*,

1975, *11*, 1020-1024.

160. Koten G Van. Tuning the reactivity. *Pure Appl Chem*. **1989**, *61*, 1681-1694.

161. Van Koten G, Timmer K, Noltes JG, Spek AL. A novel type of Pt-C interaction and a model for the final stage in reductive elimination processes involving C-C coupling at Pt; synthesis and molecular geometry of [1,N,N′-η-2,6-bis{(dimethylamino)methyl}- toluene]iodoplatinum(II) tetrafluoroborate. *J Chem Soc Chem Commun*. **1978**, *45*, 250-252.

162. Jensen CM. Iridium PCP pincer complexes: Highly active and robust catalysts for novel homogeneous aliphatic dehydrogenations. *Chem Commun*. **1999**, *3*, 2443-2449.

163. Hernández-Juárez M, Vaquero M, Álvarez E, Salazar V, Suárez A. Hydrogenation of imines catalysed by ruthenium(ii) complexes based on lutidine-derived CNC pincer ligands. *Dalt Trans*. **2013**, *42*, 351-354.

164. Danopoulos AA, Tsoureas N, Wright JA, Light ME. N-Heterocyclic Pincer Dicarbene Complexes of Iron(II): C-2 and C-5 Metalated Carbenes on the Same Metal Center. *Organometallics*. **2004**, *23*, 166-168.

165. Creaser CS, Kaska WC. Complexes of 1,3-bis(dimethylphosphinomethyl)benzene with nickel(II), paladium(II) and iron(II) halides. *Inorganica Chim Acta*. **1978**, *30*, 325-326.

166. Albrecht M, Van Koten G. Platinum group organometallics based on “pincer” complexes: Sensors, switches, and catalysts. *Angew Chemie - Int Ed*. **2001**, *40*, 3750-3781.

167. Parshall GW. Intramolecular aromatic substitution in transition metal complexes. *Acc Chem Res*. **1970**, *3*, 139-144.

168. Dehand J, Pfeffer M. Cyclometallated compounds. *Coord Chem Rev*. **1976**, *18*, 327-352.

169. Shilov AE, Shul’pin GB. Activation of C−H Bonds by Metal Complexes. *Chem Rev*. **1997**, *97*, 2879–2932.

170. Gu S, Du J, Huang J, et al. Unsymmetrical NCN-pincer mononuclear and dinuclear nickel(ii) complexes of N-heterocyclic carbene (NHC): synthesis, structure and catalysis for Suzuki-Miyaura cross-coupling. *Dalt Trans*. **2017**, *46*, 586-594.

171. Mehring M, Schürmann M, Jurkschat K. The first rigid O,C,O-pincer ligand and its application for the synthesis of penta- and hexacoordinate organotin(IV) compounds. *Organometallics*. **1998**, *17*, 1227-1236.

172. Vicente J, Arcas A, Blasco M-A, Lozano J, Arellano MCR de. Attempts To Prepare Palladium(II) Complexes with the O,C,O Pincer Aryl Ligand C6(NO2)2-2,6-(OMe)3-3,4,5. *Organometallics*. **1998**, *17*, 5374-5383.

173. Shih WC, Ozerov O V. Selective ortho C-H Activation of Pyridines Directed by Lewis Acidic Boron of PBP Pincer Iridium Complexes. *J Am Chem Soc*. **2017**, *139*, 17297-17300.

174. Tschersich C, Braun B, Herwig C, Limberg C. PBiP Pincer Complexes of Platinum, Palladium, and Iridium Featuring Metal-Metal Bonds Synthesized by Oxidative Addition of Bismuth-Halide Bonds. *Organometallics*. **2015**, *34*, 3782-3787.

175. Gafurov ZN, Kagilev AA, Kantyukov AO, Balabaev AA, Sinyashin OG, Yakhvarov DG. Classification and synthesis of nickel pincer complexes. *Russ Chem Bull*. **2018**, *67*, 385-394.

176. Lawrence MAW, Green KA, Nelson PN, Lorraine SC. Review: Pincer ligands—Tunable, versatile and applicable. *Polyhedron*. **2018**, *143*, 11-27.

177. Choi J, MacArthur AHR, Brookhart M, Goldman AS. Dehydrogenation and Related Reactions Catalyzed by Iridium Pincer Complexes. *Chem Rev*. **2011**, *111*, 1761–1779.

178. Koten G van, Milstein D. *Organometallic Pincer Chemistry*. **2013**, *33*

179. Deng QH, Melen RL, Gade LH. Anionic chiral tridentate n-donor pincer ligands in asymmetric catalysis. *Acc Chem Res*. **2014**, *47*, 3162-3173.

180. Takenaka K, Minakawa M, Uozumi Y. NCN pincer palladium complexes: Their preparation via a ligand introduction route and their catalytic properties. *J Am Chem Soc*. **2005**, *127*, 12273-12281.

181. Danopoulos AA, Pugh D, Wright JA. “Pincer” pyridine-dicarbene-iridium complexes: Facile C-H activation and unexpected η2-imidazol-2-ylidene coordination. *Angew Chemie - Int Ed*. **2008**, *47*, 9765-9767.

182. Jürgens E, Kunz D. A Rigid CNC Pincer Ligand Acting as a Tripodal Cp Analogue. *Eur J Inorg Chem*. **2017**, *2*, 233-236.

183. Gosiewska S, Veld MH in t., de Pater JJM, et al. Novel enantiopure non-C2-symmetric NCN-pincer palladium complexes with l-proline chiral auxiliaries: mer η3-N,C,N versus square planar η4-N,C,N,O coordination. *Tetrahedron Asymmetry*. **2006**, *17*, 674-686.

184. Danopoulos AA, Wright JA, Motherwell WB, Ellwood S. N-heterocyclic “pincer” dicarbene complexes of cobalt(I), cobalt(II), and cobalt(III). *Organometallics*. **2004**, *23*, 4807-4810.

185. Frank K. Paramagnetic Complexes in Solution: The NMR Approach. *Encycl Magn Reson*. **2011.**

186. Satterlee J. Fundamental Concepts of NMR in Paramagnetic Systems Part I : The Isotropic Shift. *Concepts Magn Reson*. **1990**, *2*, 69-79.

187. Satterlee J. Fundamental Concepts of NMR in Paramagnetic Systems Part II: Relaxation Effects. *Concepts Magn Reson*. **1990**, *2*,119-129.

188. Bradley DC, Fisher KJ. Bis(hexamethyldisilylamino)cobalt(II), a Two-Coordinated Cobalt Compound. *J Am Chem Soc*. **1971**, *93*, 2058-2059.

189. Murray BD, Power PP. Three-Coordinate Metal Amides of Manganese(II) and Cobalt(ii): Synthesis and x-ray Structure of the First Tris(Silylamide) of Manganese and the x-ray Crystal Structures of [M2(N(SiMe3)2)4] (M = Mn, Co). *Inorg Chem*. **1984**, *23*, 4584-4588.

190. Simler T, Choua S, Danopoulos AA, Braunstein P. Reactivity of a dearomatised pincer CoIIBr complex with PNCNHC donors: Alkylation and Si-H bond activation: Via metal-ligand cooperation. *Dalt Trans*. **2018**, *47*, 7888-7895.

191. Bryan AM, Long GJ, Grandjean F, Power PP. Synthesis, Spectroscopic Characterization, and Determination of the Solution Association Energy of the Dimer [Co{N(SiMe3)2}2]2: Magnetic Studies of Low-Coordinate Co(II)

Silylamides [Co{N(SiMe3)2}2L] (L = PMe3, Pyridine, and THF) and Related Species That . *Inorg Chem*. **2013**, *52*, 12152-12160.

192. Thomas Simler, Pierre Braunstein AD. Cobalt PNCNHC 'pincers': ligand dearomatisation, formation of dinuclear and N2 complexes and promotion of C–H activation. *Chem Commun*. **2016**, *52*, 2717-2720.

193. Bürger H, Wannagat U. Silylamido-Derivate von Eisen und Kobalt. *Monatsh Chem*. **1963**, *94*, 1007-1012.

194. Liang Q, Liu NJ, Song D. Constructing reactive Fe and Co complexes from isolated picolyl-functionalized N-heterocyclic carbenes. *Dalt Trans*. **2018**, *47*, 9889-9896.

195. Layfield RA, McDouall JJW, Scheer M, Schwarzmaier C, Tuna F. Structure and bonding in three-coordinate N-heterocyclic carbene adducts of iron(ii) bis(trimethylsilyl)amide. *Chem Commun*. **2011**, *47*, 10623-10625.

196. Breed, L. W., Whitehead, M. E., & Elliott RL. Aminolysis of alpha-omega-dichlorosiloxanes. *Inorg Chem*. **1963**, *6*, 1254-1255.

197. Simler T, Danopoulos AA, Braunstein P. Non-symmetrical, potentially redox non-innocent imino NHC pyridine "pincers": Via a zinc ion template-assisted synthesis. *Dalt Trans*. **2017**, *46*, 5955-5964.

198. Wright JA, Danopoulos AA, Motherwell WB, Carroll RJ, Ellwood S, Saßmannshausen J. "Pincer" N-heterocyclic carbene complexes of rhodium functionalised with pyridyl and bipyridyl donors. *Eur J Inorg Chem*. **2006**, *23*, 4857-4865.

199. Johnson AL, Kauer JC, Shahma DC, Dohfman RI. The Synthesis of 1-Arylimidazoles, a New Class of Steroid Hydroxylalion Inhibitors. *J Med Chem*. **1969**, *12*, 1024-1028.

200. Perry MC, Cui X, Powell MT, Hou DR, Reibenspies JH, Burgess K. Optically active iridium imidazol-2-ylidene-oxazoline complexes: Preparation and use in asymmetric hydrogenation of arylalkenes. *J Am Chem Soc*. **2003**, *125*, 113-123.

201. Klein D. *Organic Chemistry*, **2014**.

202. Gridnev AA, Mihaltseva IM. Synthesis of 1-alkylimidazoles. *Synth Commun*. **1994**, *24*, 1547-1555.

203. Ayumu Kiyomori, Jean-Francois Marcoux and SLB. An Efficient Copper-Catalyzed Coupling of Aryl Halides with lmidazoles. *Tetrahedron Lett*. **1999**, *40*, 2657-2660.

204. Abada S, Lecointre A, Christine C, et al. Phosphonated chelates for nuclear imaging. *Org Biomol Chem*. **2014**, *12*, 9601-9620.

205. Danopoulos AA, Tulloch AAD, Winston S, Eastham G, Hursthouse MB. Chelating and 'pincer' dicarbene complexes of palladium; synthesis and structural studies. *J Chem Soc Dalt Trans*. **2003**, *3*, 1009-1015.

206. Gong HY, Rambo BM, Karnas E, Lynch VM, Sessler JL. A Texas-sized molecular box that forms an anion-induced supramolecular necklace. *Nat Chem*. **2010**, *2*, 406-409.

207. Zhang M, Zhang Y, Zhang H, Zeng Y, Liu G. N-Heterocyclic Carbene Copper(I) Complex Catalyzed Coupling of (Hetero)aryl Chlorides and Nitrogen

Heterocycles: Highly Efficient Catalytic System. *Chinese J Chem*. **2020**, *38*, 1252-1256.

208. Caballero A, Díez-Barra E, Jalón FA, Merino S, Tejeda J. 1,1′-(Pyridine-2,6-diyl)bis(3-benzyl-2,3-dihydro-1H-imidazol-2- ylidene), a new multidentate N-heterocyclic biscarbene and its silver(I) complex derivative. *J Organomet Chem*. **2001**, *617*, 395-398.

209. Simler T, Karmazin L, Bailly C, Braunstein P, Danopoulos AA. Potassium and Lithium Complexes with Monodeprotonated, Dearomatized PNP and PNCNHC Pincer-Type Ligands. *Organometallics*. **2016**, *35*, 903-912.

210. Pugh D, Boyle A, Danopoulos AA. 'Pincer' pyridine dicarbene complexes of nickel and their derivatives. Unusual ring opening of a coordinated imidazol-2-ylidene. *J Chem Soc Dalt Trans*. **2008**, *8*, 1087-1094.

211. Danopoulos AA, Winston S, Motherwell WB. Stable N-functionalised 'pincer' bis carbene ligands and their ruthenium complexes; synthesis and catalytic studies. *Chem Commun*. **2002**, *2*, 1376-1377.

212. J. E. Parks BEW and RHH. Three-Dimensional Macrocyclic Encapsulation Reactions. Synthesis and Properties of Nonoctahedral Clathro Chelates Derived from Tris(2-aldoximo-6-pyridyl)phosphine and Boron Trifluoride or Tetrafluoroborate. *Inorg Chem*. **1971**, 10, 2472-2478.

213. Li X, Gibb CLD, Kuebel ME, Gibb BC. Two new ligands for carbonic anhydrase mimicry. *Tetrahedron*. **2001**, *57*, 1175-1182.

214. Zhang G, Scott BL, Hanson SK. Mild and homogeneous cobalt-catalyzed hydrogenation of C=C, C=O, and C=N bonds. *Angew Chemie - Int Ed*. **2012**, *51*, 12102-12106.

215. Rösler S, Obenauf J, Kempe R. A Highly Active and Easily Accessible Cobalt Catalyst for Selective Hydrogenation of C=O Bonds. *J Am Chem Soc*. **2015**,*137*, 7998-8001.

216. Zhong R, Wei Z, Zhang W, Liu S, Liu Q. A Practical and Stereoselective In Situ NHC-Cobalt Catalytic System for Hydrogenation of Ketones and Aldehydes. *Chem*. **2019**, *5*, 1552-1566.

217. Junge K, Papa V, Beller M. Cobalt–Pincer Complexes in Catalysis. *Chem - A Eur J*. **2019**, *25*, 122-143.

218. Zhang D, Zhu EZ, Lin ZW, Wei Z Bin, Li YY, Gao JX. Enantioselective Hydrogenation of Ketones Catalyzed by Chiral Cobalt Complexes Containing PNNP Ligand. *Asian J Org Chem*. **2016**, *11*, 1323-1326.

219. Zhang G, Vasudevan K V., Scott BL, Hanson SK. Understanding the mechanisms of cobalt-catalyzed hydrogenation and dehydrogenation reactions. *J Am Chem Soc*. **2013**, *135*, 8668-8681.

220. Ibrahim JJ, Reddy CB, Fang X, Yang Y. Efficient Transfer Hydrogenation of Ketones Catalyzed by a Phosphine-Free Cobalt-NHC Complex. *European J Org Chem*. **2020**, *28*, 4429-4432.

221. Ai W, Zhong R, Liu X, Liu Q. Hydride Transfer Reactions Catalyzed by Cobalt Complexes. *Chem Rev*. **2019**, *119*, 2876-2953.

222. Comas-Vives A, Ujaque G, Lledós A. Inner- and Outer-Sphere Hydrogenation Mechanisms: A Computational Perspective. *Elsevier Inc.* **2010**

223. Avital-Smilovici M. Structure Determination by X-ray Crystallography. *J Am Chem Soc*. **2013**, *135*,:3173-3185.

224. Engh R. *X-Ray Crystallography, Basic Principles, in Encyclopedic Reference of Genomics and Proteomics in Molecular Medicine*, **2006**.

225. Smyth MS, Martin JHJ. x Ray crystallography. *J Clin Pathol - Mol Pathol*. **2000**, *53*, 8-14.

226. Simler T, Danopoulos AA, Braunstein P. Non-symmetrical, potentially redox non-innocent imino NHC pyridine “pincers”: Via a zinc ion template-assisted synthesis. *Dalt Trans*. **2017**, *46*, 5955-5964.